Metabolic Modulation through Deletion of Hypoxia-Inducible Factor-1α and Fumarate Hydratase in the Heart

Violetta Steeples

A Thesis Submitted for the Degree of Doctor of Philosophy in Cardiovascular Medicine

Trinity Term 2014

Exeter College

Radcliffe Department of Medicine

Supervisors:
Professor Houman Ashrafian and Professor Hugh Watkins

Metabolic Modulation through Deletion of Hypoxia-Inducible Factor-1α and Fumarate Hydratase in the Heart

Violetta Steeples, Exeter College, University of Oxford

Abstract

Hypoxia inducible factor-1α (HIF-1α) plays a critical role in the oxygen homeostasis of all metazoans. HIF-1α is a master transcriptional regulator which coordinates the adaptive response to low oxygen tension. Through activation of a plethora of downstream target genes, HIF-1α facilitates oxygenation by promoting angiogenesis and blood vessel dilation, in addition to modulating metabolic pathways to inhibit oxidative phosphorylation and promote glycolytic energy production. Given the critical roles of hypoxia, insufficient blood supply and perturbed energetics in the pathogenesis of cardiovascular disorders, notably ischaemic heart disease, therapeutic modulation of HIF-1α is of significant clinical interest. Previous studies have demonstrated an acute cardioprotective role for both endogenous and supraphysiological HIF-1α signalling in the context of myocardial ischaemia. In contrast, *chronic* supraphysiological HIF-1α activation in the unstressed heart has been shown to induce cardiac dysfunction. To address the effect of chronic endogenous HIF-1α activation post-myocardial infarction (MI), the present work employed a murine coronary artery ligation (CAL) model in conjunction with temporally-inducible, cardiac-specific deletion of *Hif-1α*. While CAL surgery successfully modelled myocardial infarction – eliciting substantial adverse cardiac remodelling and contractile dysfunction – there was no evidence of chronic HIF-1α activation by CAL in HIF knockout or control left ventricular samples. In keeping with this, chronic ablation of *Hif-1α* (from 2 weeks post-CAL) had no discernible additional effect upon cardiac function. Overall, these findings do not support a potential therapeutic role for inhibition of HIF-1α signalling in the chronic phase post-MI.

The fundamental tricarboxylic acid (TCA) cycle enzyme fumarate hydratase (FH) converts fumarate to malate. FH deficiency is associated with smooth muscle and kidney tumours which exhibit normoxic HIF signalling due to fumarate accumulation. To investigate the potential for fumarate accumulation to elicit protective HIF signalling, a cardiac-specific *Fh1* null mouse was developed through Cre-*loxP* recombination. Strikingly, despite interruption of the TCA cycle in a highly metabolically demanding organ, cardiac *Fh1* null mice were viable, fertile and survived into adulthood, demonstrating the remarkable metabolic plasticity of the heart. However, by 3-4 months *Fh1* null mice develop a lethal cardiomyopathy characterised by cardiac hypertrophy, ventricular dilatation and contractile dysfunction. Despite lack of a pseudohypoxic response, *Fh1* null hearts did exhibit another phenomenon observed in FH-deficient cancers and also attributed to fumarate accumulation – activation of the nuclear factor (erythroid-derived 2)-like 2 (NRF2) antioxidant pathway. Heterozygous, but not homozygous, somatic deletion of *Nrf2* extended the life expectancy of cardiac *Fh1* null mice. Exploration of redox status revealed a more reductive environment in *Fh1* null hearts than controls. As a corollary, inhibition of the rate limiting enzyme of the pentose phosphate pathway – a major source of cellular reducing equivalents – with dehydroepiandrosterone conferred striking amelioration of the *Fh1* null cardiomyopathy, suggesting a possible pathogenic role for reductive stress. While loss of mitochondrial Fh1 activity and subsequent TCA cycle dysfunction likely contribute to the *Fh1* null phenotype, the importance of *cytosolic* FH was unclear. To clarify this, FH was expressed specifically in the cytosol *in vivo*. This was sufficient to substantially rescue the *Fh1* null cardiomyopathy, supporting a role for cytosolic FH disruption in its pathogenesis. Taken together, these findings highlight the potential for reductive stress to contribute to cardiac dysfunction and suggest a function for cytosolic FH in cardiac metabolic homeostasis.

Acknowledgements

I would like to thank my supervisors Professor Hugh Watkins and Professor Houman Ashrafian for the opportunity to work in their laboratory and for their constant advice, encouragement and guidance which has enabled me to perform this research

I would also like to thank the past and present members of the Watkins/Ashrafian group who have been patient in teaching me practical techniques and scientific principles. In particular, I would like to thank Dr Arash Yavari for his advice and support throughout my DPhil and especially his patience with echocardiography and teaching me image analysis; Dr Gabor Czibik for his advice, expertise and countless interesting discussions about FH; Dr Mohamed Bellahcene for sharing his guidance, surgical expertise and help; Dr Paul Robinson who taught me so many basic molecular biology techniques; I would also like to thank Dr Alexander Stockenhuber for comradeship and for sharing histological expertise and instruction; Dr Matthew Kelly for his advice, echocardiography and keeping the lab tidy; Mrs Sahar Ghaffari for her willing help; Dr Charles Redwood, Dr Katja Gehmlich, Dr Katalin Pinter, Dr Theo Kyriakou, Ms Rebeca Diaz, Dr Katie King and Dr Hend Farza for their advice. I would also like to thank Mr Phil Townsend and Dr James Brown for ensuring the laboratories run smoothly and providing excellent help and advice throughout.

I am grateful to Dr Craig Lygate for his advice; Mrs Debra McAndrew for her expertise in performing coronary artery ligation surgery; Dr Kiterie Faller and Miss Victoria Thornton for patience in performing MRI and extracting images; Dr Andrew Jefferson for advice with confocal microscopy; Dr Liam Sebag-Montefiore and Miss Rebecca Cross for advice on HPLC; Dr Patrick Pollard, Dr Julie Adam and Dr Linda O'Flaherty for advice and kind provision of mice and MEFs; the Functional Genomics Facility staff for animal husbandry; Professor David Ferguson for electron microscopy; Dr Antony Smith for flux-balance analysis; and Dr Warrick Dunn for metabolomic analysis.

Finally I would like to thank my parents for their unfailing love, patience, support, encouragement and belief in me.

Declaration of own work

Except where specifically outlined below, this DPhil thesis is entirely my work. It has not been submitted, either wholly or substantially, for another degree of this University, or for a degree at any other institution.

Echocardiography was performed by Dr Arash Yavari and Dr Matthew Kelly.
Coronary artery ligation surgery was performed by Dr Mohamed Bellahcene and Mrs Debra McAndrew.
Invasive haemodynamic assessment was conducted by Dr Mohamed Bellahcene.
Magnetic resonance imaging was performed by Dr Kiterie Faller and Miss Victoria Thornton.
Magnetic resonance images were analysed jointly with Dr Arash Yavari.
Histological analysis was performed jointly with Dr Alexander Stockenhuber.
Transmission electron microscopy was performed by Professor David Ferguson.
Primers for quantitative mitochondrial DNA measurement were designed by Dr Gabor Czibik.
Tissue harvest was frequently performed jointly with Dr Gabor Czibik to facilitate rapid snap freezing.
Flux balance analysis was performed by Dr Antony Smith (University of Cambridge).
Metabolite analysis and subsequent statistical analysis was performed by Dr Warrick Dunn (University of Birmingham).
FH null MEFs were generated by Drs Julie Adam and Linda O'Flaherty.
ROS assays were performed jointly with Dr Gabor Czibik.
Malondialdehyde measurements were generated by Dr Gabor Czibik.
Whilst the author performed the great majority of intraperitoneal and subcutaneous injections, Dr Mohamed Bellahcene, Dr Arash Yavari, Dr Matthew Kelly and Dr Alexander Stockenhuber kindly assisted with these.
Feeding, cleaning and daily checks of transgenic mice were performed by staff of the Functional Genomics Facility.

CONTENTS

List of Abbreviations

2-OG	2-Oxoglutarate
2-SC	S-(2-succinyl)-cysteine
α-MHC	α-myosin heavy chain
AAC	Ascending aortic constriction
Acta1	Actin, alpha 1
Actb	Actin, beta
AcCoA	Acetyl coenzyme A
AdFH	Adenovirus encoding fumarate hydratase
AdFHcyt	Adenovirus encoding cytosol-specific fumarate hydratase
AdFHΔATG	Adenovirus encoding fumarate hydratase with a mutated second start codon
AdGFP	Adenovirus encoding green fluorescent protein
ADM	Adrenomedullin
ADP	Adenosine diphosphate
AHR	Aryl hydrocarbon receptor
AICAR	5-Aminoimidazole-4-carboxamide ribonucleotide
ALDA	Aldolase A
AMP	Adenosine monophosphate
ANOVA	Analysis of variance
AOE	Antioxidant enzymes
ARE	Antioxidant response element
ARNT	Aryl hydrocarbon receptor nuclear translocator
Asn	Asparagine
ATP	Adenosine triphosphate
Atp2a2	ATPase, Ca^{2+} transporting, cardiac muscle, slow twitch 2 (Sarcoplasmic

	endoplasmic reticulum calcium-dependent ATPase)
bHLH	Basic helix loop helix
BCA	Bicinchoninic acid
bHLH	Basic helix loop helix
BNIP3	Bcl2 and nineteen-kilodalton interacting protein 3
BNIP3L	Bcl2 and nineteen-kilodalton interacting protein 3 like
bp	Base pairs
bpm	Beats per minute
BSA	Bovine serum albumin
BW	Body weight
CAIX	Carbonic anhydrase 9
CAG	cytomegalovirus early enhancer, chicken β-actin promoter, rabbit β-globin splice acceptor
CAL	Coronary artery ligation
CBP	CREB binding protein
CD	Cluster of differentiation
CHD	Coronary heart disease
CREB	cAMP-response element binding protein
CTAD	Carboxyl-terminal transactivation domain
CO	Cardiac output
COX	Cytochrome oxidase
DAPI	4',6-diamidino-2-phenylindole
DHEA	Dehydroepiandrosterone
DNA	Deoxyribonucleic acid
DMEM	Dulbecco's modified Eagle's media

DMOG	Dimethyloxalylglycine
dATP	Deoxyadenosine triphosphate
dNTP	Deoxynucleotide triphosphate
ECL	Enhanced chemiluminescence
ECG	Electrocardiogram
EDTA	Ethylenediaminetetraacetic acid
EF	Ejection fraction
EGLN	Egg laying defective nine
ENDO A	Endocardial area
ENO	Enolase
EPAS	Endothelial PAS domain protein
EPI A	Epicardial area
EPO	Erythropoietin
FAT	Fatty acid transporter
FBA	Flux balance analysis
FBS	Fetal bovine serum
FFA	Free fatty acid
FH	Fumarate hydratase
FIH	Factor inhibiting hypoxia inducible factor
FS	Fractional shortening
FT-ICR	Fourier transform ion cyclotron resonance
G6pdx	Glucose-6-phosphate dehydrogenase
GAPDH	Glyceraldehyde-3-phosphate dehydrogenase
GFP	Green fluorescent protein
GLUT	Glucose transporter

GPAT	Glycerol-3-phosphate acyltransferase
GPD	Glycerol-3-phospate dehydrogenase
GPI	Glucose-6-phosphate isomerase
GPX	Glutathione peroxidase
GSH	Glutathione
GSSG	Reduced glutathione dimer
HAF	Hypoxia associated factor
HBSS	Hank's buffered salt solution
HIF	Hypoxia inducible factor
HK	Hexokinase
HLRCC	Hereditary leiomyomatosis and renal cell carcinoma
HMOX	Haem oxygenase
HPLC	High-performance liquid chromatography
HRE	Hypoxia response element
HRP	Horse radish peroxidase
HW	Heart weight
IDH	Isocitrate dehydrogenase
IF	Immunofluorescence
IFU	Infection forming unit
IgG	Immunoglobulin G
IL	Infarcted length
iNOS	Inducible nitric oxide synthase
IP	Intraperitoneal
IPAS	Inhibitory PAS domain protein
IPC	Ischaemic preconditioning

I/R	Ischaemia reperfusion
IRES	Internal ribosomal entry site
ISCU	Iron sulphur cluster assembly enzyme
IVC	Individually ventilated cage
IVST	Intraventricular septum thickness
KEAP1	Kelch-like ECH-associated protein 1
JMJD	Jumonji domain
KDM	Lysine demethylase
KI	Knock-in
K_M	Michaelis-Menten constant
KO	Knock-out
LAD	Left anterior descending coronary artery
LAX	Long axis
LDHA	Lactate dehydrogenase A
AU	Arbitary units
LV	Left ventricle / Left ventricular
LVAWT	Left ventricular anterior wall thickness
LVC	Left ventricular circumference
LVDevP	Left ventricular developed pressure
LVEDD	Left ventricular end-diastolic diameter
LVEDP	Left ventricular end-diastolic pressure
LVEDV	Left ventricular end-diastolic volume
LVESD	Left ventricular end-systolic diameter
LVESV	Left ventricular end-systolic volume
LVPWT	Left ventricular posterior wall thickness

LVSP	Left ventricular systolic pressure
LW	Lung weight
LZIP	Leucine zipper
MAF	Musculoaponeurotic fibrosarcoma
MAP	Mean aterial pressure
MAX	Myc associated factor X
MCM	Mercremer
MCT	Monocarboxylate transporter
ME	Malic enzyme
MEF	Mouse embryonic fibroblast
MER	Mutated oestrogen receptor
MHC	Myosin heavy chain
MI	Myocardial infarct
miRNA	Microribonucleic acid
MLC2v	Myosin light chain 2v
MMP	Matrix metalloprotease
MPP	Mitochondrial processing peptidase
MRI	Magnetic resonance imaging
Mthfd2	Methylenetetrahydrofolate dehydrogenase ($NADP^+$ dependent) 2, methenyltetrahydrofolate cyclohydrolase
Mt-Nd1	NADH dehydrogenase
MTS	Mitochondrial targeting sequence
MXI	MAX interactor
Myh6	Myosin, heavy polypeptide 6, cardiac muscle, alpha
Myh7	Myosin, heavy chain 7B, cardiac muscle, beta

NAD	Nicotinamide adenine dinucleotide
NADH	Reduced nicotinamide adenine dinucleotide
NADP	Nicotinamide adenine dinucleotide phosphate
NADPH	Reduced nicotinamide adenine dinucleotide phosphate
NDUFAL2	NADH dehydrogenase (ubiquinone) 1 alpha subcomplex 4-like 2
Ndufv1	NADH dehydrogenase (ubiquinone) flavoprotein 1
NEB	New England biolabs
NEPAS	Neonatal and embryonic PAS
NHE	Sodium-hydrogen exchanger
Nppa	Natriuretic peptide type A
Nppb	Natriuretic peptide type B
NQO1	NAD(P)H:quinine oxidoreductase 1
NRF2	Nuclear factor (erythroid-derived 2)-like 2
NTAD	Amino-terminal transactivation domain
NT siRNA	Non-targeting short-interfering RNA
OCT	Optimum cutting temperature
OCT4	Octamer-binding transcription factor 4
ODDD	Oxygen dependent degradation domain
PAC	Protein aggregation cardiomyopathy
PAS	PER (Period circadian protein) ARNT (aryl hydrocarbon receptor aryl hydrocarbon receptor nuclear transloactor) SIM (single-minded domain)
PBS	Phosphate buffered saline
PCR	Polymerase chain reaction
PCr	Phosphocreatine
PDH	Pyruvate dehydrogenase

PDK	Pyruvate dehydrogenase kinase
PFKL	Phosphofructokinase liver
PGC	PPAR gamma coactivator
PGK	Phosphoglycerate kinase
PGM	Phosphoglycero-mutase
PER	Period circadian protein
PHD	Prolyl hydroxylase domain protein
PKM2	Pyruvate kinase muscle type2
PNC	Purine nucleotide cycle
PPAR	Peroxisome proliferator-activated receptor
Ppib	Peptidylprolyl isomerase B (cyclophilin B)
PPP	Pentose phosphate pathway
Pro	Proline
PSA	Phenyl succinic anhydride
pSIG1	pShuttle-IRES-hrGFP-1
PVDF	Polyvinylidene difluoride
qRT-PCR	Quantitative real time PCR
(R)-2-HG	(Right)-2-hydroxyglutarate
ROS	Reactive oxygen species
RNA	Ribonucleic acid
RT	Room temperature
SAICAR	Phosphoribosylaminoimidazolesuccinocarboxamide
SAX	Short axis
SAX FS	Short axis fractional shortening
SDH	Succinate dehydrogenase

SDS	Sodium dodecyl sulphate
SERCA	Sarcoplasmic/endoplasmic reticulum calcium ATPase
SIM	Single-minded protein
siRNA	Short-interfering ribonucleic acid
Slc2a1	Solute carrier family 2 (facilitated glucose transporter), member 1
Slc2a4	Solute carrier family 2 (facilitated glucose transporter), member 4
SOD	Superoxide dismutase
SV	Stroke volume
TA	Tartronic acid
TAC	Transaortic constriction
TAN	Total adenine nucleotide pool
TBE	Tris-borate-EDTA
TBST	Tris buffer saline with tween-20
TCA	Tricarboxylic acid
TCr	Total creatine pool
TEM	Transmission electron microscopy
TET	Ten eleven translocation
TGF-α	Transforming growth factor alpha
TL	Tibial length
TPI	Triose phosphate isomerase
UC	Urea cycle
UK	United Kingdom
UV	Ultraviolet
VDAC1	Voltage-dependent anion channel 1
VEGF	Vascular endothelial growth factor

VHL	von Hippel-Lindau
VSB	Viral storage buffer
WB	Western blot
WST	Water-soluble tetrazolium salt

1 CHAPTER 1: INTRODUCTION

1.1 Hypoxia Inducible Factors: Master regulators of oxygen homeostasis

Aerobic organisms are fundamentally dependent upon molecular oxygen to act as the final electron acceptor in oxidative phosphorylation to produce energy[1]. However, this oxygen utilisation confers the risk of producing excess reactive oxygen species (ROS) which can modify and damage cellular macromolecules leading to cellular dysfunction and death[1, 2]. Accordingly, tight control of oxygen homeostasis and the ability to adapt to conditions of low environmental oxygen tension are critical to cellular and organismal survival.

The erythropoietin-mediated production of oxygen-carrying red blood cells in hypoxic conditions is a striking example of oxygen homeostasis[3]. Study of this phenomenon led to the discovery of hypoxia inducible factors (HIF) as nuclear factors that bind the erythropoietin (*EPO*) gene enhancer augmenting expression[2-4]. Subsequently, HIFs were identified as master transcriptional regulators marshalling the adaptive response to hypoxia by activating of a plethora of target genes (Figure 1). Over 1,000 direct HIF target genes have now been identified, but only a subset of these are activated by HIF in a given cell type[5]. These target genes mediate cellular (e.g. glycolysis and apoptosis), local tissue (e.g. angiogenesis) and systemic (e.g. erythropoesis) effects, many of which enhance oxygen delivery and decrease oxygen use. HIFs are evolutionarily conserved being expressed in all metazoans studied from fruitflies and nematode worms, to mice and humans[1, 2]. Indeed, it has been proposed that HIFs have enabled the evolution of larger metazoans by co-ordinating development of oxygen delivery systems to balance oxygen supply with demand[1, 6].

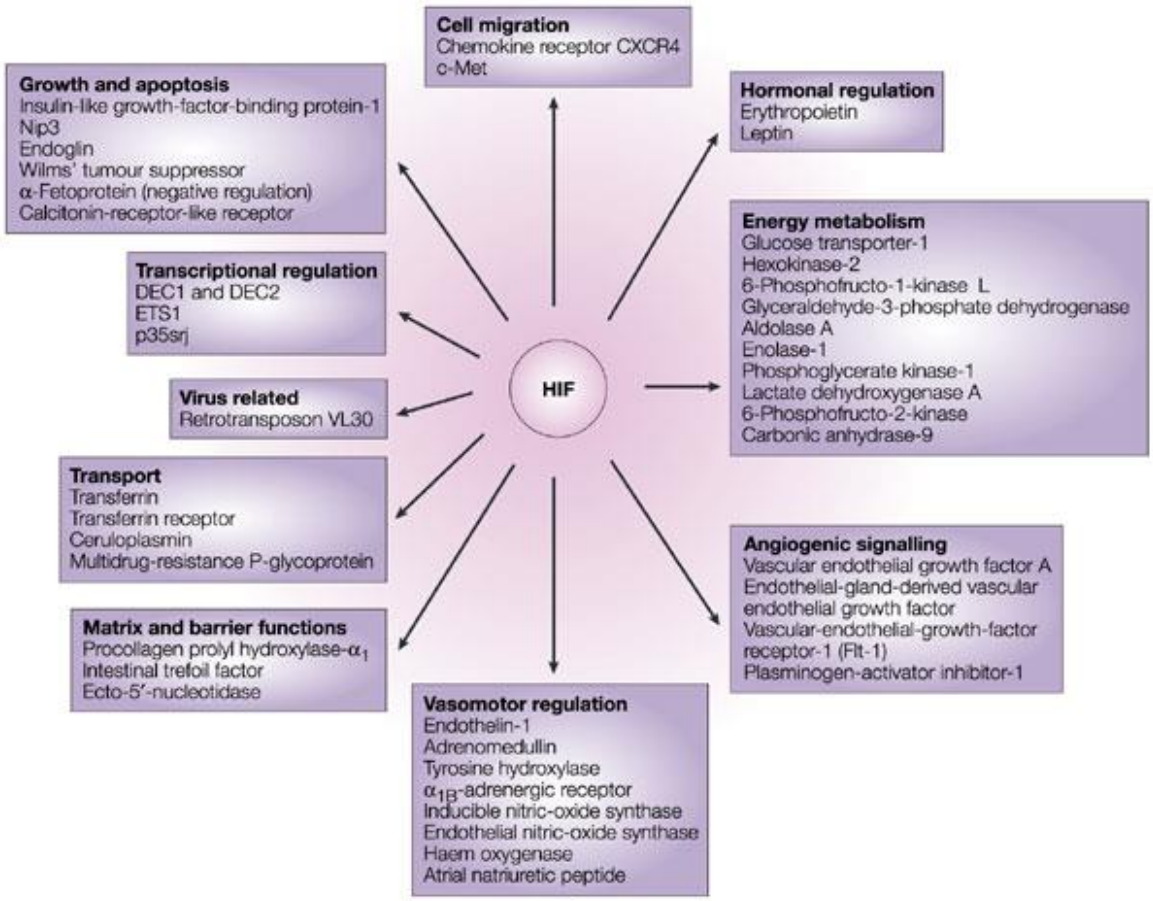

Figure 1 - A selection HIF transcription targets illustrating the wide range of biological processes they function in[1]

This figure highlights the wide range of HIF targets and the biological processes they function in. Expression of these genes adapts cells and tissues to low oxygen states. Notably, HIF augments engery production byglycolysis by inducing expression of glucose transporter 1 (*GLUT-1*) and lactate dehydrogenase A (*LDHA*) amongst others. HIFs also contribute to angiogenesis by promoting extracellular matrix remodelling and expression of proangiogenic growth factors and receptors.

1.2 Structure of HIFs

HIFs are heterodimeric transcription factors consisting of a constitutively stable HIF-β subunit (also known as aryl hydrocarbon receptor nuclear translocator [ARNT]) and a labile HIF-α subunit which is degraded in the presence of oxygen[1, 3, 7]. HIFs recognise and bind to specific deoxyribonucleic (DNA) sequences proximal to their target genes termed hypoxia response elements (HRE) which contain a core G/ACCTG motif[3, 7]. Figure 2 illustrates the domain structures of the HIF-α subunits and ARNT. HIF-α subunits and ARNT contain

[1] Adapted from Schofield, C.J. and P.J. Ratcliffe, *Oxygen sensing by HIF hydroxylases.* Nat Rev Mol Cell Biol, 2004. **5**(5): p. 343-354.

amino-terminal basic helix loop helix (bHLH) and PAS [PER (period circadian protein), aryl hydrocarbon receptor nuclear translocator (ARNT), single-minded protein (SIM)] domains which mediate heterodimerisation and DNA binding[2, 8]. In addition, most HIF-α subunits contain two oxygen-dependent degradation domains (ODDD) – where hydroxylation of specific proline residues targets the protein for degradation under normoxic conditions – and two transactivation domains [the carboxyl terminal transactivation domain (CTAD) and the amino terminal transactivation domain (NTAD)]. These transactivation domains mediate recruitment of the transcriptional coactivators CBP [CREB (cAMP-response element binding protein) binding protein) and p300, thereby facilitating activation of HIF target genes.

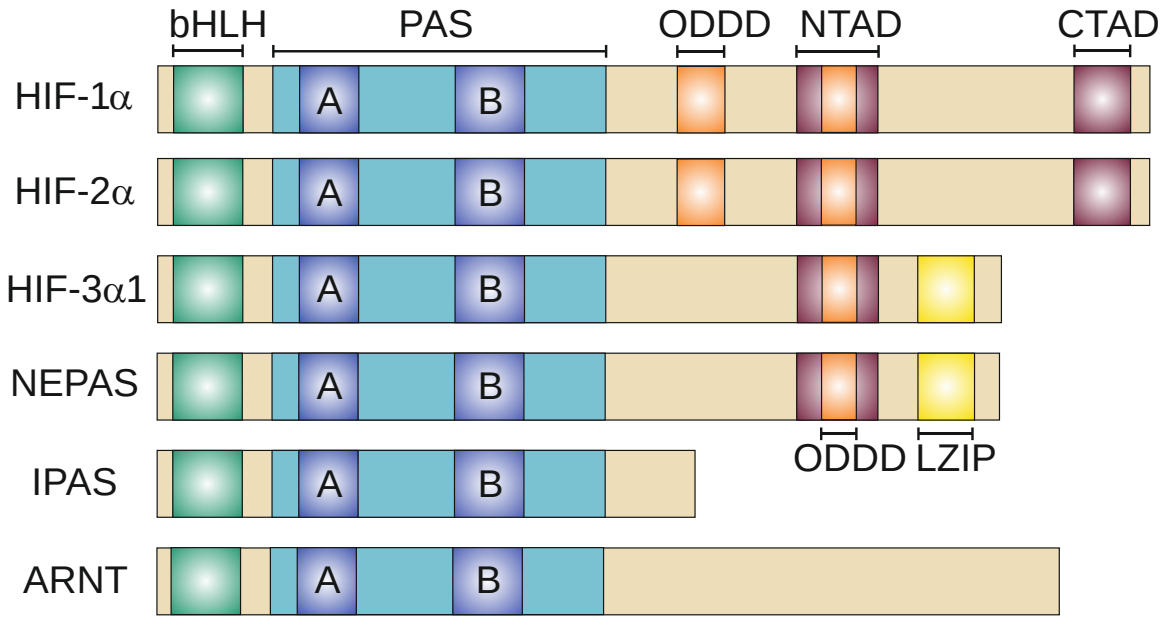

Figure 2 – The domain architecture of hypoxia inducible factors[2]
HIF proteins contain several conserved domains. Basic helix-loop-helix (bHLH) domains are involved in DNA binding. PAS [PER (period circadian protein) ARNT (aryl hydrocarbon receptor nuclear translocator) SIM (single-minded protein)] domains facilitate dimerization and consist of directly repeating PAS-A and PAS-B sequences. Oxygen-dependent degradation domains (ODDD) can be hydroxylated at proline residues. The amino terminal transactivation domain (NTAD) and carboxyl-terminal transactivation domain (CTAD) recruit transcriptional activators. Note that the NTAD overlaps with the C-terminal ODDD. Some HIF-3α splice variants also have a leucine zipper domain (LZIP.) Only some HIF-3α splice forms are shown: HIF-3α1; neonatal and embryonic PAS domain protein (NEPAS) and inhibitory pas domain protein (IPAS.) Note the similar structures of HIF-1α and HIF-2α. ARNT is HIF-β.

[2] Adapted from Schofield, C.J. and P.J. Ratcliffe, *Oxygen sensing by HIF hydroxylases.* Nat Rev Mol Cell Biol, 2004. **5**(5)

1.3 HIF-α subunits

There are 3 HIF-α subunits in mammals compared to a single HIF-α ortholog in the nematode worm. The HIF-1α and HIF-2α (also known as endothelial PAS domain protein [EPAS1]) subunits are structurally and functionally closely related. They share conserved domain architecture, are subject to oxygen-dependent degradation and stabilised in hypoxic conditions[1, 3, 8]. They activate overlapping, but distinct sets of target genes by HRE binding. However, HIF-1α and HIF-2α are not functionally redundant as demonstrated by global knockout (KO) of either gene resulting in distinct, lethal phenotypes.

1.3.1 HIF1-α and HIF-2α – Insights from murine global knock-out models

HIF-1α global KO mice exhibit developmental arrest by embryonic day 9 (E9) and lethality by E11[9]. Developmental arrest coincides with a pronounced increase in *Hif-1α* expression in wild-type embryos at this stage[2, 9]. The HIF-1α KO phenotype is characterised by neural tube defects, marked reduction in cephalic mesenchymal cell numbers, formation of abnormal large vascular structures but few small vessels, hyperplasia of the presumptive myocardium and lack of a distinct heart tube lumen and cardiac malformations[9]. This model highlights the importance of HIF-1α in the development of a functional circulatory system. Global HIF-2α KO mice exhibit a range of phenotypes depending upon their genetic background[1]. The first global HIF-2α KO developed was lethal by E15.5 due to bradycardia associated with reduced levels of the catecholamine, noradrenaline[10]. A second HIF-2α KO model exhibited defects in vascular remodelling with small blood vessels failing to fuse to form larger vessels and some vessels not sealing properly, culminating in death by E12.5[11]. On an outbred genetic background, one third of the latter mice survived post-natally for several weeks[11]. In a third model of HIF-2α deficiency, half of the offspring were observed to die at E13.5 due to cardiac failure, whilst the remainder succumbed to respiratory failure within hours of birth[12].

The potent influence of genetic background on phenotype is further highlighted by the finding that when the original embryonic lethal HIF-2α KO line[10] was outbred, some (although less than the expected Mendelian ratio) viable HIF-2α KO mice were obtained[13]. These animals exhibited multiple organ pathology, including cardiac hypertrophy, retinopathy, hepatosteatosis and mitochondrial abnormalities associated with impaired ROS homeostasis[13].

1.3.2 HIF-1α and HIF-2α – Target genes and expression patterns

HIF-1α and HIF-2α both contribute to the expression of a wide range of shared target genes, including adrenomedullin (*ADM*) and vascular endothelial growth factor (*VEGF*)[14, 15]. However some targets are exclusive to HIF-1α or HIF-2α. HIF-1α specifically mediates hypoxic activation of the pro-apoptotic and autophagic gene Bcl2/adenovirus EIB nineteen kD-interacting protein (*BNIP3*), as well as multiple genes promoting anaerobic energy production by glycolysis including: phosphoglycerate kinase (*PGK*), lactate dehydrogenase A (*LDHA*) and carbonic anhydrase-9 (*CAIX*)[15-17]. Analogously, HIF-2α exclusively activates its own target genes including octamer-binding transcription factor 4 (*OCT-4*), cyclin D1 [required for progression from cell cycle growth phase 1 (G1) to synthesis phase (S) phase] and transforming growth factor-α (*TGF-α*)[16, 17]. Interestingly, target gene specificity is not conferred by differences in the DNA-binding domain of the HIF-α subunits[14, 18, 19]. In fact, HIF-1α/ARNT and HIF-2α/ARNT dimers both recognise the same HRE. In support of this, chromatin immunoprecipitation has shown that HIF-1α/ARNT dimers bind the HREs of HIF-2α specific target genes (as well as HIF-1α responsive genes) and *vice versa*[14, 18]. Domain swap experiments have highlighted that it is the C-terminal half (especially the NTAD) of the HIF-α subunit which determines the target genes activated[7, 15, 18, 20].

HIF-1α is ubiquitously expressed, whilst HIF-2α shows a more restricted expression pattern[2, 15]. Initial reports revealed HIF-2α mRNA to be very highly expressed in vascular endothelium with lower levels evident in other cell types[21]. Subsequent studies have highlighted hypoxic HIF-2α protein expression in a wide range of tissues including heart, kidney, lung and brain[22]. In some cell types – despite binding to multiple HIF-2α target gene HREs – HIF-2α is unable to enhance transcription from these loci. It has been suggested that this is due to the presence of a titratable repressor of HIF-2α activity[14, 19, 23].

1.3.3 HIF-3α –A complex regulator of the hypoxic response

Whilst the biology of HIF-3α is less well understood than the other HIF-α subunits, it is generally viewed as a negative regulator of the hypoxic response[3, 7, 24]. Multiple splice variants of HIF-3α have been identified[24], the best studied being the inhibitory PAS domain (IPAS) protein in mouse (sharing a high similarity to HIF3A4 in humans). IPAS shares significant homology with the N-terminal bHLH and PAS domains of the other HIF-α subunits. However, IPAS lacks sequence corresponding to the transactivation domains[25]. IPAS acts as dominant negative regulator of HIF-1α mediated gene expression by binding to HIF-1α, thereby preventing its dimerisation with ARNT. IPAS shows a tissue-restricted expression pattern and is predominantly expressed in the eye, particularly the corneal epithelium, where it functions to prevent HIF-mediated induction of VEGF and subsequent maladaptive corneal vascularisation[25]. HIF-1 binds a HRE in the IPAS promoter inducing transcript expression, thus creating a negative feedback loop regulating the adaptive response to hypoxia[3, 7, 26]. Some other HIF-3α splice variants such as HIF-3α1 and neonatal and embryonic PAS protein (NEPAS) contain a region of homology to the NTAD, but none appear to contain a region homologous to the CTAD[24, 27]. These longer splice variants of HIF-3α until recently have been viewed as predominantly negative regulators which compete

with HIF-1α and HIF-2α for dimerisation with ARNT and HRE binding sites[24, 28, 29]. However, long HIF-3α isoforms can weakly activate HIF target gene expression in the presence of excess ARNT[24]. In agreement with this, recent studies demonstrate that longer isoforms of HIF-3α act as transcriptional activators inducing expression of targets both overlapping with and distinct from those of HIF-1α[28, 30].

1.4 Regulation of HIF-α stability and transactivation by oxygen

1.4.1 Prolyl hydroxylase domain proteins

The mechanism of hypoxic HIF-α stabilisation has attracted intense scientific interest and investigation. Early observations that iron chelators and cobalt chloride could facilitate normoxic stabilisation of HIF suggested that a haem-containing protein may be acting as an oxygen sensor[3]. Subsequent work demonstrated that HIF-α subunit stability and transactivation potential are co-ordinated with oxygen availability through HIF-α hydroxylation by three prolyl and one asparaginyl hydroxylases[31-33]. These non-haem ferroproteins are part of the 2-oxoglutarate dependent dioxygenase superfamily which bind a Fe^{2+} ion at their catalytic core with a 2-histidine-1-carboxylate facial triad[3, 34].

In normoxic conditions, prolyl hydroxylase domain (PHDs) proteins utilise molecular oxygen and the tricarboxylic acid (TCA) cycle intermediate 2-oxoglutarate (2-OG) as co-substrates, in the presence of the co-factors Fe^{2+} and ascorbate, to hydroxylate one or both of two conserved proline residues in the ODDD of HIF-1α or HIF-2α, producing succinate and carbon dioxide[31, 32, 35]. The von Hippel-Lindau tumour suppressor (VHL) acts as the recognition component of an ubiquitin ligase complex. VHL interacts with the prolyl-hydroxylated HIF-α subunit facilitating its ubiquitination and subsequent proteasomal

degradation (Figure 3)[36-38]. In hypoxia, PHDs are unable to hydroxylate HIF, leading to HIF stabilisation and HIF target gene activation. The Michaelis-Menten constant (K_M) of PHDs for molecular oxygen is significantly higher than physiological oxygen levels, thereby enabling PHDs to function as oxygen sensors, linking oxygen availability to HIF degradation[2, 3, 34]. As a consequence of this HIF-α subunits have an extremely short half-life.

The HIF-PHD-VHL pathway is conserved in all animals. In the nematode worm there is a single PHD ortholog termed egg laying defective nine (EGLN). In mammalian cells three PHD isoforms exist named: PHD1, PHD2 and PHD3; or EGLN2, EGLN1 and EGLN3; or HPH1, HPH2 and HPH3, respectively. PHD isoforms exhibit variable expression levels both within subcellular compartments and in different tissue locations. Whilst PHD1 is localised to the nucleus, PHD2 is predominantly cytoplasmic with some nuclear localisation, with PHD3 being found in both the nucleus and cytoplasm[34, 39]. On a tissue level, PHD1 and PHD3 are highly expressed in testis and heart respectively, however PHD2 is the most abundantly expressed PHD isoform across a range of cell types and contributes the majority of HIF prolyl hydroxylase activity in normoxia. Accordingly, PHD2 is considered to be the primary HIF prolyl hydroxylase[7, 40, 41]. This notion is supported by the observation that both PHD1 and PHD3 KO mice are viable and have a grossly normal phenotype, whilst PHD2 KO mice are non-viable, exhibiting placental and heart defects including myocardial thinning and atrial congestion with erythrocytes[27, 42].

1.4.2 Factor Inhibiting HIF

In the presence of oxygen, another 2-OG dependent dioxygenase – termed factor inhibiting HIF (FIH) – hydroxylates an asparagine residue in the CTAD of the HIF-α subunit[33]. This hydroxylation prevents the interaction of HIF-α with the co-activator p300, thereby inhibiting

HIF target gene activation in the presence of oxygen (Figure 3)[33, 43]. FIH KO mice are viable and do not show obvious developmental, angiogenic or erythropoietic phenotypes. However, they do develop multiple metabolic sequelae including: low body weight, elevated metabolic and heart rate, increased intracellular adenosine triphosphate (ATP), hyperventilation, altered lipid homeostasis and enhanced insulin sensitivity[44]. Given that *in vitro* FIH also hydroxylates a range of non-HIF substrates, including several ankyrin repeat domain containing proteins, it is uncertain whether this phenotype is due to HIF CTAD inhibition or to the effect of FIH on other targets[44].

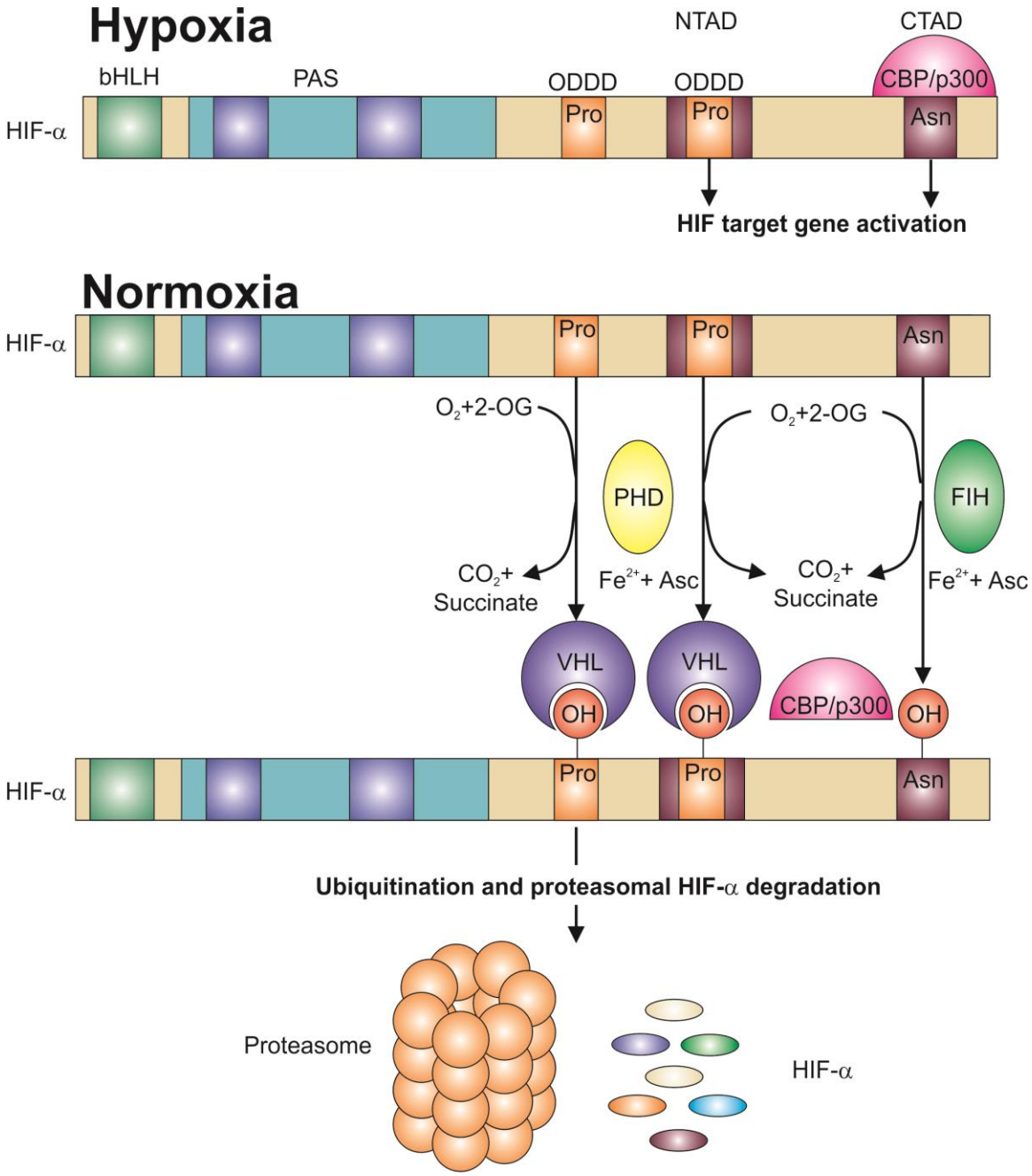

Figure 3 – Oxygen sensing by hydroxylation of HIF-α subunits
The HIF-α subunit consists of N-terminal basic helix-loop-helix (bHLH) and Per ARNT Sim (PAS) domains for dimerisation and DNA binding. The C-terminal contains the oxygen-dependent degradation domains (ODDD) and the transactivation domains (CTAD and NTAD). In hypoxic conditions, prolyl hydoxylase domain proteins (PHDs) and factor inhibiting HIF (FIH) are both inactive, thus HIF-α protein is stabilised and able to recruit co-activators such as CREB (cAMP binding protein) binding protein (CBP) and p300 to activate HIF target genes. In contrast, in normoxia molecular oxygen (O_2) and 2-oxoglutarate (2-OG) are utilised by prolyl hydroxylase domain proteins (PHDs) in the presence of the co-factors Fe^{2+} and ascorbate to hydroxylate proline residues (Pro) in the HIF-α ODDD. This facilitates recognition of the HIF-α subunit by von Hippel Lindau protein (VHL) which acts as the recognition component of an ubiquitin-E3 ligase complex, which ubiquitinates and thereby targets the HIF-α subunit for proteasomal degradation. In normoxia, FIH is also able to use O_2 and 2-OG in the presence of Fe^{2+} and ascorbate to hydroxylate an asparagine (Asn) residue in the CTAD of the HIF-α subunit. This prevents co-activator recruitment and thereby inhibits HIF target gene expression.

1.4.3 Fine-tuning the hypoxic response

The existence of multiple HIF-α and HIF hydroxylase isoforms allows fine-tuning of the cellular hypoxic response. Whilst the HIF-α subunits activate unique as well as common target genes, the PHDs manifest differing abilities to hydroxylate HIF-1α and HIF-2α. PHD2 shows a greater propensity to hydroxylate HIF-1α than HIF-2α and contributes more than PHD1 and PHD3 to controlling HIF-1α stability in normoxic conditions[40, 41]. However, PHD1 and particularly PHD3 have a greater role in HIF-2α regulation. A further level of complexity to the tightly regulated HIF system is engendered by the fact that both PHD2 and PHD3 are themselves HIF target genes, creating a negative feedback loop with enables rapid degradation of HIF-α subunits upon reoxygenation after a period of hypoxia[32, 40, 41]. Whilst PHD2 is mildly induced by hypoxia, PHD3 levels are strikingly enhanced, suggesting that PHD3 may be particularly important during and immediately post-hypoxia[40]. Hypoxic induction of the short-inhibitory HIF-3α isoforms provides a second negative feedback mechanism regulating HIF signalling.

While the CTAD contributes significantly to activation of many HIF target genes, others are predominantly activated by the NTAD[45]. FIH which represses CTAD-dependent activation has a lower K_M for oxygen than PHDs. Consequently in moderate hypoxia PHDs lose their ability to destabilise HIF, whilst FIH may still mediate repression of a subset of (CTAD-dependent) HIF targets[2, 3, 45].

It has been suggested that mitochondria act as oxygen sensors by generating ROS which inhibit HIF hydroxylase activity, potentially through oxidation of the Fe^{2+} ion at the hydroxylase catalytic core [46-48]. Whilst this theory is supported by normoxic HIF stabilisation upon treatment of cells with ROS generating agents including hydrogen peroxide[47-49], it is

considered controversial by virtue of the fact that many of the pharmacological and genetic methods used to manipulate ROS levels are likely to have confounding effects on molecular oxygen availability[7, 49, 50]. FIH exhibits even greater sensitivity than the PHDs to inhibition by hydrogen peroxide[49]. Accordingly, it appears highly likely that the HIF hydroxylases are, to at least some degree, sensitive to redox state, providing another mechanism for fine modulation of the hypoxic response[34, 49].

1.5 HIF in non-cardiac disease

Maintenance of oxygen homeostasis by the HIF pathway is pertinent to many disease pathologies with aberrant regulation of the HIF pathway implicated in several. Furthermore, hypoxia and concurrent HIF induction occur in many disorders[1].

1.5.1 Polycythaemia

Hypomorphic mutations in VHL or PHD2 and gain-of-function HIF-2α mutations can lead to HIF stabilisation and polycythaemia (elevated red blood cell count)[1, 27, 51-53]. This is mediated by elevated erythropoietin levels and enhanced erythropoietin sensitivity of erthyroid progenitors[53]. In concert with polycythaemia, hypomorphic VHL mutations in Chuvash polycythaemia result in alterations in ventilation, pulmonary vascular tone and heart rate in response to hypoxia[54].

1.5.2 Cancer

Solid tumours frequently contain hypoxic regions due to high levels of cellular proliferation coupled with abnormal vasculature[1]. Tumour hypoxia and high HIF-α levels correlate with poor prognosis for cancer patients[34]. More aggressive tumours are predisposed to grow too

large for their blood supply, leading to intra-tumoural hypoxia and elevated HIF[7]. While in this instance HIF expression could simply be considered as a prognostic marker, induction of HIF target genes could conceivably facilitate the progression of cancer. As an example, HIF contributes to the Warburg effect (aerobic glycolysis), whereby cancer cells produce energy by anaerobic rather than aerobic respiration, through increasing glucose uptake, activating glycolytic genes and inhibiting oxidative phosphorylation[7, 55]. Other HIF targets likely pertinent to cancer include factors which confer "stemness" and immortality on cells (oct4 and telomerase), growth factors (e.g. transforming growth factor α) and proangiogenic proteins which alter blood vessel growth and permeability (e.g. VEGF and angiopoietin)[27, 56, 57]. Furthermore, many HIF targets promote metastasis by facilitating extracellular matrix remodelling [e.g. matrix metalloproteases (MMP) and lysl oxidase] and extravasation of cancer cells from the blood stream to sites of metastasis (e.g. L1 cell adhesion molecule)[57].

A contributory role for HIF upregulation in cancer progression is supported by the observation that germline mutations in VHL predispose individuals to a variety of tumours including phaeochromocytomas and renal cell cancer[27]. Inactivation of VHL results in accumulation of HIF-α subunits and activation of HIF target genes. Mutations in the genes encoding TCA cycle enzymes also lead to upregulation of HIF and are associated with cancer phenotypes (see section 1.7.1.) Generally, experimental data from xenograft models indicate that HIF gain-of-function confers enhanced tumour growth and metastatic capabilities, whilst reduction in HIF activity retards tumour development[56]. However, some studies show the opposite effect. For instance, a xenograft study by Ravel *et al*. showed that whilst renal cell carcinoma cells overexpressing HIF-2α demonstrated enhanced tumour growth compared to controls, the growth of cells overexpressing HIF-1α was reduced[17].

1.6 HIF in heart disease

Coronary heart disease (CHD) is a major cause of morbidity and mortality in the United Kingdom resulting in 80,000 deaths and a cost of £19 billion to the economy[58]. Myocardial ischaemia (where cardiac oxygen demand exceeds supply) most commonly occurs in coronary artery disease (as a consequence of atherosclerotic plaques partially or completely compromising downstream myocardial blood supply) presenting as angina or myocardial infarction, but also in states of left ventricular hypertrophy such as hypertrophic cardiomyopathy (due to increased cardiac oxygen demand and capillary rarefaction)[59, 60]. HIF-1α levels are elevated in both human tissue from patients with and mouse models of myocardial infarction and hypertrophic cardiomyopathy[60-62]. However, the myriad of biological processes regulated by activation of HIF target genes makes understanding the role of HIFs in heart disease complex, since activation of some HIF targets may be deleterious, whilst others are beneficial.

1.6.1 Myocardial oxygenation

The heart is an obligatory aerobic organ with oxygen consumption vital to drive energy production primarily for contractile function, but also for action potential generation/ propagation and basal metabolic processes[63]. Unlike skeletal muscle, cardiac muscle has a continual need to contract. Accordingly, resting cardiac oxygen consumption is 20-fold higher than that of quiescent skeletal muscle when normalised per gram of tissue [63]. In order to meet these oxygen requirements, cardiac tissue maintains high basal levels of oxygen extraction (75%) from the coronary circulation, enabled in part by high capillary density[64]. During exercise, myocardial oxygen consumption increases up to 6-fold, largely due to increased heart rate and contractility[63]. While a small further increase in oxygen extraction does occur with intense exercise, the majority of the increased oxygen demand is met by

increased coronary blood flow. Coronary blood flow is closely linked to myocardial oxygen demands via metabolic feedback and neural feedforward processes which regulate coronary resistance to maintain myocardial oxygen tension[64, 65]. During systole, extravascular compression of the myocardial microvasculature occurs such that the majority of coronary blood flow occurs during diastole[66]. Determining whether these cyclical changes in coronary blood flow induce significant fluctuations in myocardial oxygen tension has been challenging. Spectrophotometric measurement of myoglobin oxygen saturation as a surrogate marker for tissue oxygen tension in isolated perfused rat hearts suggested that this does not significantly change during the cardiac cycle[67]. More recently, use of electron paramagnetic resonance spectroscopy to directly measure tissue oxygen concentration has indicated a marked reduction in myocardial oxygen concentration during systole, starting from its onset, with maximal oxygen concentration observed at the end of diastole[68]. While prolyl and asparaginyl hydroxylation affect HIF stability, nuclear translocation and/or transcriptional activity, the temporal dynamics of this entire process with altered transcription of target genes are unlikely to occur on the subsecond timescale of the cardiac cycle. However, regional or transmural anatomical differences in mean myocardial oxygen tension, such as the subendocardium which is recognised to be more prone to myocardial ischaemia, may potentially result in differential HIF transcriptional activity across the heart.

1.6.2 Enhanced oxygen delivery

Many HIF targets facilitate reoxygenation of hypoxic/ischaemic tissue. For example, erythropoietin elevates red blood cell production and thereby tissue oxygen delivery. However, excessive red blood cell production causing polycythaemia can be associated with hypertension, increasing cardiac afterload and contributing to cardiac dysfunction. Other HIF targets include vasodilators such as inducible nitric oxide synthase and adrenomedullin which

aid tissue oxygenation and reduce hypertension[55, 69]. In addition, HIFs orchestrate induction of multiple proangiogenic growth factors (e.g. VEGF and angiopoetins) in concert with their receptors [e.g. the VEGF receptor (Flt-1)] and extracellular matrix remodelling factors (e.g. MMPs and lysl oxidase) to facilitate vascularisation of ischaemic/hypoxic tissues[3, 5, 70]. Expression of constitutively active HIF-1α via deletion of the oxygen-dependent degradation domain induces formation of non-leaky blood vessels[70-73], while overexpression of the proangiogenic HIF target VEGF also enhances tissue vascularity but in this case the blood vessels formed are leaky and associated with inflammation and oedema[70-72, 74]. These findings suggest that induction of multiple targets by HIFs provides coordinated regulation of angiogenesis, which could be beneficial if harnessed to increase myocardial oxygenation in disease states.

1.6.3 Prevention of oxidative stress

In myocardial infarction, failure to reoxygenate the affected region ultimately results in cardiomyocyte death. Whilst timely reperfusion can prevent this, it risks the generation of excessive ROS and thereby oxidative damage. HIF-2α signalling combats this by activating antioxidant enzymes (AOE) such as catalase, superoxide dismutase (SOD1/2) and glutathione peroxidase (GPX)[13, 59]. Furthermore, HIFs (particularly HIF-1α) may directly reduce generation of ROS by diminishing energy production by oxidative phosphorylation (described in Section 1.6.4.2).

1.6.4 Modulation of metabolism

1.6.4.1 Fuel Choice

The heart is an omnivore capable of energy generation from a variety of substrates. Fuel choice is modified by substrate availability, tissue oxygenation and disease status[59]. The healthy adult heart preferentially generates ATP through β-oxidation of fatty acids, whilst a shift towards glucose utilisation is observed in failing hearts[5, 75]. HIF-1α mediates a switch of energy production from fatty acid oxidation to glycolytic ATP synthesis by multiple mechanisms (Figure 4). Firstly, HIF-1α upregulates the transcription factor peroxisome proliferator-activated receptor γ (PPARγ) which promotes triglyceride synthesis as opposed to fatty acid catabolism[61]. Secondly, HIF augments glucose uptake by induction of genes encoding the glucose transporters GLUT1 and GLUT3 (also known as SLC2A1 and SLC2A3)[5]. HIF also enhances glycolytic flux by activating multiple glycolytic genes, including hexokinase-2 (HK2) and glyceraldehyde-3-phosphate dehydrogenase (GAPDH)[5].

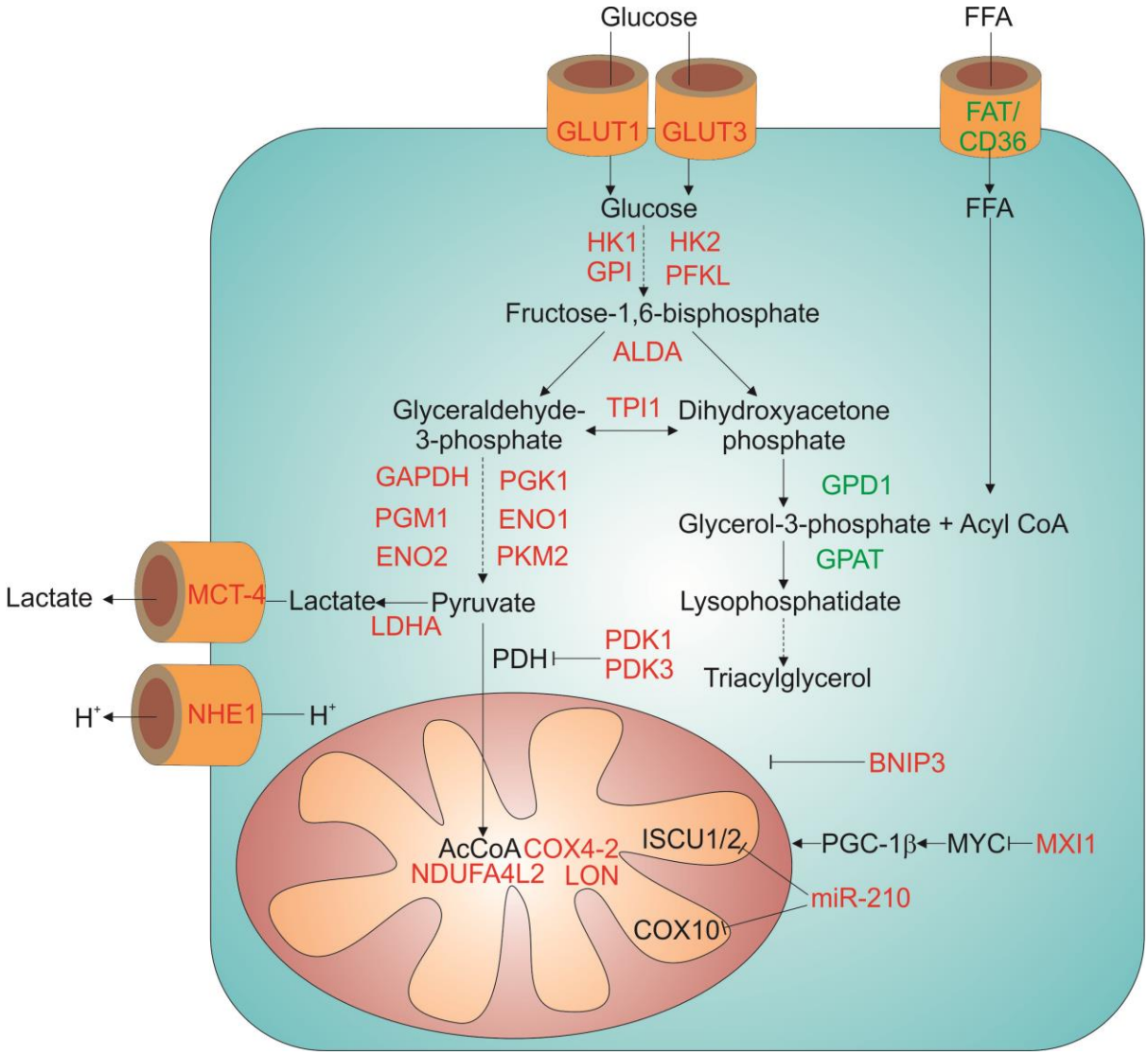

Figure 4 – Modulation of metabolism by HIF targets[3]

HIF promotes energy production by anaerobic glycolysis and inhibits mitochondrial respiration through multiple targets. HIF upregulates peroxisome proliferator-activated receptor gamma (PPARγ), supporting the accumulation of triglycerides. HIF-1α target genes are shown in red. PPARγ target genes are shown in green. AcCoA, acetyl coenzyme A; ALDA, aldolase A; BNIP, Bcl2/adenovirus EIB nineteen kD-interacting protein; CD, cluster of differentiation; COX, cytochrome c oxidase; ENO, enolase; FAT, fatty acid transporter; FFA, free fatty acid; GAPDH, glyceraldehyde-3-phosphate; GLUT, glucose transporter; GPD, glycerol-3-phosphate dehydrogenase; GPAT, Glycerol-3-phosphate acyltransferase; GPI, glucose-6-phosphate isomerase; HK, hexokinase; ISCU, iron-sulphur cluster assembly enzyme; LDHA, lactate dehydrogenase A; MCT, monocarboxylate transporter; MXI, MAX interactor; NDUFAL2, NADH (reduced nicotinamide adenine dinucleotide) dehydrogenase [ubiquinone] 1 alpha subcomplex, 4-like 2; NHE, sodium-hydrogen exchanger; PDH, pyruvate dehydrogenase; PDK, pyruvate dehydrogenase kinase; PFKL, phosphofructokinase liver; PGC, peroxisome proliferator-activated receptor gamma coactivator; PGK, phosphoglycerate kinase; PGM, phosphoglycero-mutase; PKM2, pyruvate kinase muscle type 2;TPI, triose phosphate isomerase.

[3] Adpated from Semenza, G.L., *Regulation of cancer cell metabolism by hypoxia-inducible factor 1*. Seminars in Cancer Biology, 2009. **19**(1): p. 12-16 and Krishnan, J., et al., *Activation of a HIF1α-PPARγ axis underlies the integration of glycolytic and lipid anabolic pathways in pathologic cardiac hypertrophy*. Cell Metabolism, 2009. **9**(6): p. 512-524.

1.6.4.2 Anaerobic versus oxidative metabolism

In addition to favouring use of glucose as a fuel source, HIF promotes anaerobic as opposed to oxidative energy production. This is achieved through the action of multiple HIF targets such as augmentation of lactate dehydrogenase A (LDHA) which converts pyruvate to lactate, whilst upregulation of the monocarboxylate transporter (MCT4) permits enhanced lactate cellular efflux[76]. Furthermore, HIF- induced expression of the sodium hydrogen exchanger (NHE1) and carbonic anhydrase 9 (CAIX) prevent acidification of cells during anaerobic respiration[76]. Simultaneously, activation of the HIF-1α targets pyruvate dehydrogenase (PDH) kinase 1 and 3 (PDK1 and PDK3) act to critically repress mitochondrial oxidative metabolism[5, 59, 77, 78]. By phosphorylating and thereby inactivating PDH, PDK enzymes prevent the conversion of pyruvate to acetyl coenzyme A, its entry into the TCA cycle and oxidative phosphorylation[5, 59, 77, 78].

HIF-1 limits mitochondrial oxygen consumption in multiple ways. For instance, HIF-1-mediated induction of NADH (reduced nicotinamide adenine dinucleotide) dehydrogenase [ubiquinone] 1 alpha subcomplex, 4-like 2 (NDUFA4L2) inhibits mitochondrial complex I activity, thereby reducing oxygen consumption and ROS production[79]. In hypoxia, HIF-1 transcriptionally activates the microRNA, miR-210, leading to the repression of multiple targets[80-83]. These include the cytochrome oxidase (mitochondrial complex IV) subunit (COX10) and the iron-sulphur cluster assembly proteins (ISCU1/2) which are required for the construction of iron-sulphur clusters found in aconitase and mitochondrial complex I[80, 82, 83]. Additionally, HIF mediates a switch from expression of COX4-1 in normoxia, to COX4-2 in hypoxia by directly activating the transcription of COX4-2 as well as LON, a mitochondrial protease which degrades COX4-1[5, 59, 84]. In hypoxic conditions, replacement of COX4-1 with COX4-2 results in more efficient ATP production, whilst minimising hydrogen peroxide

generation[84]. Induction of LON protease, but not COX4-2, occurs in the hearts of mice maintained at 10% oxygen levels[84], suggesting that inhibition of oxidative phosphorylation through degradation of COX4-1 rather than COX-4 isoform switching may be relevant in cardiac tissue.

Proteins and organelles can be recycled by autophagy, where they are surrounded by the double membrane of the autophagosome which fuses with a lysosome. Hypoxic induction of Bcl2/adenovirus EIB nineteen kD-interacting protein 3 (BNIP3) expression results in elevated levels of autophagy, especially mitophagy (autophagy of mitochondria)[85-87]. BNIP3-mediated mitophagy is a further mechanism by which HIF-1 promotes anaerobic energy production and diminishes mitochondrial oxidative phosphorylation. In hypoxic conditions this mitophagy may be perceived as an adaptive response, removing damaged or superfluous mitochondria in an effort to reduce ROS production. Indeed, knockdown of BNIP3 results in elevated ROS in a cellular model[87]. Furthermore, murine double knockout of BNIP3 and BNIP3L/NIX (a closely-related protein with some functional redundancy which is a HIF-1α target gene in some cell types but not in cardiomyocytes) results in cardiac hypertrophy and dysfunction associated with augmented mitochondrial content, loss of cristae structure and a wide heterogeneity of mitochondrial sizes[88]. In addition to promoting mitophagy, HIF-1α can also inhibit mitochondrial biogenesis via inhibition of myc signalling, thereby reducing PGC-1β levels[89].

In the short-term, a HIF-mediated switch from oxidative to glycolytic metabolism facilitates production of ATP in a hypoxic environment whilst simultaneously minimising ROS production. Acutely, this allows the heart to continue to function, albeit not as efficiently, whilst other HIF targets act to restore the oxygen supply. However, in the long-term

anaerobic metabolism may be insufficient to meet the energy demands of a metabolically highly active organ like the heart. Indeed, a causative role for derangement of cardiac energetics and substrate utilisation in chronic heart disease has been suggested, leading to the metaphor of the failing heart as "an engine out fuel"[75].

1.6.5 Cell Death

Experimental models demonstrate an association between cardiomyocyte dropout, adverse ventricular remodelling and the transition to heart failure[90]. In addition to its role in mitophagy, the HIF-1α target gene BNIP3 induces cell death[86, 91-93]. BNIP3 deletion preserves cardiac function in the context of ischaemia-reperfusion, whilst its overexpression is sufficient to produce a cardiomyopathy associated with elevated levels of apoptotic cell death[94]. This finding suggests that elevation of cardiac HIF-1α may be detrimental due to BNIP3-mediated cardiomyocyte dropout.

1.6.6 Genetic evidence for a role for HIFs in heart disease

Multiple mouse models have been developed to provide insights into the overall effect of HIF in heart disease. However, these models provide conflicting results, potentially due to disparities in the levels of HIF induction or reduction achieved, whether the HIF expressed was oxygen-sensitive and, perhaps critically, the differing temporal effects and importance of HIF during the progression of heart failure.

Table 1 presents an overview of these studies.

1.6.6.1 Favourable effects of HIF expression in heart disease

In ischaemic heart disease, atherosclerotic plaque stenosis or thrombotic occlusion of the coronary arteries can result in symptomatic angina and/or myocardial infarction (MI). MI results in cardiac cell death due to profound oxygen deprivation and cellular accumulation of toxic metabolites. Modern therapy of an acute MI aims to promptly restore coronary vessel patency and thus distal tissue perfusion, optimally through percutaneous coronary intervention, but also by pharmacological (thrombolytic therapy) or surgical (coronary artery bypass grafting) means. Paradoxically, acute reperfusion of the heart after an ischaemic episode can induce oxidative stress, microvascular obstruction and further cardiomyocyte death, limiting myocardial salvage, in a process termed ischaemia-reperfusion injury. In the context of chronic coronary artery occlusion reduced tissue perfusion activates HIFs and their proangiogenic targets stimulating collateral artery formation and remodelling, increasing blood flow, reducing infarct size and improving cardiac function (Figure 5)[5]. The potential clinical relevance of this is suggested by the association of single nucleotide polymorphisms in HIF-1α with alterations in human coronary artery branching and collateral artery development[5, 95-97].

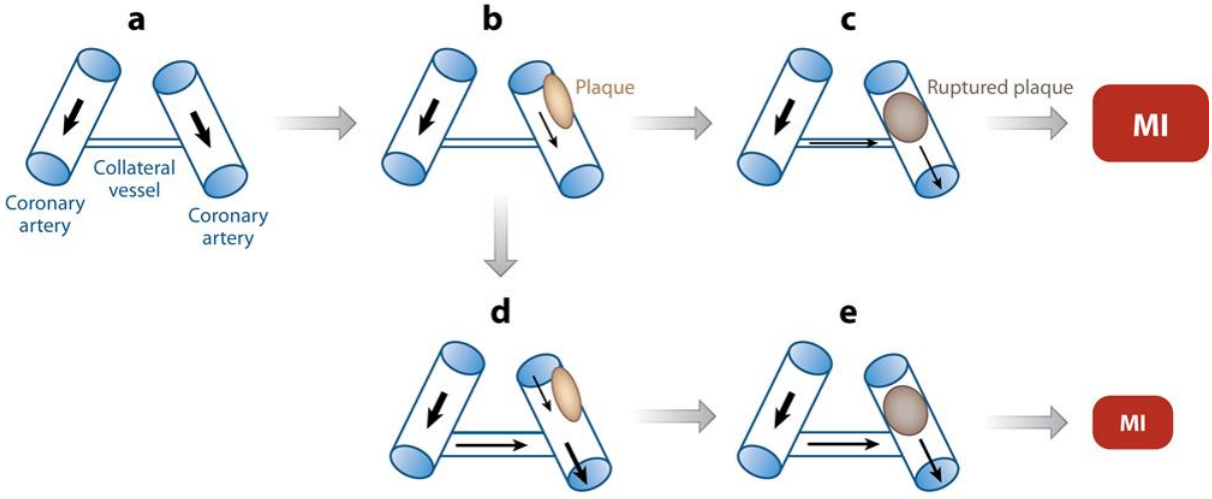

Figure 5 – Remodelling collateral blood vessels in ischaemic heart disease[4]

[4] Adapted from Semenza, G.L., *Hypoxia-inducible factor 1 and cardiovascular disease.* Annu Rev Physiol, 2014. **76**: p. 39-56.

A. Two major coronary arteries are illustrated, connected by an underdeveloped collateral vessel. **B.** An atherosclerotic plaque develops in one of the coronary arteries. **C.** In the absence of remodelling of the underdeveloped collateral vessel, rupture of the plaque results in a complete occlusion of a major coronary artery and a large myocardial infarct (MI) forms. **D.** However, reduced tissue oxygenation activates HIF and its target genes, resulting in collateral remodelling and an increased diameter of the collateral artery. **E.** In this case, plaque rupture and vessel occlusion results in a smaller MI due to the existence of some blood flow occurring through the collateral artery aiding tissue perfusion.

Ischaemic preconditioning (IPC) is a phenomenon whereby prior exposure to several brief cycles of sublethal ischaemia with intermittent periods of reperfsuion confers protection when the heart is then subjected to a longer period of (potentially lethal) ischaemia. Cardioprotection by IPC reduces infarct size and improves cardiac function through early (several hours) and delayed (from 24 hours to several days) effects[5]. HIF is stabilised by IPC and has been proposed to mediate some of the early and delayed cardioprotective effects of IPC[98].

In mouse models with reduced HIF-1α [due to haploinsufficiency or small interfering RNA (siRNA) mediated repression] the cardioprotective effect of IPC is ablated[98, 99]. Moreover, PHD2 inhibition by dimethyloxaloylglycine (DMOG) or siRNA treatment and subsequent HIF up-regulation, has a cardioprotective effect in wildtype hearts reducing infarct size[98]. Adenosine signalling has been implicated in IPC, with adenosine infusion confering acute phase cardioprotection in both wildtype and HIF-deficient hearts[99]. HIF induces expression of both CD39 and CD73 – which serve to metabolise ATP to adenosine – as well as the adenosine A2B receptor (A2BAR), suggesting that HIF may mediate acute phase cardioprotection through adenosine generation[5, 98, 99]. In fact, DMOG cannot confer cardioprotection in CD73 or A2BAR knockout hearts[98]. HIF is also thought to contribute to delayed phase preconditioning via its previously discussed roles, including modulation of vasodilation, angiogenesis and the balance between anaerobic and oxidative metabolism[5, 71].

Evidence from animal models suggests that, acutely, HIF-1α expression is beneficial in ischaemic heart disease. Depletion of cardiac HIF-1α in concert with an ischaemic insult (e.g. *ex vivo* in a perfused heart model or *in vivo* through ligation of the left anterior descending coronary artery) results in a larger infarcted area and cardiac dysfunction[98, 99]. In support of this, HIF upregulation by pharmacological[98, 100] or genetic (either directly[101, 102] or through inhibition of PHD2[69, 103-105]) manipulation in ischaemic mouse models, attenuates infarct size and improves cardiac function.

In a murine model of pressure overload (ascending aortic constriction [AAC]) , pharmacological upregulation of HIF appears to reverse cardiac dysfunction though induction of VEGF and attendant increased angiogenesis[106]. Moreover, in a similar murine pressure overload model (transverse aortic constriction (TAC)) cardiomyocyte-specific deletion of HIF-1α and inhibition of angiogenesis has been shown to prevent the development of compensatory hypertrophy resulting in cardiac dysfunction[107]. In fact, even in the absence of a challenge by ischaemia or pressure overload, cardiomyocyte-specific HIF-1α deletion has been demonstrated to result in mild cardiac hypertrophy and dysfunction associated with hypovascularity and altered calcium handling[108]. This has led to the suggestion that induction of HIF signalling would be beneficial in heart disease.

1.6.6.2 Maladaptive effects of HIF expression in heart disease

Despite the multiple favourable consequences of HIF expression in the heart, findings from models of chronic HIF activation – including transgenic overexpression studies and deletion of components of the HIF degradation pathway – suggest that cardiac HIF elevation may have deleterious consequences. Conditional somatic PHD2 deletion (which elevates HIF) in mice results in vascular dilation, polycythaemia and cardiomyopathy[109]. The latter phenotype

may, however, be potentially attributable to blood hyperviscosity, resulting in cardiac pressure overload, rather than a direct effect of PHD2 loss in cardiomyocytes *per se*[109]. In a mouse model of cardiomyocyte-specific PHD2 ablation (*cPhd2*$^{-/-}$) (lacking the potential confounder of accompanying polycythaemia) cardiac dysfunction was still observed, albeit in aged animals[110]. This phenotype was exacerbated by concomitant PHD3 deletion or pressure overload[110]. When *cPhd2*$^{-/-}$ mice were subjected to coronary artery ligation – as a model of ischaemic heart disease – they exhibited a more rapid decline in cardiac function compared to wildtype controls, despite a reduced infarct size and perioperative mortality [110]. Cardiomyocyte-specific VHL deletion (*cVhl*$^{-/-}$) results in more severe cardiac dilatation and heart failure at an earlier stage than *cPhd2*$^{-/-}$, possibly due to the compensatory effects of PHD1 and PHD3[61, 110, 111]. *cVhl*$^{-/-}$ hearts exhibited lipid accumulation, fibrosis, cardiomyocyte loss and disarray, with a significant proportion developing malignant cardiac tumours[111]. Concomitant cardiac-specific HIF-1α deletion prevented development of the *cVhl*$^{-/-}$ phenotype implicating elevation of HIF in the cardiac dysfunction observed and prompting the authors to depict *chronic* HIF activation as maladaptive and contributing to the development of heart failure[111]

Further evidence for a detrimental effect of HIF activation in heart disease is provided by studies examining the effects of chronic cardiac-specific expression of oxygen-insensitive HIF-1α or HIF-2α constructs. In these models persistent activation of HIF signalling occurs – even in the presence of oxygen – this is achieved by alanine substitution of the proline and asparagine residues normally hydroxylated by PHDs and FIH[110, 112]. Inducible cardiomyocyte-specific overexpression of a mutated, oxygen-stable variant of HIF-1α in adult mice resulted in cardiac dysfunction which was reversed when transgene expression was turned off [112]. Similarly, overexpression of a non-hydroxylatable variant of HIF-2α was

sufficient to cause left ventricular dilatation and congestive heart failure associated with histological evidence of cardiomyocyte dropout and myocardial fibrosis[110]. Indeed, even cardiac-specific overexpression of oxygen-labile HIF-1α is sufficient to induce cardiac dysfunction in aged transgenic mice and those challenged by pressure overload[60].

Krishnan *et al.* report no baseline phenotype in a mouse model of cardiac-specific HIF-1α deletion (*cHif-1α*$^{-/-}$)[61]. Moreover, they demonstrate that in the context of pressure overload, *cHif-1α*$^{-/-}$ mice are protected from cardiac hypertrophy, dysfunction, lipid accumulation and apoptosis[61]. This findings contrast with the observation of Sano *et al.* that progression to heart failure was hastened in a *cHif-1α*$^{-/-}$ model[107]. The apparent discrepancy between these findings may be explained by differences in the severity of pressure overload induced, or the use of different HIF-1α and cre recombinase mouse lines.

In summary there is clear evidence that HIF has an acute, protective effect in MI[69, 99, 101-105, 113]. In this context, HIF attenuates infarct size at least in part by mediating reoxygenation of the area at risk through activation of vasodilatory and proangiogenic targets. There is also some evidence that HIF activation of angiogenic factors in pressure overload states can facilitate compensatory hypertrophy, thereby maintaining cardiac function[106, 107]. However, emerging evidence suggests that persistent HIF activation may be detrimental in the heart, highlighting the need for caution in the therapeutic use of HIF activation to treat ischaemic heart disease beyond the acute phase [112]. Importantly, the majority of these pre-clinical studies utilised experimental paradigms of supraphysiological, oxygen-independent HIF elevation, casting doubt upon their relevance in predicting the effects of oxygen-regulated, endogenous HIF in man. Table 1 summarises the insights given by pre-clinical studies into the role of HIF in heart disease.

Model	HIF Effect	Phenotype	Ref.
HIF-1α siRNA with *in vivo* IPC followed by I/R	Beneficial	Cardioprotection by IPC was abolished by HIF-1α siRNA. PHD inactivation (DMOG or siRNA-mediated) provided cardioprotection (without IPC) reversed by HIF siRNA treatment. DMOG-mediated cardioprotection was abolished when adenosine signalling was disrupted.	[98]
HIF-1α haploinsufficiency with *ex vivo* IPC followed by I/R	Beneficial	Infarct size and apoptosis were reduced and haemodynamic function improved by IPC in WT but not HIF-1α heterozygous mice.	[99]
Pharmacological PHD inhibition *in vivo* I/R (Rat)	Beneficial	DMOG reduced infarct size and apoptosis. Increased levels of HIF and iNOS.	[100]
Oxygen labile cardiac specific HIF-1α over-expression with CAL	Beneficial	Increased capillary density, iNOS and VEGF expression in peri-infarct region. Reduced infarct size and improved cardiac function (ejection fraction and fractional shortening) 4 weeks post-CAL.	[101]
Inducible cardiac specific oxygen-stable HIF-1α overexpression with *ex vivo* I/R	Beneficial	Increased tissue viability and haemodynamic function in HIF-1α over-expressing hearts, accompanied by maintenance of mitochondrial potential.	[102]
Hypomorphic PHD2 with *ex vivo* I/R	Beneficial	Elevated HIF-1α and HIF-2α. Improved haemodynamic function post-ischaemia (no difference prior to ischaemia).	[69]
PHD2 siRNA with *ex vivo* I/R	Beneficial	PHD2 siRNA treatment elevated HIF protein levels, improved haemodynamic function and reduced infarct size. This appeared to be via HIF induction of iNOS.	[103]
Cardiomyocyte specific PHD2$^{-/-}$ (mlc2vcre) with CAL	Beneficial	Elevated HIF-1α. Increased capillary area. No difference from WT in response to TAC. Reduced infarct size and apoptosis after CAL. Improved fractional shortening 3 weeks post-CAL.	[104]
PHD2 shRNA with *in vivo* CAL model	Beneficial	PHD2 shRNA elevated HIF levels, reduced infarct size, and improved fractional shortening 2 and 4 weeks post-CAL (NB. improved function not seen at 8-weeks but plasmid degradation occurred by this point), more neovascularisation of the peri-infarct region.	[105]
Cardiac-specific HIF-1α $^{-/-}$	Beneficial	Contractile dysfunction, mild cardiac hypertrophy and hypovascularity. Reduced cell shortening, rate of cardiomyocyte calcium reuptake, cardiac tissue SERCA, high energy phosphate and lactate levels.	[108]
Dietary copper supplementation with AAC	Beneficial	Copper supplementation induces HIF, increases VEGF expression and myocardial angiogenesis whilst reversing AAC-induced hypertrophy and contractile dysfunction. VEGF antibody treatment blunted this rescue.	[106]
Inducible cardiac specific HIF-1α $^{-/-}$ with TAC	Beneficial	In TAC model HIF-1α elevation observed during compensatory hypertrophy but reduction seen during decompensated heart failure phase. HIF-1α$^{-/-}$ mice displayed attenuated hypertrophy, reduced angiogenesis and impaired cardiac function 2 weeks post-TAC. Pharmacological inhibition of angiogenesis in WT mice decreased hypertrophy and cardiac function.	[107]

Model	HIF Effect	Phenotype	Ref.
HIF-1α $^{+/-}$ with TAC	Beneficial	Despite similar hypertrophy and vessel density to WT, HIF-1α $^{+/-}$ mice demonstrate reduced cardiac function post-TAC. Reduced cardiomyocyte shortening, Ca^{2+} transients, sacroplasmic reticulum Ca^{2+} content. No change in SERCA levels.	[114]
Inducible somatic PHD2 $^{-/-}$	Adverse	PHD2 deletion during late embryogenesis results in dilated cardiomyopathy and cardiac dysfunction. Cardiac phenotype may be a consequence of polycythaemia and hyperviscosity.	[109]
Inducible cardiac specific oxygen-stable HIF-1α overexpression	Adverse	Cardiac dilatation, increased heart weight:body weight ratio, compromised ventricular function, decreased SERCA protein and slower Ca^{2+} uptake. Increased ATP:ADP ratio. Inhibition of HIF-1α overexpression restored cardiac function and SERCA levels.	[112]
Cardiomyocyte-specific VHL $^{-/-}$	Adverse	Cardiac dilatation and failure with early mortality, lipid accumulation, fibrosis, myocyte disarray and reduced mitochondria. Malignant cardiac tumours in 45% of cVHL -/- mice. Concomitant cardiac deletion of VHL and HIF-1α prevented this phenotype.	[111]
Cardiomyocyte-specific VHL $^{-/-}$	Adverse	Hypertrophy followed by dilatation. Lipid accumulation and increased apoptosis.	[61]
Cardiomyocyte-specific HIF-1α $^{-/-}$	Adverse	No basal change in cardiac function but following TAC reduced lipid accumulation and apoptosis. No hypertrophy and improved cardiac function as assessed by fractional shortening and ejection fraction.	[61]
Oxygen labile cardiomyocyte-specific HIF-1α over-expression	Adverse	No difference in cardiac function at 3 months, but increased glucose usage and capillary area. Increased Ca^{2+} transient amplitude with faster relaxation and Ca^{2+} decline, decreased SERCA2 and increased phospholamban phosphorylation. At 8 months, reduced cardiac function and increased septal and posterior left ventricular wall thickness. With TAC reduced cardiac function and elevated heart weight:body weight ratio at an earlier age.	[60]
Cardiomyocyte-specific PHD2 $^{-/-}$ global PHD3 $^{-/-}$	Adverse	Early mortality, cardiac dysfunction and dilatation, increased heart weight:body weight ratio and cardiomyocyte dropout. A cardiomyocyte-specific VHL$^{-/-}$ model showed a similar but more severe phenotype. Mitochondrial degeneration and reduced mitochondrial DNA.	[110]
Cardiomyocyte – specific PHD2 $^{-/-}$	Adverse	After TAC cPHD2 -/- mice exhibited decreased fractional shortening, cardiac dilatation, cardiomyocyte dropout and interstitial fibrosis compared to controls. Unchallenged, at 36 weeks cPHD2 -/- mice showed mild cardiac dysfunction and increased left ventricular wall thickness.	[110]
Cardiomyocyte specific PHD2$^{-/-}$ with CAL	Mixed	Smaller infarct sizes and reduced perioperative mortality in cPHD2$^{-/-}$ mice than controls, but cardiac function decreased more rapidly in cPHD2$^{-/-}$ animals.	[110]
Cardiomyocyte-specific oxygen stable HIF-2α overexpression	Adverse	Cardiac dilatation and reduced fractional shortening. Cardiomyocyte dropout and fibrosis.	[110]

Table 1 – Rodent models investigating the role of HIF in heart disease
Summarises the effect of altering HIF levels in the context of heart disease in rodent models. Prolyl hydroxylase domain (PHD) inactivation, von Hippel-Lindau (VHL) inactivation, transgenic HIF-α over-expression, DMOG and copper supplementation all serve as mechanisms to elevate HIF signalling. HIF siRNA, haploinsufficiency and knockout act to reduce HIF signalling. All models are murine unless otherwise stated. Models of ischaemic heart disease: IPC, ischaemic preconditioning; I/R, ischaemia with reperfusion; CAL, coronary artery ligation. Models of pressure overload: TAC, transverse aortic constriction; AAC, ascending aortic constriction. Other abbreviations: DMOG: Dimethyloxalylglycine; SERCA; sarcoplasmic/endoplasmic reticulum calcium ATPase.

1.7 Modulation of metabolic enzymes including fumarate hydratase

1.7.1 Mutations in metabolic enzymes can initiate a pseudohypoxic response

A pseudohypoxic response occurs when HIF-α levels are elevated and downstream cellular pathways aberrantly activated under normoxic conditions. Loss-of-function mutations in the gene encoding the metabolic enzyme fumarate hydratase (FH) initiate a pseudohypoxic response[115, 116]. FH catalyses the conversion of fumarate to malate in the mitochondrial TCA cycle. The FH substrate, fumarate, has a similar structure to the PHD co-substrate, 2-OG. In the absence of FH activity, accumulated fumarate competitively inhibits PHDs, resulting in a pseudohypoxic response (Figure 6)[116]. FH functions as a tumour suppressor, with heterozygous germline mutations in *FH* predisposing individuals to hereditary leiomyomatosis and renal cell carcinoma (HLRCC)[117-121]. The associated leiomyomata are usually benign smooth muscle tumours of the arrector pili and uterine fibroids[119]. Most leiomyomata and renal tumours demonstrate a "second hit" causing somatic inactivation of the functional allele[115-117]. Germline homozygous or compound heterozygous *FH* mutations result in severe neurodegeneration, encephalopathy and premature death[121-123].

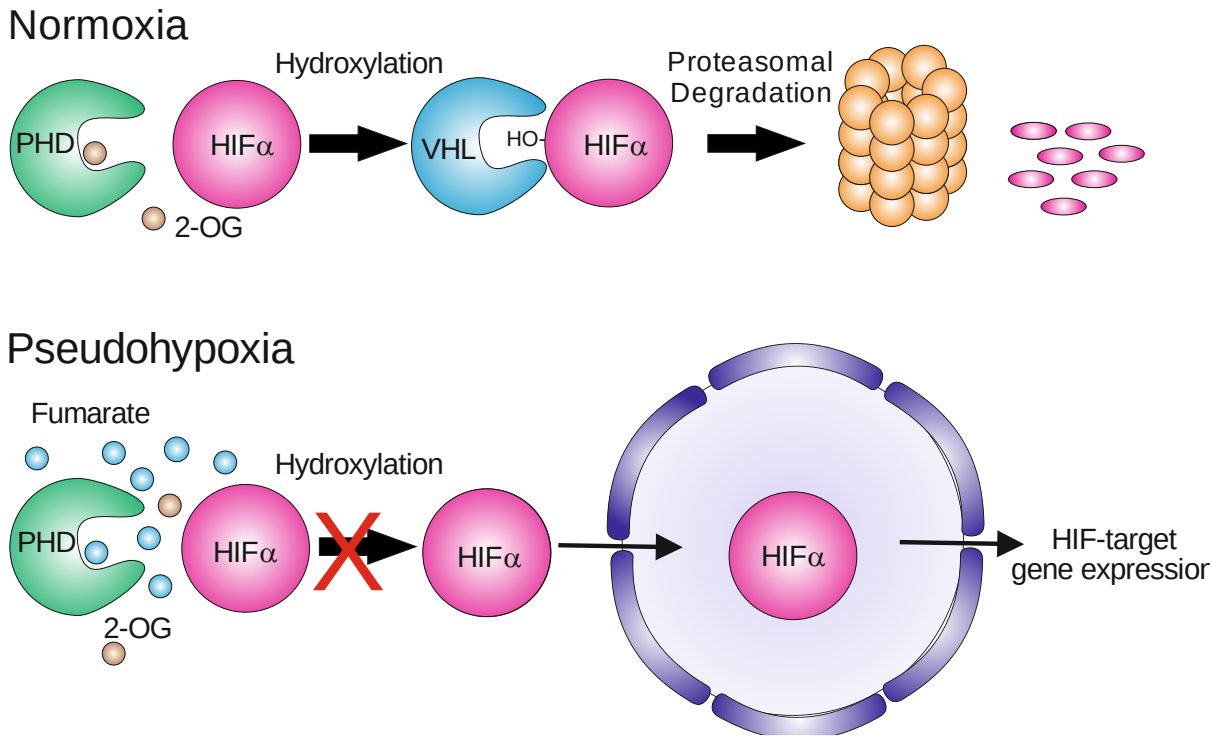

Figure 6 – Fumarate accumulation results in a pseudohypoxic response
In normoxia, hypoxia inducible factors (HIFs) are hydroxylated by prolyl hydroxylase domain proteins (PHD) in the presence of the cofactor 2-oxoglutarate (2-OG). This targets HIFs for recognition by the von Hippel-Lindau protein (VHL) and degradation by the proteasome. A pseudohypoxic response occurs when fumarate accumulates due to inactivation of fumarate hydratase (FH). The resulting excess fumarate competitively inhibits PHD activity preventing the hydroxylation and targeting of HIFs for degradation. HIFs can then translocate to the nucleus, inducing expression of target genes. Inactivation of succinate dehydrogenase leads to an accumulation of succinate which initiates a pseudohypoxic response by a similar mechanism.

Inactivation of another TCA cycle enzyme succinate dehydrogenase (SDH), which catalyses the conversion of succinate to fumarate, is also associated with a cancer phenotype. Germline heterozygous mutations in the genes encoding the SDH subunits A, B, C and D predispose carriers to developing phaeochromocytoma and paraganglioma upon somatic loss of the second allele[124-127]. In these tumours – analogous to FH neoplasms – a pseudohypoxic response is observed due to inhibition of PHDs by accumulated succinate[115, 128]. Akin to homozygous mutations in *FH*, germline homozygous *SDH* mutations result in severe neurological impairment[120, 121, 129].

Mutations in the nicotinamide adenine dinucleotide phosphate ($NADP^+$)-dependent forms of the metabolic enzyme isocitrate dehydrogenase (IDH1 and IDH2), which catalyses the

conversion of citrate and $NADP^+$ to 2-OG and NADPH in the cytoplasm (IDH1) and mitochondria (IDH2), are associated with gliomas and acute myeloid leukaemia[130-137]. However, the NAD^+-dependent isoform, IDH3, which generates 2-OG and NADH in the TCA cycle, has not been associated with a tumour phenotype[134]. Unlike FH and SDH, IDH acts as an oncogene with mutation of a single allele observed in cancers[132, 133, 138]. Cancer associated mutations in IDH1 and IDH2 are gain-of-function mutations which confer the ability to catalyse the NADPH-dependent reduction of 2-OG to (R-)-2-hydroxyglutarate [(R)-2HG][133, 138]. In some models 2-HG can inhibit 2-OG dependent dioxygenases, including PHDs, leading to a pseudohypoxic response[139-141]. Conversely, Koivunen *et al*. demonstrate that in some contexts (R)-2-HG can stimulate PHD activity[142].

The observation that mutations in key metabolic enzymes lead to the accumulation of fumarate, succinate and (R)-2-HG and development of cancer phenotypes has inspired the term oncometabolite. An oncometabolite has been described as a normal metabolic molecule whose accumulation primes cells for progression for cancer[136]. Despite the concurrence of oncometabolite accumulation, a pseudohypoxic response and cancer, evidence suggests that the pseudohypoxic response does not play a *causative* role in oncogenesis. In a murine model of *Fh1* inactivation in the kidney, renal cysts are formed[143]. These cysts resemble the early pre-neoplastic lesions observed in renal cell carcinoma and show dramatic accumulation of fumarate and activation of hypoxic signalling[143, 144]. Concurrent renal deletion of *Hif-1α* and/or *Hif-2α* with *Fh1* does not ameliorate renal cyst development, in fact, inactivation *Fh1* and *Hif-1α* in concert exacerbated the cystic phenotype[145]. While this suggests that the early stages of renal cell carcinoma are HIF-independent, it does not preclude a role for the pseudohypoxic response in later stages of tumour development.

1.7.2 Inhibition of other 2-oxoglutarate dependent oxygenases

PHDs and FIH belong to a large family of 2-OG dependent oxygenases with roles in a wide range of biological processes pertinent to both cardiovascular disease and cancer including collagen biosynthesis, DNA repair, epigenetic regulation of gene expression and oxygen sensing[146]. Oncometabolites can inhibit other members of the 2-OG dependent oxygenase family[146].

In the heart, collagen provides a supportive matrix where the cardiomyocytes and myofibrils align, however, elevated levels of cross-linked collagen result in fibrosis and increase myocardial stiffness. It has been suggested that inhibiting procollagen prolyl hydroxylases, which facilitate the maturation of collagen, may be beneficial in the setting of MI [147]. However, it is probable that the inhibitors used in these studies would also have provided cardioprotection by inhibiting HIF hydroxylases[148]. Fumarate, succinate and (R)-2-HG can all inhibit collagen prolyl hydroxylases[140, 149].

Methylation of cytosine residues in CpG islands usually leads to silencing of proximal gene expression, although in some contexts it may actually elevate expression[150-152]. The ten eleven translocation (TET) family of DNA hydroxylases are 2-OG dependent oxygenases that catalyse the first step in DNA demethylation. Haas *et al.* observed differences in DNA methylation patterns between dilated cardiomyopathy patients and controls[150, 151]. They confirmed a role for the genes identified in a zebrafish model. This emphasises the potential for inhibition of DNA hydroxylases to play a role in modifying cardiac function.

Methylation of histone lysine residues leads to transcriptional activation or silencing dependent upon the chromatin location and degree of methylation (i.e. mono-, di- or tri-

methylation)[153]. Jumonji domain (JMJD) lysine demethylases (KDMs) are 2-OG dependent dioxygenases which actively demethylate histones[151-153]. Histone methylation patterns play a role in the progression of heart disease. For example deletion or overexpression of the histone demethylase, *Jmj2a* (also known as *Kdm4a*), respectively attenuates or exacerbates the cardiac hypertrophy observed in a murine model of pressure overload[153].

It has been demonstrated that fumarate, succinate and (R)-2-HG can inhibit PHDs, collagen prolyl hydroxylases, TETs and KDMs[140, 141, 146, 154]. Mutations in *Fh1*, *Sdh* subunits, *Idh1* and *Idh2* are associated with a hypermethylator phenotype in cancers, implying that epigenetic regulation of gene expression may play a role in oncogenesis[155, 156]. In a transgenic mouse model, *Idh2* mutations cause (R)-2-HG accumulation and the development of cardiomyopathy[157]. This cardiomyopathy is associated with glycogen accumulation, cardiomyocyte apoptosis and mitochondrial degeneration[157]. Alterations in histone methylation and gene expression were observed in these hearts[157]. Nude mice implanted with (R)-2-HG secreting tumours develop cardiomyopathy, suggesting a paracrine effect of elevated serum (R)-2-HG[157].

1.7.3 Succination by fumarate

Fumarate can act as an electrophile, reacting with cysteine residues in proteins in a Michael addition reaction forming S-(2-succinyl)-cysteine (2-SC) - a process termed succination (Figure 7)[135-137, 158]. Fumarate hydratase deficient cells accumulate high levels of 2-SC, which has been suggested as a biomarker for HLRCC[159]. Succination is often connected to inactivation of protein function. For example, in diabetic models, fumarate accumulation has been associated with the succination and inactivation of GAPDH[158]. Another example is fumarate accumulation in *Fh1* deficient cells which can result in the succination and

inhibition of mitochondrial aconitase which catalyses the conversion of citrate to isocitrate in the TCA cycle[160].

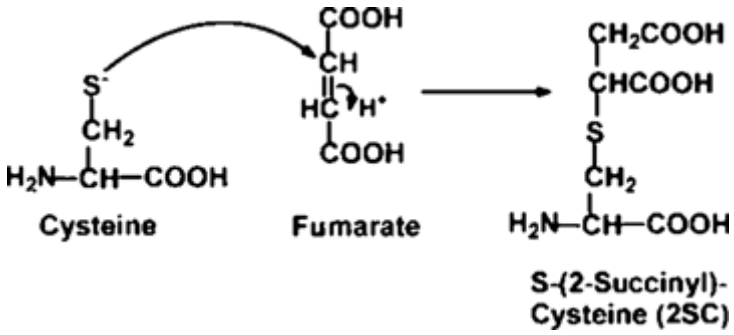

Figure 7 – Succination of cysteine residues by fumarate[5]
Illustrates the mechanism of formation of S-(2-succinyl)-cysteine by the nucleophilic addition of cysteine to fumarate by a Michael addition reaction.

1.7.3.1 NRF2 activation and modulation of metabolism in FH deficiency

KEAP1 (Kelch-like ECH-associated protein 1), a major cellular electrophile sensor, is succinated by accumulated fumarate in FH deficient cells and tissues[145, 161]. In normal physiological conditions, KEAP1 acts as an adaptor protein, interacting with the transcription factor NRF2 [nuclear factor (erythroid-derived 2)-like 2] and promoting its ubiquitination by the E3-ubiquitin ligase complex and subsequent proteasomal degradation[136, 162]. In FH deficiency, succination of key KEAP1 cysteine residues prevents its interaction with NRF2, resulting in NRF2 stabilisation (Figure 8)[145, 161]. NRF2 heterodimerizes with small MAF (musculoaponeurotic fibrosarcoma) proteins and binds to antioxidant response elements (AREs), inducing expression of cytoprotective genes that encode proteins with antioxidant and detoxifying properties, for example NAD(P)H:quinone oxidoreductase 1 (NQO1) which catalyses the reduction of reactive quinones[162].

[5] Adaptated from Blatnik, M., Thorpe, S.R. & Baynes, J.W. Succination of proteins by fumarate: mechanism of inactivation of glyceraldehyde-3-phosphate dehydrogenase in diabetes. *Ann N Y Acad Sci*, 047 (2008)

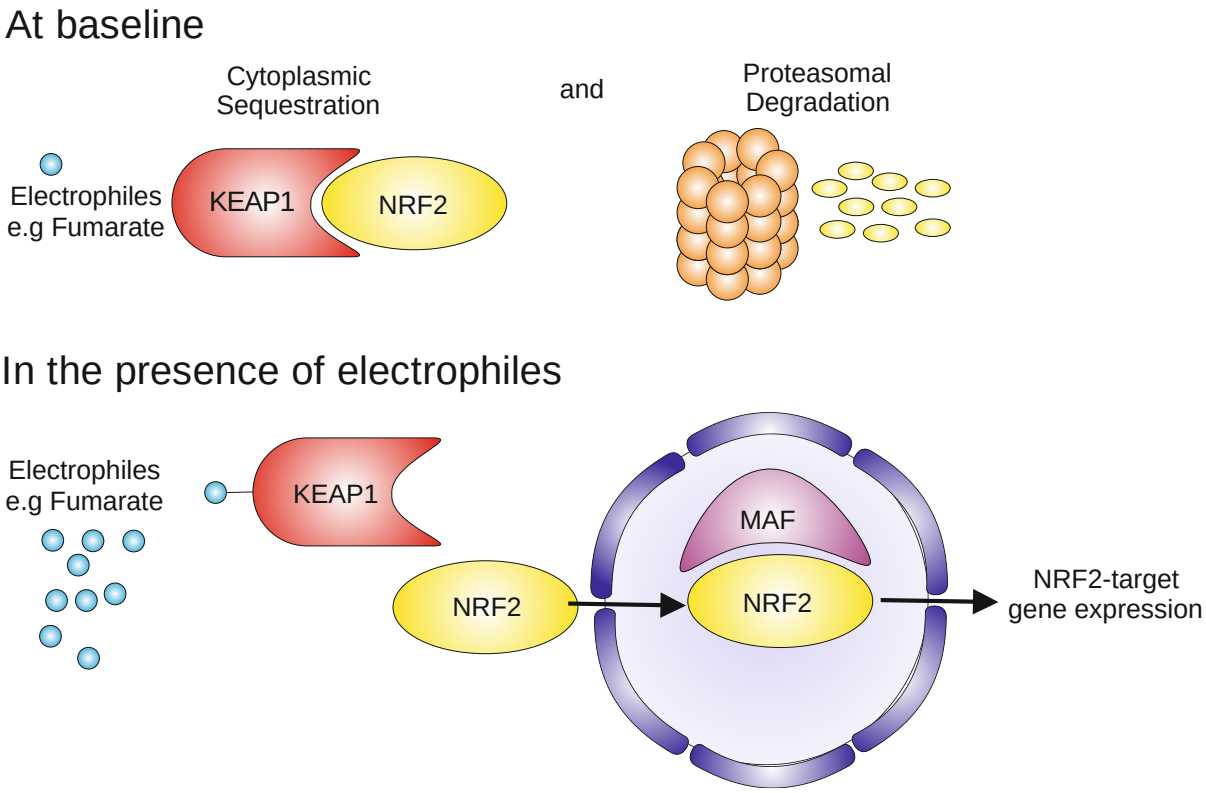

Figure 8 – Activation of NRF2 signalling by fumarate
At baseline, NRF2 (nuclear factor (erythroid-derived 2)-like 2) is sequestered in the cytoplasm and targeted for proteasomal degradation by KEAP1 (Kelch-like ECH-associated protein 1) binding. In the presence of fumarate (an electrophile) specific KEAP1 cysteine residues are succinated. This prevents KEAP1 binding to NRF2. NRF2 is then free to translocate to the nucleus where it dimerises with small MAF proteins and activates expression of genes with an antioxidant response element.

Many NRF2 target genes modulate metabolic pathways in concert with reducing oxidative stress (Figure 9). For example, NRF2 directly activates multiple genes encoding enzymes of the pentose phosphate pathway (PPP) which generates precursors for nucleotide synthesis and NADPH as reducing equivalents important for ROS elimination[163]. NRF2 also promotes glutathione (GSH) synthesis by activating the genes encoding the regulatory and catalytic subunits of γ-glutamylcysteinyl ligase[162]. In states of oxidative stress, GSH can be oxidised by ROS to produce a gluatathione dimer (GSSG) which is then converted back into GSH by glutathione reductase, utilising NADPH. In contrast to its NRF2-mediated antioxidative effect, fumarate can react with GSH to form succinated glutathione (GSF), which has an oxidising effect since NADPH is consumed to convert it back to GSS and dimethyl-succinate[164]. Another NRF2 target, haem oxygenase 1 (HMOX1), degrades potentially toxic

haem to biliverdin. FH deficient cells have been shown to use the haem biosynthesis and degradation pathway to dispose of excess succinate; as a corollary, inhibition of HMOX1 is lethal to these cells[165].

In the absence of functional FH, anaplerotic amino acid flux is predicted to ameliorate NAD^+ reduction and ATP production by the TCA cycle[166]. Glutamine can be converted to gluatamate then 2-OG, which is then channelled into the TCA cycle (Figure 9). NRF2 has been shown to promote this process[162, 163]. In models of FH deficiency, increased glutamine consumption and incorporation of labelled glutamate or glutamine into TCA cycle intermediates has been observed[165-167]. The intermediates into which labelled glutamate are incorporated include fumarate, produced by the canonical TCA cycle, and citrate thought to be produced by reductive carboxylation (where the TCA cycle flows in reverse direction to that traditionally depicted) (Figure 9)[167]. Reductive carboxylation only occurs in some models of FH deficiency; in others it appears to be inhibited, potentially by inactivation of aconitase activity by succination[160].

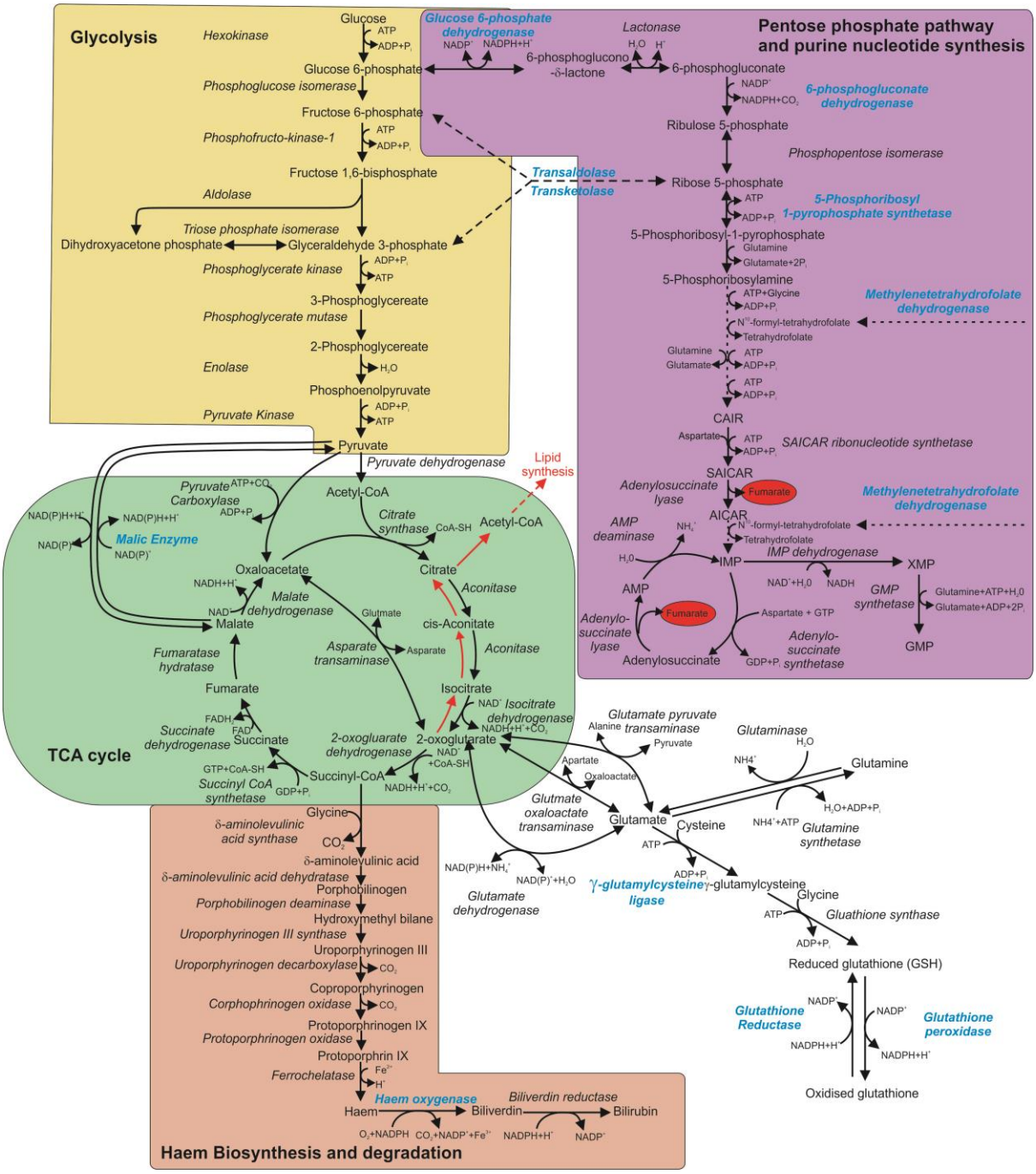

Figure 9 – NRF2 modulates multiple metabolic pathways

NRF2 promotes degradation of haem, production of NADPH and nucleotides through the pentose phosphate pathway and glutathione synthesis. Reductive carboxylation is depicted by red arrows. NRF2 target genes are shown in blue. Dotted arrows signify simplified pathways. AICAR: 5-Aminoimidazole-4-carboxamide ribonucleotide; AMP: adenosine monophosphate; CAIR: 5'-phosphoribosyl-4-carboxy-5-aminoimidazole; GMP: guanosine monophosphate; IMP inosine monophosphate; NAD: Nicotinamide adenine dinucleotide; NADP: Nicotinamide adenine dinucleotide phosphate SAICAR: succinyl-AICAR; XMP: xanthosine monophospshate;

1.7.3.2 FH deficiency, fumarate accumulation and NRF2 activation in the heart

Perfusion of rat or mouse hearts with fumarate or dimethyl-fumarate is beneficial in models of ischaemia-reperfusion, improving cardiac function and minimizing the area of necrosis[166, 168]. This protection is abrogated in NRF2-deficient hearts[166]. In accordance with this, overexpression of the NRF2 target gene *Hmox1* confers dose-dependent cardioprotection against ischaemia[169]. NRF2 also protects the heart during haemodynamic stress, with its loss resulting in earlier onset of cardiac dysfunction, enhanced fibrosis and cardiomyocyte apoptosis following TAC in mice[170]. Cardiac-specific *Fh1* deletion elevates cardiac fumarate and NRF2 (but not HIF-1α) levels conferring protection against myocardial ischaemia. This protection is abolished by pre-treatment with a HMOX1 inhibitor[166]. At around 3 months of age, cardiac-specific *Fh1* knockout mice develop ventricular dysfunction[166].

1.7.4 Fumarate hydratase localisation

1.7.4.1 Mechanisms

Although the traditional function of FH takes place in the mitochondrial TCA cycle, there is a role for cytoplasmic FH eliminating fumarate produced by the urea cycle (UC) and purine nucleotide cycle (PNC). FH is dual-localised to the mitochondria and the cytoplasm by an N-terminal mitochondrial-targeting sequence (MTS), but by slightly different mechanisms in different model organisms (Figure 10)[171-173]. In yeast, fumarase is produced as a single translation production (with an MTS) which initially targets to the mitochondria[174]. Fumarase molecules begin to be transported into the mitochondrion with the ribosome still attached to the nascent fumarase chain. The MTS is then removed by mitochondrial processing peptidase (MPP). Dependent upon folding of the nascent chain, fumarase then either shifts back into the cytosol or progresses into the mitochondrion[171, 174, 175]. In contrast, in mammalian cells FH is thought to undergo differential translation to produce FH protein with an MTS – which

translocates to the mitochondria (where MPP removes the MTS upon entry) – and without an MTS, which remains in the cytosol[171, 176, 177]. In plants, FH is encoded by two genes one with and one without an MTS, thus targeting it to the mitochondria or cytosol, respectively[171]. In both yeast and mammals, there are start codons situated at the beginning and immediately after the MTS. In yeast, mutation of the second start codon results in all the fumarase localising to the mitochondria, with very little cytoplasmic fumarase[178].

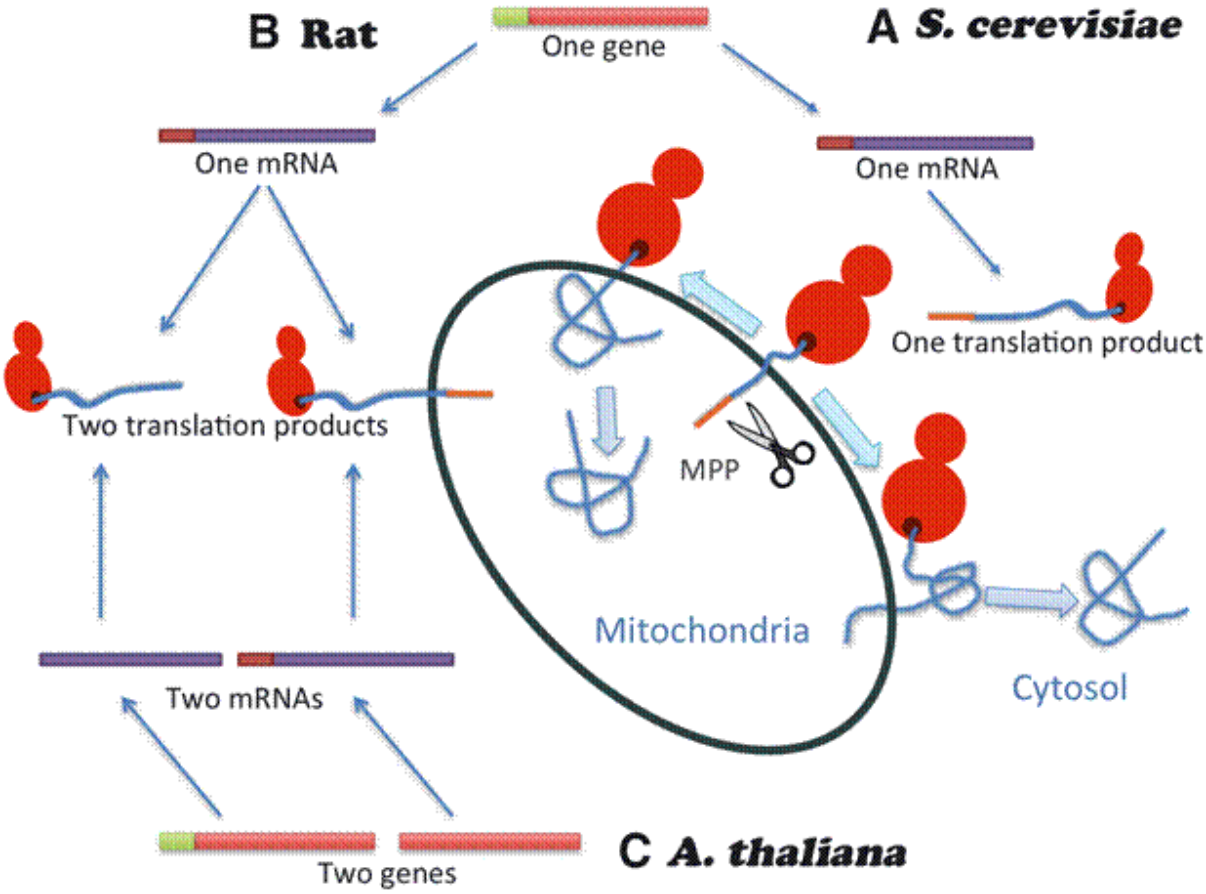

Figure 10 – Mechanisms of FH dual localisation[6]
A. In budding yeast *(S. cerevisiae)* fumarase is transcribed from a single gene and translated as only one translation product with a mitochondrial targeting sequence (MTS). All fumarase molecules are initially targeted to the mitochondria by the MTS and begin mitochondrial import whilst still attached to the ribosome. Mitochondrial processing peptide (MPP) cleaves the MTS. If the nascent fumarase chain begins to fold before entering the mitochondrion, the fumarase molecule moves back into the cytosol (reverse translocation), otherwise the fumarase molecule is imported into the mitochondrion. **B.** In rat, FH is transcribed to a single mRNA, differential translation results in two peptides being formed, one with an MTS which targets to the mitochondrion and one without, which remains in the cytoplasm. **C.** In *Arabidopsis thaliana* two highly homologous genes containing or lacking an MTS encode mitochondrial and cytoplasmic fumarase, respectively.

[6] Adapted from Yogev, O., A. Naamati, and O. Pines, *Fumarase: a paradigm of dual targeting and dual localized functions.* FEBS Journal, 2011. **278**(22): p. 4230-4242.

1.7.4.2 A role for cytosolic FH in cancer models

PHDs and KEAP1 are located in the cytoplasm and therefore inhibited or modified by cytosolic fumarate accumulation. Indeed, extra-mitochondrial FH reintroduction ameliorates the constitutive activation of HIF and NRF2 signalling in *Fh1* knockout mouse embryonic fibroblasts[145, 179]. Augmentation of cytosolic FH in a murine kidney specific *Fh1* knockout background is sufficient to prevent development of the cystic phenotype[180]. In the cytoplasmic urea cycle, fumarate is generated when argininosuccinate is converted to arginine. In Fh1 deficient cells, this reaction is reversed with fumarate and arginine combining to produce argininosuccinate[180]. In *Fh1* knockout kidneys, cytosolic FH augmentation restores urea cycle metabolites towards normal levels[180]. These observations highlight that fumarate hydratase deficiency influences multiple aspects of cellular metabolism and not only ATP generation through the mitochondrial TCA cycle.

1.8 Aims and hypotheses

1.8.1 Original Hypotheses

The preceding introduction has highlighted the critical role played by HIF in marshalling the cellular and systemic response to hypoxia, the complexity of HIF biology in the heart and the multi-faceted interface of HIF with cellular metabolism, in particular the ability of intermediate metabolites, such as fumarate, to generate a pseudohypoxic response thereby potentially activating HIF signalling in the absence of hypoxia.

Accordingly, the central hypotheses of this thesis are that:

i) Chronic upregulation of endogenous oxygen labile HIF-1α is detrimental following myocardial infarction.

ii) Cardiac-specific deletion of fumarate hydratase – as a mechanism to elevate endogenous fumarate levels – will elicit a pseudohypoxic response in the heart and thereby augment cardiac HIF signalling with beneficial consequences.

iii) Given the central metabolic role played by the TCA cycle, selective cardiac genetic ablation of a key enzyme – fumarate hydratase – will have profound consequences for myocardial metabolism and be associated with a significant phenotype.

iv) The phenotype of the FH null model will be amenable to rescue by metabolic modulation, both pharmacologically and genetically, the latter via replenishment of cytosolic FH alone.

1.8.2 Aims

In order to address these hypotheses, the specific aims of this thesis are (with associated chapter number in parentheses):

Aim 1 - To elucidate whether chronic elevation of endogenous, oxygen-labile HIF-1α is beneficial or detrimental in the context of myocardial infarction using a coronary artery ligation model in conjunction with an inducible, cardiac-specific murine knockout (Chapter 3).

Aim 2 – To investigate the physiological role of fumarate hydratase (FH) within the heart by developing, validating and phenotyping an *Fh1* knockout mouse model (Chapter 4).

Aim 3 – To delineate whether excess endogenous cardiac fumarate, consequent to cardiac-restricted *Fh1* deletion, is sufficient to induce a pseudohypoxic response (Chapter 4).

Aim 4 – To seek to define the mechanistic pathways underpinning the cardiac phenotype of the *Fh1* knockout mouse model and utilise these to attempt a pharmacological rescue (Chapter 5).

Aim 5 – To utilise *in vitro* models to validate selective targeting of FH to the cytosol or the mitochondria and seek to extend these *in vivo* both to attempt genetic rescue of the FH null phenotype and to help shed light on the relative roles of cytosolic versus mitochondrial FH within the heart (Chapter 6).

2 CHAPTER 2: MATERIALS AND METHODS

All chemicals were obtained from Sigma unless otherwise stated.

2.1 Buffers and Media

Buffer	Constituents
Genotyping lysis buffer	50 mM Tris-HCl, 100 mM ethylenediaminetetraacetic acid [EDTA], 100 mM NaCl, 1% sodium dodecyl sulphate [SDS], 0.2 mg/mL proteinase K (Bioline)
6x DNA loading buffer	40% Glycerol, 25 mM EDTA pH 8, 0.01% bromophenol blue
Viral Storage buffer	20 mM Tris, 5 mM KCl, 1 mM $MgCl_2$, 137 mM NaCl
Dialysis buffer	10 mM Tris HCl, 220 mM sucrose, pH 7.8
Complete media	Dulbecco's Modified Eagle's Media (DMEM), 10% foetal bovine serum (FBS) 200 µM L-glutamine, penicillin (10 units/mL) – Streptomycin (10 µg/mL)
Dialysis buffer	10 mM Tris HCl, 220 mM sucrose, pH 7.8
Adenoviral storage buffer	80% foetal bovine serum, 20 % glycerol
Urea lysis buffer	7 M Urea, 10% glycerol (v/v), 10 mM Tris-HCl (pH6.8), 1% SDS, 1 mM dithiothreitol, 1mM EDTA, 0.1mM phenylmethylsulphonyl fluoride [PMSF], protease inhibitor cocktail tablet (1 per 10 mL)
6x protein loading buffer	100 mM Tris HCl (pH 6.8), 2.5 % SDS, 5 % 2-mercaptoethanol, 10 % glycerol, 0.01% bromophenol blue
Transfer buffer	48 mM Tris base, 390 mM glycine, 0.1 % SDS, 20% methanol (v/v)
Tris buffer saline tween-20 (TBST)	15 mM Tris-HCl, 137 mM NaCl, 0.1% Tween-20, pH 7.6
Stripping buffer	2% SDS, 62.5 mM Tris-HCl, pH 6.8 and 100 mM 2-mercaptoethanol
Immunofluorescence blocking buffer	1X phosphate buffered saline (PBS), 3% goat serum, 1% BSA, 0.2% triton
Mobile phase	3.5% acetonitrile, 215 mM potassium dihydrogen (ortho)phosphate (KH_2PO_4) and 2.3 mM tetrabutyl ammonium hydrogen sulphate (tetrabutylammonium bisulphate) ($C_{16}H_{37}NO_4S$)
HPLC standard solution	0.4 N perchloric acid, 242 µM creatinine, 180 µM creatine, 144 µM phosphocreatine, 35 µM adenosine monophosphate (AMP), 56 µM adenosine diphosphate (ADP), 118 µM adenosine triphosphate (ATP), 127 µM deoxyadenosine triphosphate (dATP)
Krebs-Hepes Buffer	99 mM NaCl, 4.7 mM KCl, 1.2 mM $MgSO_4$, 1 mM KH_2PO_4, 1.9 mM $CaCl_2$, 25 mM $NaHCO_3$, 11.1 mM Glucose and 20 mM HEPES; pH-7.4)

Table 2 – Buffers and Media

2.2 Mice

2.2.1 Animal Husbandry

Mice were maintained in individually ventilated cages (IVCs) in a specified pathogen-free facility with a 12 hour light-dark cycle and controlled temperature (20-22 °C) and humidity. Water and standard rodent chow diet (Teklad Global Diet: 16% protein, 4% fat; Harlan Laboratories, UK) were provided *ad libitum.* Animal procedures were carried out in accordance with the 1986 British Home Office Animals Scientific Procedures Act.

2.2.2 Extraction of genomic deoxyribonucleic acid (DNA) and genotyping

Mouse ear notches were incubated in 500 µL of genotyping lysis buffer overnight at 55 °C. Lysates were centrifuged at 13,000 g for 5 minutes to pellet debris. Supernatants were transferred to fresh tubes. DNA was precipitated with an equal volume (500 µL) of isopropanol and incubated on ice for 20 minutes. The DNA was pelleted by centrifugation at 13,000 g for 15 minutes at 4 °C. The supernatant was discarded and the pellet washed with 70% ethanol. DNA was pelleted by centrifugation at 13,000 g for 15 minutes at 4 °C and the supernatant was discarded. DNA pellets were air dried at room temperature and resuspended in 50 µL nuclease-free water. DNA was quantified by spectrophotometry with a Nanodrop (ND-1000). PCR was performed using a thermal cycler (DNA Engine Tetrad 2 Peltier thermal cycler, Bio-Rad; see description of each transgenic line for specific primers and reaction conditions utilised). PCR products were diluted in 6x DNA loading buffer and visualised on agarose gels (1xTBE [Tris-borate-EDTA]) with 0.002% ethidium bromide using ultraviolet (UV) transillumination.

2.2.3 Inducible cardiac-specific deletion of hypoxia-inducible factor-1α (HIF-1α)

2.2.3.1 HIF-1α conditional knockout line

HIF-1α floxed mice (Figure 11) originate from the laboratory of Professor Randall Johnson and were a kind gift via Dr. Patrick Pollard[181]. These mice were genotyped by polymerase chain reaction (PCR) using the primers and condition shown in Table 3. The genotyping strategy utilized for these mice uses primers binding in the intron 2 regions surrounding the lox-P site giving different sized PCR products in the presence/absence of the lox-P site. The resulting PCR products were separated on a 2 % agarose gel (Figure 12).

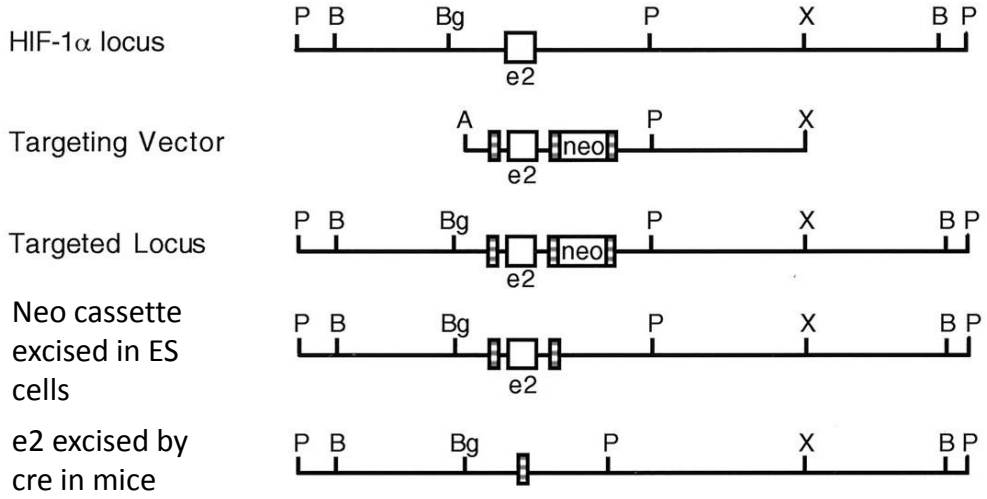

Figure 11 – Gene-targeting strategy for the *HIF-1α* floxed line[7]
Homologous recombination was utilised to incorporate *Hif-1α* exon 2 (e2) flanked by lox-P sites and a neomycin cassette (neo) into the endogenous *Hif-1α* locus. The neomycin cassette was removed by transient cre-recombinase expression in embryonic stem cells. Embryonic stem (ES) cell clones in which the neomycin cassette but not exon 2 was excised were selected for generation of this mouse strain. When crossed with cre-expressing mice, *Hif-1α* exon 2 is deleted.

[7] Reproduced from Ryan, H.E. et al. Hypoxia-inducible factor-1α is a positive factor in solid tumor growth. *Cancer Research* **60**, 4010-4015 (2000)

***Hif-1α* Genotyping**						
Primer			**Sequence**			
HIF-1α_f1			GCAGTTAAGAGCACTAGTTG			
HIF-1α_f2			TTGGGGATGAAAACATCTGC			
HIF-1α _r			GGAGCTATCTCTCTAGACC			
Reaction Mix			**Reaction conditions**			
			Step	Temp.	Time	Cycles
Genomic Mouse DNA	50	ng	Denaturing	95 °C	600 s	**1 x**
Primers	10	pmol	Denaturing	95 °C	45 s	
dNTPs	0.20	mM	Annealing	57 °C	45 s	**35 x**
Reaction Buffer	0.1	Vol	Extension	72 °C	45 s	
$MgCl_2$	1.5	mM				
Taq Polymerase (Immolase)	1.0	U	Final Extension	72 °C	420 s	**1 x**
Reaction Volume	20.0	µL				
Amplification Product			**Size**			
WT HIF-1α (0-loxP)			240 bp			
LoxP flanked HIF-1α exon 2 (2-loxP)			260 bp			
Excised HIF-1α exon 2 (1-loxP)			270 bp			

Table 3 – PCR conditions used for *Hif-1α* conditional knockout genotyping

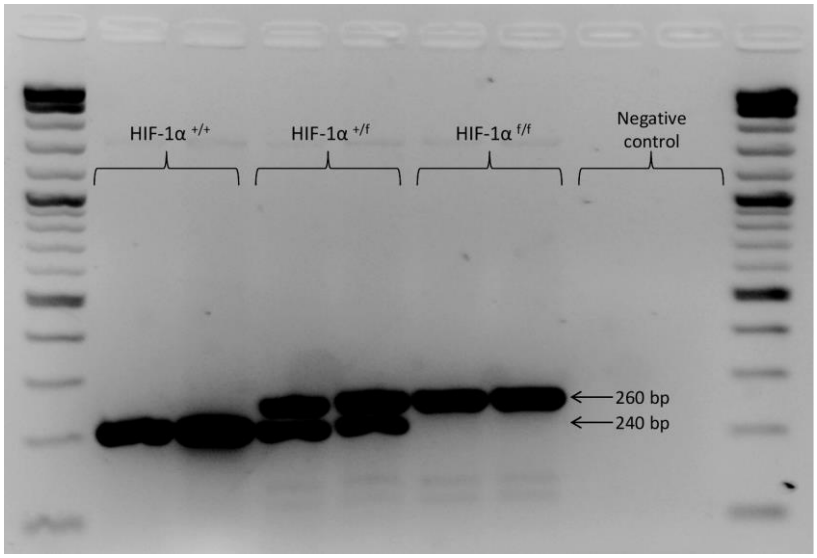

Figure 12 – *Hif-1α* conditional knockout genotyping gel
2% agarose gel electrophoresis showing PCR products from HIF-1α conditional knockout genotyping PCR. From left to right: lane 1 - 2-log ladder (New England Biolabs); lanes 2 and 3 – Wildtype; lanes 4 and 5 – HIF-$1\alpha^{+/f}$ (heterozygous); lanes 6 and 7 – HIF-$1\alpha^{f/f}$ (homozygous); lanes 8 and 9 - no DNA control; lane 10 - 2-log ladder.

2.2.3.2 αMHC-Mercremer line

αMHC-Mercremer (Mcm) mice originate from the laboratory of Professor Jeffrey Molkentin and were a kind gift via Dr. Patrick Pollard[182]. In this line, a cardiac-specific α-myosin heavy

chain (αMHC) promoter is used to drive expression of cre-recombinase flanked by mutated oestrogen receptor (MER) ligand binding domains (Figure 13). The MER domains instigate sequestration of cre-recombinase in the cytoplasm by heat shock proteins in the absence of its ligand, tamoxifen (the mutation rendering it insensitive to oestrogen). In the presence of tamoxifen, Mcm protein translocates to the nucleus where it catalyses recombination between lox-P sites, allowing temporal regulation of gene ablation. Mcm mice were genotyped by PCR, with the primers binding within the Mcm coding region (

Table 4) and the resulting PCR products visualised on a 1% agarose gel (Figure 14).

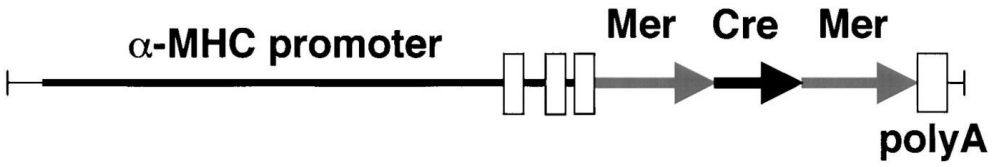

Figure 13 – *Mercremer* construct[8]
The α-MHC (myosin heavy chain) promoter drives cardiac-specific expression of the mercremer transcript. The mutated oestrogen receptor domains (Mer) sequester Mercremer protein in the cytoplasm until tamoxifen treatment initiates its translocation to the nucleus.

***Mercremer* Genotyping**						
Primer			**Sequence**			
Mcm_fw			CGGTCGATGCAACGAGTGATGAGG			
Mcm_rv			CCAGAGACGGAAATCCATCGCTCG			
Reaction Mix			**Reaction conditions**			
			Step	Temp.	Time	Cycles
Genomic Mouse DNA	50	ng	Denaturing	95 °C	600 s	**1 x**
Primers	10	pmol	Denaturing	95 °C	45 s	**35 x**
dNTPs	0.20	mM	Annealing	57 °C	45 s	
Reaction Buffer	0.1	Vol	Extension	72 °C	45 s	
$MgCl_2$	1.5	mM				
Taq Polymerase (Immolase)	1.0	U	Final Extension	72 °C	420 s	**1 x**
Reaction Volume	20.0	µL				
Amplification Product			**Size**			
Mercremer (mcm)			700 bp			

Table 4 – PCR conditions used for mercremer genotyping

[8] Reproduced from Sohal, D.S. *et al*. Temporally regulated and tissue-specific gene manipulations in the adult and embryonic heart using a tamoxifen-inducible cre protein. *Circulation Research* **89**, 20-25 (2001).

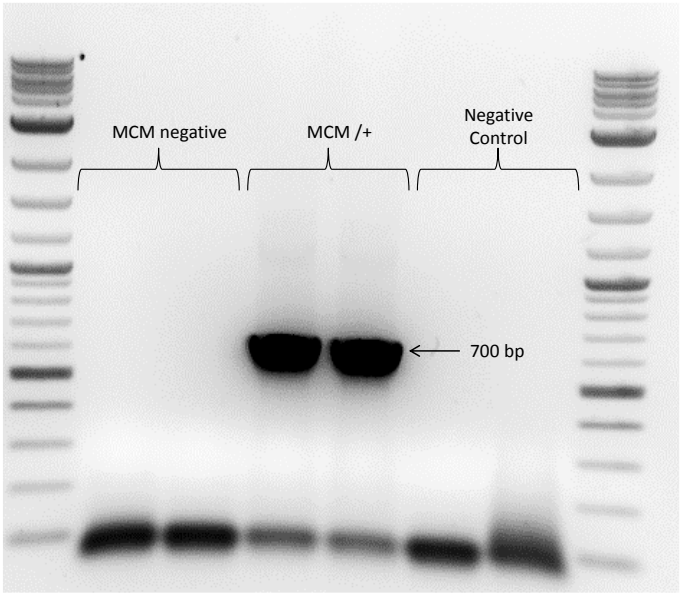

Figure 14 – Mercremer genotyping gel
1% agarose gel electrophoresis showing PCR products from mercremer genotyping. Lane 1 – 2-log ladder. Lanes 2 and 3 – wildtype. Lanes 4 and 5 – Mcm/+. Lanes 6 and 7 – No DNA control. Lane 8 – 2-log ladder.

2.2.3.3 Breeding strategy

Hif-1α homofloxed (*Hif-1α*$^{f/f}$) mice were bred with mercermer positive (*Mcm/+*) mice to produce *Hif-1α*$^{f/+}$ *Mcm/+* and *Hif-1α*$^{f/+}$ *Mcm-/-* animals. *Hif-1α*$^{f/+}$ *Mcm/+* were backcrossed for 6 generations onto a C57BL/6J background. These mice were then crossed to produce *Hif-1α*$^{f/f}$ *Mcm/+* and *Hif-1α*$^{+/+}$ *Mcm/+* mice which were utilised for further breeding. To minimise the number of non-experimental *Hif-1α* heterozygous and wildtype mice produced, *Hif-1α*$^{+/+}$ *Mcm/+* were subsequently bred with *Hif-1α*$^{+/+}$, whilst *Hif-1α*$^{f/f}$ *Mcm/+* were mated with *Hif-1α*$^{f/f}$ mice to generate experimental animals.

2.2.3.4 Tamoxifen dosing pilot study

A pilot study was performed to determine the optimal dose of tamoxifen required to excise the *Hif-1α* floxed allele. 20 mg/kg, 40 mg/kg or 80 mg/kg tamoxifen diluted in 10% ethanol in cornoil was administered to *Hif-1α*$^{f/f}$ *Mcm/+* by intraperitoneal injection (IP) for 5 consecutive days. Echocardiography (described in 2.2.9) was performed on day 5 of tamoxifen treatment. Body weight and condition of mice were monitored daily. Mice were

maintained for 18 days post-commencement of treatment, then humanely euthanased and tissues harvested (described in 2.2.12).

2.2.3.5 Baseline phenotyping of HIF-1α conditional knockout mice

To explore the baseline phenotype associated with *Hif-1α* deletion, *Mcm/+* and *HIF-1α$^{f/f}$ Mcm/+* mice were treated with 20 mg/kg tamoxifen IP for 5 days. These animals underwent echocardiography (see 2.2.9) and tissue collection at 70 days post-tamoxifen treatment.

2.2.3.6 Phenotyping of HIF-1α conditional knockout mice in the context of coronary artery ligation (CAL)

CAL or sham surgery (see 2.2.8) was performed upon *Mcm/+* or *Hif-1α$^{f/f}$ Mcm/+* female mice weighing 20-25 g. Mice were observed twice daily in the peri-operative period and daily after this. If exhibiting signs of distress, mice were given analgesia (1 mg/kg buprenorphine subcutaneously) or euthanised as appropriate. 10-14 days after surgery, mice underwent screening echocardiography to assess infarct size (see 2.2.9). Two weeks after surgery mice were treated with 20 mg/kg tamoxifen IP for 5 days. Magnetic resonance imaging (MRI) (see 2.2.10) was performed 77-83 days after surgery to assess cardiac function and infarct size. Invasive haemodynamic assessment of cardiac function (see 2.2.11) and tissue harvest were performed 80-86 days post-surgery.

2.2.4 Cardiac-specific fumarate hydratase (Fh1) knockout mice

2.2.4.1 Fh1 conditional knockout line

Fh1 conditional knockout mice were from a kind gift from Dr Patrick Pollard[143]. Figure 15 shows the gene targeting strategy adopted to generate this line. These mice were genotyped by PCR using the primers and conditions shown in

Table 5. The genotyping strategy uses a common forward primer and differential reverse primers which specifically bind either the wildtype or the floxed allele. The resulting PCR products were separated on 2% agarose gels (Figure 16).

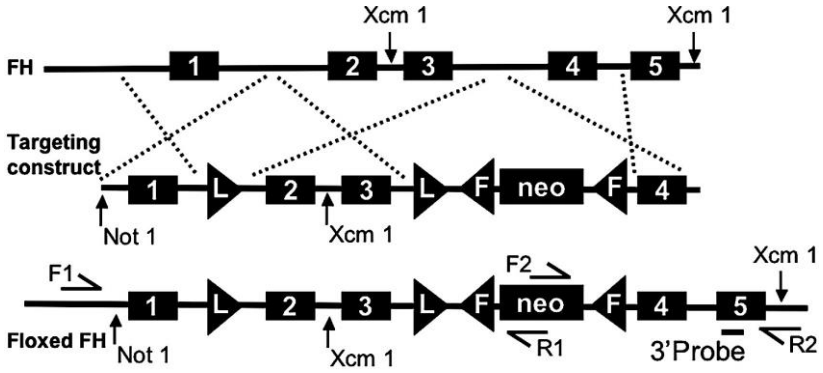

Figure 15 - Gene-targeting strategy for *Fh1* conditional knockout mice[9]
The wild-type *Fh1* allele was replaced with the targeted allele, in which exons 2 and 3 are flanked by lox P (L) sites, by homologous recombination. The neomycin selection cassette was excised by flp (F) recombinase.

Fh1 conditional knockout genotyping						
Primer			**Sequence**			
FH_fw			ACCCTGCTAGGTGTCACCAC			
FH_rv1 (flox-specific)			CCTGGCACTGCAGACTACAA			
FH_rv2 (wildtype-specific)			GCTCAGTCACCCATCCAAAT			
Reaction Mix			**Reaction conditions**			
Genomic Mouse DNA	50	ng	**Step**	**Temp.**	**Time**	**Cycles**
Primers	10	pmol	Denaturing	95 °C	600 s	**1 x**
dNTPs	0.20	mM	Denaturing	95 °C	45 s	**32 x**
Reaction Buffer	0.1	Vol	Annealing	60 °C	45 s	
$MgCl_2$	1.5	mM	Extension	72 °C	60 s	
Taq Polymerase (Immolase)	1.0	U				
Reaction Volume	20.0	µL	Final Extension	72 °C	420 s	**1 x**
Amplification Product			**Size**			
FH lox-P			450 bp			
FH WT			230 bp			

Table 5 – PCR reaction and thermal cycling conditions used for genotyping *Fh1* flox mice

[9] Reproduced from Pollard, P.J. et al. Targeted inactivation of Fh1 causes proliferative renal cyst development and activation of the hypoxia pathway. *Cancer Cell* **11**, 311-319 (2007).

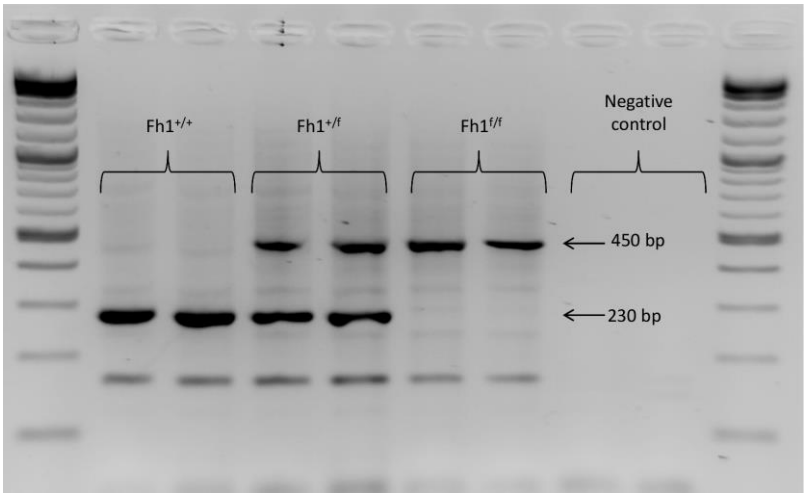

Figure 16 – *Fh1* conditional knockout genotyping gel
2% agarose gel electrophoresis showing PCR products from Fh1 flox genotyping. From left to right: lane 1 – 2-log ladder; lanes 2 and 3 - wildtype; lanes 4 and 5 – heterozyote; lanes 6 and 7 - *Fh1* flox homozyote; lanes 8 and 9 - no DNA control; lane 10 - 2-log ladder.

2.2.4.2 Mlc2vcre line

Mlc2vcre knock-in mice were a kind gift from Professor Ken Chien and are referred to simply as *Cre/+* hereafter[183]. In this mouse line cre recombinase is inserted into the myosin light chain 2v locus resulting in tissue specific expression of cre recombinase in ventricular cardiomyocytes[184]. Figure 17 shows the gene-targeting strategy adopted by Professor Chien's laboratory to create these mice. The primers and PCR conditions used for genotyping are shown in

Table 6. The forward primer binds upstream of the myosin light chain 2v (*myl2*) gene, whilst the reverse is within the cre recombinase encoding region. The resulting PCR products were visualised on 1% agarose gels (Figure 18).

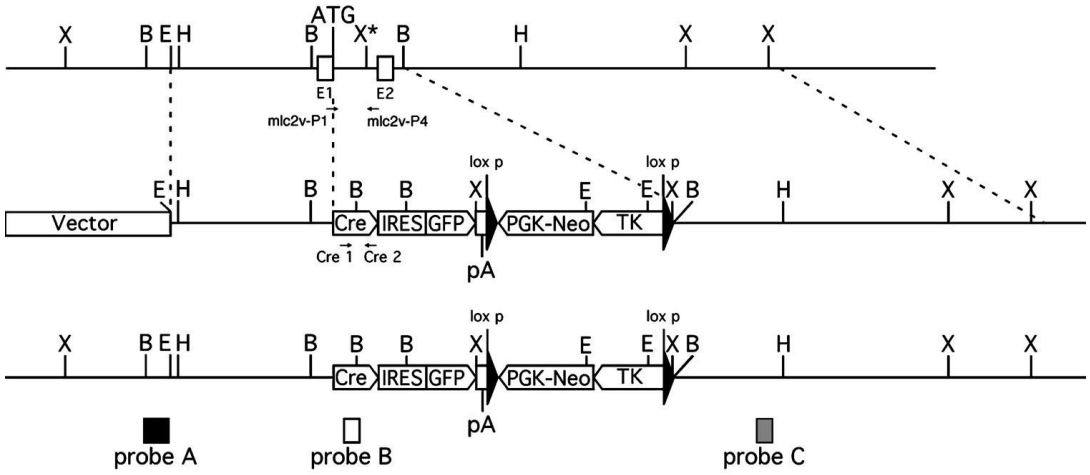

Figure 17 – Gene-targeting strategy for MLC2vcreKI (*Cre/+*) mice[10]
Homologous recombination was utilised to replace part of intron 1 to intron 3 of the mlc2v gene with DNA encoding cre recombinase, an internal ribosome entry site (IRES), green fluorescent protein (GFP) and a neomycin resistance cassette.

Mlc2creKI genotyping						
Primer			**Sequence**			
Mlc2vcre fw			CCAGGGGAGAGGTATTTATTG			
Mlc2vcre rv			CGCATAACCAGTGAAACAGCATTGC			
Reaction Mix			**Reaction conditions**			
Genomic Mouse DNA	50	ng	Step	Temp.	Time	Cycles
Primers	10	pmol	Denaturing	95 °C	600 s	**1 x**
dNTPs	0.20	mM	Denaturing	95 °C	30 s	**30 x**
Reaction Buffer	0.1	Vol	Annealing	57 °C	30 s	
$MgCl_2$	1.5	mM	Extension	72 °C	30 s	
Taq Polymerase (Immolase)	1.0	U				
Reaction Volume	20.0	µL	Final Extension	72 °C	300 s	**1 x**
Amplification Product			**Size**			
Mlc2vcre			500 bp			

Table 6 – PCR reaction used for genotyping MLC2vcreKI mice

[10] Reproduced from Chen, J. et al. Selective requirement of myosin light chain 2v in embryonic heart function. *Journal of Biological Chemistry* **273**, 1252-1256 (1998)

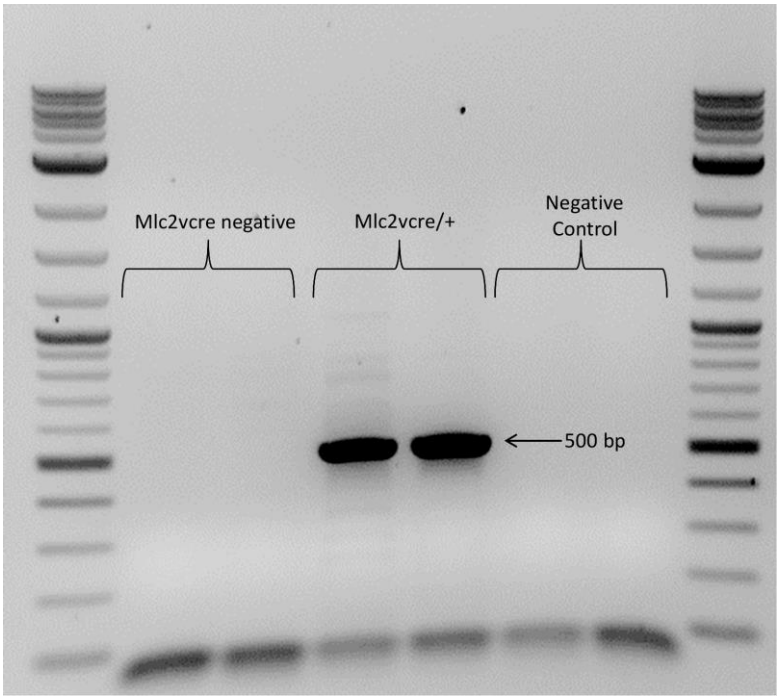

Figure 18 – Mlc2vcre genotyping gel
1% agarose gel electrophoresis showing PCR products from mlc2vcre genotyping. Lane 1 – 2-log ladder. Lanes 2 and 3- wildtype. Lanes 4 and 5 *Cre/+*. Lanes 6 and 7 – No DNA control. Lane 8 – 2-log ladder.

2.2.4.3 Breeding and phenotyping

To investigate the role of Fh1 in the heart, *Fh1* homozygous flox ($Fh1^{f/f}$) mice were crossed with *Cre/+* mice to generate $Fh1^{+/f}$ and $Fh1^{+/f}$ *Cre /+* mice. These were interbred to create $Fh1^{f/f}$ and $Fh1^{f/f}$ *Cre /+* mice for experiments and further breeding. $Fh1^{f/f}$ and $Fh1^{f/f}$ *Cre/+* mice underwent echocardiography (see 2.2.9) at 99-103 days and invasive haemodynamics (see 2.2.10) at 101-107 days. Animals were euthanized and tissues harvested at 102-107 days (see 2.2.12) unless otherwise stated. $Fh1^{f/f}$ mice showed no abnormalities compared to wildtype animals and were used as controls. Littermate controls were used where possible. For Kaplan-Meier survival analysis, a cohort of mice were kept until death or until they developed pronounced lethargy and/or laboured breathing and were euthanized.

2.2.4.4 Pharmacological treatment of Fh1 cardiac-specific knockout mice

2.2.4.4.1 Tartronic acid

Fh1$^{f/f}$ and *Fh1*$^{f/f}$ *Cre* /+ mice aged 41-47 days were given the malic enzyme inhibitor tartronic acid (Alfa Aesar) at 60 mg/kg dissolved in saline (pH was adjusted to 6), or saline control by daily IP injection for 6 days (dose chosen was previously described by Iakusheva[185]). On the 6th day invasive haemodynamic assessment of cardiac function was performed, followed by tissue harvest.

2.2.4.4.2 Dehydroepiandrosterone

Fh1$^{f/f}$ and *Fh1*$^{f/f}$ *Cre* /+ mice were treated with 400 mg/kg dehydroepiandrosterone (DHEA) diluted in hydroxypropyl-β-cyclodextrin (vehicle) or vehicle only by daily subcutaneous injection from age 40 days until terminal haemodynamic studies (dose used was previously described by Boros *et al*.[186]) Mice underwent echocardiography (see 2.2.9) at 100-105 days followed by invasive haemodynamics (see 2.2.10) and tissue harvest at 102-106 days.

2.2.5 Cardiac-specific Fh1 Hif-1α double knockout

2.2.5.1 Breeding and phenotyping

Fh1$^{f/f}$ *Cre* /+ mice (see 2.2.4) were bred with the *Hif-1α*$^{f/f}$ mice (see 2.2.3.1) to generate *Fh1*$^{f/w}$ *Hif-1α*$^{f/w}$ *Cre/*+ and *Fh1*$^{f/w}$ *Hif-1α*$^{f/w}$ mice. These mice were crossed to generate *Fh1*$^{f/f}$ *Hif-1α*$^{f/f}$ and *Fh1*$^{f/f}$ *Hif-1α*$^{f/f}$ *Cre/*+ mice which were used for further breeding. Since *Fh1*$^{f/f}$ *Hif-1α*$^{f/f}$ *Cre/*+ died earlier than *Fh1*$^{f/f}$ *Cre* /+ mice, tissue was collected at an earlier time-point of 90-94 days. Kaplan-Meier survival was performed as in 2.2.4.3.

2.2.6 Cardiac-specific Fh1, somatic Nuclear factor erythroid-derived 2-like 2 (Nrf2) double knockout

2.2.6.1 Somatic Nrf2 knockout line

The *Nrf2* somatic knockout mouse line originated from the laboratory of Professor Yamamoto and was obtained from Riken, Japan.[187] Homologous recombination had been utilised to achieve somatic disruption of *Nrf2* by insertion of a β-galactosidase construct (Figure 15).[187] These mice were genotyped by PCR using the primers and conditions shown in

Table 7. The genotyping strategy used a common forward primer and differential reverse primers which specifically bind either the β-galactosidase insert of the disrupted allele or the wildtype allele. PCR products were separated on a 2% agarose gel.

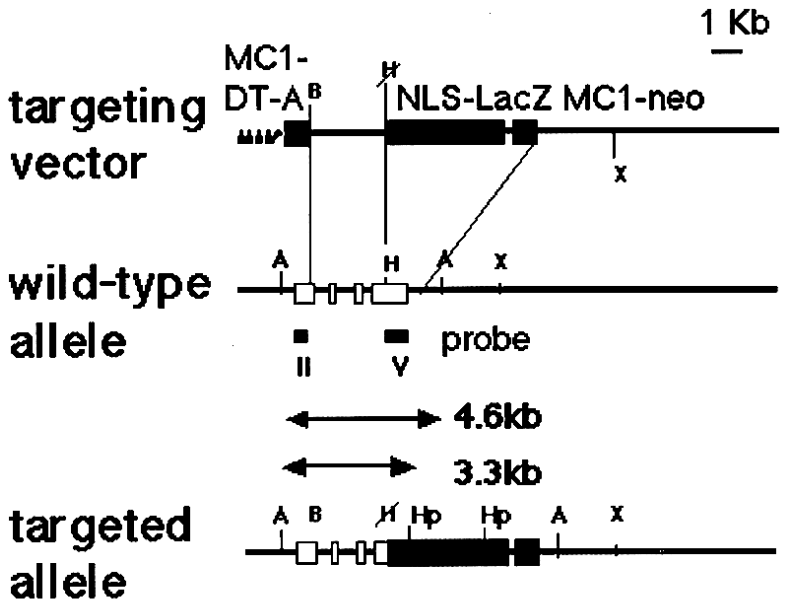

Figure 19 – Gene-targeting strategy used to generate *Nrf2* knockout mice[11]
Homologous recombination was utilised to incorporate NRF2 disrupted by a β-galactosidase gene into the NRF2 locus. DT-A: A diphtheria toxin gene for negative selection of non-homologous recombinant. NLS-LacZ: Nuclear localisation sequence β-galactosidase. Neo: Neomycin resistance cassette.

[11] Reproduced from Itoh, K. et al. An Nrf2/small Maf heterodimer mediates the induction of phase II detoxifying enzyme genes through antioxidant response elements. *Biochemical and Biophysical Research Communications* **236**, 313-322 (1997).

Nrf2 somatic knockout genotyping						
Primer			**Sequence**			
Nrf2_fw			TGGACGGGACTATTGAAGGCTG			
Nrf2_rv1 (flox-specific)			GCGGATTGACCGTAATGGGATAGG			
Nrf2_rv2 (wildtype-specific)			GCCGCCTTTTCAGTAGATGGAGG			
Reaction Mix			**Reaction conditions**			
Genomic Mouse DNA	50	ng	**Step**	**Temp.**	**Time**	**Cycles**
Primers	10	pmol	Denaturing	95 °C	600 s	**1 x**
dNTPs	0.20	mM	Denaturing	95 °C	45 s	**32 x**
Reaction Buffer	0.1	Vol	Annealing	60 °C	45 s	
$MgCl_2$	1.5	mM	Extension	72 °C	60 s	
Taq Polymerase (Immolase)	1.0	U				
Reaction Volume	20.0	µL	Final Extension	72 °C	420 s	**1 x**
Amplification Product			**Size**			
Nrf2 KO			400 bp			
Nrf2 WT			734 bp			

Table 7 – PCR conditions used for *Nrf2* genotyping

2.2.6.2 Breeding and phenotyping

Fh1$^{f/f}$ *Cre* /+ (see 2.2.4) mice were bred with *Nrf2*$^{-/-}$ mice to generate *Fh1*$^{f/w}$ *Nrf2*$^{+/-}$ *Cre*/+ and *Fh1*$^{f/w}$ *Nrf2*$^{+/-}$ mice. These mice were crossed to generate *Fh1*$^{f/f}$ *Nrf2*$^{-/-}$and *Fh1*$^{f/f}$ *Nrf2*$^{-/-}$*Cre*/+ mice which were used for experiments and further breeding and other genotypes which were euthanized. Tissue collection and Kaplan-Meier survival analysis were performed as in 2.2.4.3.

2.2.7 Complementation of cardiac-specific Fh1 knockout with knock-in (KI) of either dual-localised or cytosol-specific FH at the Rosa26 locus

2.2.7.1 KI^{FH} and KI^{FHcyt} lines

KI^{FH} and KI^{FHcyt} mice were created by Dr Patrick Pollard and Dr Ben Davis[180]. In these mice the human fumarate hydratase coding sequence – either with (KI^{FH}) or without (KI^{FHcyt}) its mitochondrial targeting sequence (MTS) – was inserted into the Rosa26 open chromatin locus utilising PhiC31 integrase-mediated cassette exchange[188]. The composite CAG

(cytomegalovirus early enhancer, chicken β-actin promoter, rabbit β-globin splice acceptor) promoter resulted in ubiquitous transgene expression. The gene-targeting strategy adopted to create these lines is illustrated in Figure 20. To determine the presence of a knock-in allele (either KI^{FH} or KI^{FHcyt}), a forward primer in the rabbit β-globin pA region and a reverse primer in the human FH coding region were utilised (

Table 8 and Figure 21). To determine whether the knock-in allele was KI^{FH} or KI^{FHcyt}, primers flanking the MTS (in the FH coding region and the CAG promoter) were utilised to generate products of different size (

Table 9 and Figure 22).

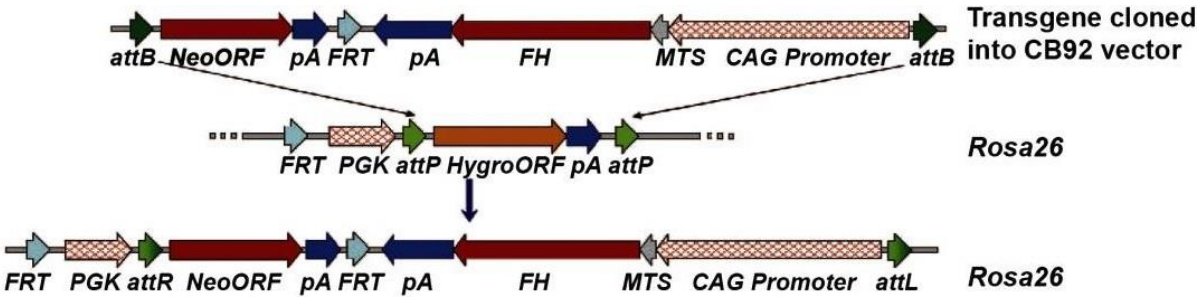

Figure 20 – KI^{FH} and KI^{FHcyt} gene-targeting strategy[12]
PhiC31 integrase and FH [with or without MTS (grey arrow)] expression cassettes were co-electroporated into acceptor embryonic stem cells. PhiC31 integrase catalyses exchange between attB sites in the vector and attP sites in the acceptor embryonic stem cells, resulting in insertion of the FH transgene driven by a CAG promoter at the Rosa26 locus.

[12] Reproduced from 180. Adam, J. et al. A role for cytosolic fumarate hydratase in urea cycle metabolism and renal neoplasia. *Cell Reports* **3**, 1440-1448 (2013).

KI genotyping						
Primer			**Sequence**			
FH KI fw			ATTAGCCAGAAGTCAGATGCTCAAGGGG			
FH KI rv			CATTGCTGCTGCAATAGAAGTTCATGA			
Reaction Mix			**Reaction conditions**			
			Step	Temp.	Time	Cycles
Genomic Mouse DNA	50	ng	Denaturing	95 °C	600 s	**1 x**
Primers	10	pmol	Denaturing	95 °C	30 s	
dNTPs	0.20	mM	Annealing	65 °C	30 s	
Reaction Buffer	0.1	Vol	decreasing by 0.5 °C per cycle			**10 x**
$MgCl_2$	1.5	mM	Extension	72 °C	70 s	
Taq Polymerase (Immolase)	1.0	U	Denaturing	95 °C	30 s	
			Annealing	60 °C	30 s	**24 x**
Reaction Volume	20.0	µL	Extension	72 °C	70 s	
			Final Extension	72 °C	600 s	**1 x**
Amplification Product			**Size**			
KI^{FH} or KI^{FHcyt}			1121 bp			

Table 8 – PCR conditions for KI^{FH} and KI^{FHcyt} genotyping

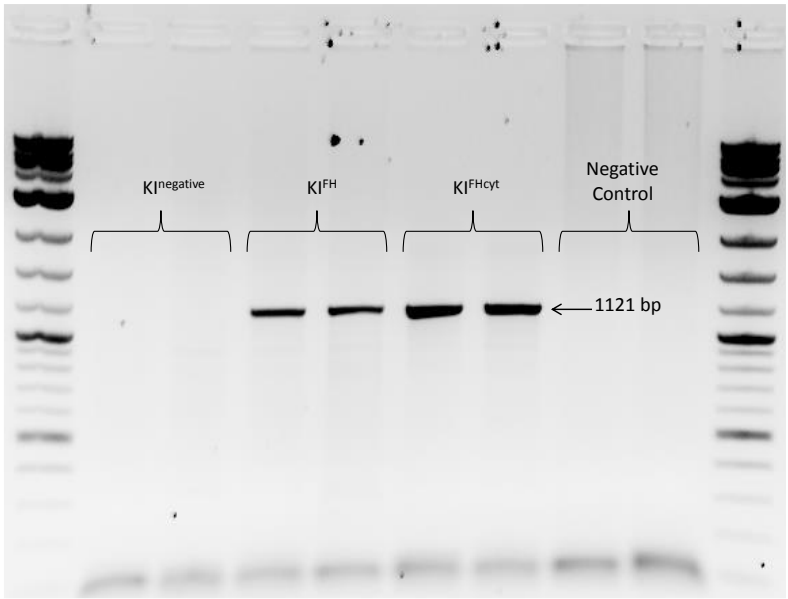

Figure 21 - KI genotyping gel
1% agarose gel electrophoresis showing PCR products from KI^{FH} PCR. From left to right: lane 1 - 2-log ladder; lanes 2 and 3 – KI negative; lanes 4 and 5 - KI^{FH}; lanes 6 and 7 - KI^{FHcyt}; lanes 8 and 9 - no DNA control; lane 10 - 2-log ladder.

MTS genotyping						
Primer			**Sequence**			
MTS1			CATTGCTGCTGCAATAGAAGTTCATGA			
MTS2			GCCTCTGCTAACCATGTTCATGCCTTCT			
Reaction Mix			**Reaction conditions**			
			Step	Temp.	Time	Cycles
Genomic Mouse DNA	50	ng	Denaturing	95 °C	600 s	**1 x**
Primers	10	pmol	Denaturing	95 °C	45 s	**35 x**
dNTPs	0.20	mM	Annealing	68 °C	45 s	
Reaction Buffer	0.1	Vol	Extension	72 °C	45 s	
$MgCl_2$	1.5	mM				
Taq Polymerase (Immolase)	1.0	U	Final Extension	72 °C	600 s	**1 x**
Reaction Volume	20.0	µL				
Amplification Product			**Size**			
KI^{FH}			639 bp			
KI^{FHcyt}			510 bp			

Table 9 – PCR conditions used for MTS genotyping to differentiate between KI^{FH} and KI^{FHcyt}

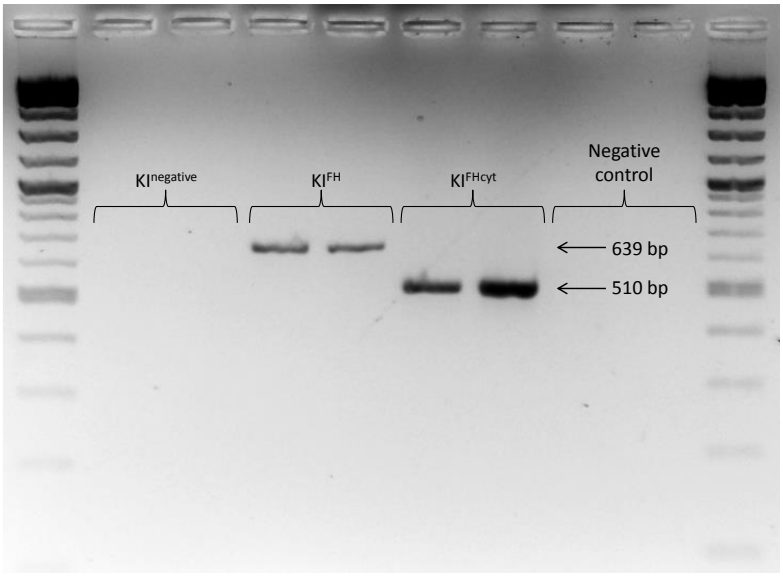

Figure 22 – MTS genotyping gel
2% agarose gel electrophoresis showing PCR products from MTS genotyping PCR. From left to right: lane 1 - 2-log ladder; lanes 2 and 3 – KI negative; lanes 4 and 5 - KI^{FH}; lanes 6 and 7 - KI^{FHcyt}; lanes 8 and 9 - no DNA control; lane 10 - 2-log ladder.

2.2.7.2 Breeding and phenotyping

To investigate the potential for genetic rescue of the *Fh1*$^{f/f}$ *Cre* /+ phenotype, *Fh1*$^{f/f}$ *Cre* /+ mice were bred with *Fh1*$^{+/f}$ *KI*^{FH} or *Fh1*$^{f/+}$ *KI*^{FHcyt} to generate: *Fh1*$^{f/f}$, *Fh1*$^{f/f}$ *Cre* /+, *Fh1*$^{f/f}$ *KI*^{FH}

and *Fh1*$^{f/f}$ *KI*^{FH} *Cre* /+; or *Fh1*$^{f/f}$, *FH1*$^{f/f}$ *Cre* /+, *Fh1*$^{f/f}$ *KI*^{FHcyt} and *Fh1*$^{f/f}$ *KI*^{FHcyt} *Cre* /+ for experiments. *Fh1*$^{f/f}$ *KI*^{FH} *Cre* /+ or *Fh1*$^{f/f}$ *KI*^{FHcyt} *Cre* /+ were bred with *Fh1*$^{f/f}$ to generate mice for further experiments without producing unneeded *Fh1* heterozygous animals. Phenotyping, tissue collection and Kaplan-Meier survival were performed as in 2.2.4.3.

2.2.8 Coronary artery ligation (CAL) surgery

Following administration of buprenorphine (1 mg/kg subcutaneously) pre-operatively, mice were anaesthetised with isofluorane (induction 4%, maintenance 2% in 100% O_2), intubated and ventilated at 150 breaths/minute with a tidal volume of 250 μL with a respirator (Harvard Apparatus). A thoracotomy was made between the fourth and fifth ribs and the underlying lung collapsed using saline-soaked gauze. The ribs were then retracted and pericardium removed to allow visualisation of the left anterior descending (LAD) coronary artery using a dissecting microscope. The LAD was ligated close to its origin using non-absorbable synthetic suture (Prolene). The lung was re-inflated and the chest wall closed. Mice were administered subcutaneous 0.9% saline (500 μL) and allowed to recover in a heated chamber. Sham-operated mice were subject to an identical procedure except that the LAD was not ligated.

2.2.9 Transthoracic Echocardiography

After induction of general anaesthesia with 3-4% isofluorane, mice were placed in a supine position and the chest shaved prior to application of pre-warmed ultrasound coupling gel. Anaesthesia was maintained using 1-1.5% isofluorane in 100% oxygen administered via a nosecone. Images were acquired at a stable heart rate above 450 beats/min. Transthoracic echocardiography was performed with a 40MHz linear array transducer coupled to a Vevo 2100 Imaging System (VisualSonics.) Parasternal short- and long-axis images were taken and mice recovered in a heat incubator prior to being returned to their cage. For screening of

infarct size, mice were scanned 2 weeks after CAL surgery and a careful visual estimate of infarct size made blind to genotype by an experienced operator to screen out small infarct sizes (infarct size < 15 % excluded). For functional studies, image analysis was performed blinded to genotype off-line using Vevo software. Ventricular dimensions and function were assessed from averaged measurements of 3-5 cardiac cycles. Left ventricular end-diastolic diameter (LVEDD); left ventricular end-systolic diameter (LVESD); left ventricular anterior wall thickness (LVAWT) and left ventricular posterior wall thickness (LVPWT) were measured from M-mode recordings obtained from parasternal short axis images at mid-papillary muscle level.

Left ventricular fractional shortening (FS) was calculated using the formula [189-191]:

$$FS = \frac{LVEDD - LVESD}{LVEDD} \times 100$$

Left ventricular end systolic volume (LVESV), left ventricular end diastolic volume (LVEDV) and Teicholz ejection fraction (EF) were calculated using the following equations [191]:

$$LVESV = \frac{7LVESD^3}{2.4+LVESD}\ ,\ LVEDV = \frac{7LVEDD^3}{2.4+LVEDD}\ ,\ EF = \left(\frac{LVEDV-LVESV}{LVEDV}\right) \times 100$$

Left ventricular mass was estimated using M-mode long-axis views using the intraventricular septum thickness (IVST), left ventricular posterior wall (LVPWT) and the LVEDD using the equation below:

$$LV\ mass\ = 1.05 \times (IVST + LVEDD + LVPWT)^3 - (LVEDD)^3$$

2.2.10 Cine-magnetic resonance imaging (MRI)

Cardiac cine-MRI was used to determine cardiac contractile function *in vivo* and provide a highly accurate measurement of infarct size. General anaesthesia was induced with 4% isoflurane in oxygen and maintained at 1.5-2.5%, with adjustment according to cradle temperature, heart rate and respiratory signal. Continual electrocardiographic (ECG) monitoring was undertaken using subcutaneous needle electrodes. Scanning was performed

in a horizontal 9.4 T MR system (Varian) using radiofrequency coils designed for mouse. 8-10 multi-frame contiguous slices spanning the entire left ventricle from base to apex were taken at 1mm intervals. Sequence acquisition was ECG-triggered and respiratory-gated.

Images were reconstructed as tiff files using custom written software. Infarct size was assessed using Image J software. The mid-line left ventricular circumference (LVC) and mid-line length of the infarcted region (IL) were measured from all slices and used to calculate infarct size using the equation below[192]:

$$Infarct\ size\ (\%) = \frac{\sum LVC}{\sum IL} \times 100$$

For functional analysis, manual image segmentation was performed using AMIRA software (Visual Imaging). End-diastolic and end-systolic frames were selected and manual tracing used to define the epicardial border, whilst the LV cavity was segmented by thresholding[193]. Volumes were calculated by multiplying the number of pixels of each compartment by the voxel size. The end-diastolic and end-systolic volume of all slices were summated to give the LV end-diastolic volume (LVEDV) or end-systolic volume (LVESV), respectively. Derived functional parameters – ejection fraction (EF) and cardiac output (CO) – were by calculated according to the equations below:

$$EF = \frac{LVEDV - LVESV}{LVEDV} \times 100\% \ , \ CO = (LVEDV - LVESV) \times Heart\ rate$$

LV tissue volume was estimated by subtracting LV cavity volume from LV epicardial volume. Papillary muscles were included in the LV mass. LV mass was obtained by multiplying the LV tissue volume by the specific gravity of cardiac tissue (1.05 g/cm^3.)

2.2.11 Invasive haemodynamic assessment of left ventricular function

Anaesthesia was induced with 4% isoflurane in oxygen and maintained by administration of 2% isofluorane via a nose cone. The carotid artery and jugular vein were dissected and a 1.4

F pressure catheter (Millar Mikro-tip) inserted into the aortic root via the carotid artery where a 30 second pressure recording was acquired. The pressure catheter was then moved into the LV cavity. The jugular vein was cannulated for subsequent infusion of dobutamine. Anaesthesia was then reduced to 1.5% isoflurane in oxygen and LV pressure allowed to equilibrate for 15 minutes before the baseline LV pressure was recorded. PowerLab 4SP data acquisition system (ADInstruments) was used to record the aortic, LV systolic and LV diastolic pressures from which the dP/dt (change in LV pressure with time) was derived. Baseline recording of LV pressure was continued for a further 15 minutes. Contractile reserve was then assessed by infusion of a low dose (4 ng/g body weight/minute) of dobutamine via the jugular vein for 5 minutes, followed by infusion of high dose (16 ng/g body weight/minute) dobutamine for 5 minutes. Animals were subsequently euthanized by cervical dislocation and organs harvested. Pressure tracings were analysed using LabChart Pro software (version 7, ADInstruments).

2.2.12 Tissue harvesting and powdering

Mice were culled by cervical dislocation. Hearts were rapidly removed from the thorax.

2.2.12.1 Tissue powdering

Whole heart or left ventricle intended for reactive oxygen species (ROS) measurements, high performance liquid chromatography (HPLC), DNA, ribonucleic acid (RNA) or protein extraction were briefly washed in ice cold phosphate buffered saline (PBS), snap frozen in liquid nitrogen and stored at -80 °C. Tissues were then powdered using a pestle and mortar cooled with liquid nitrogen. Great care was taken not to allow tissue/powder to thaw. Powdered tissue was rapidly aliquoted on dry ice for immediate use or storage at -80 °C.

2.2.12.2 Cardiac extraction for histology

Hearts intended for histological analysis were perfused via the aorta with ice cold PBS, followed by formalin (VWR). Hearts were then placed in 10% neutral buffered formalin fixative solution for 24-48 hours at 4 °C and stored at 4 °C in PBS until embedding. A further subset of hearts were perfused via the aorta with ice cold PBS and frozen in O.C.T. (optimum cutting temperature) compound (VWR) on dry ice. These hearts were stored at -20 °C for subsequent cryosection.

2.3 Tissue Culture

2.3.1 Generation of Fh1 $^{-/-}$ and Fh1$^{+/+}$ mouse embryonic fibroblasts (MEFs)

Immortalised *Fh1*$^{-/-}$ and *Fh1*$^{+/+}$ MEFs were a kind gift from Dr Linda O'Flaherty and Dr Julie Adam[179]. To generate MEFs, female breeders were plug checked daily and sacrificed 14.5 days *post coitum*. Placenta, head and dark red organs were then removed from embryos with the head retained for DNA extraction for genotyping. Embryos were minced and incubated in trypsin EDTA at 37 °C with agitation for 15 minutes. The resulting cell suspension was passed through a 70 μm pore cell strainer, cells pelleted by centrifugation at 300 g and resuspended in complete media. At the third passage cells were immortalised by transfection with pBabe PURO Large T antigen retrovirus in complete media supplemented with 5 μg/mL polybrene (to improve transfection efficiency). Immortalised cells were selected by supplementation of complete media with 2 μg/mL puromycin. *Fh1* exons 2 and 3 were excised by treatment of *Fh1* homozygous flox MEFs with an adenovirus-type 5 (dE1/E3) vector driving expression of cre recombinase and a green fluorescent protein (GFP) tag (Vector Biolabs). Control cells were treated with a GFP tag-expressing virus. Single-cell derived clones were established.

2.3.2 Maintenance of immortalised Fh1$^{-/-}$ and Fh1$^{+/+}$ MEFs.

MEFs were cultured in complete media and maintained in a humidified atmosphere at 37 °C and 5% CO_2. 90% confluent cells were passaged twice per week at a ratio of 1:8 (*Fh1$^{-/-}$)* or 1:16 (*Fh1$^{+/+}$*). For passaging, media was aspirated, cells washed with phosphate buffered saline (PBS) and incubated with 0.05% trypsin/EDTA for 3-10 minutes. Once cells were dissociated, complete media was added to stop the action of the trypsin and cells were pelleted by centrifugation at 300 g for 5 minutes. Pellets were then resuspended in complete media and transferred to fresh flasks.

2.3.3 Maintenance of Ad293 cells

Ad293 cells (Stratagene) were used for adenovirus production as described later. They were maintained as described above for MEFs with biweekly 1:10 passages.

2.3.4 Adenoviral treatment of Fh1$^{-/-}$ and Fh1$^{+/+}$ MEFs for RNA and protein extraction

MEFs were seeded at 2 X 10^5 cells/well in 6-well plates and allowed to adhere overnight. MEFs were treated with 1.4 X 10^8 infection forming units (IFU)/well of adenovirus in complete media supplemented with 5 µg/mL polybrene for 12 hours. Media was then replaced with complete media.

2.3.5 siRNA knockdown in Fh1$^{-/-}$ and Fh1$^{+/+}$ MEFs

Fh1$^{-/-}$ and *Fh$^{+/+}$* MEFs were seeded at 5 X 10^4 cells/well in 6-well plates and 2 X 10^3 cells/well in 96-well plates in complete media without antibiotics and allowed to adhere overnight. They were transfected using Dharmafect 1 and ON-TARGET plus smartpool siRNAs (Dharmacon) targeting the gene of interest malic enzyme 1 (*Me1*), a positive control gene cyclophilin B [peptidylprolyl isomerase B (Ppib)] or non-targeting siRNA according to the manufacturer's protocol. Briefly, separate siRNA/optiMEM and Dharmafect/optiMEM mixes were incubated at RT for 5 minutes. Equal volumes were then mixed and incubated at

RT for 20 minutes to create siRNA/Dharmafect complexes. Complete media without antibiotics was added to a final concentration of 25 nM siRNA and 0.2% Dharmafect 1 (v/v). Proliferation assays were performed and RNA was harvested 48 hours post-treatment.

2.3.6 Proliferation Assays

2.3.6.1 Seeding

For trypan blue staining, *Fh1* +/+ and *Fh1* -/- MEFs were seeded at 1 X 10^5 cells/well in 12-well plates in complete medium. For water-soluble tetrazolium salt (WST-8) proliferation assays, cells were seeded at 2000 (for siRNA treatment) or 5000 (for drug treatment) cells per well in 96-well plates in complete media. A calibration curve of 0, 156, 312, 625, 1250, 2500, 5000 and 10,000 cells/well was plated by serial dilution. Cells were allowed to adhere overnight.

2.3.6.2 Drug treatments

Tartronic acid (TA) (Alfa Aesar) was diluted in complete medium, the pH adjusted to 7 and filter sterilised. Medium was aspirated from cells and replaced with drug diluted in media. Cells were incubated at 37 °C for 16 hours.

2.3.6.3 Trypan blue staining

Cells were dissociated and pelleted as described above. Pellets were resuspended in Hank's balanced salt solution (HBSS), mixed with an equal volume of 0.4% trypan blue solution and incubated at RT for 5-15 minutes. Total and blue (unviable) cell numbers were counted using a haemocytometer with 6 counts averaged per sample.

2.3.6.4 Cell count kit-8 proliferation assay

Media was aspirated and replaced with WST-8 [2-(2-methoxy-4-nitrophenyl)-3-(4-nitrophenyl)-5-(2,4-disulfophenyl)-2H-tetrazolium, monosodium salt] from cell count kit-8

(Sigma) diluted 1:10 in complete medium. Cells were incubated at 37 °C for a further 3 hours. Absorbance at 450 nm was measured on a microplate reader (VMax kinetic, Molecular Devices). Cell numbers were estimated by extrapolation from the calibration curve optical densities using 4-parameter logistic regression.

2.4 Adenovirus production

Adenoviruses were produced using the AdEasy Adenoviral Vector System (Stratagene).

2.4.1 Amplification of FH and FHcyt

hFHMTS_fw or hFHnoMTS_fw primer was used in conjunction with hFHcommon_rv to amplify FH with its MTS (FH) and FH without its MTS (FHcyt), respectively. The forward primers introduce a SalI restriction site whilst the reverse introduces a XhoI restriction site. Primer sequences and reaction details are listed in

Table 10. A plasmid (kindly donated by Dr. Patrick Pollard) containing human wildtype FH were used as a template.

Amplification of FH with and without MTS						
Primer			**Sequence**			
hFHMTS_fw			**Aaatgtcgacatgtaccgagcacttcggctcct**			
hFHnoMTS_fw			**Aaatgtcgacatggcaagccaaaattccttcc**			
hFHcommon_rv			**Aaatctcgagctttggacccagcatgtccttag**			
Reaction Mix			**Reaction conditions**			
			Step	Temp.	Time	Cycles
Plasmid DNA	1	ng	Denaturing	95 °C	60 s	**1 x**
Primers	10	pmol	Denaturing	95 °C	30 s	
dNTPs	0.20	mM	Annealing	57 °C	30 s	**32 x**
5 x high fidelity buffer	0.2	Vol	Extension	72 °C	60 s	
$MgCl_2$	1.5	mM				
Phusion DNA polymerase	1.0	U	Final Extension	72 °C	420 s	**1 x**
Reaction Volume	50	µL				
Amplification Product			**Size**			
FH			1533 bp			
FHcyt			1404 bp			

Table 10 – PCR conditions to amplify FH and FHcyt

2.4.2 Mutagensis PCR to amplify ΔATGFH

To introduce an ATG→TTG missense mutation of the 2nd start codon of FH, a two-step site-directed mutagenesis PCR was used. Complementary primers incorporating the mutation (FH mut_rv and FHmut_fw) were used with external primers (hFHMTS-FW and hFHcommon_rv, respectively) to amplify two portions of the FH sequence. These products were purified using a Qiaquick purification kit (Qiagen) according to the manufacturer's protocol. The cleaned PCR products were then used to self-prime for 10 PCR cycles to produce full-length product containing the desired mutation. Twenty further rounds of PCR amplification with the external primers were performed.

Table 11 lists the PCR primers and conditions. Bands were excised under UV transillumination and PCR products purified using Qiaquick gel extraction kit (Qiagen) as per the manufacturer's protocol.

Amplification of FH with and without MTS						
Primer			**Sequence**			
hFHMTS_fw			**Aaatgtcgacatgtaccgagcacttcggctcct**			
hFHcommon_rv			**Aaatctcgagctttggacccagcatgtccttag**			
FHmut_rv			**Gaaggaattttggcttgccaatcg**			
FHmut_fw			**Cgattggcaagccaaaattccttc**			
Reaction Mix			**Reaction conditions**			
Reaction 1	**Reaction 2**		Step	Temp.	Time	Cycles
Plasmid DNA	Plasmid DNA	1 ng	Denaturing	95 °C	60 s	**1 x**
hFHMTS_fw	FHmut_fw	10 pmol				
FHmut_rv	hFHcommon_rv	10 pmol	Denaturing	95 °C	30 s	
dNTPs	dNTPs	0.20 mM	Annealing	57 °C	30 s	**30 x**
5 x high fidelity buffer	5 x high fidelity buffer	0.2 Vol	Extension	72 °C	60 s	
$MgCl_2$	MgCl2	1.5 mM				
Phusion DNA polymerase	Phusion DNA polymerase	1.0 U	Extension	72 °C	420 s	**1 x**
Reaction Volume		50 µL				
Reaction 3						
Reaction 1 product			Denaturing	95 °C	60 s	**1 x**
Reaction 2 product			Denaturing	95 °C	30 s	
dNTPs		0.20 mM	Annealing	57 °C	30 s	**10 x**
5 x high fidelity buffer		0.2 Vol	Extension	72 °C	60 s	
$MgCl_2$		1.5 mM	Extension	72 °C	420 s	**1 x**
Phusion DNA polymerase		1.0 U				
Reaction Volume		50 µL				
Reaction 4			Denaturing	95 °C	60 s	**1 x**
Mix from Reaction 3			Denaturing	95 °C	30 s	
hFHMTS_fw		10 pmol	Annealing	57 °C	30 s	**20 x**
hFHcommon_rv		10 pmol	Extension	72 °C	60 s	
Reaction Volume		70 µL	Extension	72 °C	420 s	**1 x**
Product			**Size**			
Reaction 1			150 bp			
Reaction 2			1407 bp			
Reaction 4			1533 bp			

Table 11 – Mutagenesis PCR conditions used to amplify FHΔATG

2.4.3 Cloning FH into the Shuttle Vector

FH PCR products and pShuttle-IRES-hrGFP-1 plasmid (pSIG1) (Figure 23A) were digested using SalI and XhoI restriction enzymes (New England Biolabs [NEB]). pSIG1 vector was treated with alkaline phosphatase (NEB). PCR products were ligated into the pSIG1 multiple

cloning site using T4 DNA ligase (NEB). Plasmids were transformed into calcium-competent DH10β *E. Coli* by heatshock: DH10β *E. Coli* were defrosted on ice and incubated with ligation mix for 15 minutes, followed by heat shock for 5 minutes at 37 °C and returned to ice for 5 minutes. DH10β *E. Coli* were then recovered at 37 °C for 30 minutes in Luria broth (LB) without antibiotics before plating on 20 µg/mL kanamycin LB agar plates. Plates were incubated at 37 °C overnight. Kanamycin resistant colonies were picked into 20 µg/mL kanamycin LB and incubated 37 °C overnight with shaking at 200 rpm. Plasmid DNA was extracted using a Qiagen mini-prep kit according to the manufacturer's protocol. Plasmid DNA was linearised by digestion with PME1 and transformed into BJ5183 *E. Coli* containing the pAdeasy-1 adenoviral backbone vector Figure 23B by electroporation (200 Ω, 2.5 kV, 25 µF). In BJ5183 cells, homologous recombination between the pSIG1 plasmid and the pAdeasy-1 vector unites the FH and GFP expression cassette with the adenoviral backbone. BJ5183 cells were recovered in antibiotic-free LB at 37 °C for 1 hour and plated on kanamycin LB agar plates. Plates were incubated overnight at 37 °C. Large colonies were expected to contain non-recombined pSIG1, whilst small colonies were potential recombinants. The latter were picked into kanamycin LB, incubated overnight at 37 °C, then DNA isolated using a Qiagen miniprep kit and screened for recombination by diagnostic PAC1 and BSTX1 digests (NEB) (Figure 24). Recombinant plasmids were transformed into DH10β *E. Coli* by heat shock as described above and DNA extracted using plasmid maxi-prep kit (Qiagen) following the manufacturer's protocol.

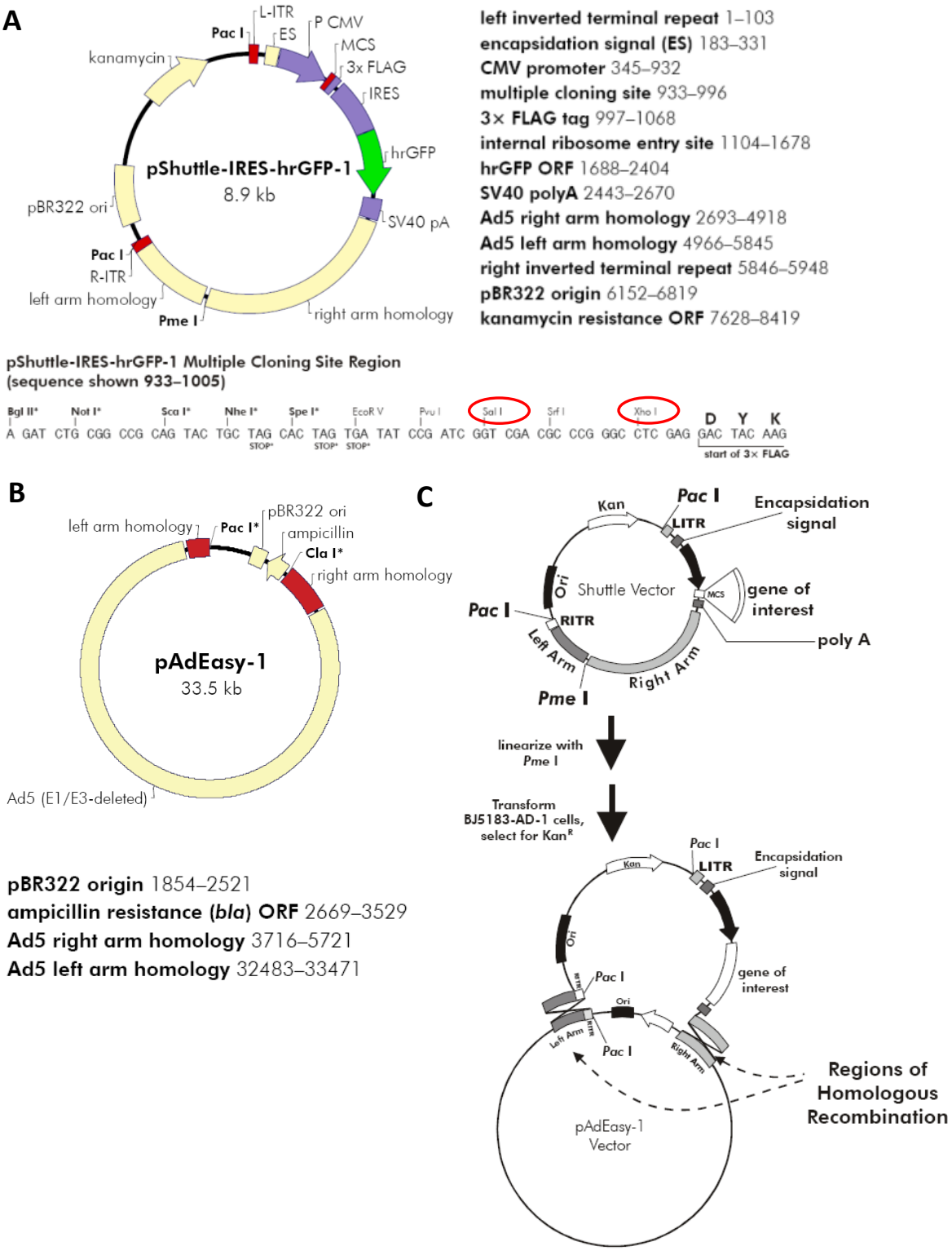

Figure 23 – AdEasy adenoviral vector system[13]
A. pShuttle-IRES-hrGFP-1 (pSIG) vector map - FH was cloned into the multiple cloning site between the SalI and Xho1 restriction sites in frame with the 3x FLAG tag sequences. The kanamycin resistance cassette enables selection. **B.** pAdEasy-1 vector map. This plasmid encodes most of the adenovirus genome except for genes E1 and E3 which enable self-replication. **C.** Homologous recombination between the pShuttle-IRES-hrGFP-1 and the pAdEasy-1 in BJ5183 cells combines the FH expression cassette with the adenoviral backbone.

[13] Modified from AdEasy adenoviral vector system instruction manual (Strategene).

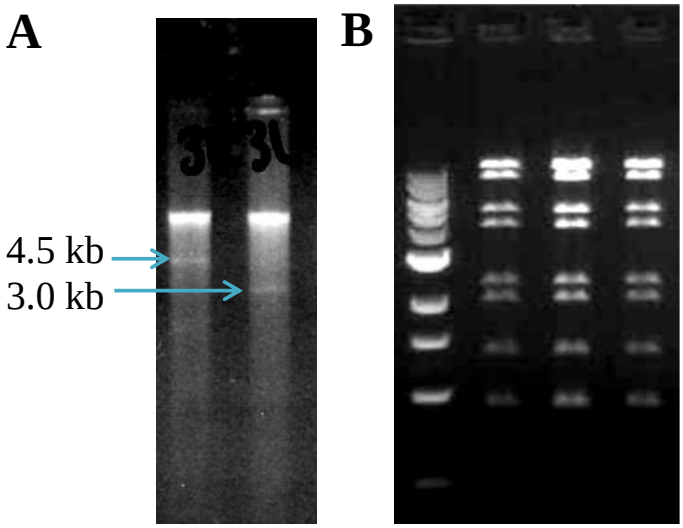

Figure 24 – Restriction digests signifying recombination between pSIG1 and AdEasy-1 vectors
A Pac1 digest of recombined pSIG1-AdEasy1 plasmids. 3.0 kb fragment indicates recombination between the left arms of homology whilst the 4.5 kb product denotes recombination between origins of replication. **B** BSTXI digest pattern confirms recombination has occurred.

2.4.4 Adenovirus production

PacI-digested, recombined plasmid was transfected into a 25 cm^2 flask of ad293 cells using Lipofectamine 2000 (Invitrogen) according to the manufacturer's protocol. Transfected flasks were incubated at 37 ºC for 10 days. Virus was harvested by scraping transfected cells in PBS and released by rapidly snap freezing in liquid nitrogen, thawing at 37 °C and vortexing four times. Lysates were then used to infect a 75 cm^2 flask. Lysate from this flask was used to infect a single 175 cm^2flask, then 5 x 175 cm^2 flasks and finally 25 x 175 cm^2 flasks.

2.4.5 Purification of adenovirus

Adenoviruses were purified by caesium chloride density gradient centrifugation [194]. To create a gradient, 1.3 g mL^{-1} (density) CsCl in Viral Storage Buffer (VSB) was layered above 1.4 g mL^{-1} CsCl in VSB in a thin wall polyallomer tube (Beckman-Coulter, # 367280). The pellet from 25 T175 adenovirally transfected flasks was resuspended in viral storage buffer (VSB) without NaCl and freeze-thaw-vortexed four times. The resulting lysate was cleared by centrifugation at 500 g and the supernatant was supplemented with CsCl to a density of 1.1 g mL^{-1}. Virus was carefully placed on top of the gradient. The gradient was centrifuged at

200,000 x g overnight at 4ºC in a Beckman-Coulter Optima Max-XP ultracentrifuge (MLS-50 rotor). The white adenoviral band was collected using a 2 mL syringe and 18 gauge needle. Adenovirus was desalted by placing in 12,000-14,000 molecular weight dialysis tubing and leaving it in three changes of dialysis buffer for 2 hours and one overnight at 4 °C. Adenoviruses were then diluted in adenoviral storage buffer and stored at -80 °C.

2.4.6 Calculating adenoviral titre

Adenoviral titre was estimated using the AdEasy Viral Titer Kit (Agilent technologies). Ad293 cells were seeded at 5 X 10^5 cells per well in 12-well plates and allowed to adhere overnight. Cells were treated with 10^{-3}, 10^{-4}, 10^{-5}, 10^{-6}, 10^{-7} and 10^{-8} dilutions of adenovirus in duplicate for 8 hours. Media was then replaced. At 48 hours post-adenoviral treatment, concentrations resulting in significant numbers of non-adherent cells were discarded. Cells were then fixed with ice-cold methanol and washed with PBS 1% BSA prior to incubation with 1:500 anti-hexon antibody at 37 ºC for 1 hour. Wells were washed, then incubated with 1:1000 HRP-conjugated goat anti-mouse antibody at 37 ºC for 1 hour. Cells were washed again, followed by incubation with 3,3'-diaminobenzidine (DAB) substrate at 4ºC overnight. Based on this, the 10^{-6} dilution of adenovirus was used for titre calculations as this was the highest concentration with fewest non-adherent cells. Five images per well were captured using a Nikon Eclipse TE2000U inverted microscope. The number of brown cells was counted using ImageJ and adenoviral titre in infection forming units (IFU) estimated. Figure 25 shows representative images of cells treated with each adenovirus.

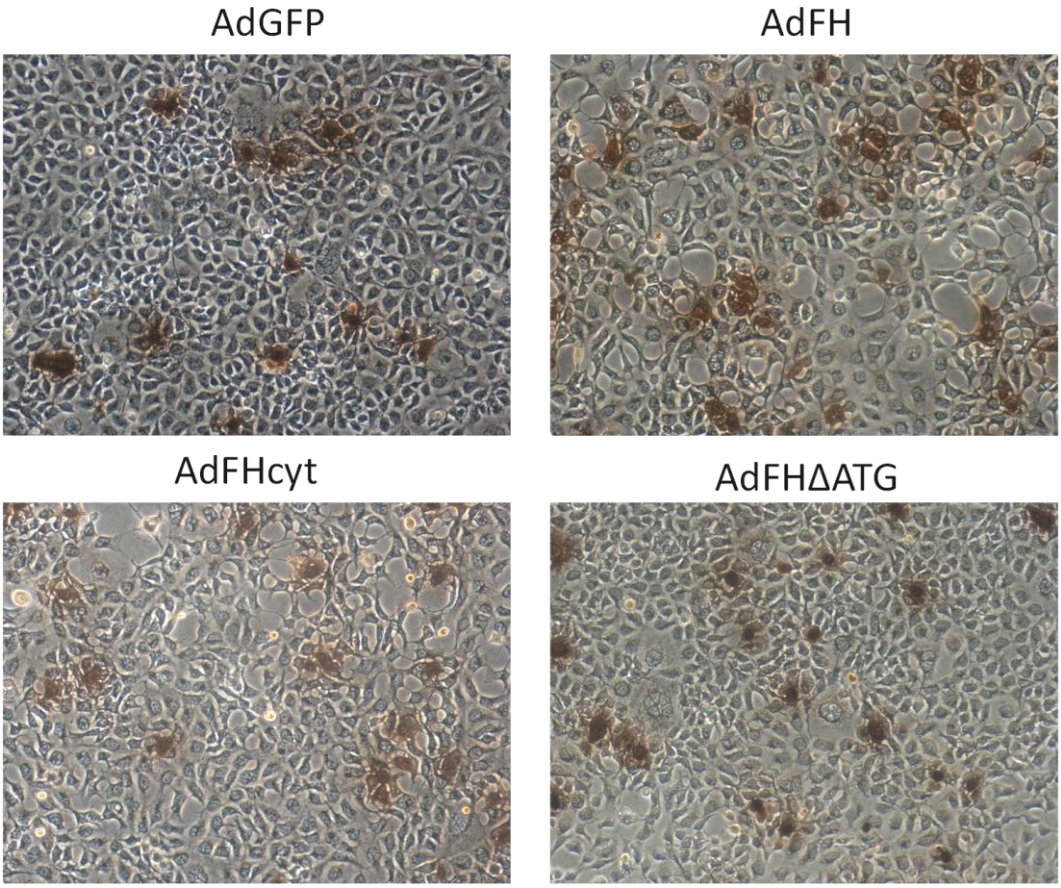

Figure 25 – Staining of ad293 cells expressing the adenoviral capsid hexon protein
Adenovirally infected cells are stained in brown.

2.5 RNA extraction and quantification

2.5.1 Production of lysates from cells

Cells were washed briefly with PBS, then homogenised on ice by scraping in Qiagen's lysis/RNase-inactivating buffer (RLT) and passing through a 21 gauge needle 5 times.

2.5.2 Production of lysates from powdered tissue

300 μL of Qiagen's RLT buffer was added to a 15 mg tissue aliquot which was then mechanically disrupted on ice with a homogeniser (Ultra-Turrax, VWR).

2.5.3 RNA isolation

RNA extraction from cells or powdered tissue were performed using an RNeasy mini kit or RNeasy mini fibrous tissue kit, respectively, according to the manufacturer's directions including on column DNase digestion.

2.5.4 RNA assessment of RNA and quality

RNA yield and quality of samples was verified by measuring absorbance at 260 and 280 nm using a spectrophotometer (Nanodrop ND-1000) and RNA integrity checked by agarose gel electrophoresis.

2.5.5 cDNA synthesis

Applied Biosystems' high capacity cDNA reverse transcription kit was used to create cDNA following the manufacturer's protocol.

2.5.6 qRT-PCR

Quantitative real-time PCR (qRT-PCR) was performed using TaqMan Fast Universal Mastermix (Applied Biosystems) and a FAM-labelled probe for the gene of interest multiplexed with a VIC-labelled probe for the housekeeping control gene β-actin (Applied Biosystems).

Table 12 lists the probes used. TaqMan assay-based qRT-PCR was run on a StepOne Real Time PCR system using the program listed in

Table 13. Relative expression was calculated using the comparative C_T method using Applied Biosystems' StepOne Software.

Gene Symbol (Alias)	Gene Name (Synonym)	Applied Biosystems Catalogue Number
Acta1	Actin, alpha 1, skeletal muscle	Mm00808218_g1
Actb	Actin, beta	4352341E
Atp2a2	ATPase, Ca^{2+} transporting, cardiac muscle, slow twitch 2 (Sarcoplasmic endoplasmic reticulum calcium-dependent ATPase)	Mm01201431_m1
Bnip3	BCL2/adenovirus E1B interacting protein 3	Mm01275601_g1
Egln3	EGL nine homolog 3 (Prolyl hydroxylase domain protein 3)	Mm00472200_m1
G6pdx	Glucose-6-phosphate dehydrogenase	Mm00656735_g1
Hif-1a	Hypoxia inducible factor 1, alpha subunit	Mm01283757_m1
Hmox1	Haemoxygenase 1	Mm00516005_m1
Ldha	Lactate dehydrogenase A	Mm01612132_g1
Me1	Malic enzyme 1, NADP(+)-dependent, cytosolic	Mm00782380_s1
Mthfd2	Methylenetetrahydrofolate dehydrogenase (NADP+ dependent) 2, methenyltetrahydrofolate cyclohydrolase	Mm00485276_m1
Myh6	Myosin, heavy polypeptide 6, cardiac muscle, alpha	Mm00440359_m1
Myh7	Myosin, heavy chain 7B, cardiac muscle, beta	Mm01319006_g1
Nppa	Natriuretic peptide type A	Mm01255747_g1
Nppb	Natriuretic peptide type B	Mm01255770_g1
Nqo1	NAD(P)H dehydrogenase, quinone 1	Mm01253561_m1
Pdk1	Pyruvate dehydrogenase kinase, isoenzyme 1	Mm00554306_m1
Ppib	Peptidylprolyl isomerase B (cyclophilin B)	Mm00478295_m1
Slc1a3	Solute carrier family 1 (glial high affinity glutamate transporter), member 3	Mm00600697_m1
Slc2a1	Solute carrier family 2 (facilitated glucose transporter), member 1	Mm00441480_m1
Slc2a4	Solute carrier family 2 (facilitated glucose transporter), member 4	Mm00436615_m1
Vegfa	Vascular endothelial growth factor A	Mm01281449_m1

Table 12 – Applied Biosystems murine TaqMan gene expression assays used for qRT-PCR

Step	Temp.	Time	Cycles
Denaturing	95 °C	20 s	**1 x**
Denaturing	95 °C	1 s	**35 x**
Annealing and extension	60 °C	20 s	

Table 13 – Taqman qPCR thermal cycling program

2.6 Mitochondrial and nuclear DNA quantification

DNA was extracted using a DNeasy blood and tissue kit (Qiagen) according to the manufacturer's protocol. qRT-PCRs for the gDNA-encoded *Ndufv1* [NADH dehydrogenase (ubiquinone) flavoprotein 1] and the mtDNA-encoded *Mt-Nd1* (NADH dehydrogenase) gene was performed using the conditions in

Table 14. Analysis was performed by a modified comparative C_T method where gDNA-encoded *Ndufv1* served as an endogenous control and mtDNA-encoded *Mt-Nd1* as the target gene.

Mitochondrial DNA quantification						
Primer or Probe			**Sequence**			
Mt-Nd1 fw			TCGACCTGACAGAAGGAGAATCA			
Mt-Nd1 rv			GGGCCGGCTGCGTAT			
Mt-Nd1 probe			AATTAGTATCAGGGTTTAACG			
Nuc-Ndufv1 fw			GAGCAGGACTTCTCCTTCACATC			
Nuc-Ndufv1 rv			CCCGTCTCAGGGCACCTT			
Nuc-Ndufv1probe			TTTCCTACTCTGTCCAGGCT			
Reaction Mix			**Reaction conditions**			
			Step	**Temp.**	**Time**	**Cycles**
Mouse DNA	50	Ng	Denaturing	95 °C	20 s	**1 x**
Forward primer	900	nM	Denaturing	95 °C	1 s	**35 x**
Reverse primer	900	nM	Annealing	60 °C	20 s	
Probe	200	nM	and extension			
2 X Taqman fast mastermix	**0.5**	**Vol**				

Table 14 – Taqman assay-based qRT-PCR employed to quantify mitochondrial relative to nuclear DNA.

2.7 Protein extraction and Western blotting

2.7.1 Lysates from cell culture samples

Cells were washed briefly with PBS, then scraped in buffer RLT and passed through a 21 gauge needle 10 times on ice to homogenise.

2.7.2 Lysates from powdered tissue samples

400 μL urea lysis buffer was added to a 15 mg powdered tissue aliquot and which was then mechanically disrupted on ice with a homogeniser (Ultra-Turrax, VWR). To pellet any debris lysates were centrifuged at 10,000 g for 10 minutes at 4 °C then transferred to fresh tubes.

2.7.3 Lysates from subcellular fractions

Mitochondrial and cytoplasmic fractions were isolated using the Q-proteome mitochondria isolation kit (Qiagen) according to the manufacturer's protocol, except that the cytosolic fraction underwent one further centrifugation step at 100,000 g for 2 hours to remove any contaminants.

2.7.4 Bicinchoninic acid (BCA) assay

Samples were diluted appropriately (1:5 for mitochondrial fractions, 1:10 for cytosolic fractions, 1:20 for whole cell and tissue lysates) in the initial lysis. BCA assay (Pierce, Thermo Scientific) was performed according to the manufacturer's protocol with bovine serum albumin (BSA) standards. Absorbance at 562 nm was measured using a plate reader (VMax kinetic, Molecular Devices). In accordance with the BCA assay result, samples were diluted to equal concentrations in the original lysis buffer, mixed with 0.2 volumes of 6x protein loading buffer, vortexed and heated to 95 °C for 5 minutes.

2.7.5 Western blotting

Equal amounts of protein lysates and 5 μL of protein molecular weight marker (Amersham full-range rainbow marker, GE Healthcare) were loaded onto pre-cast polyacrylamide gels (Nupage 4-12% Bis Tris gel, Novex, Invitrogen) and separated by electrophoresis at 200 V for 1 hour. Proteins were transferred onto polyvinylidene difluoride (PVDF) membrane (Immun-Blot, Bio-Rad) using an electrophoretic transfer cell (Mini Trans-Blot, Bio-Rad) in ice-cold transfer buffer.at 300 mA for 2-3 hours. Membranes were blocked in 5% (w/v) low-

fat milk powder in tris-buffered saline tween-20 (TBST) for 2 hours at room temperature. Blocked membranes were then incubated at 4 °C overnight with primary antibody diluted in 5% milk-TBST. Antibody concentrations used are shown in

Table 15. 5 x 5 minute washes in TBST were performed, followed by 40 minutes incubation in the appropriate horseradish peroxidase-conjugated secondary antibody diluted 1:4000 in 5% milk TBST. Blots were developed using enhanced chemiluminescence (ECL) reagents and film (GE Healthcare). Western blots were usually stripped of antibodies and reprobed (often with a loading control antibody). For this, membranes were placed in stripping solution and incubated at 50 °C with rotation for 40 minutes, followed by 5 washes in TBST and reblocking.

Antibody	Dilution	Source	Catalogue number
Goat anti-fumarase	1:4000 WB	Sigma	SAB2500433
Monoclonal ANTI-FLAG® M2 antibody	1:2000 WB 1:50 IF	Sigma	F1804
Anti-V5 antibody		Invitrogen	46-0705
Rabbit anti-β-Tubulin	1:2000 WB	Abcam	Ab6046
Rabbit anti-VDAC1	1:1000 WB	Cell signalling	4866
Rabbit anti-Histone (H4)	1:1000 (WB)	Abcam	Ab7311
ECL Anti-mouse IgG, peroxidase-linked whole antibody (from sheep)	1:4000 (WB)	GE Healthcare	NXA931
Donkey Anti-Rabbit IgG, Whole Ab ECL Antibody, HRP Conjugated	1:4000 (WB)	GE Healthcare	NA934v
Rb PAb to Goat IgG (HRP)	1:4000 (WB)	Abcam	Ab6741
Alexa Fluor® 633 F(ab') 2 Fragment of Goat Anti-Mouse IgG	1:100 (IF)	Invitrogen	A-21053

Table 15 – Antibodies used for western blotting and immunofluorescence. WB – western blot. IF – immunofluorescence.

2.7.6 Densitometry

Films were scanned using scanned with a flatbed scanner (CanoScan LiDE 100, Canon UK) and digital images imported into ImageJ (NIH) for analysis and quantification of signals as outlined (http://www.lukemiller.org/journal/2007/08/quantifying-western-blots-without.html).

2.8 Immunofluorescence (IF)

MEFs were plated at 1 X 10^4 cells per chamber in Nunc 4-well chamber slides and allowed to adhere overnight, then treated with 2 X 10^4 IFU adenovirus for 12 hours. 48 hours post-adenoviral treatment, cells were incubated with 200 nM MitoTracker Red CMXRos (Invitrogen) in DMEM. MEFs were fixed in 4% PFA for 10 minutes and blocked in immunofluorescence blocking buffer. Slides were incubated in 1:50 monoclonal ANTI-FLAG® M2 antibody (Sigma) in immunofluorescence blocking buffer overnight at 4 ºC, washed with PBS, incubated with then 1:100 Alexa Fluor 633 labelled goat anti-mouse IgG (Invitrogen), washed with PBS. Slides were mounted with Prolong Gold antifade reagent (Invitrogen). Images were acquired using a Leica TCS SP5X confocal microscope system with a 63x oil immersion lens.

2.9 Histology

2.9.1 Embedding

Formalin fixed hearts were processed in an automatic tissue processor overnight using the program listed in Table 16 (Bavimed Histomaster, Germany). Processed tissue was subsequently manually aligned and embedded in blocks using hot paraffin wax.

Step	Time
1. 70% Ethanol	45 min
2. 95% Ethanol	30 min
3. 95% Ethanol	45 min
4. 100% Ethanol	30 min
5. 100% Ethanol	45 min
6. 100% Ethanol	45 min
7. Hisoclear	30 min
8. Hisoclear	30 min
9. Hisoclear	30 min
10. Paraffin	30 min
11. Paraffin	45 min
12. Paraffin	45 min

Table 16 – Program followed by tissue processor to prepare tissue for embedding

2.9.2 Sectioning

Formalin fixed, paraffin embedded hearts were cut into 7 µm cardiac cross-sections using a rotary microtome (Leica) and floated on a 40 °C water bath, then placed on polysine-coated glass slides and dried at 40 °C.

OCT embedded frozen hearts were cut into 7 µm cross-sections using a cryostat (Leica) and placed on electrostatic slides (VWR) and air dried.

2.9.3 Haematoxylin and eosin staining

Haematoxylin and eosin staining to assess general microscopic morphology was performed on paraffin embedded sections following the steps in Table 17. Slides were mounted with Neomount (Merck).

Step	Time
Histoclear	5 min
Histoclear	5 min
100% Ethanol	1 min
100% Ethanol	1 min
95% Ethanol	1 min
70% Ethanol	1 min
30% Ethanol	1 min
Deionised water	5 min
Haematoxylin	10 min
Running tap water	2 min
Eosin	30 sec
Tap water	30 sec
30% Ethanol	1 min
70% Ethanol	1 min
95% Ethanol	1 min
100% Ethanol	1 min
Histoclear	5 min
Histoclear	5 min

Table 17 – Haematoxylin and eosin staining procedure

2.9.4 Picrosirius red staining

Picrosirius red staining for collagen was performed on paraffin embedded sections using a picrosirius red stain kit (Polysciences Inc) according to the manufacturer's protocol (for steps see Table 18) and slides were mounted using Neomount. Both bright and dark field images

were acquired using a Nikon Eclipse TE2000U inverted microscope. Metamorph image analysis software was used to quantify total fibrotic area from dark field images. This was then expressed as a percentage of the total tissue area from a bright field image of the same region.

Step	Time
Histoclear	5 min
Histoclear	5 min
100 % Ethanol	1 min
100 % Ethanol	1 min
95 % Ethanol	1 min
70 % Ethanol	1 min
30 % Ethanol	1 min
Deionised water	5 min
Solution A	2 min
Deionised water	2 min
Solution B	60 min
Solution C	2 min
70 % Ethanol	1 min
95 % Ethanol	1 min
100 % Ethanol	1 min
Histoclear	5 min
Histoclear	5 min

Table 18 – Picrosirius red collagen staining procedure

2.9.5 Wheat germ agglutinin staining

Cryosections were fixed by incubation with 4% paraformaldehyde (TAAB laboratories) for 15 minutes at 37 °C. Slides were washed 4 times in PBS for 5 minutes. 2 µg/mL wheat germ agglutinin-texas red X [Invitrogen (W21405)] diluted in PBS was applied to the slides and incubated at room temperature for 1 hour. Slides were washed 4 times in PBS for 5 minutes. Slides were mounted in vectorshield with DAPI (4',6-diamidino-2-phenylindole) (Vector labs). Images were acquired using a Nikon Eclipse TE2000U inverted microscope. Cardiomyocyte cross-sectional area was analysed using ImageJ.

2.10 Electron microscopy

Small blocks (less than 1 mm^3) were cut from the left ventricular myocardium. These were fixed in 2.5% glutaraldehyde in 100 mM phosphate buffer. Fixative was replaced with fresh 2.5% glutaraldehyde in 100 mM phosphate buffer after 20 minutes and samples fixed at 4 °C overnight. Post-fixation, samples were washed with 1% osmium tetroxide in 100 mM cacodylate buffer for 1-2 hours at 4 °C. Samples were washed 8 times with distilled water and then stained *en bloc* with 0.5% aqueous uranyl acetate for 16 hours at 4 °C in the dark. Samples were dehydrated using a series of acetones each for 15 minutes (30 % acetone, 50 % acetone, 70 % acetone, 90 % acetone) then 100 % acetone 3 X 30 minutes, followed by 2 X 15 min in propylene oxide. Samples were embedded in epoxyresin (Agar Scientific) using a graded infiltration of propylene oxide:resin mix each for 1 hour (2:1 propylene oxide:resin, 1:1 propylene oxide:resin, 1:2 propylene oxide:resin) then overnight in 100 % resin. This was changed for fresh resin and samples then placed in embedding moulds and polymerised by incubation at 60 °C for 24 hours. Blocks were sectioned using an ultramicrotome (Reichert Ultracut E, Germany). Sections were floated on distilled water and collected on a copper grid. These were allowed to dry before further staining with 2% aqueous uranyl acetate and lead citrate. Sections were imaged with a Philips Technai 12 electron microscope.

2.11 Metabolite Analysis

Metabolite analysis and subsequent statistical analysis was kindly performed by Dr Warrick Dunn at the University of Birmingham using Fourier transform ion cyclotron resonance mass Spectroscopy. The methods used were as described in Ashrafian *et al* (2012), supplementary information[166].

2.12 Flux Balance Analysis

Flux balance modelling of mitochondrial (and selected aspects of cytosolic) metabolism was kindly performed by Dr Anthony Smith (University of Cambridge), using the *iAS253* model of the human heart mitochondrion. This model utilises the MitoMiner database to integrate metabolic pathway and protein expression data and takes into account partitioning of the mitochondria and cytosol along with thermodynamic favourability. Smith *et al*. (2011) describe this model in detail[195]. Some relaxation of directionality constraints was applied, where new evidence suggests the reversibility of a reaction.

2.13 High-performance liquid chromatography (HPLC) for creatine and adenine nucleotides

The HPLC column used was a Supelcosil™ LC-18-T, 5 µM, (Sigma Supelco, catalogue number 58971) maintained at 30 °C with a mobile phase flow rate of 0.7 mL/min and a UV detector wavelength of 206 nm. Azur software was used for data collection and analysis. HPLC standard solution samples were run in duplicate before and after each round of HPLC. All buffers, tubes and pipettes were pre-chilled on ice and all steps of sample preparation were performed at 4 °C. 10 mg of tissue was homogenised in 550 µL of 0.4 N perchloric acid at 1100 rpm using a dounce homogeniser (IKA). A 100 µL aliquot was taken for a Lowry protein assay and added to an equal volume of 1 M sodium hydroxide incubated at 60 °C for 2 hours. The remaining sample was neutralised with 1 M potassium hydroxide, centrifuged at 3000 g for 5 minutes and the supernatant filtered through a 45 µm PVDF filter. 100 µL of sample was loaded onto the HPLC machine.

Lowry assay (Sigma) quantification of total protein was performed according to the manufacturer's protocol. Absorbance at 750 nm was measured using an ultrospec 2100 pro

spectrophotometer (G E Healthcare). Values were normalised based upon dilution volume and Lowry assay protein quantification.

2.14 ROS measurement by lucigenin-enhanced chemiluminescence

A homogeniser (Ultra-Turrax, VWR) was used to disrupt 15 mg of powdered cardiac tissue in Krebs-HEPES buffer supplemented with a complete-mini protease inhibitor cocktail (Roche). Protein concentrations were determined by BCA assay (see 2.7.4). 37 °C Krebs-HEPES buffer aerated with 95 % O_2, 5% CO_2 containing 5 μM lucigenin was placed into a single tube luminometer (Berthold FB12). Once a stable baseline reading was achieved, 2 mg of sample was added and when the trace again reached equilibrium, the luminescence was recorded.

2.15 Malondialdehyde

Protein was precipitated from 30 mg powdered cardiac tissue using 2 volumes of cold 10 % trichloroacetic acid. Samples were sonicated for 2 X 30 seconds and then centrifuged at 13,000 g for 1 minute at room temperature. The supernatant was reacted with an equal volume of 0.67% (w/v) thiobarbituric acid at 100 °C for 10 minutes. To prepare a standard curve, 1 mmol of malondialdehyde tetrabutylammonium salt was hydrolysed in 1 % sulphuric acid for 2 hours, diluted to 1-10 μM in 10% trichloroacetic acid and reacted with thiobarbituric acid as described above. After cooling, the absorbance at 532 nm was read using a plate reader (SpectroMax 250, Molecular Devices) and the concentration of malondialdehyde calculated based upon the standard curve.

2.16 Data analysis and statistics

Data were acquired and analysed blind to genotype or treatment. Statistical analyses were performed using Graphpad Prism Software (version 6). Student's t-test was used for comparison of 2 groups when data were parametric. The Mann-Whitney U-test was used for

comparison of 2 groups when data were non-parametric. Three or more groups of parametric data were compared using 1-way analysis of variance (ANOVA), with Tukey's correction for multiple comparisons. If 3 or more groups of non-parametric data were compared using the Kruskal-Wallis test followed by Dunn's post-hoc test for multiple comparisons. To compare between data for the same cohort of subjects at different time points (for example to determine the ability of a genotype to respond to dobutamine stress during invasive haemodynamic assessment of cardiac function) 2-way ANOVA with Tukey's correction for multiple comparisons was utilised. Data are represented as mean ± standard error of the mean unless otherwise stated. Annotation used: *$p<0.05$ compared to indicated groups, **$p<0.01$ compared to indicated groups, ***$p<0.001$ compared to indicated groups, Ψ $p<0.05$ compared to all groups unless otherwise indicated, Φ $p<0.01$ compared to all groups unless otherwise indicated, ξ $p<0.001$ compared to all groups unless otherwise indicated.

3 CHAPTER 3: THE CHRONIC ROLE OF HIF-1α IN MYOCARDIAL INFARCTION

3.1 Hypothesis and aims

The overall aim of the work presented in this chapter was to define the chronic role of endogenous oxygen-labile HIF-1α after myocardial infarction – an area which existing murine models fail to adequately address. In order to do so, the well-established murine coronary artery ligation (CAL) paradigm of post-myocardial infarction heart failure was applied to a cardiomyocyte-specific, temporally inducible *Hif-1α* knockout mouse model which was induced at two weeks post-infarction. Cardiac function was subsequently assessed *in vivo* at a chronic time point. This approach was designed to permit the beneficial acute effects of HIF-1α signalling to proceed unperturbed during infarction, but to ablate HIF-1α beyond this acute phase, to negate its potentially deleterious chronic effects.

The main hypotheses of this chapter are:

i. In the absence of cardiac challenge (e.g. by myocardial ischaemia), gross cardiac function will be unaffected by cardiac-specific deletion of *Hif-1α*, as previously described[61, 107].

ii. In contrast to the benefits observed with acute HIF-1α activation in ischaemic heart disease, prolonged HIF-1α activation will be deleterious to cardiac function in post-infarction heart failure.

iii. As a corollary of (ii), ablation of HIF-1α beyond the acute phase of myocardial infarction in mice will improve cardiac function as assessed by invasive pressure measurements and contractility assessment by cine MRI.

Accordingly, the key aims of this chapter are to:

i. Generate and validate a temporally inducible model of cardiac-specific HIF-1α deletion.

ii. Assess cardiac function in this model at baseline.

iii. Utilize this model to elucidate whether chronic elevation of endogenous, oxygen sensitive HIF-1α is beneficial or detrimental in the context of myocardial infarction using a murine CAL model.

3.2 Results

3.2.1 Optimisation of Tamoxifen Dose

Mice with exon 2 of *Hif-1α* flanked by loxP sites (*Hif-1a*$^{f/f}$) were crossed with the cardiac-specific, tamoxifen-inducible cre recombinase expressing mouse line, *αMHC-MerCreMer* (*Mcm*)[181, 182]. These mice were backcrossed for 6 generations to a C57BL/6J genetic background. Tamoxifen treatment of *Mcm*/+ mice has been associated with a transient but profound dilated cardiomyopathy, hence it was important to establish the minimum dose of tamoxifen required for efficient excision of the *Hif-1α* floxed allele [196]. Previous studies have shown that 5 days of 20 mg/kg tamoxifen treatment is the minimum required for floxed allele excision, whilst others have suggested this dose to be insufficient for excision at some genomic loci[182, 196].

Accordingly, a small pilot study treating *Hif1α*$^{f/f}$ *Mcm/+* mice with 0, 20, 40 and 80 mg/kg body weight of tamoxifen for 5 days by intraperitoneal injection was performed to identify the tamoxifen dose resulting in excision of the *Hif-1α* floxed allele with minimal side-effects. Mice treated with both 40 and 80, but not 20 mg/kg tamoxifen, demonstrated a non-significant trend towards weight loss (Figure 26). Due to signs of overt distress, including lethargy and rapid loss of body weight, the 80 mg/kg tamoxifen treatment was terminated after 4 doses. Echocardiographic assessment of cardiac function was performed at baseline and after 5 days of tamoxifen treatment in all mice. Reduced cardiac contractility [reflected by calculated left ventricular (LV) ejection fraction and fractional shortening] and LV dilatation were observed in animals receiving higher (40 and 80 mg/kg) doses of tamoxifen (Figure 27).

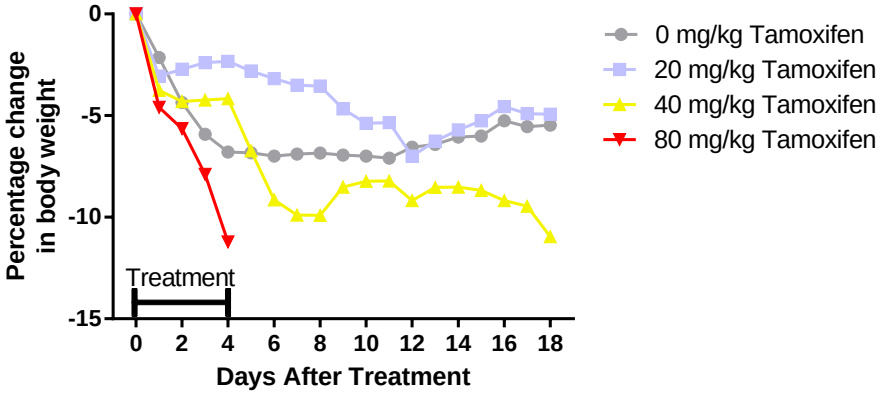

Figure 26 – Percentage change in body weight during and post-tamoxifen treatment
The percentage change in body weight of *Hif-1α$^{f/f}$ Mcm/+* mice treated with the indicated doses of tamoxifen. Treatment with the 80 mg/kg dose was terminated after 4 doses due to signs of distress.

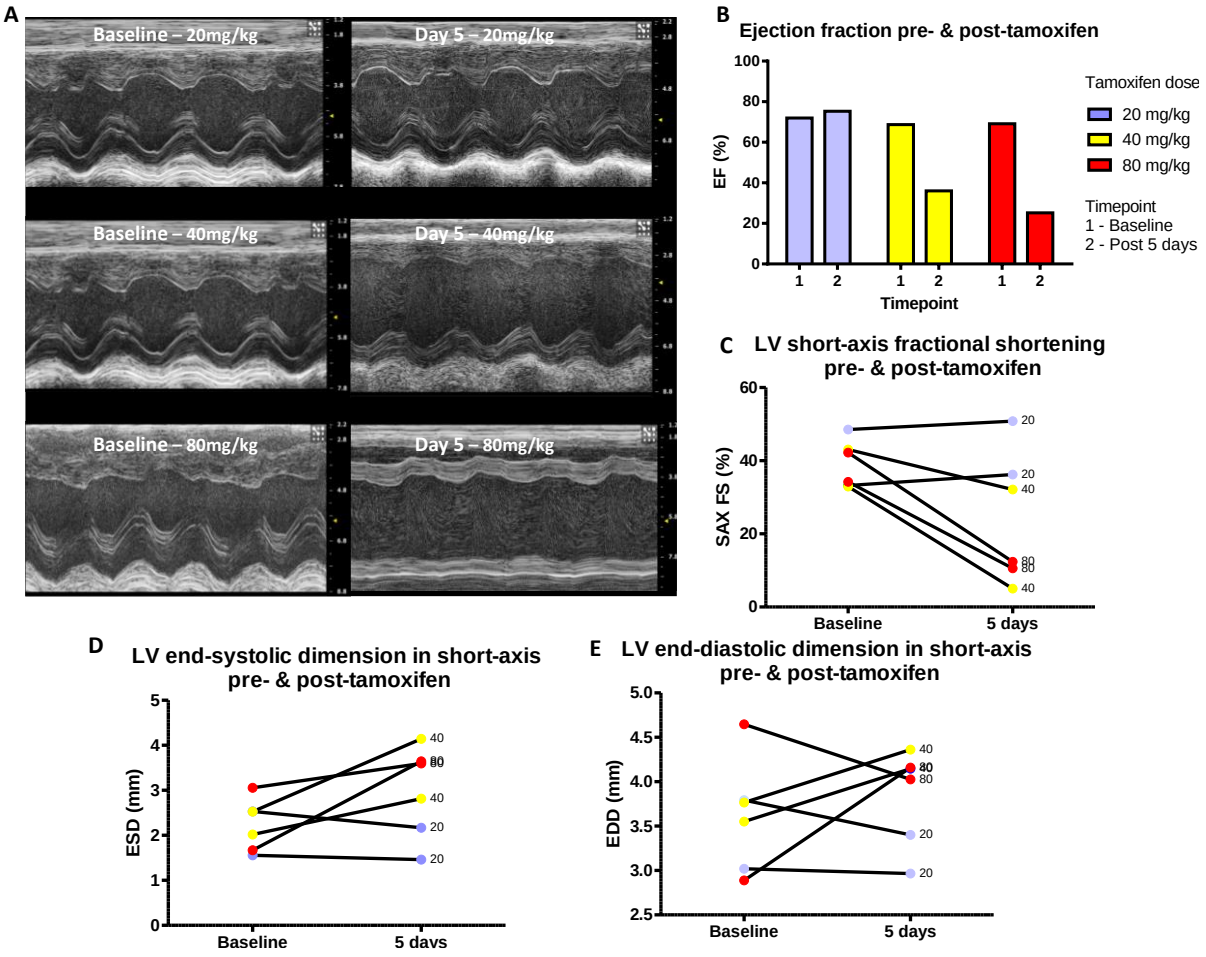

Figure 27 – Assessment of cardiac function in tamoxifen treated *Hif-1α$^{f/f}$ Mcm/+* mice demonstrating compromised cardiac function with 40 and 80 but not 20 mg/kg tamoxifen
A. Representative M-mode echocardiograms at baseline and after tamoxifen treatment. **B.** Left ventricular (LV) ejection fraction **C.** LV short-axis fractional shortening. **D.** LV end-systolic dimension **E.** LV end-diastolic dimension.

Excision of the *Hif-1α* floxed allele in left ventricular DNA from *Hif-1a*$^{f/f}$ *Mcm/+* mice treated with 20 mg/kg tamoxifen was confirmed by amplification of a recombined 1-loxP PCR product. Excision of the floxed allele was not observed in the LV of mice treated with vehicle or in non-cardiac tissues (Figure 28A). This was corroborated by a 79% reduction in *Hif-1a* transcript expression by qRT-PCR (Figure 28B). Based on these findings, 5 doses of 20 mg/kg tamoxifen were used to induce cardiac *Hif-1α* excision for all subsequent experiments.

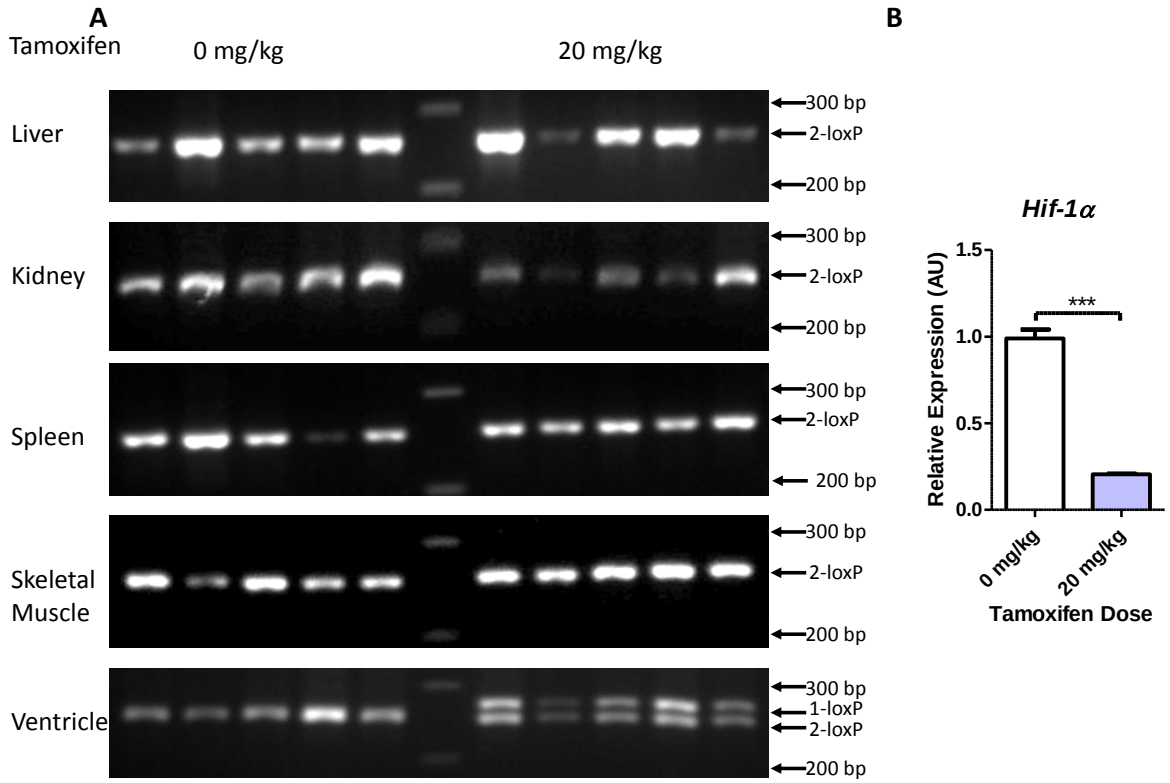

Figure 28 – Specific ablation of cardiac *Hif-1α* by 20 mg/kg tamoxifen treatment in cardiac tissue from *Hif-1α*$^{f/f}$ *Mcm/+* mice
A. The presence of the 1-loxP [270 base pairs (bp)] band in left ventricular samples indicates excision of the *Hif-1α* floxed allele. The absence of a 1-loxP band indicates that non-specific excision was not occurring in vehicle treated ventricular samples and a range of other tissues. The presence of a 2-loxP (260 bp) band indicates the presence of a non-excised *Hif-1α* floxed allele **B.** A 79% reduction in *Hif-1α* transcript expression determined by qRT-PCR and analysed by the $2^{-\Delta\Delta Ct}$ or comparative C_T method using the internal control in cardiac beta actin (encoded by *Actb*) in left ventricular samples from the 20 mg/kg tamoxifen treated group compared to vehicle treated controls. *** $p<0.001$.

3.2.2 Chronic Hif-1α ablation does not affect baseline cardiac function

To assess the effect of chronic cardiac *Hif-1α* ablation at baseline, tamoxifen-treated *Hif-1α*$^{f/f}$ *Mcm/+* (n=13) and *Mcm/+* (n=10) control mice underwent echocardiography and tissue collection 70 days after tamoxifen treatment. No significant differences were observed between genotypes using transthoracic echocardiography in measures of: cardiac contractility [left ventricular end-systolic dimension (LVESD), left ventricular end-systolic volume (LVESV), ejection fraction (EF) and radial systolic peak velocity of the posterior wall measured by tissue Doppler], dilatation [left ventricular end-diastolic dimension (LVEDD) and left ventricular end-diastolic volume (LVEDV)] or cardiac hypertrophy [LV mass, LV anterior wall thickness and LV posterior wall thickness] (Figure 29). Heart rates did not significantly differ between groups during image acquisition.

Elevated heart weight is often associated with cardiac hypertrophy and dysfunction, whilst elevated lung weight in this context reflects left ventricular contractile impairment and the development of congestive heart failure. No significant differences were observed between *Hif-1α*$^{f/f}$ *Mcm/+* and *Mcm/+* groups in absolute heart or lung weights, including when these parameters were normalised to either body weight or tibial length (Figure 30).

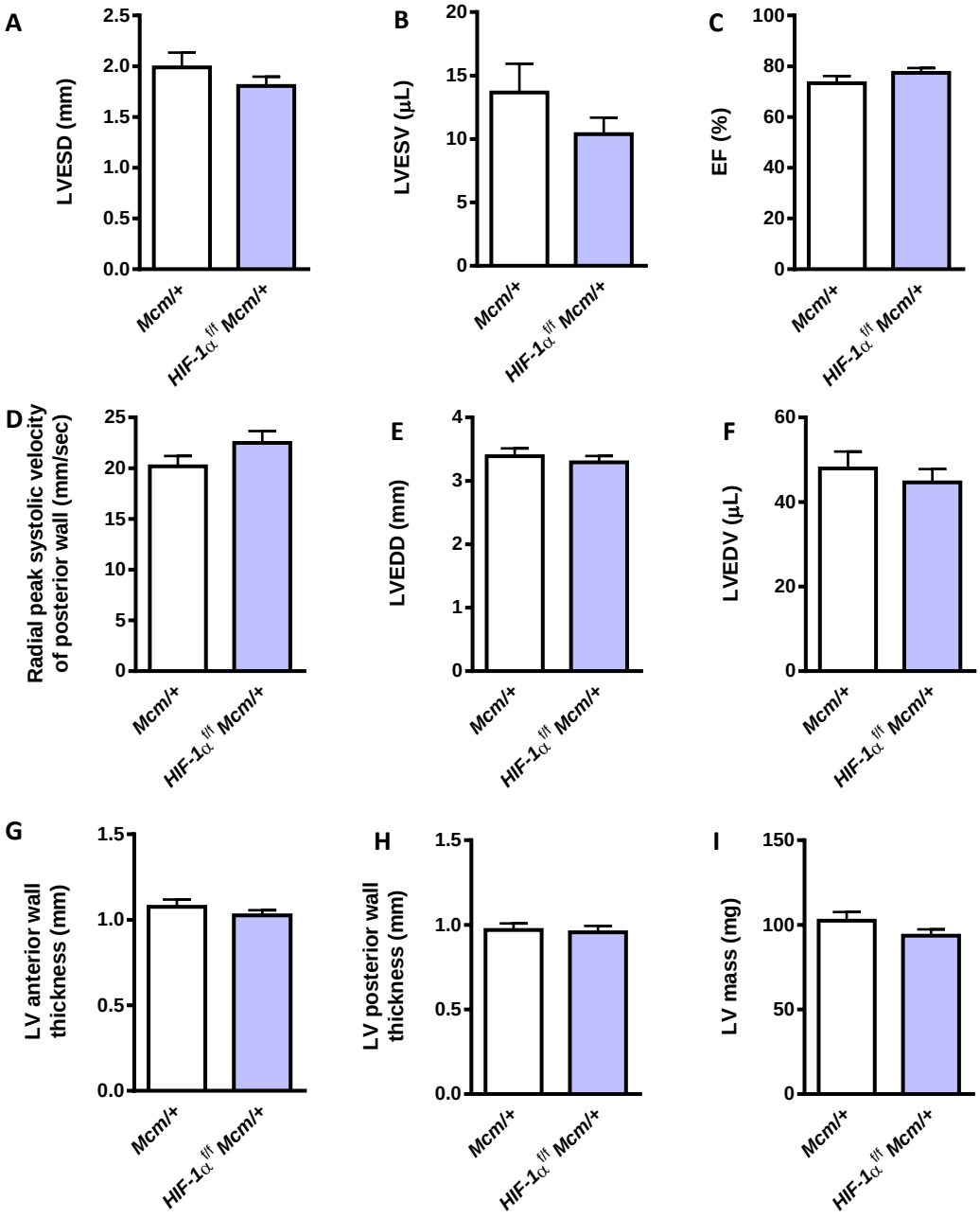

Figure 29 – Echocardiographic assessment of cardiac function in tamoxifen treated *Mcm/+* and *Hif-1α$^{f/f}$ Mcm/+* mice measured at 70 days in the baseline state

A-D. Measures of cardiac function: **A.** Left ventricular end-systolic dimension (LVESD); **B.** Left ventricular end-systolic volume (LVESV); **C.** Ejection fraction (EF); **D.** Radial peak systolic velocity of the posterior wall. **E and F.** Measures of cardiac dilatation: **E.** Left ventricular end-diastolic dimension (LVEDD); **F.** Left ventricular end-diastolic volume (LVEDV). **G-I.** Measures of cardiac hypertrophy: **G.** Left ventricular anterior wall thickness (LVAWT); **H.** Left ventricular posterior wall thickness (LVPWT); **I.** Left ventricular mass.

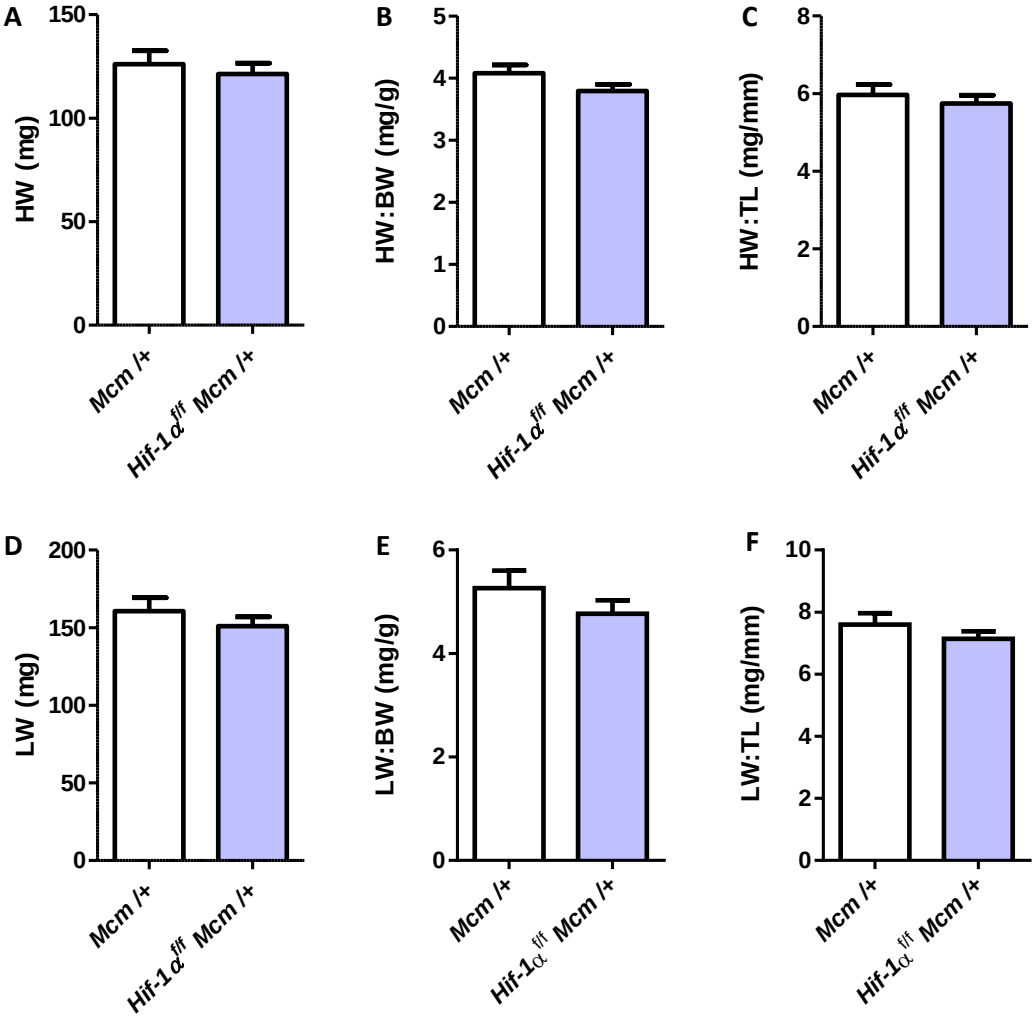

Figure 30 – Terminal absolute and normalised heart and lung weights at 70 days in tamoxifen treated *Mcm/+* and *Hif-1α Mcm/+* mice
A. Heart weight (HW). **B.** Heart weight to body weight ratio (HW:BW). **C.** Heart weight to tibial length ratio (HW:TL). **D.** Lung weight (LW). **E.** Lung weight to body weight ratio. **F.** Lung weight to tibial length ratio.

3.2.3 The chronic effect of Hif-1α ablation in a murine model of ischaemic heart disease

To investigate the *chronic* role of HIF-1α in myocardial infarction *Mcm/+* and *HIF-1α$^{f/f}$ Mcm/+* were subjected to left anterior descending (LAD) coronary artery ligation (CAL) or sham surgery. Two weeks after CAL, animals were treated with tamoxifen for 5 days to induce translocation of cre recombinase to the nucleus and subsequent excision of floxed alleles, thus ensuring that the acute effects of HIF-1α signalling were unperturbed in the early phase post-infarction. 12 weeks after surgery, detailed cardiac functional analysis was performed using cine magnetic resonance imaging (MRI) and invasive haemodynamic assessment. Figure 31 depicts the time course of this experiment for a mouse. Given that

some CAL-operated mice had a very small or in fact no visible myocardial infarct (MI) at subsequent MRI, a screening echo blinded to genotype was employed at 10-14 days after CAL in order to select out any mice deemed to have small (less than 15 %) infarcts from further progress on the protocol. Importantly, there were no significant differences between genotypes in the numbers of mice excluded by non-invasive imaging (excluded based upon less than 15 % infarct upon screening echo or less than 25 % infarct upon MRI). Almost 90 % of mice operated died or were excluded during progression through the CAL-protocol. Table 19 shows the numbers of mice excluded at each stage of the study. Most of these losses were due to death during or in the 2 week period after surgery (~35 %) or exclusion on account of small infarct size (~40 %). Figure 32 shows representative screening echo images from sham and CAL-operated mice. The infarcted area is visualised as a thinned, akinetic (i.e. absence of systolic myocardial wall thickening) or dyskinetic (absence of systolic thickening with systolic *expansion* away from the ventricular cavity) region of left ventricular wall.

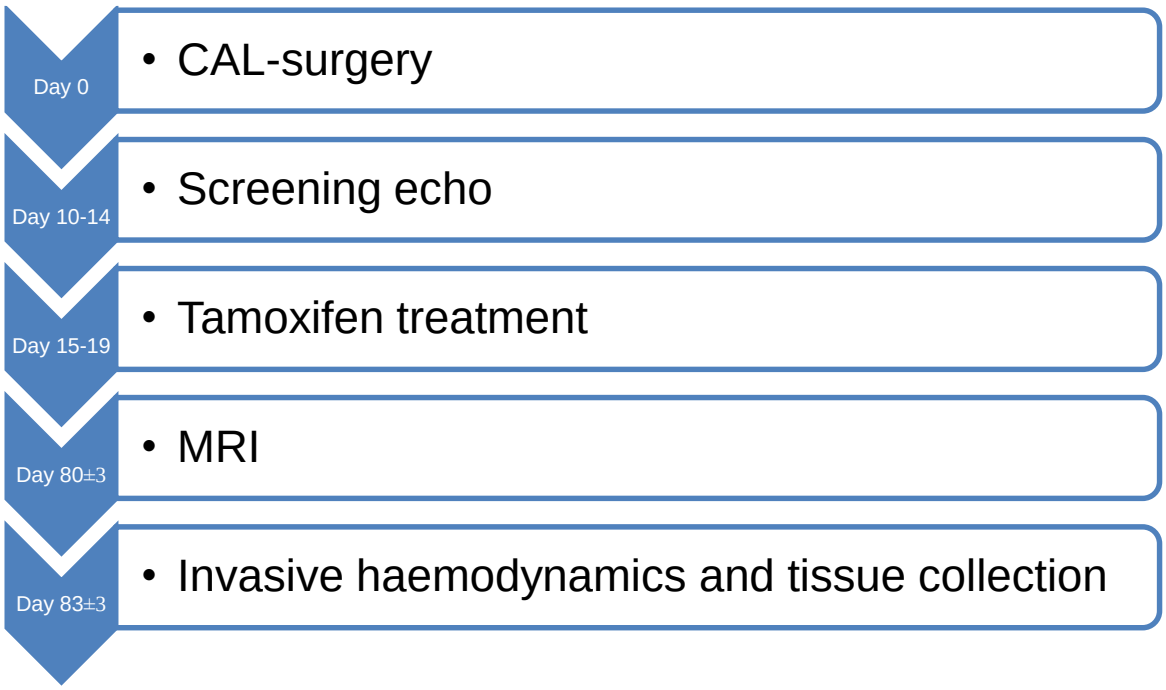

Figure 31 – Time course of the experiment to assess the effect of chronic HIF-1α ablation on cardiac function post-myocardial infarction

Reason for exclusion	***Mcm/+* Sham**	***Hif-1α$^{f/f}$ Mcm/+* Sham**	***Mcm/+* MI**	***Hif-1α$^{f/f}$ Mcm/+* MI**
Died during surgery	0 (0 %)	3 (20 %)*$	24 (19 %)*	30 (26 %)*
Died 0-14 days post-surgery	1 (9 %)	1 (7 %)	11 (9 %)*	18 (16 %)*
Died 14-80 days post-surgery	0 (0 %)	0 (0 %)	6 (5 %)	2 (2 %)
Died during MRI	0 (0%)	0 (0 %)	2 (2 %)	1 (1 %)
Died during invasive haemodynamics	1 (9 %)	0 (0 %)	5 (4 %)	2 (2 %)
Poor MRI images	0 (0 %)	0 (0 %)	2 (2 %)	1 (1 %)
Excluded due to infarct < 25% upon non-invasive imaging	NA	NA	58 (45 %)	41 (36 %)
No pair match available	NA	NA	7 (5 %)	5 (4 %)
Number used in functional analysis	**9 (81 %)**	**11 (73 %)**	**14 (11 %)**	**14 (12 %)**
Total	11 (100%)	15 (100%)	129 (100%)	114 (100%)

Table 19 – The numbers of mice lost or excluded from the CAL surgery protocol

The percentage of mice entering the protocol lost at each stage are given in brackets. *1 *Hif-1α$^{f/f}$ Mcm/+* sham mouse, 5 *Mcm/+* MI mice and 9 *Hif-1α$^{f/f}$ Mcm/+* mice died due to tracheal damage during intubation – these mice are included in the numbers that died during surgery. A further Mcm/+ MI mouse and 4 *Hif-1α$^{f/f}$ Mcm/+* MI mice recovered from surgery but developed symptoms of tracheal damage in the perioperative period these mice are including in the "died 0-14 day post-surgery" group. $ 1 *Hif-1α$^{f/f}$ Mcm/+* sham mouse died during surgery due to excessive bleeding. NA: Not applicable – as expected sham surgery mice did not have infarcted regions and were not excluded based up small infarct size or infact size pair matching.

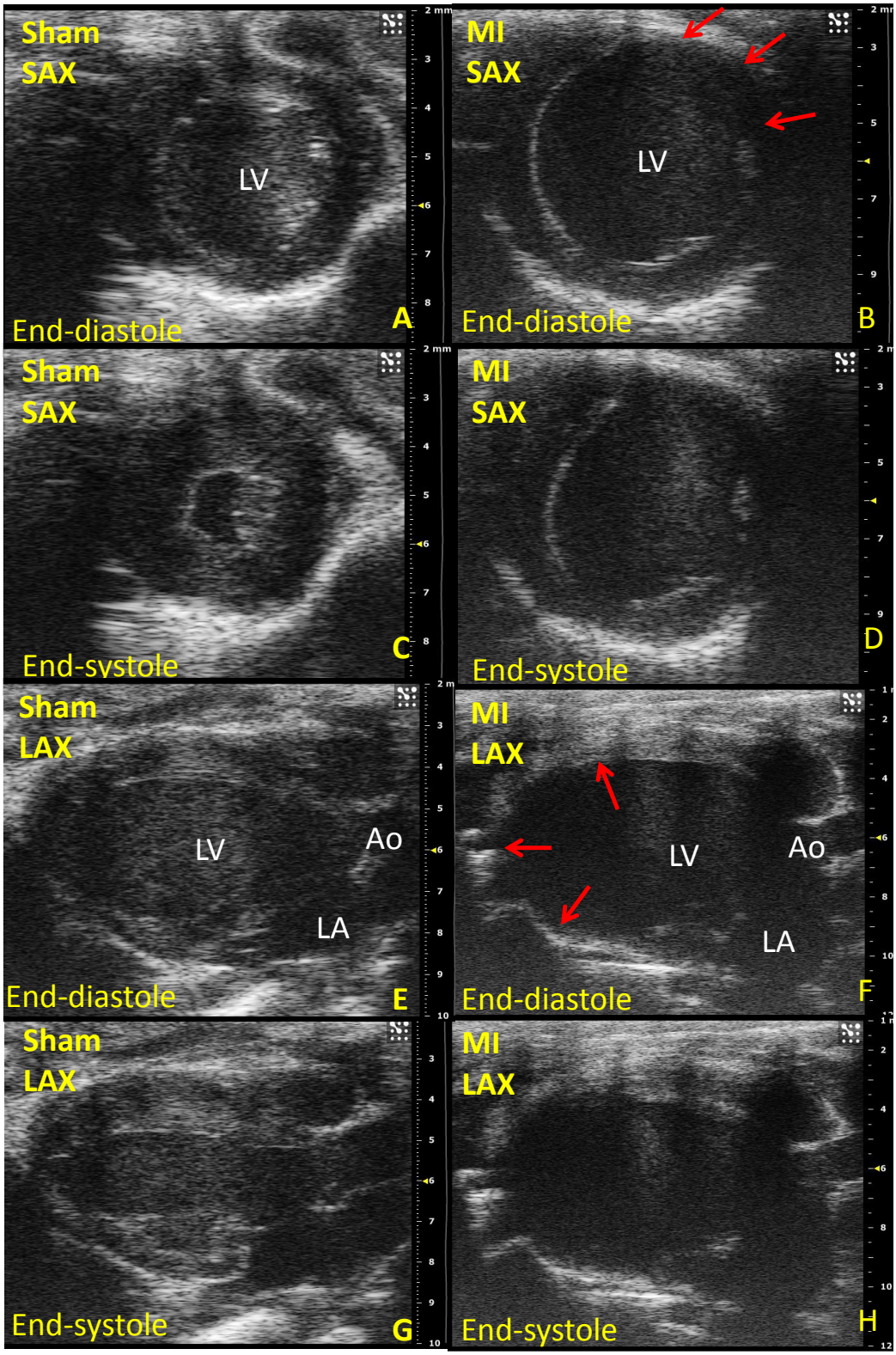

Figure 32 – Representative transthoracic echocardiographic screening images of sham operated and infarcted mouse hearts

A. Short-axis view (SAX) of end-diastolic sham-operated mouse heart. LV marks the left ventricular cavity. **B.** SAX view of end-diastolic infarcted mouse heart. Red arrows indicate the akinetic myocardial infarct (MI) region. **C.** SAX view of end-systolic sham-operated mouse heart. **D.** Short-axis view of end-systolic infarcted mouse heart. **E.** Long-axis (LAX) view of end-diastolic sham-operated mouse heart. Ao indicates the aorta. LA marks the left atrium. **F.** LAX view of end-diastolic infarcted mouse heart. **G.** LAX view of end-systolic sham-operated mouse heart. **H.** LAX view of end-systolic infarcted mouse heart.

3.2.4 Cardiac function as assessed by cine-MRI is unaltered by Hif-1α ablation post-MI

Asymmetrical remodelling of the LV that takes place after a significant myocardial infarction results in the normally valid geometric assumptions made during 2-dimensional echocardiographic assessment of cardiac function not being fulfilled[197]. Accordingly, high-resolution cine-MRI imaging was used as a highly accurate, non-invasive method to assess cardiac mass, function and infarct size. Figure 33 shows representative end-diastolic and end-systolic MRI images of *Mcm/+* and *Hif1a$^{f/f}$ Mcm/+* sham and post-MI hearts. In sham-operated hearts of both genotypes, normal concentric thickening of the LV wall during systole compared with diastole was evident. In contrast, post-MI hearts of both genotypes revealed thickening of the LV wall during systole only in the non-infarcted region. The infarcted region was thinned and akinetic in both post-MI groups and associated with clear dilatation of the LV cavity consistent with significant LV remodelling.

Infarct sizes in the *Mcm/+* and *Hif-1a$^{f/f}$ Mcm/+*groups were retrospectively matched for infarct size prior to assessment of cardiac function as recommended by Lygate and Neubauer[197]. Significant LV remodelling and changes in haemodynamic indices associated with heart failure are rarely seen in smaller infarcts, consequently all infarcts measured to be less than 25% by MRI were ultimately excluded from subsequent analysis[197, 198]. After pair-matching, the mean infarct size in the *Mcm/+* group was 44.8% with a standard deviation of 11.14%, whilst in the *Hif-1α$^{f/f}$ Mcm/+* group the mean infarct was 44.6% with a standard deviation of 10.84%. This is depicted in Figure 34.

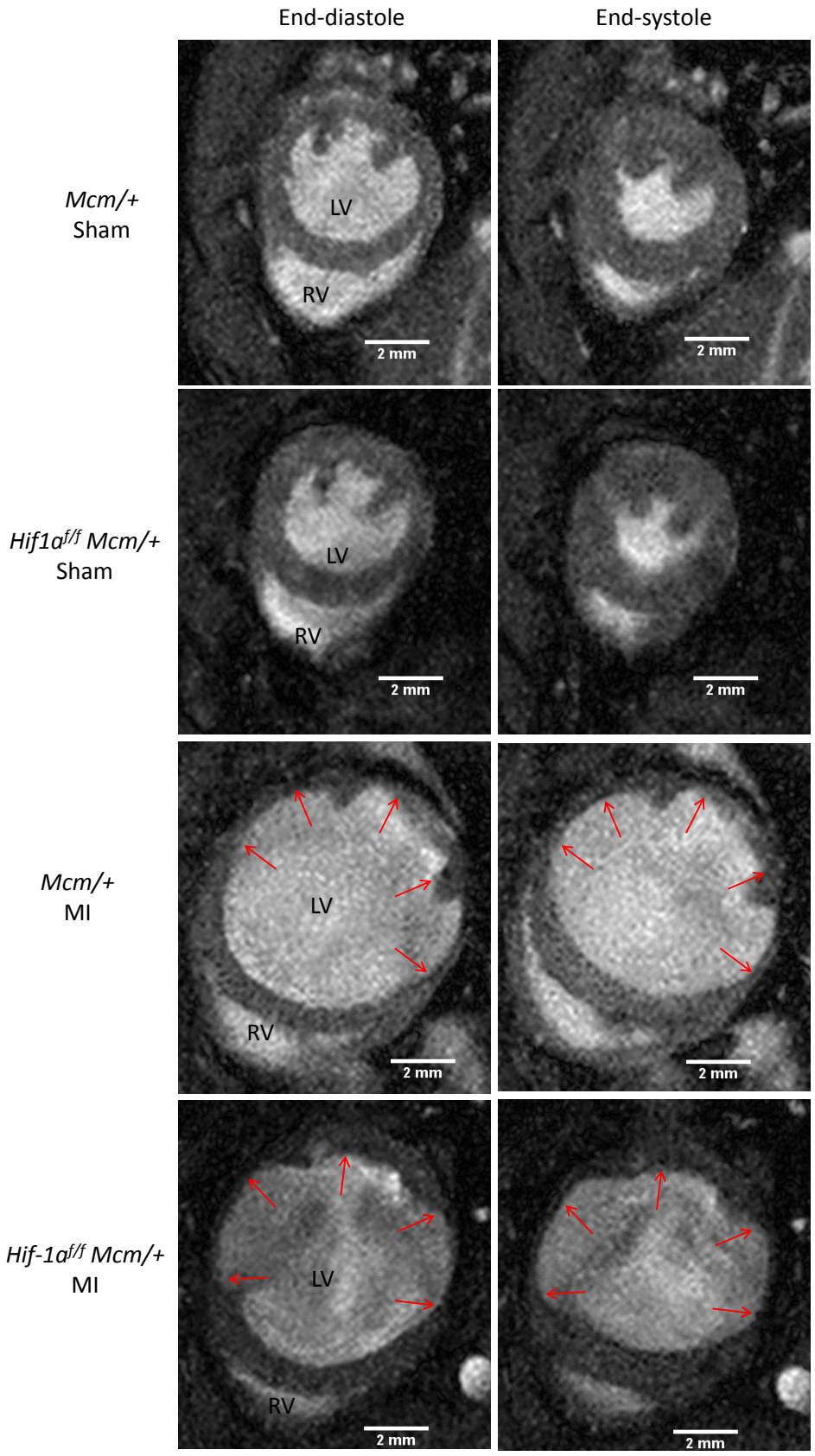

Figure 33 – Representative mid-ventricular, end-diastolic and end-systolic short-axis cine-MRI images from sham and CAL-operated *Hif-1af/f Mcm/+* and *Mcm/+* mice
LV, left ventricular cavity; RV, Right ventricular cavity. Red arrows indicate the thin, akinetic myocardial infarct (MI) region.

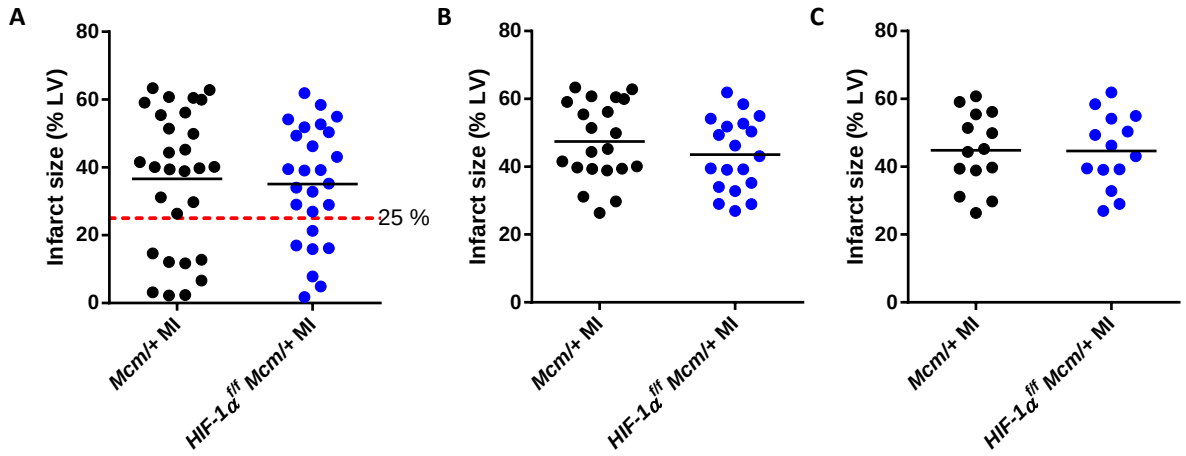

Figure 34 – Pair-matching of infarct sizes
A. Depicts the infarct sizes estimated as a percentage of left ventricular mass determined from magnetic resonance images. **B.** A 25 % cut-off threshold was applied and all mice with less than a 25 % infarct size were excluded from further analysis. **C.** Infarct sizes of the *Mcm/+* and *HIF-1α Mcm/+* groups were pair-matched so that the mean and variance were similar.

Cine-MRI revealed severe impairment of cardiac contractility (as reflected by LV end-systolic volume, ejection fraction and cardiac output) for both MI groups compared to sham-operated controls (Figure 35), consistent with successful modelling of ischaemic heart failure induced by CAL. However, no significant difference was demonstrated between genotypes in these indices of global cardiac contractility between mice subjected to the same surgery.

Highly statistically significant LV dilatation was observed in both MI groups compared to sham-operated mice (Figure 35) but, as observed with markers of systolic function, no significant differences were identified between genotypes in dilatation parameters within the sham-operated or MI groups. There was a trend towards LV hypertrophy in the MI mice compared to sham-operated mice, which achieved statistical significance between the *Mcm/+* groups (Figure 35). No differences in absolute or normalised LV mass were observed between genotypes within the sham-operated or MI groups, arguing against an effect of genotype on cardiac hypertrophy. Linear regression analysis validated the MRI assessment of

LV mass by demonstrating a clear correlation with total wet *cardiac* weight measured *ex vivo* (Figure 36).

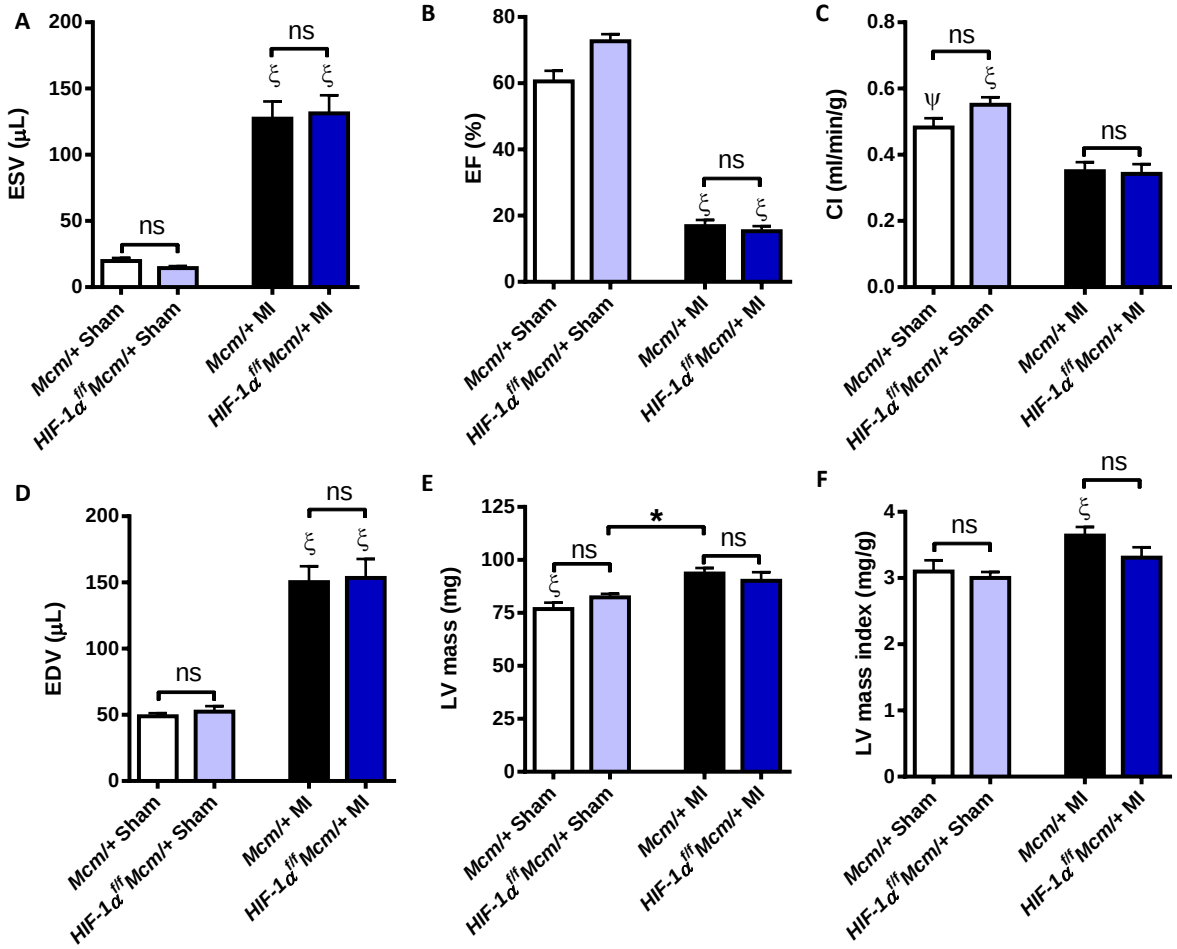

Figure 35 – Cardiac function, hypertrophy and dilatation assessed by magnetic resonance imagingin *Mcm*/+ and *Hif-1a*$^{f/f}$ *Mcm*/+ subjected to sham or myocardial infarction surgery and subsequent tamoxifen treatment

A-C. Measures of cardiac function. **A.** End-systolic volume indexed to body weight (ESVI) **B.** Ejection fraction (EF). **C.** Cardiac output indexed to body weight (CI). **D-F.** Measures of dilatation and hypertrophy. **D.** End-diastolic volume (EDV). **E.** LV mass. **F.** LV mass indexed to body weight. * $p<0.01$ between indicated groups. Ψ $p<0.05$ compared to all other groups except where indicated. ξ $p<0.001$ compared to other groups except where indicated and ns, no significant difference between indicated groups.

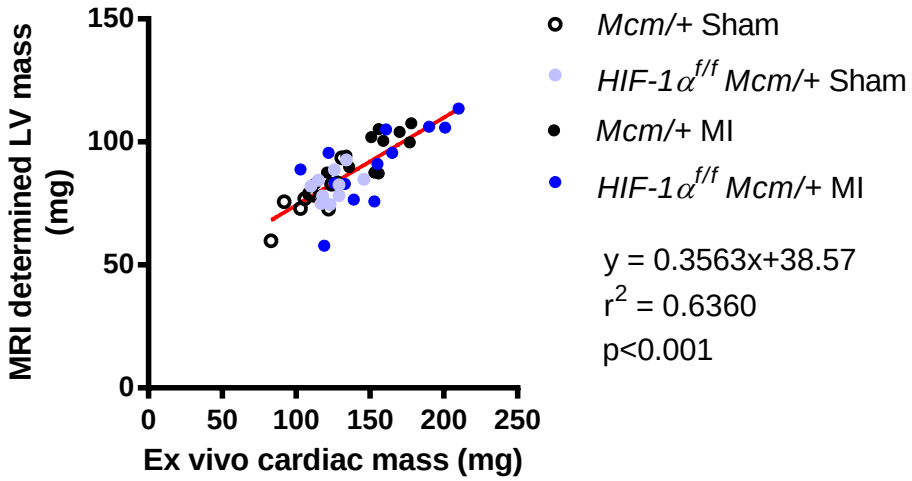

Figure 36 – LV mass estimated by MRI shows a linear relationship with total wet *ex vivo* cardiac mass

3.2.5 Invasive haemodynamic assessment of cardiac function

To further elucidate the functional consequences of *Hif-1α* ablation in myocardial infarction, invasive haemodynamic assessment of aortic and LV pressures, heart rate and derived indices of cardiac contraction and relaxation (e.g. those obtained from the first derivative of LV pressure, $+dP/dt_{max}$ and $-dP/dt_{max}$) were performed. The contractile reserve of sham-operated and MI hearts of both genotypes was assessed by the contractile response to administration of the β1-adrenoceptor agonist, dobutamine – a positive inotrope. In clinical studies, maintenance of contractile reserve correlates with a favourable prognosis, whilst it has been employed in transgenic murine cardiac phenotyping to reveal subtle but biologically relevant differences between genotypes not apparent in the baseline unstimulated state[199].

Figure 37 illustrates the effect of chronic cardiac *Hif-1α* ablation post-myocardial infarction on haemodynamic function. No significant differences in any of the parameters measured were observed between genotypes subject to the same type of surgery. In general, deterioration of cardiac function was observed after MI surgery. Basal mean aortic (i.e. systemic) pressure was unchanged by CAL surgery. Although basal peak left ventricular systolic pressure (LVSP) and left ventricular end-diastolic pressure (LVEDP) were only

significantly impaired in the MI groups when compared to sham *Hif-1α*$^{f/f}$ *Mcm/+*, there was a non-significant trend towards deterioration in these parameters when MI groups were compared to the sham *Mcm/+* group. A significant reduction in the derived parameter – left ventricular developed pressure (LVDevP = LVSP-LVEDP) – was observed in both MI groups when compared to either sham group. In response to high dose (16 ng/g BW/min) dobutamine challenge, both sham groups significantly increased their heart rate and maximal rate of increase in pressure with time ($+dP/dt_{max}$) – a sensitive measure of the cardiac contractility. Both MI groups failed to do this, however, demonstrating reduced contractile reserve in response to inotropic challenge. However, *Hif-1α*$^{f/f}$ *Mcm/+* MI mice showed some evidence of chronotropic reserve by significantly elevating their heart rate in response to low dose (4 ng/g BW/min) dobutamine and in their rate of cardiac relaxation as reflected by $-dP/dt_{max}$ following high dose dobutamine. *Mcm/+* MI mice exhibited no significant response to dobutamine challenge.

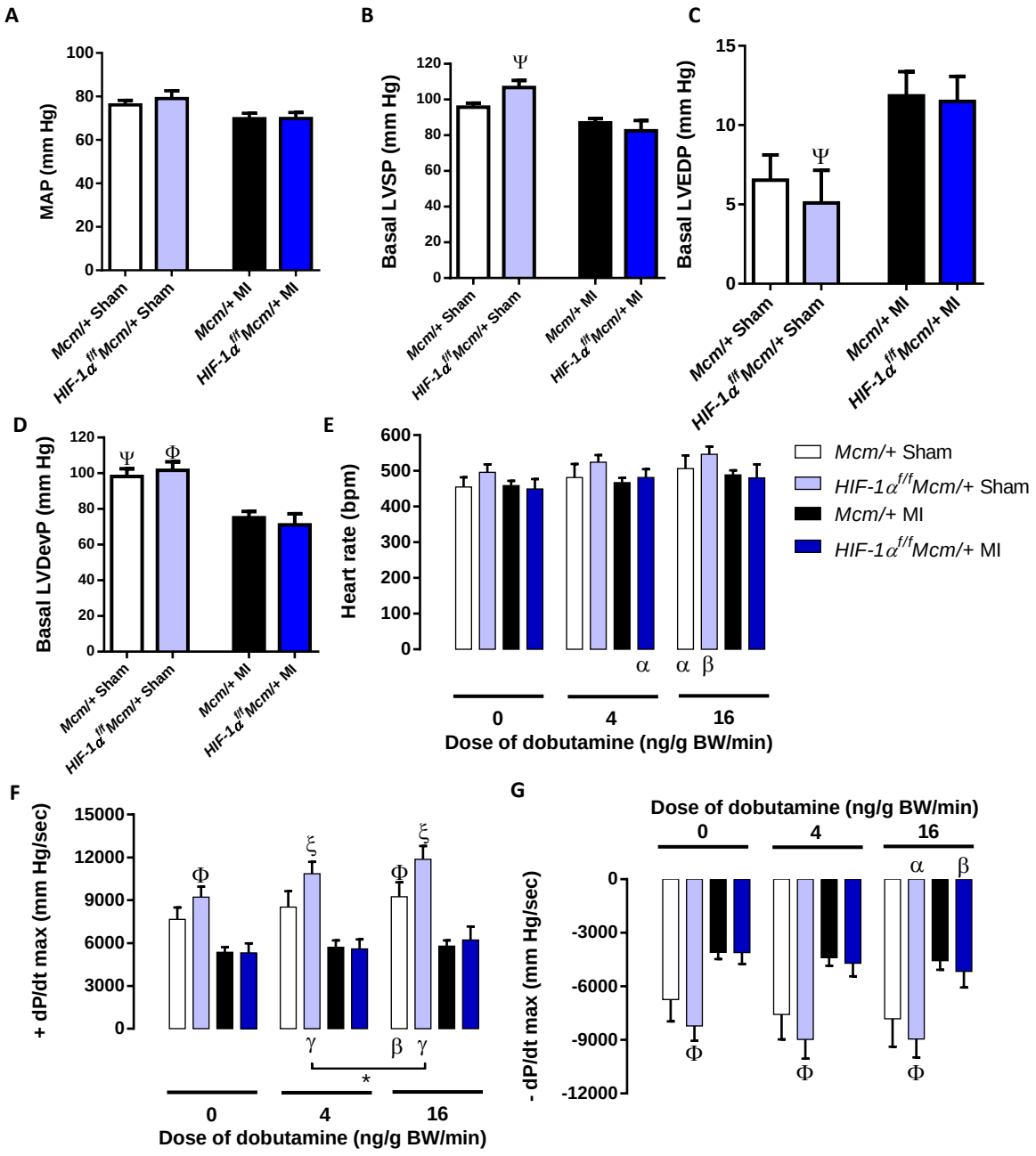

Figure 37 – Invasive haemodynamic assessment of cardiac function in *Mcm/+* and *Hif-1a$^{f/f}$ Mcm/+* subjected to sham or myocardial infarction surgery and subsequent tamoxifen treatment

A. Basal mean aortic pressure (MAP). **B.** Basal left ventricular systolic pressure (LVSP). **C.** Basal left ventricular end-diastolic pressure (LVEDP). **D.** Basal left ventricular developed pressure (LVDevP). **E.** Heart rate in beats per minute (bpm). Dobutamine dose infused is indicated (nanograms per gram body weight per min, ng/g BW/min). **F.** The maximal rise in left ventricular pressure with respect to time (+dP/dt max). **G.** The maximal rate of decrease in systolic pressure with time (–dP/dt)**.** Ψ $p<0.05$ compared to MI groups. Φ $p<0.01$ compared to MI groups. ξ $p<0.001$ compared to MI groups. α $p<0.05$ compared to no dobutamine. β $p<0.01$ compared to no dobutamine. γ $p<0.001$ compared to no dobutamine. * $p<0.05$ between indicated groups.

3.2.6 Ex vivo organ weights

Both absolute and normalised heart weights (indexed to either body weight or tibial length) were seen to be significantly increased in the MI groups compared to sham operated mice, consistent with hypertrophic remodelling of the heart post-CAL induced MI (Figure 38). No significant differences in absolute or normalised heart weights were observed between genotypes within surgical groups, hwever. Similarly, no significant differences in absolute or normalised lung weights were observed between genotypes, although there was a trend towards elevated lung weight in the MI groups compared to sham-operated mice.

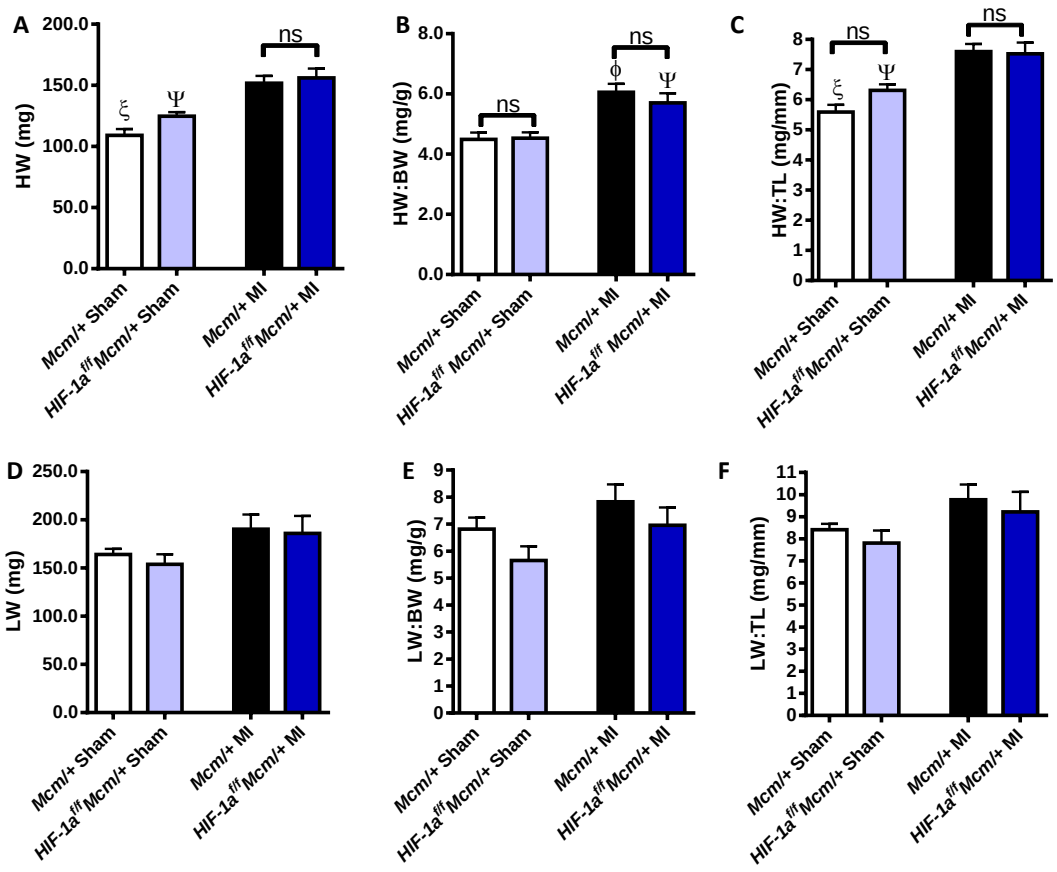

Figure 38 – Organ weight as an indicator of cardiac stress in *Mcm*/+ and *Hif-1a*$^{f/f}$ *Mcm*/+ mice subjected to sham or myocardial infarction surgery and subsequent tamoxifen treatment
A. Heart weight (HW). **B.** Heart weight to body weight ratio (HW:BW). **C.** Heart weight to tibial length ratio (HW:TL). **D.** Lung weight (LW). **E.** Lung weight to body weight ratio (LW:BW). **F.** Lung weight to tibial length ratio (LW:TL). Ψ $p < 0.05$ compared to all other groups. Φ $p < 0.01$ compared to all other groups except where indicated. ξ $p < 0.001$ compared to all other groups except where indicated. * $p<0.05$ between indicated groups. ** $p<0.01$ between indicated groups and ns, no significant difference between indicated groups.

3.2.7 Expression of cardiac stress markers

Heart failure is associated with a reversion from a pattern of adult to foetal gene expression in the heart[200, 201]. Cardiac expression of the typically adult expressed genes *Atp2a2* [encoding the sacroplasmic-endoplasmic reticulum ATPase 2a (SERCA)], *Slc2a4* (encoding the glucose transporter GLUT4) and *Myh6* [encoding the cardiac sarcomeric protein α-myosin heavy chain (α-MHC)] were all significantly downregulated in both MI groups compared to sham-operated hearts (Figure 39). The foetally expressed genes, *Acta1* (α-actin), *Myh7* (β-myosin heavy chain), *Nppa* (natriuretic peptide A) and *Nppb* (natriuretic peptide B) were all significantly elevated in the MI groups relative to sham groups. The only significant difference between genotypes was an observed reduction in expression of the foetal gene, *Acta1*, in *Hif-1a*$^{f/f}$ *Mcm/+* MI compared to *Mcm/+* MI hearts.

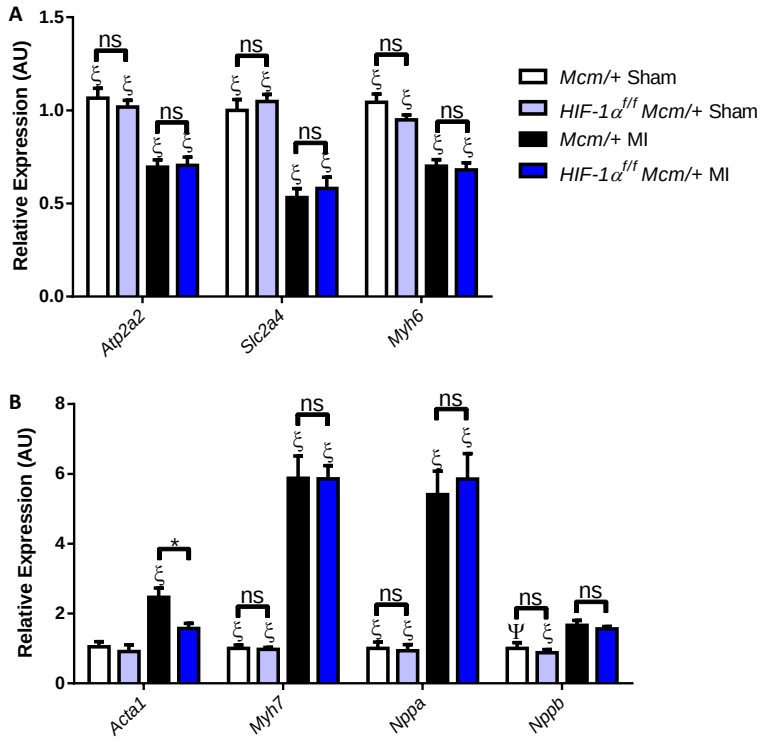

Figure 39 – Reversion from adult to foetal gene expression after myocardial infarction of *Mcm/+* and *Hif-1α Mcm/+* mice
Relative expression in arbitrary units assessed by qRT-PCR and analysed by the $2^{-\Delta\Delta Ct}$ or comparative C_T method using the internal control in cardiac beta actin (encoded by *Actb*) and normalised to expression in the *Mcm/+* sham group. **A.** Expression of adult genes. *Atp2a2*: sarcoplasmic-endoplasmic reticulum ATPase 2a; *Slc2a4*: Glucose transporter 4; *Myh6*: α-myosin heavy chain. **B.** Expression of foetal genes. *Acta1*: α-actin; *Myh7*: β-myosin heavy chain; *Nppa*:,natriuretic peptide A; *Nppb*: natriuretic peptide B. Ψ $p<0.05$ compared to other groups except where indicated, ξ $p<0.001$ compared to other groups except where indicated, ns no significant difference between indicated groups.

3.2.8 Infarct size correlates with molecular markers of cardiac stress

In the *Mcm/+* group absolute and normalised heart weights correlated significantly with infarct size Figure 40. This was not seen in the *Hif-1α$^{f/f}$ Mcm/+* group, with Pearson's correlation p values of 0.67 or higher. Although there was no statistically significant difference between absolute or normalised lung weight between sham and MI groups, a clear positive correlation between infarct size and lung weight (absolute or normalised) was observed in both genotypes, suggestive of some degree of congestive cardiac failure in mice with the largest infarcts. A negative correlation of cardiac function – as assessed by ejection fraction – with infarct size was demonstrated in both genotypes. Transcript levels of the adult expressed genes, *Atp2a2* and *Slc2a4*, negatively correlated with infarct size in *Mcm/+* mice, with trends to significant correlation (p=0.067 and p= 0.0514 respectively) in *Hif-1a$^{f/f}$ Mcm/+* mice.

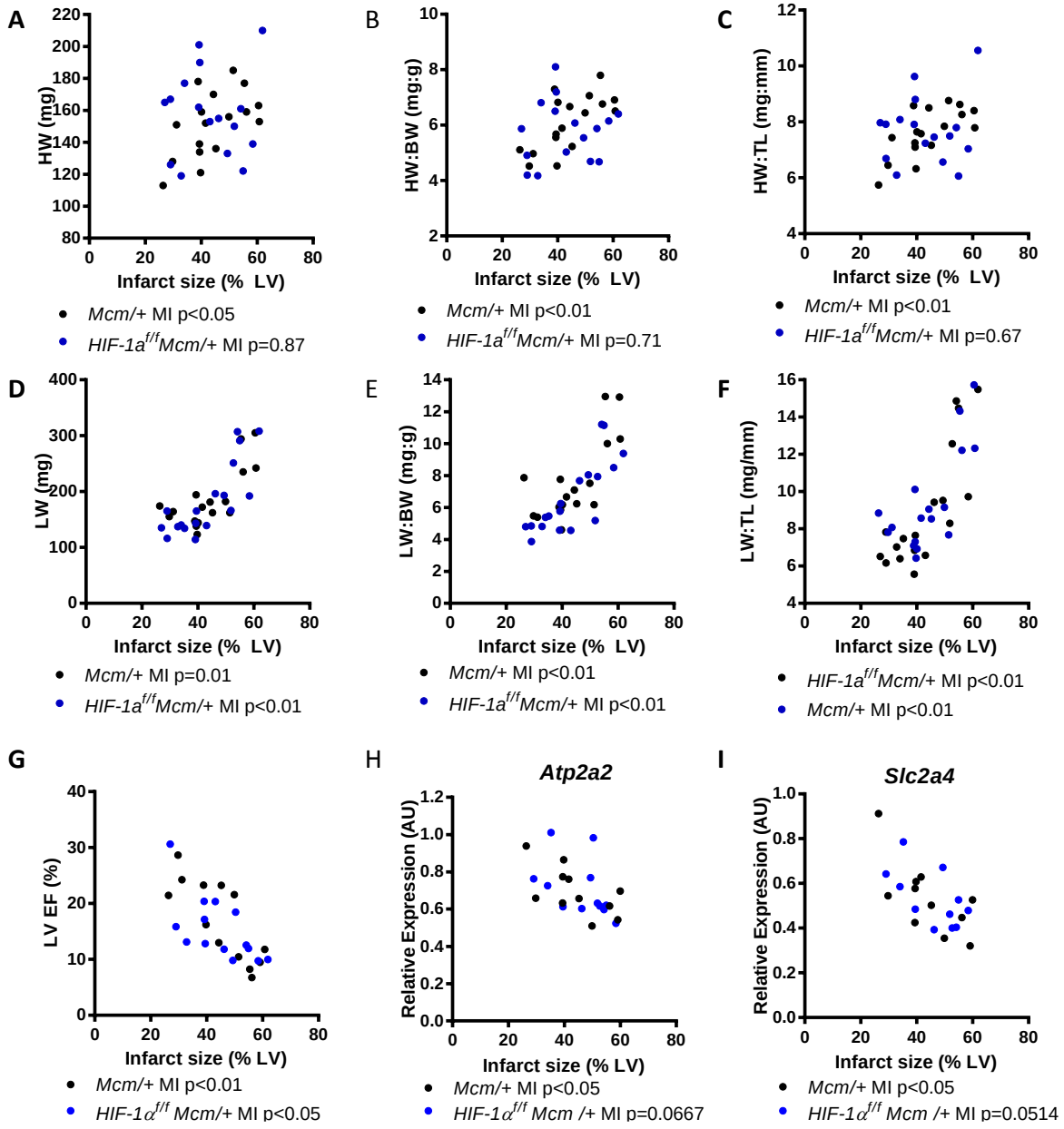

Figure 40 – Infarct size correlates with gross morphometric and molecular markers of cardiac dysfunction or stress
Correlation with infarct size of: A. Heart weight (HW); **B.** Heart weight to body weight ratio (HW:BW); **C.** Heart weight to tibial length ratio (HW:TL); D. Lung weight (LW); E. Lung weight to body weight ratio (LW:BW); F. Lung weight to tibial length ratio (LW:TL); G. Left ventricular ejection fraction (LV EF); H. *Atp2a2* (sarcoplasmic/endoplasmic reticulum calcium ATPase) transcript expression; I. *Slc2a4* (glucose transporter 4) transcript expression.

3.2.9 Confirmation of Hif-1α floxed allele excision and assessment of Hif-1α target gene expression in sham and MI cohorts

Excision of the *Hif-1α* floxed allele in DNA extracted from the left ventricles of *Hif-1α*$^{f/f}$ *Mcm/+* mice was confirmed by PCR amplification of a 1-loxP band (Figure 41). Measured

by qRT-PCR, the expression of *Hif-1α* transcript was reduced by 85% in the *Hif-1α*$^{f/f}$ *Mcm/+* sham group and 75% in the *Hif-1α*$^{f/f}$ *Mcm/+*MI group with respect to the *Mcm/+* sham and MI groups. HIF target gene transcript expression was not significantly altered between genotypes, although there was a consistent trend towards down-regulation in the *Hif-1α*$^{f/f}$ *Mcm/+* groups compared to *Mcm/+* for all targets tested. Of the HIF target genes assessed, 4 of 7 showed significantly reduced expression in MI compared to sham-operated mice, with trends to reduction in the remainder.

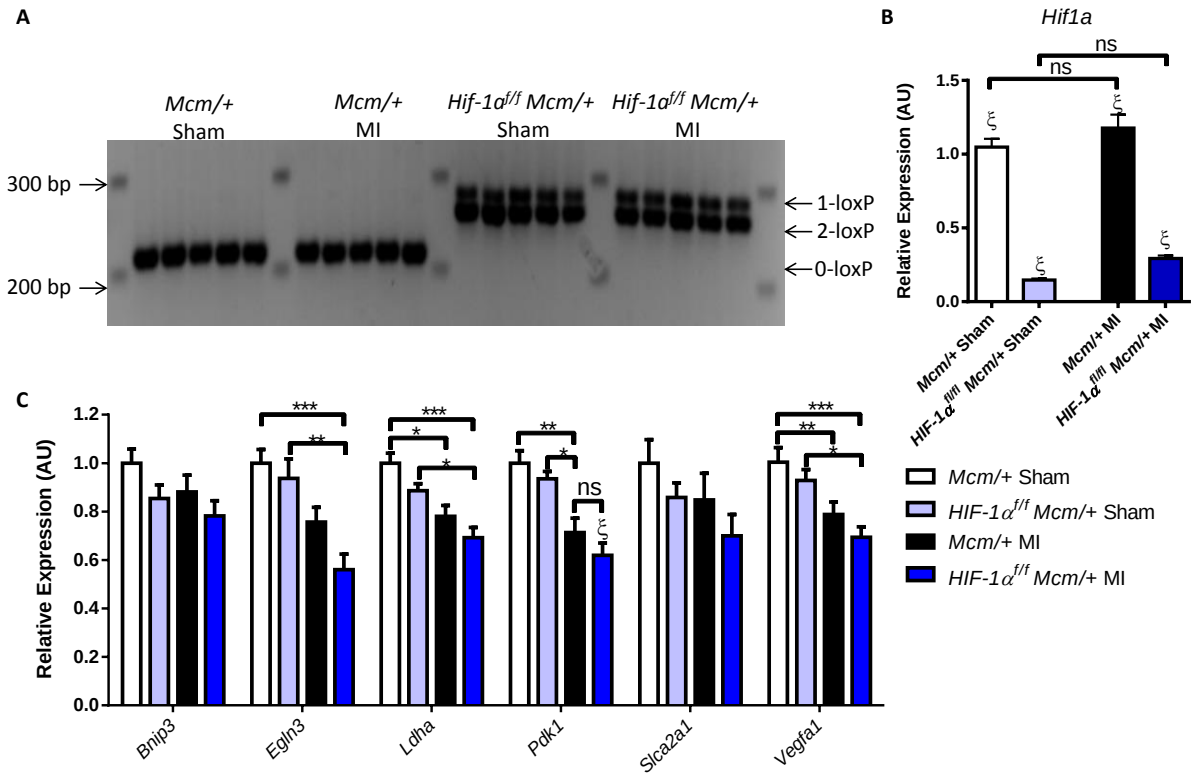

Figure 41 – Confirmation of excision of *Hif-1α* floxed allele and expression of HIF target genes in left ventricle

A. Genotyping PCR from DNA extracted from the left ventricles of sham and CAL operated mice. **B.** Relative expression of *Hif-1α* transcript in left ventricle samples assessed by qRT-PCR. C. Relative expression of select HIF target genes in left ventricular samples assessed by qRT-PCR and analysed by the $2^{-\Delta\Delta Ct}$ or comparative C_T method using the internal control in cardiac beta actin (encoded by *Actb*). *Bnip3*: Bcl2 and nineteen-kilodalton interacting protein 3; *Egln3*: Prolyl hydroxylase domain protein 3; *Ldha*: lactate dehydrogenase A; *Pdk1*: pyruvate dehydrogenase kinase 1; *Slc2a1*: glucose transporter 1; *Vegfa1*: vascular endothelial growth factor. ξ p<0.001 compared to all groups except where indicated, * p<0.05 between indicated groups, ** p<0.01 between indicated groups, *** p<0.001 between indicated groups and ns, no significant difference between indicated groups.

3.3 Discussion

3.3.1 Summary of chapter findings

Using a temporally-inducible model of cardiac *Hif-1α* deletion, the work presented in this chapter demonstrates:

- The validation of a cardiac-specific, temporally-inducible model of *Hif-1α* ablation.
- That *Hif-1α* ablation has no discernible effect on baseline cardiac morphology or function as assessed by echocardiography and *ex vivo* organ weight.
- That CAL surgery successfully induced myocardial infarction with significant adverse structural remodelling, marked contractile dysfunction and loss of contractile reserve to inotropic stimulation as indicated by *in vivo* (cine-MRI, invasive haemodynamics), *ex vivo* (absolute and normalised heart weights) and molecular readouts (reversion to a foetal programme of cardiac gene expression). Unexpectedly, there was no evidence of chronic *Hif-1α* activation.
- Chronic *Hif-1α* ablation had no significant impact on late-phase cardiac function post-coronary artery ligation.
- Infarct size is a critical determinant of cardiac function post-CAL surgery.

3.3.2 Validation of a cardiac-specific temporally-inducible model of Hif-1α ablation

Amplification of a 1-loxP product by genotyping PCR from left ventricular DNA of *Hif-1α*$^{f/f}$ *Mcm/+* mice indicated successful excision of the *Hif-1α* floxed allele. However, a 2-loxP band was also observed. This is likely to be due to amplification of DNA from non-cardiomyocyte cell populations such as fibroblasts and endothelial cells of the left ventricle. Indeed, the 75-85 % reduction in *Hif-1α* transcript levels is in accordance with the greater than 70 % recombination efficiency described by Sohal *et al* who developed the Mcm mouse

model[182]. Importantly, use of tamoxifen doses higher than the present study in an attempt to achieve greater recombination efficiency has been associated with a dose-dependent mortality from lethal heart failure thought to be due to DNA damage, cardiomyocyte apoptosis, myocardial fibrosis and altered cardiac bioenergetics[202, 203].

Given that the relative expression of HIF-1α at mRNA or protein level was not specifically determined from myocyte versus non-myocyte fractions, it is possible that a proportion of the ~20% detectable *Hif-1α* mRNA from the hearts of *Hif-1α*$^{f/f}$ *Mcm/+* mice may derive from cardiomyocytes. In addition, given that the regulation of HIF-1α stability and transcriptional activity occur primarily at the protein (post-transcriptional) level, one limitation of relying on an mRNA readout for adequacy of 'knockout' is the potential non-linear relationship between mRNA reduction and alteration in HIF-1α transcriptional activity. These limitations could potentially be overcome by direct separation of the myocyte fraction from isolated perfused hearts followed by protein measurement by immunoblotting. However, the labile nature of HIF-1α in oxygenated cells is recognised to complicate its direct measurement. Importantly, the lack of a 1-loxP band in vehicle-treated *Hif-1α Mcm/+* left ventricles and a panel of non-cardiac tissues from tamoxifen-treated *Hif-1α Mcm/+* mice demonstrates the cardiac-specific excision of *Hif-1α* induced by tamoxifen treatment.

3.3.3 Chronic Hif-1α ablation has no effect on cardiac function

At baseline and in the context of sham-surgery no significant differences in cardiac function were observed with *Hif-1α* ablation. In contrast, Huang *et al.* reported cardiac dysfunction with cardiac-specific *Hif-1α* deletion[108]. A key difference with this model, however, is that it is expected to result in cardiac *Hif-1α* excision during embryogenesis, hence the authors' findings may reflect a deleterious effect of *Hif-1α* depletion during cardiac development. The

observation of no baseline change in cardiac function is in agreement with studies by Sano *et al.* and Krishnan *et al.*, both of which demonstrated no baseline phenotype in sham-operated, cardiac-specific *Hif-1α* knockout hearts[61, 107].

CAL surgery resulted in a substantial reduction of cardiac function as indicated by MRI, invasive haemodynamic recordings, *ex vivo* heart weights and a reversion to a foetal program of cardiac gene expression. These findings confirm that the success of CAL in modelling key features associated with post-MI heart failure, including significant ventricular dysfunction and adverse structural remodelling. However, a key finding from the work presented here is that no significant differences in multiple readouts of cardiac function, dilatation, hypertrophy or molecular markers of cardiac stress were observed between the *Mcm/+* and *Hif-1α$^{f/f}$ Mcm/+* MI groups, except for elevation of a single foetal gene, *Acta1*. These findings suggest that *chronic* reduction in endogenous levels of oxygen-labile Hif-1α have no discernible beneficial (or adverse) effect on the progression of CAL-induced cardiac dysfunction. This finding contrasts with the documented detrimental effects of reduced Hif-1α[98, 99] and beneficial effects of supraphysiological Hif-1α augmentation, observed in acute models of ischaemic heart disease[101, 102]. This result also contrasts with the chronic detrimental effect attributed to long-term expression of supraphysiological levels of oxygen-stabile Hif-1α[60, 110, 112]. However, these variances may be explained by temporal and HIF expression level differences between the models.

One limitation of the current study's approach was the use of a single final MRI time point to assess cardiac remodelling and global systolic function. By virtue of its non-invasive nature, MRI is well suited to serial longitudinal study in murine models of cardiomyopathy and has been used to generate cardiac growth curves in the same animals, improving statistical power

and potentially reducing N numbers required for identification of a significant difference between groups[204]. An alternative study approach would have been to undertake cardiac MRI at 2 weeks immediately pre-tamoxifen, at 12 weeks immediately prior to haemodynamics (as performed in the current study) and at several time points in between. This would allow earlier and more accurate assessment of infarct size than echocardiography (which was used primarily to screen out very small infarcts) and exclusion of these mice early on in the protocol prior to administration of tamoxifen, potentially resulting in a more homogeneous and comparable range of infarct sizes at the study end. It would also allow sequential interrogation of cardiac structure and function during the study which would enable potentially early beneficial or adverse transient changes in these parameters to be identified. One potential drawback of undertaking MRI relatively soon after CAL surgery is the requirement for general anaesthesia to a deeper level and for a significantly longer time than a screening echocardiogram, which could result in additional stress immediately prior to a series of daily intraperitoneal injections and/or premature loss of mice. This effect could be minimised by employing careful physiological monitoring during scans (as during the current study) with close attention to maintaining body temperature, near physiological levels of heart rate and appropriate levels of general anaesthesia[205]. In addition wall thinning, as a marker for infarcted tissue, is less apparent on MRI undertaken early after infarction[206].

3.3.4 No evidence of chronic HIF activation at baseline or with MI

Although successful ablation of *Hif-1α* was demonstrated at the DNA and RNA level, no significant change in total left ventricular expression of HIF targets was observed between *Hif-1α*$^{f/f}$ *Mcm/+* and *Mcm/+* mice subject to the same surgery. This finding suggests that the chronic contribution of HIF-1α to expression of these genes in the context of the entire left ventricle is negligible both at baseline and after MI. The latter finding is somewhat

unexpected in suggesting that infarct generation by CAL surgery did not induce chronic activation of the HIF-1α pathway. Given that the assessment of Hif-1α target gene expression in whole left ventricle samples was performed at a single late time point (~70-80 days), it is feasible that Hif-1α activation may have occurred more acutely, or that it does occur chronically but may be restricted to the peri-infarct region, limiting the utility of whole ventricular samples to delineate a difference. In support of the latter, ventricular biopsies from patients with early or evolving myocardial infarction undergoing coronary bypass surgery identified HIF-1α immunoreactivity only in infarcted or ischaemic regions, albeit relatively acutely from the initial ischaemic insult[207]. While sufficient infarct-size pair-matched histological tissue was not available to directly probe this during the course of the present experiments, it is possible that a similar approach looking for spatial pattern of HIF-1α protein stabilisation may have identified differences in the immediate peri-infarct zones whose signal was otherwise obscured on molecular assessment of entire left ventricle.

Assessment of HIF target gene expresson was determined by qRT-PCR and analysed by the $2^{-\Delta\Delta Ct}$ or comparative C_T method whereby the expression of the gene of interest was expressed relative to an internal control[208], in the present work that of cardiac beta actin (encoded by *Actb*). In addition to methodological assumptions about qPCR efficiency and similarity for both target and endogenous control genes inherent to the comparative C_T approach[208], the use of a single internal control gene has limitations. Perhaps unsurprisingly given the heterogeneity of the heart's structure and cellular composition, spatial differences in genes considered to be stably expressed and widely used as reference genes for normalisation have been demonstrated in a rat model of ischaemia-reperfusion, with significant differences in expression between regions subject to ischaemia-reperfusion and areas remote to injury[209]. Extending these insights to the present study, confirmation of

stability of expression of the selected internal control gene between mice subject to infarct or sham surgery and across different cardiac regions post-CAL would have increased confidence in its use as a reference gene for normalisation. A more optimal approach to the analysis of relative gene expression would have been to undertake separate analysis of gene expression from infarct, peri-infarct and remote regions, in combination with more stringent normalisation by geometric averaging of the expression of multiple internal reference genes[210] previously selected for stability of expression across different cardiac regions and experimental conditions of sham/infarct surgery.

As an alternative to qPCR, the emerging technology of digital PCR (dPCR) could have been adopted to quantify gene expression. In dPCR, sample cDNA is diluted into many tiny partitioned reactions which contain one or no copies of the sequence of interest, amplified as in qPCR and the presence or absence of a fluorescent signal used to indicate the presence or absence of the sequence of interest in each reaction[211, 212]. The number of positive and negative reactions are counted and Poisson probabilities used to determine the number of DNA molecules in the orginal sample[213]. The exponential nature of qPCR and use of the comparative CT method limits its ability to detect small differences in gene expression, whilst the linear nature of dPCR allows detection of smaller changes in and absolute quantitation of gene expression[211-213]. If resources allowed it may be illuminating to investigate whether the higher sensitivity of dPCR could reveal any significant difference in target gene expression between the *Hif-1α*$^{f/f}$ *Mcm/+* and *Mcm/+* groups subjected to the same treatment.

In contrast to the absence of differences between genotypes, a consistent and often significant trend toward reduced HIF target gene expression between infarcted and sham surgery hearts

of the same genotype was identified. At first sight, this finding appears unexpected since elevation of HIF has been observed by Krishnan *et al* in both human and mouse hypertrophic cardiomyopathy samples, and by Holscher *et al* in human dilated cardiomyopathy and ischaemic cardiomyopathy samples [60, 61]. However, in failing human hearts Zolk *et al* noted an up-regulation of negative regulators of the HIF pathway, including a natural anti-sense *HIF-1α* transcript, PHD3 and HIF-3α [214]. Given that *Hif-1α* transcript levels were unchanged between the *Mcm/+* sham and MI groups, it is unlikely that the *Hif-1α* antisense transcript is playing a role in the current presented model. However PHD3 or HIF-3α activation could plausibly prevent activation of HIF-1α target genes. In cancer studies, hypoxia-associated factor (HAF) has been identified as a ubiquitin-E3-ligase that binds to and ubiquitinates HIF-1α in an oxygen-independent manner [215]. HAF is decreased during acute hypoxia, but increases with prolonged hypoxia and could conceivably be a negative regulator of HIF in the setting of chronic myocardial ischaemia[216].

Critically, failure of MI to chronically activate the Hif-1α pathway in the myocardium in this model may explain why Hif-1α ablation has no additional effect upon cardiac function. If Hif-1α signalling is not activated, it will not be able to drive the deleterious changes observed in models of supraphysiological overexpression.

3.3.5 The key importance of infarct size in determining cardiac function

The clear correlation of infarct size with multiple parameters indicative of cardiac dysfunction highlights its powerful effect upon cardiac performance. Indeed, infarct size appears to have a far greater influence than genotype upon cardiac function in this study. A corollary of this is that the ability of modulating a single gene to mitigate the profound negative effects of infarction upon myocardial contractility and structure, or to discern a

subtle effect of genetic manipulation (even with highly sensitive *in vivo* phenotypic tools) is a considerable challenge.

The absolute and normalised heart weight parameters of the *Hif-1α*$^{f/f}$ *Mcm/+* group failed to correlate with infarct size, whilst a clear correlation of these measures was demonstrated in the *Mcm/+* group. Intriguingly, previous studies have implicated HIF-1α in the transition to hypertrophy, which may explain the lack of correlation between heart weight parameters and infarct size in the absence of HIF-1α[61, 107].

3.3.6 Insights into the role of Hif-1α in ischaemic heart disease

Unaltered cardiac function with chronic Hif-1α ablation in comparison to control mice suggests that physiologically relevant levels of oxygen-labile HIF-1α are not deleterious either at baseline or in the context of myocardial infarction. Due to the proven acute favourable effect of HIF-1α activation in ischaemic heart disease, therapeutic HIF activation has been proposed in the setting of acute coronary syndromes[99]. Multiple studies indicate that HIF-1α induction can reduce infarct size [98-100, 110]. The robust correlation between increased infarct size and cardiac dysfunction observed both in the present and other studies, is consistent with the concept that harnessing the therapeutic potential of HIF-1α activation in the *acute* phase of myocardial infarction to diminish infarct size might be clinically beneficial [101, 198]. Whilst studies from other groups using models of supraphysiological Hif-1α signalling indicate that therapeutic HIF activation should not be prolonged beyond the acute remodelling phase, the present work suggests that employing therapeutic strategies to reduce HIF activation in the context of chronic ischaemic heart failure is unlikely to be of clear benefit.

3.3.7 Limitations of this study

3.3.7.1 The murine coronary artery ligation model

The CAL model of heart of ischaemic heart failure is well established and in many respects recapitulates the pathophysiology of myocardial infarction in human [197, 217, 218]. For example changes in haemodynamic profile, left ventricular hypertrophy and dilatation, lung congestion and increased levels of natriuretic peptides are observed in both the human disease and the mouse model [197]. However, there are disadvantages to using mouse models of cardiac disease in general and the CAL model of myocardial infarction in particular. For example, relative levels of contractile protein isoforms vary in mice compared to humans [e.g. the predominant myosin heavey chain isoform in adult mice is α-MHC (Myh6) whilst β-MHC (Myh7) is the major isoform in adult humans][219, 220], and the small heart size and naturally high resting heart rate make surgery and phenotyping of mice technically challenging. However, the availability of powerful transgenic technology mice to facilitate precise dissection of the role of a particular gene with temporal and tissue specificity continues to contribute to their widespread appeal as a disease model. Two major limitations of CAL surgery encountered during this study were the high rate of perioperative mortality and the wide variation in infarct sizes produced (especially the number of small (<25%) infarcts). These are discussed in further detail below.

CAL is recognised to produce a wide range of infarct sizes (from 10-70%) due to variation in branching of the LAD coronary artery[197, 218, 221]. As highlighted earlier, infarct size is a key determinant of left ventricular function, remodelling and, ultimately, survival hence differences in infarct size between groups could potentially obscure the effect of HIF-1α ablation or lead to erroneous conclusion about the effect of the genetic intervention when infarct size differences were primarily responsible[197, 221]. To minimize this, infarct sizes were

tightly matched between groups retrospectively but before functional analysis was performed as suggested by Lygate and Neubauer[197]. As only mice with larger infarcts (typically >25-30 %) develop significant haemodynamic changes or ventricular remodelling, many mice (~40 % of mice operated) with minimal infarcts were excluded from the study based upon pre-defined screening-echo and/or MRI results and fully blind to genotype[197, 198].

The present study adopted the standard approach to CAL in the mouse, namely a ligature applied to the left anterior descending (LAD) coronary artery at the atrio-ventricular border prior to the main bifurcation[197] to produce a significant sized MI with associated structural remodelling. An alternative approach to CAL surgery has been described based on detailed investigation of common non-visible LV branching patterns of the LAD using latex coronary artery casting to guide 'blind' ligation of common specific branches. This has been shown to produce more uniform transmural infarct size and location. A limitation of this approach, however, is the relatively small size of infarcts obtained, producing infarcts of typically either ~5% or 16% in 57% of mice and no reported mortality[222]. Other approaches to induce reproducible transmural lesions which do not rely on coronary artery ligation have also been described, e.g. cryoinjury, with low reported perioperative mortality in male mice[223]. The physiological relevance of cryoinjury as a model for human (ischaemic) heart failure is questionable however.

A limitation of the current CAL model is the relatively high mortality rate observed in the immediate perioperative period. To reduce these losses, only female mice were used for the study as cardiac rupture is more prevalent in males post-CAL[197]. Finally, the paradigm of a single coronary artery subject to rapid and permanently complete occlusion modelled by CAL contrasts with the clinical scenario where patients often have chronic partial occlusion of one

or multiple coronary vessels prior to myocardial infarction. It also fails to faithfully reflect the current optimal approach to treatment for acute total coronary vessel occlusion – namely, primary percutaneous coronary intervention – which uses coronary angioplasty and stenting to promptly restore coronary blood flow, thereby salvaging downstream ischaemic myocardium to reduce infarct size[197, 218].

In the present study, cine MRI was used to determine infarct size by assessing for regions of wall thinning and lack of motion (akinesis). To maximise the reliability of the measures obtained, infarct size was primarily determined by the author after progression through a series of archived, in-house training studies, while a subset of scans from the present study were independently and simultaneously assessed by an experienced operator and proved to be in high agreement (within 3%) with the author's measurments.

In humans with ischaemic heart disease the reference approach for non-invasive assessment of myocardial infarction and viability is late-gadolinium enhancement (LGE) MRI. This has been applied successfully to mice using intraperitoneal or intravenous administration of gadolinium-based contrast and shown to be reproducible and correlate well with histological quantification of infarct size using triphenyltetrazolium chloride (TTC) staining[206]. The use of LGE MRI to characterise myocardial tissue itself, as opposed to inferring damage based on wall motion/thining[206], may potentially have increased the accuracy of infarct size determination in the present work at the late timepoint. Determination of infarct size soon after CAL surgery may be less accurate when certain markers, e.g. wall thinning which are less obvious early after the ischaemic insult, are used. Alternative *in vivo* methods of infarct assessment include use of cardiac positron emission tomography to assess [^{18}F]

fluorodeoxyglucose uptake by metabolically active myocytes, but are limited by spatial resolution[224].

The present study's assessment of infarct size could have been improved by concomitant histological evaluation using either standard haematoxylin and eosin or Masson trichrome staining[225], or alternatively TTC staining of thick sections used to stain viable tissue where it is converted into a dark red-coloured insoluble precipitate[226]. Non-uniform apperances of the infarct-TTC positive border zone are recognised with the use of the latter approach, however, and related to the presence of haem-containing proteins[226]. While formal TTC staining was considered, the diasadvantage of leaving no tissue for further biochemical or molecular analysis and the corresponding need for significantly greater numbers of mice undergoing the entire CAL protocol was considered to largely outweigh its advantages.

3.3.7.2 A snapshot in time

Commencement of tamoxifen treatment to ablate *Hif-1α* at 14 days post-CAL was selected because the majority of collagen deposition and remodelling occurs within this period, resulting in the formation of a mature infarct scar. Using the murine CAL model, Huang *et al*. demonstrated that HIF-1α is rapidly elevated post-myocardial infarction, reaching a peak by 2 weeks post-MI surgery[105]. Accordingly, the current study design ensured that for 14 days post-surgery the infarcted heart would retain the putative beneficial acute effects of HIF-1α, such as induction of its pro-angiogenic targets. However, after this acute period, ablation of Hif-1α would prevent its chronic potentially deleterious effects. Thus, a limitation of this study is that the effect of *Hif-1α* ablation was only investigated at one carefully-chosen time-point. It is thus possible that ablation of HIF-1α at a different time point (including earlier) may have resulted in a different experimental outcome.

3.3.7.3 Mice as a model for congestive heart failure and systemic adaptations

Beyond the initial perioperative period, mice on the CAL protocol generally survived to the final assessments of cardiac structure and function by MRI and invasive haemodynamics and largely appeared physically well. This may seem surprising given a mean infarct size of ~45% in both *Hif-1α*$^{f/f}$ *Mcm/+* and *Mcm/+* groups, profound reduction in cardiac contractility and the documented high mortality of human heart failure, (50% survival at 5 years post-diagnosis)[227]. These observations point to inter-species differences, the limitations of rodents in modelling human disease and the likelihood of a stable state of subclinical left ventricular dysfunction without symptomatic heart failure likely as a result of systemic compensation. Mice undergoing CAL surgery in this study were uniformly young, female and experienced a dramatic sudden ischaemic insult. In contrast, heart failure in humans is a chronic, progressive disorder, often on the background of multiple co-existing diseases, is more common in the elderly and affects both males and females[227, 228].

Why did mice on the CAL protocol not appear more symptomatic with overt heart failure during the course of the protocol? Given the divergence of humans and mice ~75 million years ago[229], the differences in environmental threat incurring an evolutionary need for mice to 'hide' overt signs of sickness from potential predators, in addition to differences in body size and longevity, it is feasible that more subtle signs indicating early decompensated congestive heart failure towards the end of the protocol may not have been readily apparent despite daily observation. A selection bias may also have occurred in that the sickest mice on the CAL protocol were those most likely to die in the immediate peri-operative period and so not reach the final timepoint for assessment.

The lack of a clear symptomatic congestive heart failure phenotype in mice undergoing CAL has been reported in young mice aged 2-3 months (who often lived more than 12 months post-CAL) suggesting a significant ability to tolerate high levels of myocyte necrosis[230]. To overcome this and better model clinically relevant endpoints of human heart failure post-MI, the use of older mice aged 14 months (described as 'late middle age' in the mouse) has been shown to be associated with higher mortality, greater infarct expansion and higher incidence of signs of advanced heart failure[230], but with significant resource implications.

While the endpoints used in this study, including non-invasive imaging and left ventricular haemodynamics are standard means to investigate outcome after CAL surgery, they do not provide direct insight into systemic compensatory mechanisms that may have taken place, or the whole-animal response to MI. Neurohormonal activation is recognised to be both a response and contributor to the progression of heart failure and affects organ systems beyond the heart including the kidney, peripheral vasculature and skeletal muscle[231]. Heart failure is therefore a systemic disorder[231]. These initial compensatory mechanisms, include activation of the adrenergic nervous and renin-angiotensin aldosterone systems, withdrawal of cardiac vagal activity and cytokine release. Initially these are thought to be beneficial and aimed at restoring cardiac output, but are ultimately maladaptive and induce multiple negative effects including salt and water retention, arrhythmia, vasoconstriction increasing cardiac afterload and cardiomyocyte apoptosis[231, 232]. Inhibition of these neurohormonal maladaptations using β-adrenoceptor blockers and angiotensin-converting enzyme inhibitors is therefore used to treat patients with heart failure.

Potential differences in neurohormonal response to the initial MI between genotypes could potentially affect the final readouts used, in particular that of invasive haemodynamics and

assessment of contractile response to dobutamine. While evaluation of *in vivo* β-adrenoceptor function following administration of β-adrenoceptor agonist is regarded as an important method of assessing *in vivo* cardiac function in small-animal models of heart failure[233], its optimal interpretation depends on understanding the levels of sympathetic nervous system activity and status of the cardiac β-adrenergic system in the respective groups. Activation of sympathetic outflow is an early feature of heart failure resulting in enhanced circulating noradrenaline and adrenaline levels[232]. End-stage failing human hearts display lower β-adrenoceptor expression, impaired adenylate cyclase signalling and reduced sensitivity to β-adrenoceptor stimulation in comparison to non-failing hearts[234]. Chronic, excessive stimulation of cardiac β-adrenoceptors is thought to lead to both a selective downregulation in β_1-adrenoceptor density and uncoupling of β-adrenoceptors from G-proteins resulting in desensitisation of remaining sarcolemmal β-adrenoceptors via altered G protein-coupled receptor kinase (e.g. GRK2) expression which phosphorylates agonist-bound receptors uncoupling them from downstream G proteins[235]. Accordingly, the finding of a degree of preservation of chronotropic reserve in *Hif-1α*$^{f/f}$ *Mcm/+* MI mice compared to *Mcm/+* MI mice in response to low dose (4 ng/g BW/min) dobutamine challenge could be interpreted as indirect evidence for less neurohormonal activation in the former with a corresponding reduction in pathological cardiac β-adrenoceptor downregulation and uncoupling, suggesting a less severe heart failure state. Greater insight into this possibility may be provided by direct assays of neurohormonal activation in the mice, e.g. measurement of circulating (or urinary) catecholamines, natriuretic peptides, angiotensin or inflammatory markers such as TNF-α and IL-6.

3.3.7.4 αMHC-Mercremer

As previously described, induction of Mcm translocation to the nucleus by tamoxifen is associated with a transient dilated cardiomyopathy irrespective of the presence of *loxP* transgenes[196, 203]. This cardiomyopathy has only been described in animals treated with higher doses of tamoxifen than those used in this study. Additionally, both groups investigating this cardiomyopathy report complete phenotype reversal within 1 month of tamoxifen treatment [196, 203]. Given the importance of minimising the risk of confounding of the result due to direct Mcm toxicity, in this study functional analysis was performed 2 months after tamoxifen treatment when full recovery from any Mcm-related cardiomyopathy was anticipated. Furthermore, ligand treated *Mcm/+ loxP* deficient mice were utilised as appropriate genetic controls to account for any non-specific effect of Mcm activation *per se* upon cardiac function[202].

Notably, tamoxifen administration alone to wildtype mice has been shown to induce changes in global gene expression (5.6% of genes assessed by microarray), irrespective of the presence of Mcm, although this appeared to have minimal impact on protein abundance after short-term administration[236]. Published studies have reported no cardiomyopathy at any tamoxifen dose used in Mcm negative mice, irrespective of the presence of floxed genes[196].

A potential approach to avoid the transient severe dilated cardiomyopathy associated with tamoxifen-mediated Mcm translocation is the use of the alternative selective oestrogen receptor modulator, raloxifene. Whilst still interacting with the mutated oestrogen receptor (Mer), raloxifene exhibits differences in oestrogen related receptor binding (e.g. ERRγ) and coactivator recruitment compared with tamoxifen that may explain its lack of apparent toxicity in the Mcm/+ mice despite inducing similar levels of nuclear Cre localisation and gene knockdown[196]. This approach is limited by poor drug solubility and lower binding to

Mer, necessitating prolonged administration, ideally orally, at high dose[196]. In addition, chronic use of raloxifene has been shown to protect against cardiac hypertrophy and systolic dysfunction in a murine model of cardiac pressure overload (aortic banding)[237], complicating its use in genetic manipulation studies with readouts of cardiac remodelling and function.

A further important consideration with the *Hif-1α* floxed *Mcm* model used is that the Hif-1α ablation induced is cardiomyocyte-restricted. Many other cell types, such as endothelial cells, smooth muscle cells and fibroblasts, are found in and have an influence upon cardiac function in health and disease and, in the current study's model, these other cell types will still be expected to express HIF-1α. Using Tie2-Cre to delete of *Hif-1α* (or *Hif-1β*) in bone marrow and vascular endothelial cells, ablates the ability of ischemic preconditioning to protect the heart in an murine *ex vivo* model of ischaemia reperfusion, suggesting a role of endothelial cell Hif-1α in acute myocardial infarction[238]. It is possible that endothelial Hif-1α expression may also play more chronic role in ischemic heart disease. The current study design allows investigation of the effect of endogenous HIF-1α post-infarction in cardiomyocytes only.

3.3.7.5 Potential for compensation by HIF-2α

Notably, HIF-2α is not knocked-out in this model and, due to their overlapping target genes, alterations in HIF-2α may to some degree compensate for HIF-1α ablation. Furthermore, a reciprocal interaction between HIF-1α and HIF-2α levels has been observed in VHL-deficient renal cell carcinoma cell lines[17]. This observation suggests that HIF-2α may be up-regulated in the absence of HIF-1α, with consequent induction of common target gene expression. However, transcript expression of *Vegf*, a target of both HIF-1α and HIF-2α, showed the same non-significant trend towards down-regulation as other HIF-1α targets in *Hif-1α* knockout hearts suggesting this is not occurring. In addition, the HIF targets postulated to

have a chronic negative effect in the context of ischaemic heart disease such as the proapoptoic, mitophagy-promoting BNIP3 and genes perturbing energy production by oxidative phosphorylation are predominantly activated by HIF-1α but not HIF-2α.

4 CHAPTER 4: PHENOTYPE OF CARDIAC-SPECIFIC FH1 KNOCKOUT MICE

4.1 Hypotheses and aims

This chapter utilises a murine cardiac-specific fumarate hydratase (encoded by *Fh1*) knockout, both as model of fumarate excess to induce normoxic stabilisation of hypoxia-inducible factors (HIF) within the heart (via competition with the PHD co-substrate, 2-oxoglutarate) and as a platform to explore the effect of disruption of the tricarboxylic acid (TCA) cycle in a highly metabolically active tissue. Existing data indicate that, despite this interruption of a key metabolic enzyme, these mice are viable to young adulthood[166]. The potential compensatory mechanisms underlying this and indeed the long-term phenotype of these mice are unclear. Studies in the cancer field have demonstrated that FH deficiency can, in addition to activation of HIFs, also aberrantly activate nuclear factor (erythroid-derived 2)-like 2 (NRF2), a master regular of the cellular antioxidant response. Accordingly, exploration of the phenotype and underlying mechanisms of the cardiac-specific *Fh1* null has the potential to inform our understanding of the plasticity of the TCA cycle (traditionally regarded as a rigid series of one-way reactions) and Nrf2 biology within the heart. The main hypotheses of this chapter are:

i. That ablation of a key TCA cycle enzyme, fumarate hydratase (FH), in the heart, a tissue with perpetually high energy requirements, will lead to the development of a substantial adverse phenotype.
ii. Cardiac inactivation of FH will initiate a pseudohypoxic response, thereby providing a model with which to investigate the sequelae of normoxic HIF stabilisation.
iii. FH deletion in the heart will elicit stabilisation of NRF2 and subsequent activation of NRF2 target genes.

Consequently, the specific aims of this chapter are to:

i. Validate a murine model of cardiac fumarate hydratase (*Fh1*) deletion.

ii. To interrogate the long-term phenotype associated with cardiac *Fh1* ablation.

iii. To establish whether a pseudohypoxic response is elicited in this model and investigate the role played by HIF-1α in any phenotype observed with cardiac *Fh1* deletion.

iv. To determine whether activation of NRF2 targets occurs and plays a role in the long-term phenotype associated with cardiac *Fh1* deletion.

4.2 Results

4.2.1 Successful ablation of Fh1 in cardiac tissue

Mice with exons 2 and 3 of the fumarate hydratase (*Fh1*) gene flanked by loxP sites[143] were crossed with mice with the mlc2v promoter driving expression of cre recombinase specifically in cardiomyocytes (referred to simply as Cre/+ hereafter)[183]. *Fh1*$^{+/f}$ and *Fh1*$^{+/f}$ *Cre/+* offspring were subsequently bred together to generate a cardiac-specific *Fh1* knockout: *Fh1*$^{f/f}$ *Cre/+*. *Fh1*$^{f/f}$ *Cre/+* mice were obtained in the expected Mendelian ratios from heterozygous crosses, demonstrating that cardiomyocyte *Fh1* ablation is not embryonically lethal. *Fh1*$^{f/f}$ mice were phenotypically normal and therefore used as controls throughout this study. Western blotting confirmed depletion of Fh1 protein by 75 % (when normalised to α-actinin expression) in heart tissue from *Fh1*$^{f/f}$ *Cre/+*mice comparative to *Fh1*$^{f/f}$ controls (Figure 42). Due to contamination from the non-cardiomyocyte fraction of the heart, this is still likely to be an underestimate of the true efficiency of Fh1 ablation in cardiomyocytes. Notably, the magnitude of reduction in expression in whole heart samples is concordant with that observed in other cardiomyocyte-specific knockout models[184].

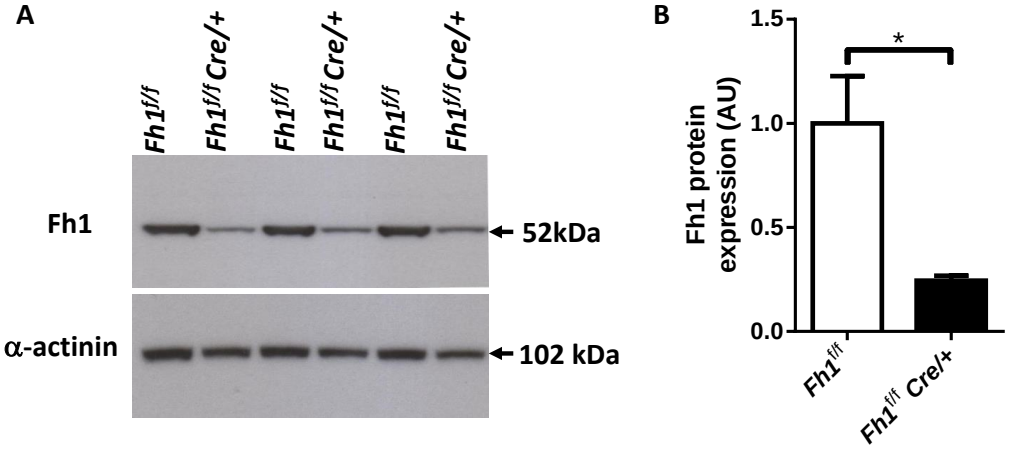

Figure 42 – Confirmation of Fh1 protein depletion in cardiac tissue from *Fh1*$^{f/f}$ *cre/+* mice
A. Western blot for Fh1 and α-actinin loading control. **B.** Relative expression of Fh1 protein assessed by densitometry with Fh1 expression normalised to α-actinin expression. *p<0.05.

4.2.2 Cardiomyocyte-specific Fh1 deletion is prematurely lethal

Longitudinal assessment of *Fh1*$^{f/f}$ *Cre/+* mice demonstrated loss of condition, exemplified by reduced body weight, rapidly succeeded by lethargy, piloerection and death. Their median life expectancy was 108.5 days, with a range of 85-140 days (Figure 43). In contrast, no overt deterioration or fatalities were observed in any *Fh1*$^{f/f}$ controls monitored until 200 days of age, with Kaplan-Meier survival analysis confirming a highly significant difference between genotypes.

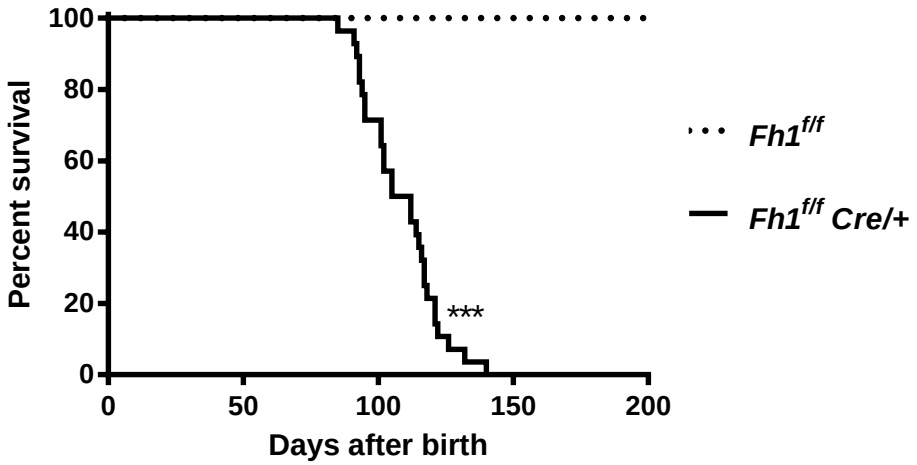

Figure 43 – Kaplan-Meier survival curve demonstrating increased lethality in *Fh1*$^{f/f}$ *Cre/+* mice compared to *Fh1*$^{f/f}$ controls
*** p<0.001

4.2.3 Cardiomyocyte-specific Fh1 knockout mice exhibit impaired cardiac function

A cohort of *Fh1*$^{f/f}$ and *Fh1*$^{f/f}$ *Cre/+* mice aged 100 days underwent echocardiographic assessment of cardiac function (Figure 44). No significant differences in heart rate were observed between groups during image acquisition. *Fh1*$^{f/f}$ *Cre/+* mice displayed severely compromised cardiac systolic function reflected in raised left ventricular end-systolic dimension and left ventricular end-systolic volumes and an ejection fraction reduced from 68% in *Fh1*$^{f/f}$ controls to 12%. *Fh1*$^{f/f}$ *Cre/+* mice demonstrated LV dilation signified by elevated left ventricular end-diastolic dimension (LVEDD) and left ventricular end-diastolic volumes (LVEDV). Whilst individual LV anterior and posterior wall thickness (LVPWT and LVAWT) were not significantly altered between genotypes, given the dilatation of the entire

heart, the net LV mass was more than doubled in *Fh1*$^{f/f}$ *Cre/+* mice comparative to controls consistent with cardiac hypertrophy.

Further delineation of the late-*Fh1* null phenotype by invasive haemodynamic assessment confirmed the echocardiographic signals for severe cardiac dysfunction in *Fh1*$^{f/f}$ *Cre/+* mice (Figure 45). Whilst any apparent difference in mean arterial pressure (MAP) (representative of systemic pressure) and was statistically insignificant, indicators of cardiac function: LV systolic pressure (LVSP); LV end-diastolic pressure; and LV developed (LVDevP) were significantly compromised in *Fh1*$^{f/f}$ *Cre/+* hearts. Heart rates were comparable between groups throughout haemodynamic assessment, with mice of both genotypes raising their heart rate appropriately in response to chronotropic stimulation with high-dose (16 ng/g BW/min) dobutamine. The maximal rate of cardiac contraction (+dP/dt) was diminished in *Fh1*$^{f/f}$ *Cre/+* animals at baseline and upon challenge with low (16 ng/g BW/min) or high dose dobutamine. Similarly, the maximal rate of cardiac relaxation (-dP/dt) was impaired in *Fh1*$^{f/f}$ *Cre/+* hearts. Unlike *Fh1*$^{f/f}$ controls *Fh1*$^{f/f}$ *Cre/+* hearts were unable to respond to inotropic stimulation with low or high dose dobutamine by significantly increasing their maximal rate of contraction consistent with loss of contractile reserve.

Ex vivo morphometric indices were consistent with the *in vivo* findings in suggesting cardiac dysfunction and marked cardiac hypertrophy (Figure 46). Concordant with the increase in LV mass demonstrated by echocardiography, direct measurement of whole heart weight revealed a more than two-fold increase in *Fh1*$^{f/f}$ *Cre/+* mice relative to controls. This signal persisted when heart weight was normalised to either body weight or tibial length. Both absolute and normalised wet-weights of the lungs were raised in *Fh1*$^{f/f}$ *Cre/+* mice, suggestive of pulmonary congestion and development of heart failure.

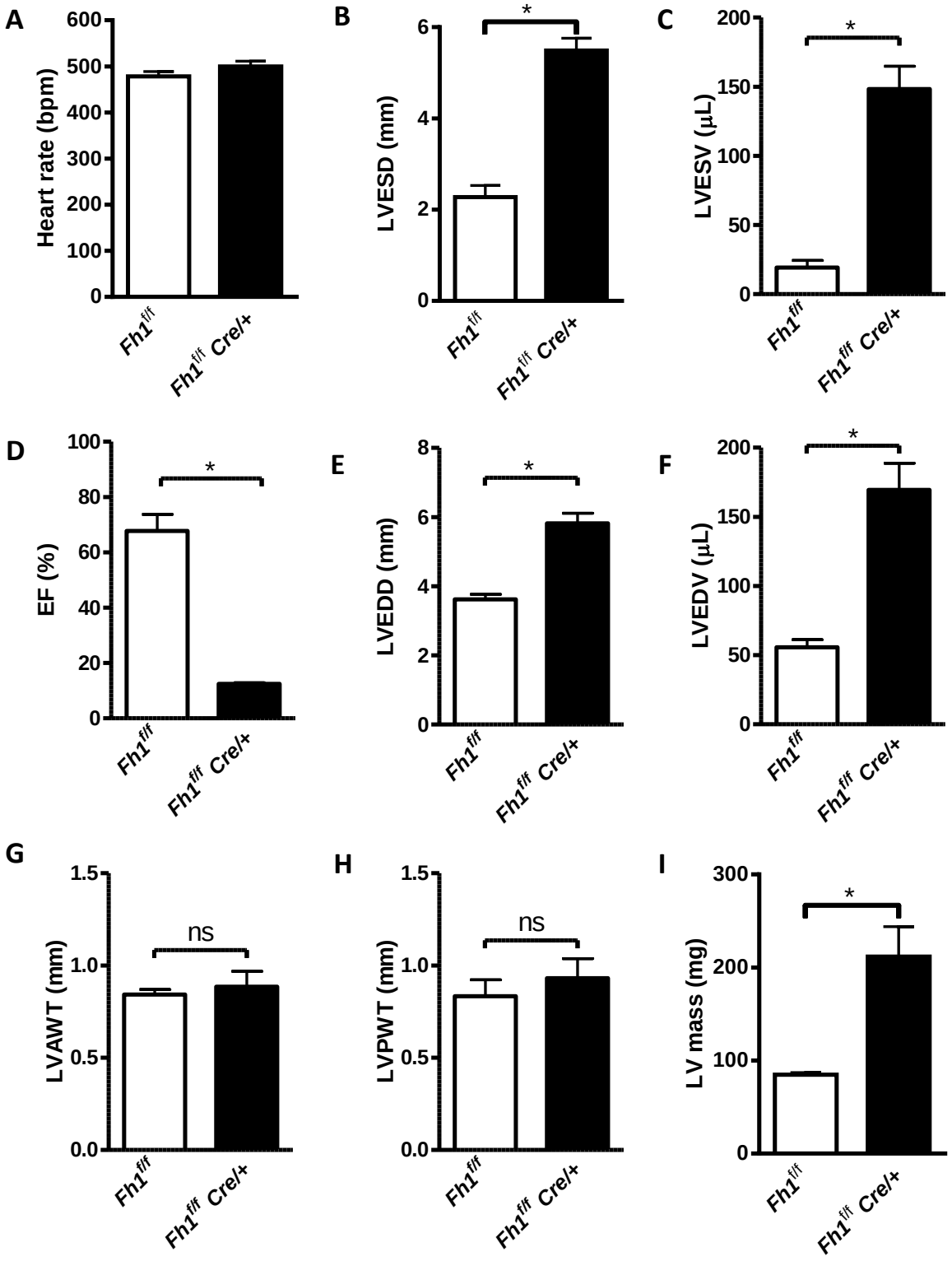

Figure 44 – Echocardiographic assessment demonstrates cardiac systolic dysfunction, dilatation and hypertrophy in *Fh$^{f/f}$ Cre/+* mice compared to *Fh1$^{f/f}$* controls

A. Heart rate in beats per min (bpm). **B-D.** Measures of cardiac function: **B.** Left ventricular end-systolic dimension (LVESD) in millimetres (mm); **C.** Left ventricular end-systolic dimension (LVESD) in microlitres (µL); **D.** Ejection fraction (EF) as a percentage of left ventricular volume; **E-F.** Measures of cardiac dilatation: **E.** Left ventricular end-diastolic dimension (LVEDD); **F.** Left ventricular end-diastolic volume; **G-I.** Measures of cardiac hypertrophy: **G.** Left ventricular anterior wall thickness; **H.** Left ventricular posterior wall thickness; **I.** Left ventricular mass in milligrams (mg). *p<0.05

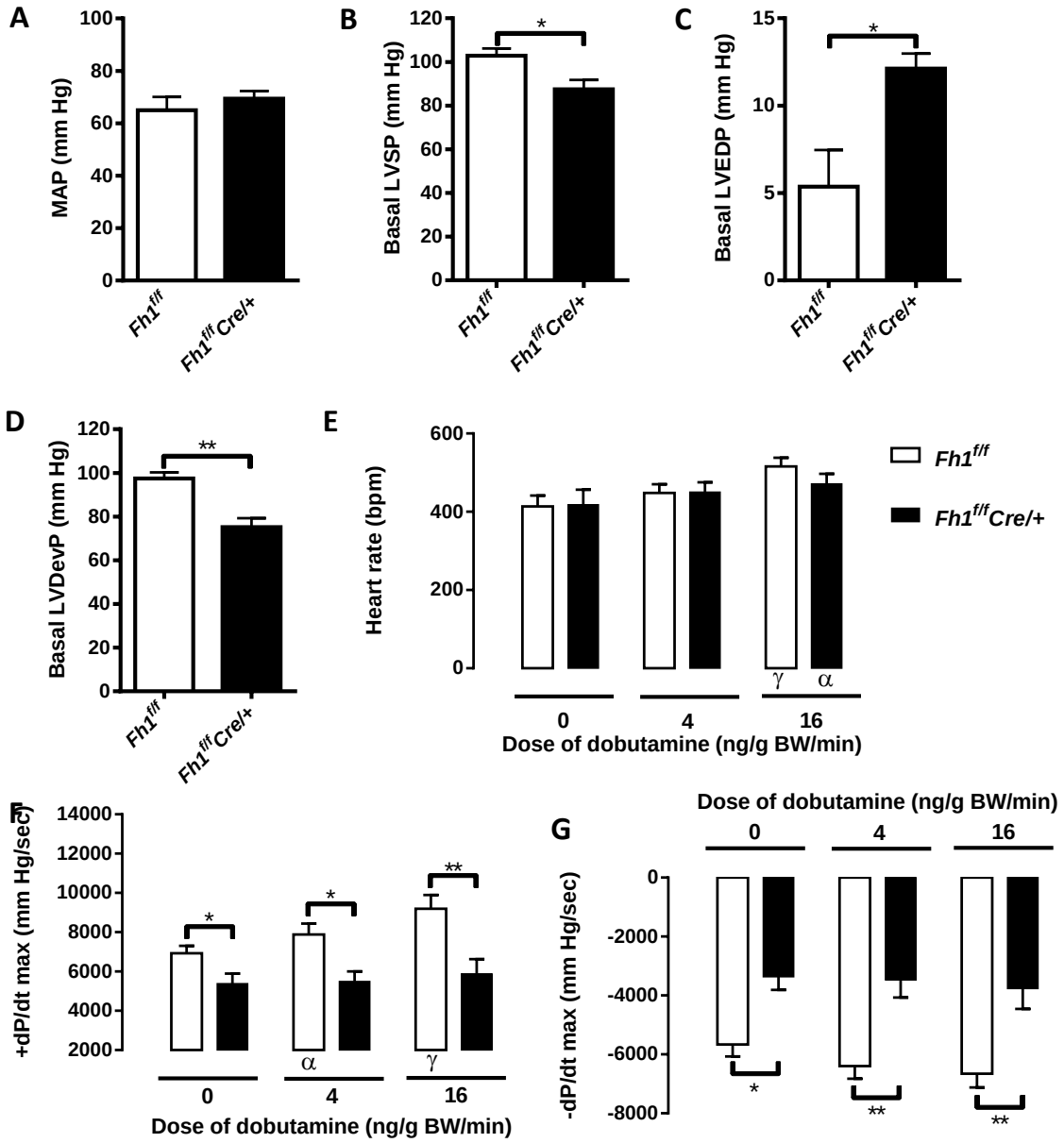

Figure 45 – Invasive left ventricular haemodynamic assessment reveals loss of contractile reserve in *Fh1$^{f/f}$ Cre/+* mice compared to *Fh1$^{f/f}$* controls

A. Mean arterial pressure (MAP) in millimetres of mercury (mm Hg). **B.** Basal left ventricular systolic pressure (LVSP). **C.** Basal left ventricular end-diastolic pressure (LVEDP). **D.** Left ventricular developed pressure (LVDevP). **E.** Heart rate in beats per minute (bpm). Dobutamine dose infused is given in nanograms per gram body weight per min (ng/g BW/min). **F.** The maximal rise in left ventricular pressure with time (+dP/dt) and **G.** the maximal decrease in systolic pressure with time (-dP/dt), both measured in millimetres of mercury per second (mm Hg/sec). * $p<0.05$, ** $p<0.01$, *** $p<0.001$, α $p<0.05$ compared to no dobutamine, γ $p<0.001$ compared to no dobutamine.

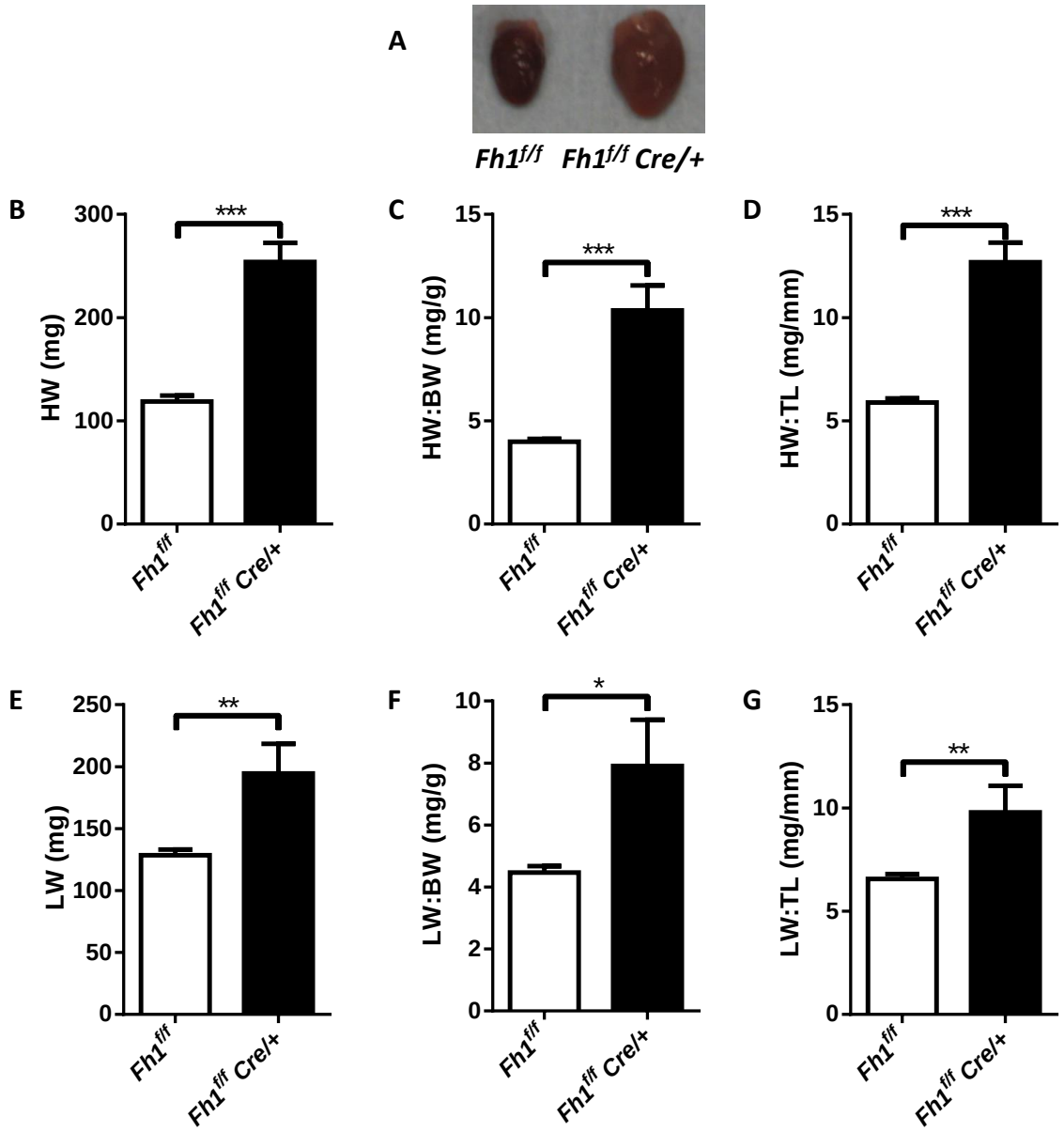

Figure 46 –*Ex vivo* morphometric indices demonstrate cardiac hypertrophy and pulmonary congestion in *Fh1*$^{f/f}$ *Cre*/+ mice compared to *Fh1*$^{f/f}$ controls
A. Representative photograph of *Fh1*$^{f/f}$ and *Fh1*$^{f/f}$ *Cre*/+ hearts. **B.** Heart weight (HW) in milligrams (mg). **C.** Heart weight to body weight ratio (HW/BW) in milligrams/gram (mg/g). **D.** Heart weight to tibial length ratio (HW/TL) in milligrams/mm (mg/mm). **E.** Lung weight (LW). **F.** Lung weight to body weight ratio. **G.** Lung weight to tibial length ratio. * $p<0.05$, ** $p<0.01$, *** $p<0.001$.

4.2.4 Sirus red and wheat germ agglutinin staining and transmission electron microscopy imaging of Fh1 knockout hearts

Increased myocardial fibrosis is often observed in the progression towards heart failure and is associated with stiffening of the cardiac muscle, impairing the ability of the myocardium to

relax in diastole[239]. The aforementioned finding of reduced maximal rate of LV relaxation *in vivo* was supportive of this process occurring in *Fh1*$^{f/f}$ *Cre/+* hearts. Consistent with this, sirius red staining of collagen fibres was performed on *Fh1*$^{f/f}$ *Cre/+* hearts and *Fh1*$^{f/f}$ controls (n=3 per group, 3 images per heart), Figure 47 shows representative images of Sirius red stained sections from each group which are suggestive of mild fibrosis in *Fh1*$^{f/f}$ *Cre/+* hearts but not controls. Indeed, quantification of fibrosis using dark field images normalised to bright field tissue area of the same region demonstrates significantly elevated fibrosis in *Fh1*$^{f/f}$ *Cre/+* hearts comparative to *Fh1*$^{f/f}$ controls (Figure 84). In agreement, with the observed increase in left ventricular mass, wheat germ agglutinin staining revealed clear hypertrophy of individual cardiomyocytes in hearts from *Fh1*$^{f/f}$ *Cre/+* mice (Figure 48 and Figure 83).

Transmission electron microscopy (TEM) was employed to assess myocardial ultrastructure of *Fh1*$^{f/f}$ *Cre/+* and *Fh1*$^{f/f}$ *Cre/+* hearts (2 per group) (Figure 49). Although no obvious abnormalities in sarcomeric integrity were observed, there was a visual trend towards more mitochondria. In order to verify this in a quantitative manner, quantification of mitochondrial DNA was performed by qRT-PCR and normalised to nuclear DNA levels. In support of the visual impression obtained at the time of TEM imaging, a 75 % increase in mitochondrial DNA levels was identified in *Fh1*$^{f/f}$ *Cre/+* cardiac tissue compared to *Fh1*$^{f/f}$ control samples (Figure 50).

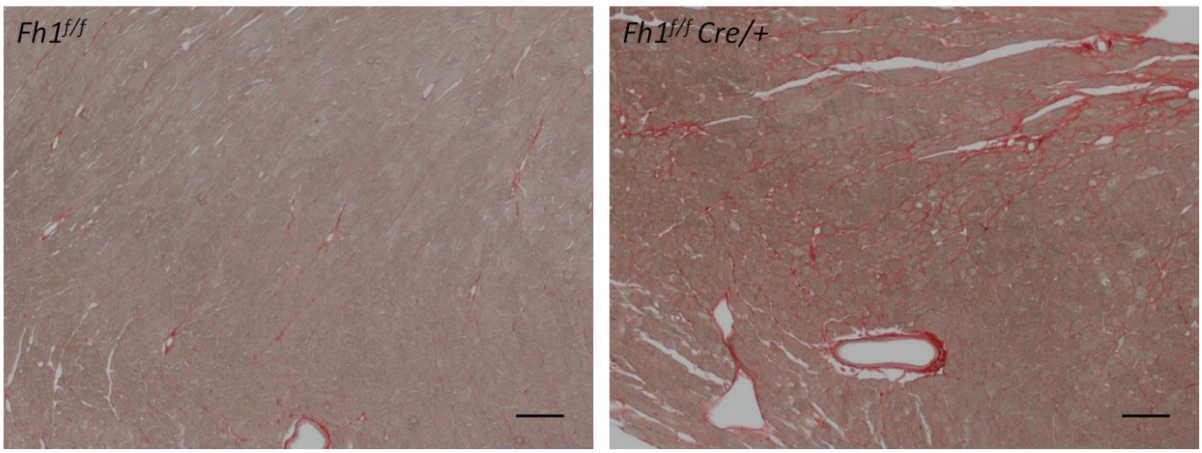

Figure 47 – Sirius red staining demonstrates mildy increased fibrosis in *Fh1*$^{f/f}$ *Cre/+* hearts
Scale bar = 100 µm.

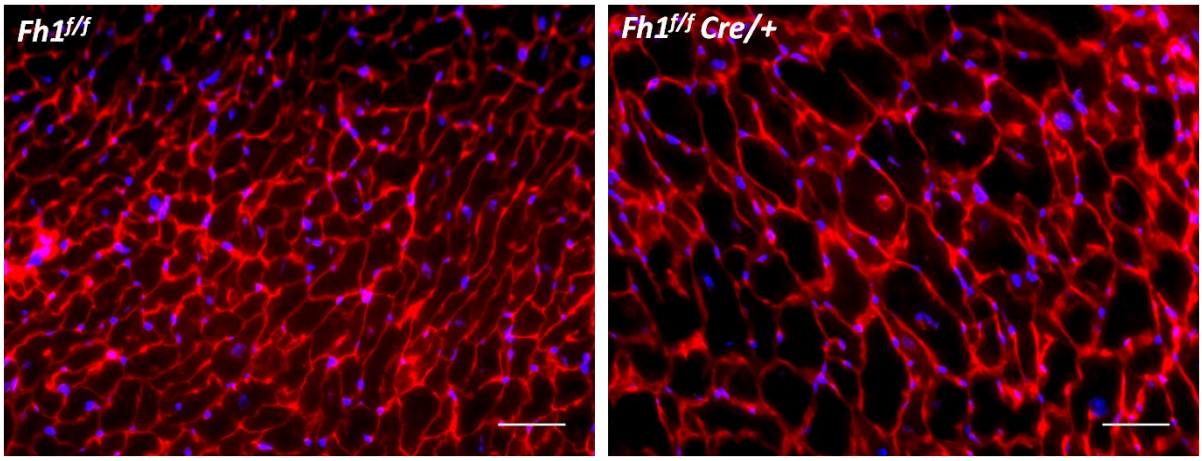

Figure 48 – Wheat-germ agglutinin staining demonstrates increased cardiomyocyte size in *Fh1*$^{f/f}$ *Cre/+* hearts relative to *Fh1*$^{f/f}$ controls
Scale bar = 50 µm.

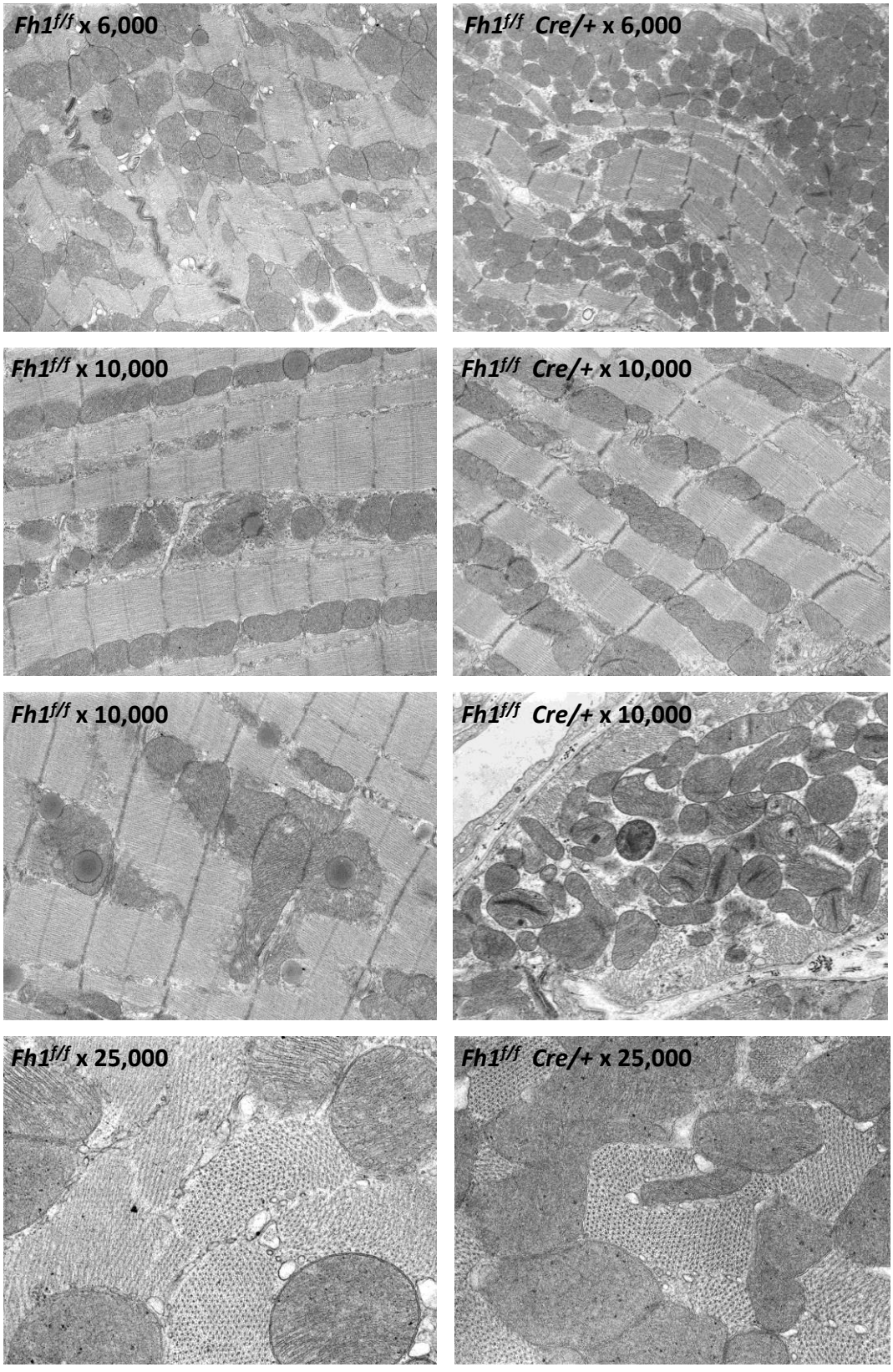

Figure 49 – Transmission electron microscopy showing the ultrastructure of cardiac muscle at different levels of magnification in *Fh1*$^{f/f}$ *Cre*/+ and *Fh1*$^{f/f}$ control mice.

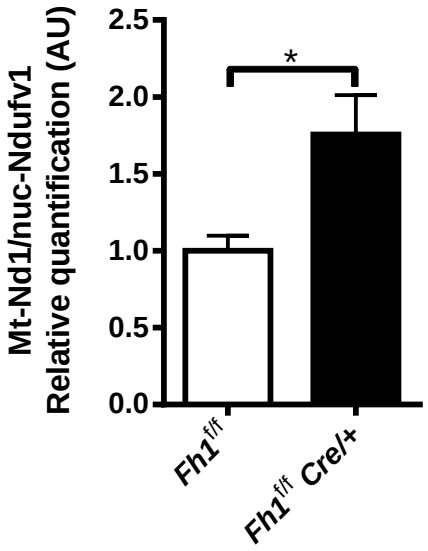

Figure 50 – Elevated mitochondrial DNA in *Fh1*$^{f/f}$ *Cre/+* heart tissue comparative to *Fh1*$^{f/f}$ controls
Relative quantification of expression of the mitochondrial gene NADHdehydrogenase 1 (*Mt-Nd1*), compared to nuclear gene NADH dehydrogenase (ubiquinone) flavoprotein 1 (nuc-*Ndufv1*), both encoding subunits of complex I of the mitochondrial respiratory chain.

High-performance liquid chromatography (HPLC) was use to investigate cardiac high-energy phosphate levels. Both total adenine nucleotide and total creatine pools were significantly reduced in *Fh1*$^{f/f}$ *Cre/+* hearts relative to *Fh1*$^{f/f}$ controls.

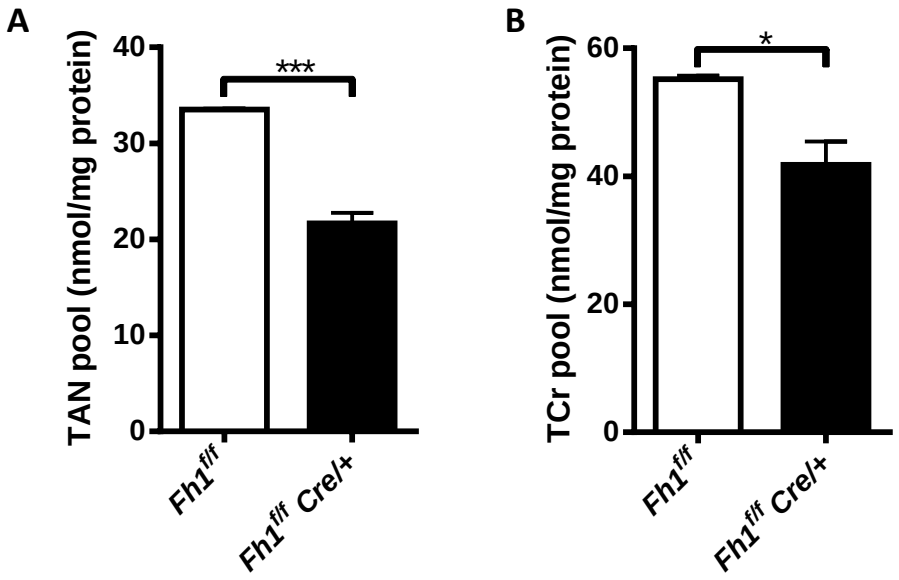

Figure 51 – Reduced total adenine nucleotide (TAN) and total creatine (TCr) pools in *Fh1*$^{f/f}$ *Cre/+* hearts
A. Total adenine nucleotide pool (TAN). **B.** Total creatine pool (TCr). Both measured by high performance liquid chromatography and normalised to protein measured by Lowry assay.*p<0.05. *** p<0.001.

4.2.5 Absence of a pseudohypoxic response in Fh1$^{f/f}$ Cre/+ hearts

Expression of a panel of HIF target genes was assessed by qRT-PCR. This provided no evidence of elevated HIF target gene transcript levels in *Fh1$^{f/f}$ Cre/+* hearts comparative to *Fh1$^{f/f}$* controls. This finding indicates that, despite successful ablation of Fh1, a pseudohypoxic response does not occur in Fh1-deficient cardiac tissue.

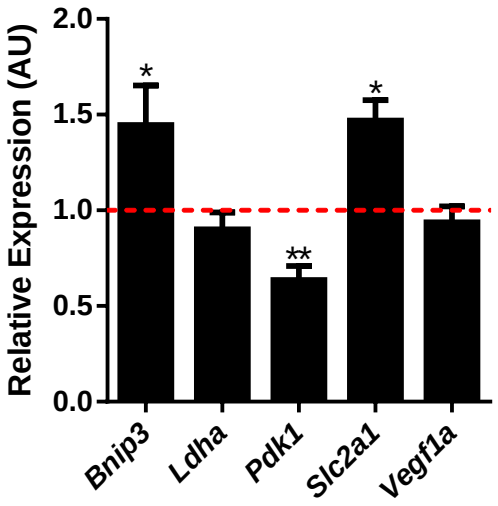

Figure 52 – HIF target gene expression is not consistently elevated in *Fh1$^{f/f}$ Cre/+* hearts
Relative expression in arbitrary units (AU) of HIF target genes in *Fh1$^{f/f}$ Cre/+* cardiac tissue assessed by qRT-PCR determined by qRT-PCR and analysed by the $2^{-\Delta\Delta Ct}$ or comparative C_T method using the internal control in cardiac beta actin (encoded by *Actb*) and normalised to levels in *Fh1$^{f/f}$* controls. Red dashed line represents the mean expression level in *Fh1$^{f/f}$* hearts. *Bnip3*: Bcl2 and nineteen-kilodalton interacting protein 3; *Ldha*: lactate dehydrogenase A; *Pdk1*: pyruvate dehydrogenase kinase 1; *Slc2a1*: glucose transporter 1; *Vegfa1*: vascular endothelial growth factor. * $p<0.05$ compared to *Fh1$^{f/f}$*, ** $p<0.05$ compared to *Fh1$^{f/f}$*.

4.2.6 Concomitant cardiac-specific deletion of Hif-1α exacerbates the Fh1$^{f/f}$ Cre/+ phenotype

To explore the possible role of Hif-1α in the development of the cardiac *Fh1*-deletion phenotype, *Fh1$^{f/f}$ Cre/+* mice were crossed with *Hif-1α$^{f/f}$* mice and the resulting offspring were interbred. As expected, no deaths were observed in control *Hif-1α$^{f/f}$ Fh1$^{f/f}$* mice. Similarly, no *Fh1$^{f/+}$ Hif-1α$^{f/f}$ Cre/+* mice died or exhibited signs of illness during the period of monitoring for Kaplan-Meier analysis, demonstrating that cardiac-specific deletion of *Hif-1α* was not lethal. Ideally, *Fh1$^{+/+}$ Hif-1α$^{f/f}$ Cre/+* would have been used to show this but very

small numbers of mice of this genotype were available. Whilst cardiac-specific deletion of *Hif-1α* was not lethal, cardiac deletion of *Hif-1α* and *Fh1* in concert significantly reduced median life-expectancy from 113.5 days in $Fh1^{f/f}$ *Cre/+* mice to 102.5 days in compound transgenic $Fh1^{f/f}$ $Hif\text{-}1\alpha^{f/f}$ *Cre/+* littermates (Figure 53). Consistent with this signal for deterioration with loss of HIF-1α, both absolute and bodyweight normalised heart weight were seen to be elevated in $Fh1^{f/f}$ $Hif\text{-}1\alpha^{f/f}$ *Cre/+* comparative to $Fh1^{f/f}$ *Cre/+* mice (Figure 54).

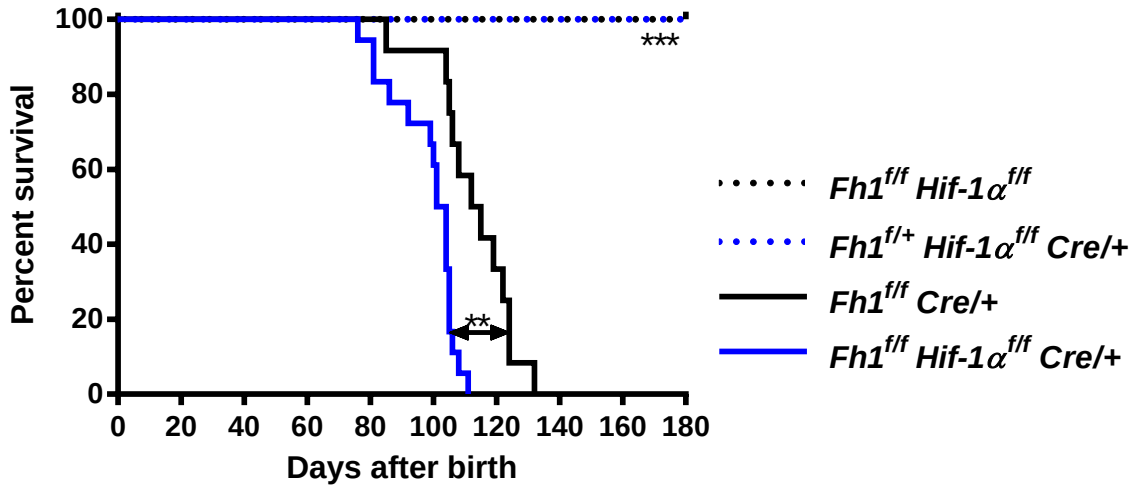

Figure 53 – Kaplan-Meier survival curve demonstrating that concomitant deletion of *Hif-1α* with *Fh1* significantly enhances lethality of the $Fh1^{f/f}$ *Cre/+* phenotype
Note, $Fh1^{f/+}$ $Hif\text{-}1\alpha^{f/f}$ *Cre/+* mice (blue dotted line) are used as a surrogate for $Fh1^{+/+}$ $Hif\text{-}1\alpha^{f/f}$ *Cre/+* to confirm that cardiac ablation of *Hif-1α* is non-lethal.
** $p<0.05$ between indicated, *** $p<0.001$ compared to $Fh1^{f/f}$ *Cre/+* and $Fh1^{f/f}$ $Hif\text{-}1\alpha^{f/f}$ *Cre/+*.

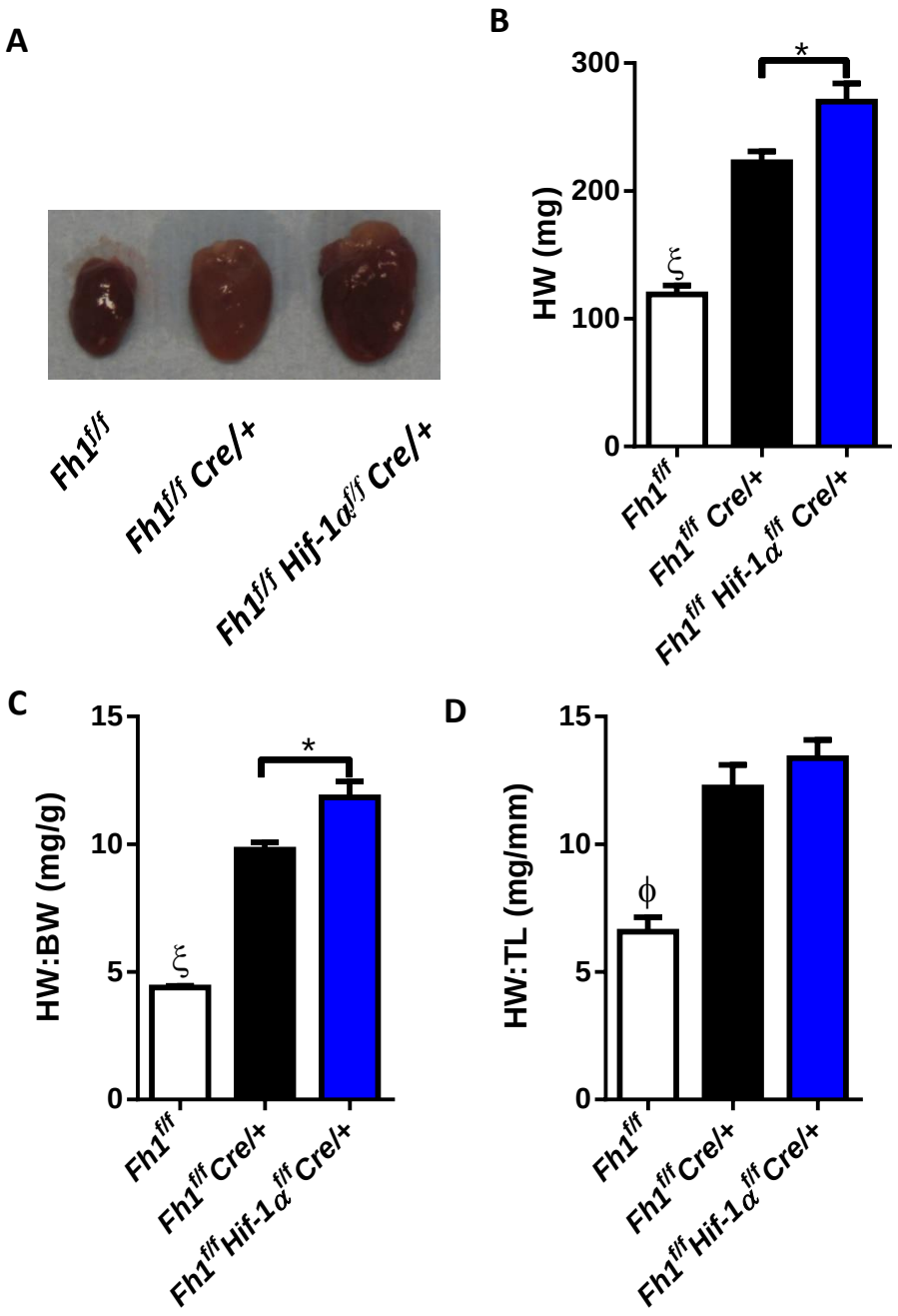

Figure 54 – Concomitant loss of *Hif-1α* exacerbates the cardiac hypertrophic phenotype of *Fh1*$^{f/f}$ *Cre/+* mice.
A. Representative photograph of *Fh1*$^{f/f}$, *Fh1*$^{f/f}$ *Cre/+* and *Fh1*$^{f/f}$ *Hif-1α*$^{f/f}$ *Cre/+* hearts. **B.** Heart weight (HW) in milligrams (mg). **C.** Heart weight to body weight ratio (HW:BW) in milligrams/gram (mg/g). **C.** Heart weight to tibial length ratio (HW:TL) in milligrams/millimetre (mg/mm). * $p<0.05$ between the indicated groups. ξ $p<0.001$ compared to all other groups. Φ $p<0.01$ compared to all groups.

4.2.7 Nrf2 target genes are activated in Fh1$^{f/f}$ *Cre/+ hearts*

Activation of the NRF2 antioxidant pathway has previously been observed in FH-deficient cell lines, fibroids, renal cysts and hearts[145, 161, 166]. Consistent with these data, qRT-PCR

assessment revealed upregulation of NRF2 target gene expression in *Fh1*$^{f/f}$ *Cre/+* hearts. To further delineate the role played by NRF2 in cardiac Fh1-deletion phenotype, *Fh1*$^{f/f}$ *Cre/+* mice were crossed with somatic Nrf2 knockout (*Nrf2*$^{-/-}$) mice and the resulting offspring interbred. Elevation of Nrf2 target genes was seen to be reversed in *Fh1*$^{f/f}$ *Cre/+Nrf2*$^{-/-}$ hearts demonstrating that their activation in *Fh1*$^{f/f}$ *Cre/+* hearts is through Nrf2 activation.

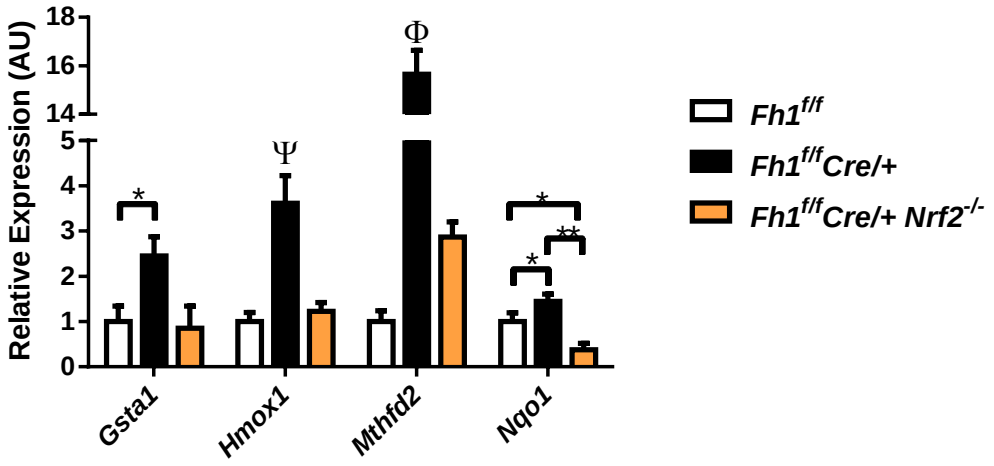

Figure 55 – The elevation of NRF2 target gene expression in *Fh1*$^{f/f}$ *cre/+* hearts is reversed by somatic NRF2 deletion
Relative expression in arbitrary units (AU) of NRF2 target genes assessed by qRT-PCR and analysed by the $2^{-\Delta\Delta Ct}$ or comparative C_T method using the internal control in cardiac beta actin (encoded by *Actb*) and normalised to levels in *Fh1*$^{f/f}$ controls. *Gsta1*: Glutathione S transferase A1; *Hmox1*: Haem oxygenase 1; *Mthfd2*: methylenetetrahydrofolate-dehydrogenase 2; *Nqo1*: NAD(P)H dehydrogenase, quinone 1. * $p<0.05$ between the indicated groups. ** $p<0.01$ between the indicated groups. Ψ $p<0.05$ compared to all other groups. Φ $p<0.01$ compared to all other groups.

4.2.8 Fh1 knockout lifespan is prolonged by heterozygous but not homozygous somatic deletion of Nrf2

Having generated this compound transgenic, the model was used to evaluate whether Nrf2 played a beneficial or maladaptive role in the phenotype of *Fh1*$^{f/+}$ *Cre/+* mice. Somatic deletion of Nrf2 was not prematurely lethal for the duration studied (180 days) as evidenced by survival of *Fh1*$^{f/+}$ *Cre/+ Nrf2*$^{-/-}$ mice (Figure 56). In comparison to *Fh1*$^{f/f}$ *Cre/+* mice, *Fh1*$^{f/f}$ *Cre/+ Nrf2*$^{+/-}$ animals exhibited a significant extension of their lifespan from a median

of 109 to 118.5 days. In contrast, no significant difference in survival was observed between *Fh1*$^{f/f}$ *Cre/+* and *Fh1*$^{f/f}$ *Cre/+ Nrf2*$^{-/-}$. Indeed, the median survival of *Fh1*$^{f/f}$ *Cre/+ Nrf2*$^{-/-}$ animals was only 101.5 days.

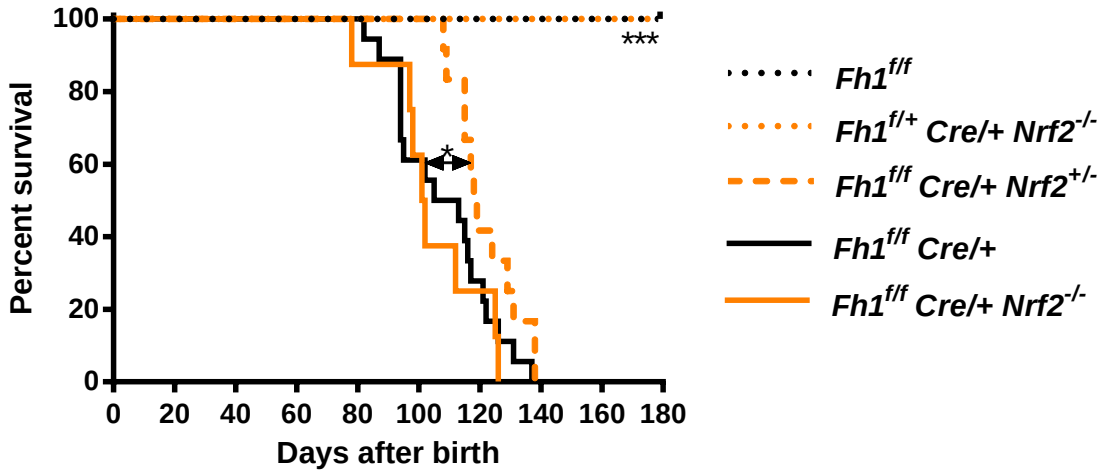

Figure 56 – Kaplan-Meier survival curve demonstrates a small but significant rescue of *Fh1*$^{f/f}$ *Cre/+* lethality by heterozygous (but not homozygous) somatic *Nrf2* deletion
*** p<0.001 compared to *Fh1*$^{f/f}$ *Cre/+*, *Fh1*$^{f/f}$ *Cre/+ Nrf2*$^{-/-}$ and *Fh1*$^{f/f}$ *Cre/+ Nrf2*$^{+/-}$. *p<.0.05 compared to *Fh1*$^{f/f}$ *Cre/+* and *Fh1*$^{f/f}$ *Cre/+ Nrf2*$^{-/-}$ mice.

4.2.9 Heterozygous or homozygous Nrf2 ablation does not rescue the cardiac hypertrophy of cardiac-restricted Fh1 null mice

Fh1$^{f/f}$ *Cre/+*, *Fh1*$^{f/f}$ *Cre/+ Nrf2*$^{+/-}$ and *Fh1 Cre/+ Nrf2*$^{-/-}$ mice all displayed a significant elevation in absolute and normalised heart and lung weights compared to *Fh1*$^{f/f}$ controls (Figure 57). However, no significant rescue of these parameters was identified with either homozygous or heterozygous *Nrf2* deletion. Sirius red staining revealed a trend towards mild interstitial fibrosis in both *Fh1*$^{f/f}$ *Cre/+* and *Fh1*$^{f/f}$ *Cre/+ Nrf2*$^{-/-}$ hearts compared to controls (n=2 per group, 3 images per heart) (Figure 58).However, upon quantification this was statistically insignificant with the modest numbers available.

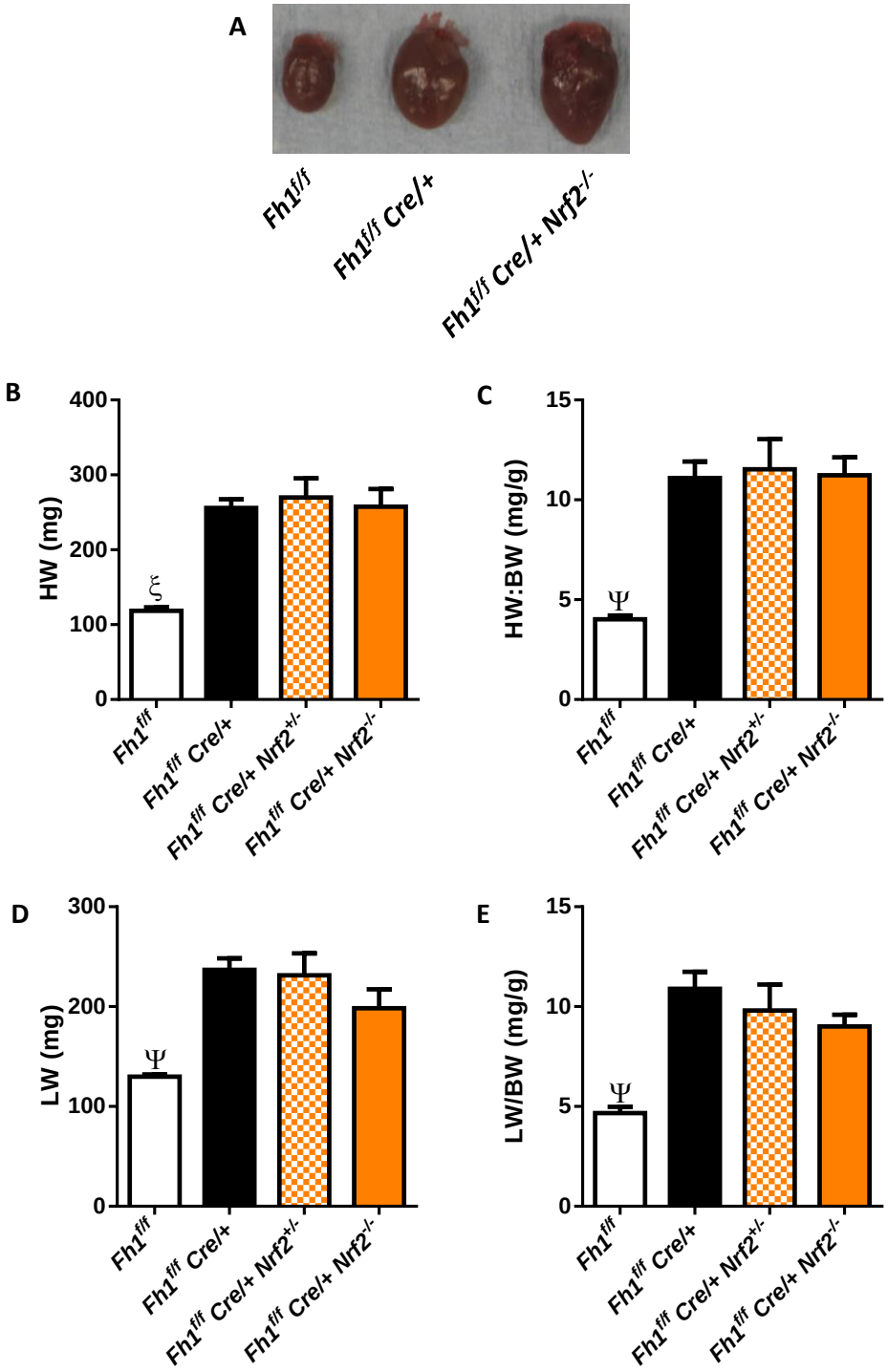

Figure 57 – Loss of Nrf2 does not significantly alter the cardiac hypertrophy or pulmonary congestion identified in older *Fh1*$^{f/f}$ *Cre*/+ adult hearts.
A. Photograph showing *Fh1*$^{f/f}$, *Fh1*$^{f/f}$ *Cre*/+ and *Fh1*$^{f/f}$ *Cre*/+ *Nrf2*$^{-/-}$ hearts. B. Heart weight (HW) in milligrams (mg). C. Heart weight to body weight ratio (HW:BW) in milligrams/gram (mg/g). D. Lung weight (LW). E. Lung weight to body weight ratio (LW:BW). Ψ p<0.05 relative to all other groups. Φ p<0.01 relative to all other groups.

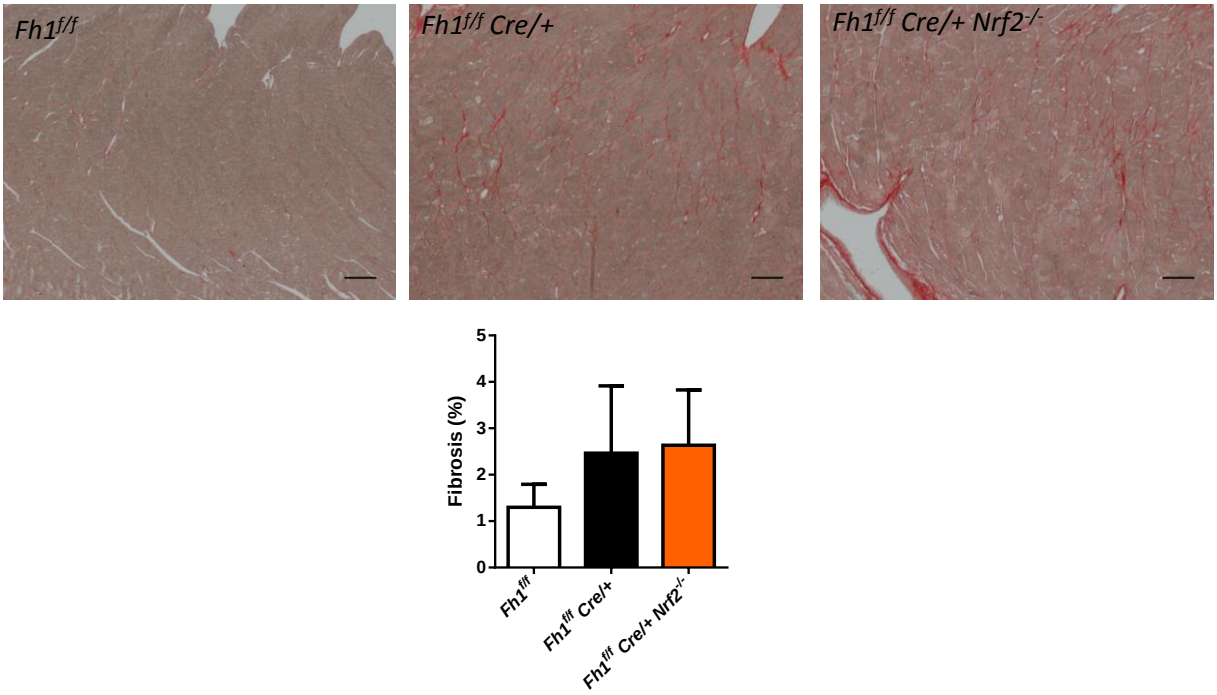

Figure 58 – Representative sirius red stained micrographs demonstrating a trend towards mildly enhanced fibrosis in *Fh1*$^{f/f}$ *Cre/+* and *Fh1*$^{f/f}$ *Cre/+ Nrf2*$^{-/-}$ hearts
Scale bar = 100 µm.
Graph presents fibrosis (assessed using dark field images) as a percentage of total tissue area (from bright field images of the corresponding region).

4.3 Discussion

4.3.1 Summary of chapter findings

Using a murine model of cardiac-specific Fh1 deletion the work presented in this chapter demonstrates:

- Despite cardiac-specific deletion of a key tricarboxylic acid cycle enzyme – fumarate hydratase – *Fh1* $^{f/f}$ *Cre/+* mice are viable, fertile and survive into adulthood.
- Although initially healthy in appearance, *Fh1* $^{f/f}$ *Cre/+* mice develop heart failure resulting in lethality at 3-4 months.
- Despite successful deletion of Fh1, these hearts do not exhibit the anticipated pseudohypoxic response.
- Concomitant cardiac ablation of Hif-1α exacerbates the *Fh1*$^{f/f}$ *Cre/+* cardiac phenotype, with earlier mortality in double knockout mice.
- Nrf2 targets are consistently elevated in *Fh1* knockout cardiac tissue, in keeping with Nrf2 activation in this model.
- Heterozygous *Nrf2* deletion results in a slight amelioration of the Fh1 deletion phenotype, whilst homozygous Nrf2 ablation has no significant effect.

4.3.2 The cardiac Fh1 deletion phenotype

Somewhat surprisingly, despite disruption of the TCA cycle in cardiomyocytes – a cell-type with perpetually high metabolic demands – cardiac *Fh1* knockout mice survive into adulthood. Ultimately, however, these mice go on to develop severe, lethal, heart failure. Echocardiographic and invasive haemodynamic assessment revealed significantly compromised systolic and diastolic cardiac function. Echocardiography and *ex vivo* heart weight measurements demonstrated LV dilatation and hypertrophy in Fh1 knockout hearts.

Although left ventricular anterior and posterior wall thickness in diastole were not significantly increased in Fh1 knockout hearts (as measured by echocardiography), the marked global LV cavity dilatation, increased LV mass (*in vivo* and *ex vivo* measurements) and cardiomyocyte size by wheat germ agglutinin staining were indicative of cardiac hypertrophy.

4.3.3 Reduced total adenine nucleotide and creatine pools: a cause or consequence of heart failure?

The total adenine nucleotide pool refers to the combined levels of ATP, ADP and AMP within the cell. Estimates for free levels of these nucleotides have been obtained using ^{31}P spectroscopy assessment of *ex vivo* perfused rat hearts, revealing order of magnitude concentration differences: [ATP] 11.7 mM, cytosolic [ADP] 41.9 µM and cytosolic [AMP] 0.2 µM, with the latter two calculated using the creatine kinase and adenylate kinase equilibrium, respectively[240]. Accordingly, changes in the total adenine nucleotide pool largely reflect alterations in [ATP].

Steady state [ATP] reflects the balance between anabolic ATP-producing pathways and catabolic ATP-consuming ones. Within the heart the main consumers of ATP are the myofibrillar actomyosin ATPase, the sarcoplasmic reticulum Ca^{2+}-ATPase and the sarcolemmal Na^+/K^+-ATPase, in addition to macromolecule synthesis[241]. Production of ATP is largely met by mitochondrial oxidative phosphorylation, with additional smaller contributions from glycolysis and the citric acid cycle[241]. Given the fundamental importance of the above ATPases in cardiac contractility, excitation-contraction coupling and regulation of intracellular ionic concentration, a steady ATP supply is needed to ensure normal cardiac function. Thus a reduction in the intracellular pool of adenine nucleotides is likely to reflect significant perturbation in ATP provision that is insufficient to meet the cell's demands.

Mitochondrial adenine nucleotide pool size has been shown to be regulated by multiple factors, including substrate/oxygen provision, mitochondrial energy status, [Ca^{2+}], and extramitochondrial ATP levels (reflecting ATP consumption) and thought to reflect adenine nucleotide transport across the mitochondrial membrane via calcium-dependent carriers (the ATP-Mg/P_i carrier and mitochondrial permeability transition pore) as well as AMP nucleotide degradation to adenosine by 5'-nucleotidase activity[242]. Adenosine or inosine monophosphate (IMP) produced by the degradation of AMP can diffuse into the extracellular space (the latter as inosine) reducing total intracellular purine content[243]. Intracellular metabolism of adenosine to inosine, hypoxanthine, xanthine and ultimately uric acid may also contribute to reduction in the adenine nucleotide pool.

Intuitively, the reduction in both total adenine nucleotide (TAN) pool and total creatine (TCr) pool in aged *Fh1* knockout hearts, together with the subsequent progression to overt heart failure, seem a logical consequence of ablating an integral TCA cycle enzyme. However, in young (5 weeks) *Fh1* knockout hearts, no difference in either of these pools or the phosphocreatine- (PCr) to-ATP ratio (as an index of cardiac energetic status) were observed (Dr Gabor Czibik personal communication)[166], implying that depletion of these key energetic entities may be secondary to the development of heart failure. In support of this, depletion of TAN and TCr pools is a commonly observed correlate of end-stage heart failure[75, 244], suggesting that the decline in TAN and TCr in *Fh1* knockout hearts may be a consequence rather than a cause of heart failure in this model. It is plausible, indeed likely, that both sustained TCA compromise over time and the added metabolic demands imposed by heart failure *per se* contribute to the observed reduction in high-energy phosphate pools in these mice.

4.3.4 No pseudohypoxic response in Fh1 knockout hearts

The inability of cardiac Fh1 ablation (as modelled by the *Fh1*$^{f/f}$ *Cre/+* mouse) to induce normoxic HIF signalling (a pseudohypoxic response) was initially surprising given that this has been reported in multiple human and mouse models of Fh1 depletion, including the archetypal clinical scenario of hereditary leiomyomas and renal cell cancers (HLRCC). Indeed, in chapter 6 a pseudohypoxic response is demonstrated in Fh1 null mouse embryonic fibroblasts (MEFs). However, the cell-type restricted prevalence of cancers associated with FH deficiency suggests that at least some of the features associated with TCA cycle disruption and fumarate accumulation may be unique to these tissues. The mechanism underlying normoxic HIF stabilisation in this setting is thought to be the competition of accumulated fumarate with the prolyl hydroxylase domain protein co-substrate, 2-OG. In fact, the addition of excess 2-OG to Fh1-deficient cells can reverse the pseudohypoxic response, demonstrating that the ratio of fumarate:2-oxogluatarate is key. Published data demonstrate that levels of fumarate accumulation in these cancer models are spectacular, with fumarate elevation in uterine fibroids from HLRCC patients of 400-fold, whilst in renal cysts from Fh1-deficient mice this is 48-fold and in MEFs 30-fold[115, 144, 160]. However, in cardiac tissue from young (5 week old) *Fh1*$^{f/f}$ *Cre/+* mice, fumarate is only elevated 1.63-fold[166], a level likely to be insufficient to induce a pseudohypoxic response.

4.3.5 Concomitant Hif-1α deletion exacerbates the Fh1 deletion phenotype

Consistent elevation of HIF target genes was not seen in Fh1-deficient hearts, suggesting no pseudohypoxic response or elevation of HIF in response to cardiac failure. However, simultaneous deletion of cardiac *Fh1* and *Hif-1α* aggravated the *Fh1* null cardiac phenotype leading to earlier death, in conjunction with greater heart and lung weights suggestive of more florid congestive heart failure. Together these findings suggest a mildly protective role for HIF-1α in the progression of the cardiomyopathy associated with cardiac Fh1-ablation. It

is probable that the contribution of Hif-1α to basal expression of its targets is *protective* in the Fh1-depleted myocardium. For example, the maintenance of glycolytic gene expression (in part regulated by HIF-1α) is likely to be particularly beneficial in the context of a disrupted TCA cycle.

4.3.6 Heterozygous but not homozygous somatic Nrf2 deletion extends the lifespan of mice with cardiac Fh1 ablation

Homozygous somatic knockout of Nrf2 had no significant effect on lifespan or the heart and lung weights of cardiac *Fh1* knockout mice. However, despite no discernible effect of heterozygous knockout of Nrf2 on heart and lung weight, $Fh1^{f/f}$ *Cre/+* $Nrf2^{+/-}$ mice exhibited a small but significant extention of life span compared to $Fh1^{f/f}$ *Cre/+* mice. This mild rescue raises the intriguing possibility that reductive stress may in part contribute to the phenotype of the *Fh1* cardiac knockout. Indeed, in support of this hypothesis, precedent exists for reductive stress resulting in cardiac dysfunction in a murine model of protein aggregation cardiomyopathy (PAC) [245]. Analaogous to Fh1-deficient cells and tissues, sustained activation of NRF2 has been observed in PAC hearts[145, 161, 166, 246]. However, unlike the present study's model, crossing PAC mice with homozygous NRF2 knockout led to a compelling amelioration of the phenotype[247]. The explanation for this apparent discrepancy is likely to be more nuanced, however, given that NRF2 has numerous target genes, many of which encode enzymes involved in diverse metabolic pathways. Thus, reduced expression of some of these proteins may relieve reductive stress, whilst lowering levels of other, or even the same targets, may be detrimental to the overall complex remodelling of metabolic flux required to compensate for loss of a key TCA cycle gene. Further investigation into the potential role of reductive stress in cardiac Fh1 null phenotype targeted toward the pentose phosphate pathway, is described in chapter 5.

4.3.7 Limitations

4.3.7.1 Mixed genetic background

Unfortunately the *Fh1*$^{f/f}$ *Cre/+* and *Nrf2*$^{-/-}$ stains were received on a mixed genetic background and due to time constraints it was not possible to backcross these mice onto a pure strain background prior to this study. Genetic background is widely known to have a profound effect upon genetically modified mouse phenotypes and frequently results in differences in the penetrance or expressivity of a phenotype[248]. Significant differences in parameters of cardiac function (ejection fraction) and calcium handling have been observed between mice of different genetic backgrounds in the absence of a transgene[249]. Differences in genetic background are likely to contribute to the variation in median age of death for *Fh1*$^{f/f}$ *Cre/+* mice from the original colony (108.5 days), crossed on to the genetic background of Nrf2 null mice (109 days) or on to a C57Bl6J background (for 1 generation) of *Hif-1α* floxed animals (113.5 days). In order to control for differences in genetic background, mice were maintained as separate colonies and littermate controls used for survival, phenotyping and molecular analysis wherever possible.

4.3.7.2 The question of fumarate

The present study used a model of cardiac fumarate excess dependent upon adequate genetic ablation of *Fh1* in murine heart. The protein product of *Fh1*, fumarate hydratase, catalyses the conversion of fumarate to malate in the citric acid cycle. Western blotting confirmed a 75 % reduction in Fh1 protein cardiac tissue from *Fh1*$^{f/f}$ *Cre/+*mice compared to *Fh1*$^{f/f}$ controls, likely at least in part to reflect residual non-cardiomyocyte Fh1 expression which is not subject to *Mlc2vcre* mediated excision. A more precise assessment of the degree of Fh1 knockout in cardiomyocytes would require assessment of Fh1 transcript and protein expression from isolated cardiomyocytes. Importantly, use of this approach in cardiomyocytes derived from younger *Fh1*$^{f/f}$ *Cre/+*mice demonstrated near complete absence

of Fh1[166]. An alternative approach to measurement of absolute protein levels would be to assess fumarate hydratase activity.

Total cardiac levels of fumarate have been shown to be increased by 1.6-fold in young *Fh1*$^{f/f}$ *Cre/+*mice compared to *Fh1*$^{f/f}$ controls using ^{1}H-NMR spectroscopy[166]. Significantly, such measurements do not provide insight into fumarate metabolic flux. The absolute value of fumarate based on a single reading may provide limited information about the degree of fumarate repletion of the cell reflected not only by effectively 'free' fumarate, but also in its spontaneous and irreversible incorporation into proteins by non-enzymatically reacting with sulphydryl groups of cysteine residues by a Michael reaction to form a stable protein modification, S-(2-succinyl)cysteine (or 2SC), in a process termed succination[159, 250]. Immunoblotting of young *Fh1*$^{f/f}$ *Cre/+* hearts for 2SC has shown pan-upregulation of succination, supporting a biologically important increase in fumarate repletion of cardiomyocytes in hearts from *Fh1*$^{f/f}$ *Cre/+* mice[166]. While cysteine is one of the least common amino acids in eukaryotic proteins and cysteine-containing proteins represent only ~2.5% of the eukaryotic proteome, cysteine is regarded as one of the most reactive of all amino acids[251], hence the functional impact of cysteine modification by fumarate may exert a greater effect than these figures or a 1.6-fold increase in fumarate would suggest. Cysteine is often exposed on the surface of proteins or at the active site of enzymes and is found in key proteins regulating metabolism, acting as molecular chaperones, mediating signal transduction and involved in transcription[250, 251]. In support of this, post-translational modification of proteins by succination has been identified to have significant functional effects, including inactivation of the glycolytic enzyme glyceraldehyde-3-phosphate dehydrogenase[250], binding to the cysteine of glutathione, an abundant intracellular antioxidant

resulting in excess reactive oxygen species accumulation[164], or modification of tubulin to inhibit its polymerisation potentially affecting microtubule dynamics[252].

A key protein shown to be succinated under conditions of fumarate excess (e.g. *Fh1*$^{-/-}$ MEFs) is the protein Kelch-like ECH-associated protein 1 (KEAP1)[145] which represses Nuclear factor (erythroid-derived 2)-like 2 (NRF2)-dependent transcription by forming a functional subunit of the E3 ubiquitin ligase[253]. NRF2 plays a key role in cellular defence by coordinating the transcriptional response to oxidative stress, including expression of haem oxygenase 1 (HMOX1) and superoxide dismutase (SOD)[253]. Under basal conditions, KEAP1 sequesters NRF2 in the cytosol and targets NRF2 for ubiquitination and proteasomal degradation[253]. KEAP1 has multiple cysteine residues (27 in human) of which several are thought to form part of a molecular switch highly sensitive to changes in intracellular redox state. Their post-translational modification by electrophiles or reactive oxygen species leads to a conformational change in KEAP1, NRF2 stabilisation and translocation of free NRF2 to the nucleus to bind anti-oxidant response elements enhancing downstream target gene transcription, including HMOX1. High levels of succination of key redox sensitive cysteine residues in KEAP1 have been identified in *Fh1*$^{-/-}$ MEFs by tandem mass spectrometry, including Cys151 and Cys288 shown to have regulatory roles in KEAP1 activity[145]. The finding of a marked upregulation of NRF2-mediated antioxidant signalling in both Fh1 deficient mouse kidneys[145] and heart[166], the latter verified in the present work, underlines the functional importance of KEAP1 succination by fumarate. While the levels of fumarate increase identified in hearts of young *Fh1*$^{f/f}$ *Cre/+*mice[166] may not appear high, the functional consequences on NRF2 signalling support this as being biologically important and suggest that control of fumarate levels is likely to be important for proper cellular function[254].

The finding that urea cycle metabolites accumulate in *Fh1*-deficient kidneys, with marked increases in argininosuccinate and citrulline but reduction in aspartate levels,[180] points to another 'location' for the fumarate excess induced by loss of *Fh1* in the heart and may further explain why the levels are not as high as might be predicted from genetic deletion of *Fh1*. In *Fh1*$^{-/-}$ MEFs the increase in argininosuccinate synthesis has been shown to occur directly from fumarate through a reversal of argininosuccinate lyase (ASL) using arginine[180]. Supporting the extension of these findings to the *Fh1* deficient heart, flux-balance analysis simulation of myocardial mitochondrial metabolism in the absence of FH predicted a partial reversal of the urea cycle which metabolised excess fumarate to form argininosuccinate. This *in silico* prediction was supported in *Fh1*$^{f/f}$ *Cre/+* hearts by the accumulation of argininosuccinate identified by using Fourier transform ion cyclotron resonance (FT-ICR) mass spectrometry (results presented and discussed further in chapter 5). However, flux analysis using isotope-labelled TCA cycle intermediates or anaplerotic metabolites would be required to elucidate if incorporation of fumarate into argininosuccinate occurrs in the Fh1-null heart. Alternatively, argininosuccinate accumulation may be due to end-product inhibition (by fumarate) of argininosuccinate lyase activity.

A potentially important factor leading to the molecular and gross cardiac functional phenotype of *Fh1*$^{f/f}$ *Cre/+*mice is that of chronicity. Long-term low-level increase in a reactive intermediary metabolite such as fumarate may exert prominent effects on key cellular signalling networks when occurring over the lifetime of an animal. Furthermore, it is feasible that the levels of fumarate increase identified in young *Fh1*$^{f/f}$ *Cre/+*mice may increase over time; hence fumarate assays undertaken in aged hearts may be informative.

4.3.7.3 Mitochondrial phenotype

The heart has perpetually high energy requirements, with human hearts estimated to cycle through 6 kg of ATP each day[75], a need largely met by mitochondrial oxidative metabolism of carbon substrates. Accordingly an important question to address in the course of investigating the consequences of Fh1 cardiac deletion was the effect on mitochondrial phenotype.

Investigation of the effect of Fh1 loss on cardiac ultrastructure by transmission electron microscopy (TEM) suggested a visual trend to more mitochondria. Whilst formal quantitiative analysis by image morphometry[256] was not undertaken due to limited samples, a qPCR identified a 75% increase in mitochondrial to nuclear DNA ratio in hearts from *Fh1*$^{f/f}$ *Cre/+* mice, supporting a significant alteration in the number/density of these organelles.

These findings suggest that mitochondrial biogenesis may be enhanced in the hearts of *Fh1*$^{f/f}$ *Cre/+* mice, an intuitive response to energetic deficiency caused by interruption of the TCA cycle. Mitochondrial biogenesis requires the coordinated expression of a series of nuclear and mitochondrial DNA-encoded genes and is mediated by a number of transcription factors and cofactors, including mitochondria transcription factor A (TFAM), the nuclear respiratory factors 1 and 2 and peroxisomal proliferating activating receptor-γ coactivator α (PGC-1α)[257]. Future assessment of gene (by qRT-PCR) or protein (by immunoblotting) expression of these factors, or expression of key mitochondrial enzymes regulated by them (e.g. the β-subunit of ATP synthase or cytochrome c oxidase subunits) from *Fh1*$^{f/f}$ *Cre/+* and control hearts may provide further indirect support for enhanced mitochondrial biogenesis in the face of cardiac Fh1 deficiency. A limitation of the latter approach is the potential transient upregulation of

these transcription factors, potentially leading to an in mitochondrial mass evaluated by TEM without a corresponding increase in transcription factor expression[256].

Whilst increased biogenesis is expected to increase total mitochondrial energy producing capacity in normal cells, in the setting of citric acid cycle disruption through Fh1 loss, the question arises as to whether the increased mitochondria identified in *Fh1*$^{f/f}$ *Cre/+* hearts remain fully functional. Mitochondrial form and its bioenergetic function are thought to be tightly linked[258]. Accordingly, indirect insights into this question could come from more detailed analysis of TEM images on a macrocellular level, e.g. assessment of mitochondrial tubular network organisation or spatial localisation (subsarcolemmal or interfibrillar), or suborganelle appearances, e.g. with respect to internal cristal morphology and integrity[258]. Potential limitations of this include the responsivity of mitochondrial structure to alterations in cellular homeostasis such that pathological changes in other organelles or cellular structures can themselves alter mitochondrial morphology, in addition to current incomplete understanding of the implications of different cristal configuration (e.g. lamelliform versus tubular)[259].

Transmission electron microscopy is regarded as the gold standard for assessment of alterations in mitochondrial biogenesis[256], however inferences on mitochondrial function are indirect. More direct evaluation of mitochondrial function includes assessment of individual enzyme activity, or direct measurement of mitochondrial respiration from freshly permeabilised cardiac fibres. A commonly used approach to the former is the determination of maximal citrate synthase (a mitochondrial matrix enzyme) activity from frozen tissue. While likely to provide support for alterations in mitochondrial oxidative capacity, the ability of a the maximal activity of a single enzyme measured from powdered frozen cardiac tissue

to adequately capture changes in whole mitochondrial oxidative capacity may be limited[260]. Using a similar approach in hearts from young *Fh1*$^{f/f}$ *Cre/+* mice, measurement of respiratory chain complex activity and myofibre oxygen consumption using a Clark-type oxygen electrode revealed no differences with control hearts[166], arguing against a major alteration of mitochondrial oxidative capacity. This may reflect the fact that, on a per organelle basis, cardiac mitochondrial function is impaired in *Fh1*$^{f/f}$ *Cre/+* mice and effectively compensated by an increase in mitochondrial density per cell.

A complementary approach to assessment of mitochondrial function is to focus on the end-product of its oxidative metabolism, i.e. ATP or a surrogate measure in the form of total adenine nucleotides, in the whole heart. Using high-performance liquid chromatography, in the present study the total adenine nucleotide pool was observed to be significantly reduced in *Fh1*$^{f/f}$ *Cre/+* hearts relative to *Fh1*$^{f/f}$ controls. In contrast, measurement of a related readout of energetic sufficiency by ^{31}P MRS, the phosphocreatinine to ATP ratio, from *ex vivo* perfused hearts was found to be unaltered in young *Fh1*$^{f/f}$ *Cre/+* mice[166].

4.3.7.4 Histological phenotype

The present study's assessment of histological phenotype focused on sirius red staining of collagen fibres to identify increased myocardial fibrosis and use of wheat germ agglutinin staining to demonstrate cardiomyocyte hypertrophy. Both approaches identified significant differences between *Fh1*$^{f/f}$ *Cre/+* and *Fh1*$^{f/f}$ control hearts. In support of the histological signal for hypertrophy consequent to *Fh1* deletion, both echocardiography and measurement of *ex vivo* organ weight demonstrated clear increases in cardiac mass, while molecular data (presented in chapter 6) confirmed a switch from an adult to a foetal pattern of cardiac gene

expression, a feature associated with, but not specific for, pathological cardiac hypertrophy[201].

Improved specificity for collagen requires the use of antibodies or proteins that bind collagen, Fluorescently labelled CNA35, a truncated collagen adhesion protein derived from *Staphylococcus aureus* bacteria has high specificity and affinity for collagen and has been used both in tissue sections[261] and coupled to gold nanoparticles as a collagen-homing ligand to non-invasively probe myocardial scar in mice using computed tomography[262].

Alternative non-histological methods of evaluating myocardial fibrosis which may provide further support for the findings obtained with Sirius red quantification include biochemical measurement of hydroxyproline (the result of post-translational proline hydroxylation), highly specific for collagen. While providing an accurate assessment of total collagen content, the requirement to homogenise tissues for measurement leads to loss of information on fibrosis distribution within tissue[261]. Measurement of gene expression could also be employed to further corroborate the fibrotic phenotype of *Fh1*$^{f/f}$ *Cre/+* hearts and has been used successfully in rodent models of heart disease[263], for example: growth factors stimulating collagen synthesis, such as transforming growth factor β (TGF-β), matrix metalloproteinase enzymes mediating collagen degradation, or of lysyl oxidase (LOX) which is the extracellular enzyme responsible for cross-linking of fibrillary collagen.

While increased collagen production and deposition is observed in a broad range of cardiac pathologies, making it hard to attribute any observed increase to fumarate increase *per se*, administration of a cell-permeable ester of fumarate, dimethylfumarate (DMF), has been shown to prevent renal fibrosis via NRF2-mediated inhibition of TGF-β/Smad3 signalling[264].

Whether this applies to *Fh1*$^{f/f}$ *Cre/+* hearts is uncertain but, if so, would suggest that the observed levels of myocardial fibrosis reflect competing contributions from primary interruption of the TCA cycle causing heart failure and activation of NRF2 signalling.

4.3.7.5 Does fumarate accumulation contribute to the Fh1$^{f/f}$ *Cre/+ cardiac phenotype?*

Whilst mitochondrial dysfunction and subsequent energetic compromise may contribute to the Fh1 null cardiac phenotype it is possible that accumulation of the Fh1 substrate fumarate may contribute to this phenotype. Pharmacological augmentation of intracellular fumarate with DMF in wild-type mice could be used as a strategy to better define the likely contributions of fumarate excess versus TCA cycle disruption *per se* to the phenotype of *Fh1*$^{f/f}$ *Cre/+* mice. Chronic treatment of WT mice with DMF (in comparison to *Fh1*$^{f/f}$ *Cre/+* mice treated with vehicle) could be used to test the hypothesis that chronic fumarate excess *per se* can induce significant hypertrophy and dysfunction at both the cellular (isolated adult cardiomyocyte) and whole-organ level (*in vivo* readouts of cardiac structure and function). DMF and other fumaric acid esters, usually administered by oral gavage, have been used successfully in experimental murine models of multiple sclerosis[265], melanoma[266] and ischaemia-reperfusion injury[166]. In addition, DMF has been shown to activate the Nrf2 antioxidant pathway, recapitulating a feature of *Fh1*$^{f/f}$ *Cre/+* hearts[166, 267]. There are limitations to such an approach, however. While dose ranges are published in mouse models, it is not entirely clear what dose of DMF would be 'equivalent' to the present *Fh1*$^{f/f}$ *Cre/+* cardiac mouse model. While administration of exogenous fumarate to wild-type mice might appear to be a simple intervention (in comparison to the direct and secondary effects of TCA cycle disruption), such fumaric acid esters have been shown to induce multiple effects not limited to cardiomyocytes, including inhibition of nuclear factor κB (NF-κB) and extracellular signal-regulated kinase 1 and 2 (ERK1/2) signalling[268], inhibition of cellular

proliferation and promotion of apoptosis[266], inhibition of angiogenesis[269], stabilisation of Nrf2 and upregulation of its attendant signalling[166, 267], altered neutrophil adhesion and migration[270].

In addition, long-term administration of DMF may induce systemic HIF-1α stabilisation and activation of a pseudohypoxic response through fumarate-induced inhibition of prolyl-hydroxylase domain enzymes[149]. Consequent induction of HIF target genes, including erythropoietin may (as with somatic PHD2 inactivation in mice[109]) result in marked polycythaemia, volume overload and cardiomyopathy independent of any direct effect of fumarate within the cardiomyocyte. This may limit the ability of such an approach to understand the mechanism underlying the phenotype of cardiac-restricted Fh1 deletion. In addition, it would be difficult – particularly *in utero* – to ensure mice received a cardiac dose of DMF equivalent to chronic fumarate accumulation associated with *Fh1* deletion during embryogenesis.

An alternative *in vitro* experimental approach could use isolated cardiomyocytes from WT and *Fh1*$^{f/f}$ *Cre/+* hearts, with subsequent direct application of DMF or vehicle solution and cellular phenotypic screening. Readouts could include markers of cellular hypertrophy (e.g. wheat germ agglutinin staining for myocyte cross-sectional area), cardiomyocyte stress (e.g. expression of *Acta1*, *Myh7, Nppa* and *Nppb* by qRT-PCR) and assessment for reorganisation of the actin cytoskeleton which occurs during hypertrophic stimulation[271] (e.g. by fluorophore-labelled Phalloidin conjugates to stain filamentous actin). If excess intracellular fumarate were the predominant cause of the *Fh1*$^{f/f}$ *Cre/+* cardiac phenotype, it would be anticipated that administration of DMF to WT control cells treated with DMF may induce a

similar cellular phenotype to that of vehicle treated *Fh1*$^{-/-}$ cells. DMF administration to *Fh1*$^{-/-}$ cells may induce a worsening of the existing pro-hypertrophic phenotype.

An experimental approach utilising isolated cardiomyocytes has the potential advantages of reducing animal use, elimination of other cell types within the heart that may influence readouts (particularly in a model using ventricular cardiomyocyte-specific deletion of Fh1 using the Mlc2v-cre promoter), the potential for the cells to act as their own control in time-course studies and greater control over experimental variables compared to whole-animal or whole-organ approaches[272]. However, short-term administration of DMF to terminally differentiated primary murine cardiomyocytes may be insufficient to mirror the effects of long-term fumarate excess *in vivo*, exacerbated by the limitations of primary adult cardiomyocyte culture with limited lifespan and progressive functional and morphological changes occurring over time in culture conditions[273].

4.3.7.6 Direct clinical relevance

One criticism of the present model is that it does not directly reflect a known human disease and therefore has limited clinical relevance. Whilst the direct relevance of the end-stage Fh1 knockout cardiac phenotype may be questionable, the model provides a tractable experimental platform with which to interrogate the consequences of perturbing TCA flux and altered intermediary metabolism, provides insights into the biology of fundamental metabolic pathways within the heart and highlights the incredible potential level of metabolic plasticity of adult myocardium, that adapts to allow mice to survive despite disruption of the TCA cycle in an organ that consumes more energy than any other in the body[75]. An enhanced understanding of the compensatory pathways by which these hearts survive holds the promise

of identifying novel therapeutic strategies that may be harnessed to maintain or ameliorate cardiac energetics in the setting of clinical heart failure.

4.3.7.7 Choice of Cre

A further limitation relates to the use of cre-recombinase driven by the Mlc2v promoter. This approach will mean that excision of the *Fh1* floxed allele is likely to occur at around embryonic day 8[183, 184]. Thus this model will not reflect any role played by Fh1 prior to this point in development. However, after this time there exists potential for adaptive developmental and metabolic remodelling to occur, facilitating survival of the Fh1-deficient heart. Due to this potential (embryonic) remodelling, the phenotype observed in these mice may not reflect that which would develop if *Fh1* were acutely ablated postnatally during adulthood using an alternative promoter to drive cre recombinase activity.

The ablation of Fh1 throughout the cardiomyocyte does not permit differentiation between the effects of subcompartmental fumarate accumulation, notably in the cytosol and mitochondria, or readily discern the relative roles of disruption of the mitochondrial TCA cycle, aberrant succination of cytosolic (and mitochondrial) proteins and disruption of cytosolic, metabolic pathways, such as the urea cycle and purine nucleotide cycle, by fumarate accumulation to the final phenotype. Chapter 6 attempts to address this to some degree by investigating the effect of reintroduction of FH specifically to the cytosol.

4.3.7.8 Selection of the phenotyping timepoint

Single phenotyping time points were selected for echocardiography (99 – 103 days) and invasive haemodynamics/tissue harvest (101 – 107 days) based on the very first cohort of mice evaluated. These demonstrated only mild weight loss and no other signs of sickness

(e.g. hunching, piloerection) or sudden death before 120 days. Accordingly it was anticipated that investigation of the phenotype at ~ 100 days would permit sufficient time for emergence of left ventricular dysfunction, but precede the period of frank symptomatic decompensation with heart failure. Subsequently, however, it was found that some of the *Fh1*$^{f/f}$ *Cre/+* mice died before this selected phenotyping time point. Exclusion of some of the sickest mice from the *Fh1*$^{f/f}$ *Cre/+* dataset may introduce a degree of bias in the results such that the true severity of the *Fh1* null phenotype is under-represented, particularly with regard to invasive haemodynamic assessment. In retrospect, selection of an earlier phenotyping timepoint would have been helpful. To aid more precise decision making, serial non-invasive assessment of cardiac function by echocardiography would have been valuable. Furthermore, longitudinal assessment of cardiac function together with evaluation of energetic status by ^{31}P nuclear magnetic resonance spectroscopy may have identified whether the functional or energetic phenotype emerged first and hence shed light upon whether the cardiopmyopathy of *Fh1*$^{f/f}$ *Cre/+* mice results directly from, or is the consequence of, energetic compromise. A single earlier harvest time-point of 90-94 days for *Fh1*$^{f/f}$ *Hif-1α*$^{f/f}$ *Cre/+* mice and their littermate controls was used given that *Fh1*$^{f/f}$ *Hif-1α*$^{f/f}$ *Cre/+* mice were observed to die earlier than *Fh1*$^{f/f}$ *Cre/+* mice.

5 CHAPTER 5: METABOLIC MODULATION IN FH DEFICIENT HEARTS

5.1 Hypothesis and aims

The preceding chapter described the long term cardiac dysfunction associated with ablation of fumarate hydratase (*Fh1*) in the mouse heart. The focus of the work presented in the current chapter was to investigate the potential to modulate the cardiac phenotype of *Fh1* null mice by pharmacological inhibition of key metabolic pathways predicted by *in silico* analysis and/or cancer studies to have augmented flux in the absence of *Fh1*.

Specifically, in *Fh1* deficient hearts, replenishment of tricarboxylic acid (TCA) cycle oxaloacetate (an intermediate downstream of the ablated FH enzyme) by conversion of pyruvate to malate by malic enzyme, followed by oxidation of malate to oxaloacetate by malate dehydrogenase, is predicted to be beneficial. Furthermore, as described in Chapter 4, nuclear factor (erythroid-derived 2)-like 2 (NRF2) signalling was found to be upregulated in *Fh1* knockout hearts. Several NRF2 targets genes encode for enzymes in the pentose phosphate pathway (PPP) – a key cellular anabolic pathway involved in the production of NADPH for reductive biosynthesis. This finding suggests that the production of reducing equivalents by the PPP will be increased in *Fh1* null hearts. Should this up regulation represent a maladaptive response, the increased reducing equivalent represents a potential target for drug manipulation.

Accordingly, the key hypotheses of this chapter are:

i. The replenishment of malate/oxaloacetate through the activity of malic enzyme is a critical cellular adaptive mechanism in *Fh1* null hearts, such that even transient interruption will exacerbate the associated cardiac dysfunction.

ii. Inhibition of the PPP will ameliorate the *Fh1* knockout cardiac phenotype through alleviation of reductive stress.

Consequently, the aims of this chapter are:

i. To determine the effect of malic enzyme inhibition in *Fh1* null MEFs and upon cardiac function in cardiac-specific *Fh1* knockout mice

ii. To examine the ability of inhibition of PPP to ameliorate the cardiac *Fh1* knockout chronic phenotype.

5.2 Results

5.2.1 Flux-balance analysis of cardiac mitochondrial metabolism in the absence of Fh1

Flux balance analysis (FBA) was performed by Dr Anthony Smith using the *iAS253* model of the human heart mitochondrion[195]. This model uses the MitoMiner database which integrates experimental data indicating mitochondrial localisation with metabolic pathway data. The partitioning of metabolites into the mitochondrial matrix or cytosol is taken into account in this model and as there is no known specific fumarate transporter constraints were placed upon the flow of fumarate between compartments[166]. Where there is evidence to suggest that metabolic reactions in a given direction are irreversible or thermodynamically unfavourable directionality constraints were applied and the objective function of the mitochondrion was set as maximal ATP production.

This FBA modelling suggests a partial TCA cycle in *Fh1* null cardiomyocytes that is supplemented by increased anaplerosis of amino acids. Specifically, glutamate and proline are predicted to enter the TCA cycle as 2-oxoglutarate, whilst aspartate is predicted to enter the TCA cycle via transamination of aspartate to oxaloacetate with subsequent conversion to malate and import into the mitochondria through the malate-aspartate shuttle. Importantly, this would allow replenishment of the oxaloacetate pool available to condensate with acetyl coenzyme A, facilitating an additional turn of the traditional TCA cycle wheel. Augmentation of other anaplerotic mechanisms to regenerate the oxaloacetate pool is also predicted in this model, for example the conversion of pyruvate to oxaloacetate by pyruvate carboxylase, utilising a bicarbonate ion and ATP.

Traditionally, malic enzymes catalyse the conversion of malate to pyruvate, reducing $NAD(P)^+$ to NADPH and releasing carbon dioxide. However, there is evidence to suggest

that this reaction can be reversed in the myocardium to produce malate from pyruvate[274-276]. This process is particularly likely to occur in the context of Fh1 ablation with a predicted increase in NADPH availability via enhanced PPP flux. Following this, malate dehydrogenase can convert this malate to oxaloacetate, thus maintaining the oxaloacetate pool and producing an NADH reducing equivalent that can be utilised by the electron transport chain to generate ATP. Whilst this route of oxaloacetate production is preferred over the ATP consuming pyruvate carboxylase reaction both routes may in fact be active *in vivo*. A further consideration of the model is how accumulated cellular fumarate is removed. This FBA model predicts that succinyl co-A (which is two steps before fumarate in the TCA cycle) is removed through the haem biosynthesis and degradation pathways. However, it would be energetically more favourable to remove carbon later in the TCA cycle. This may be achieved through partial reversal of the urea cycle and the purine nucleotide cycles, generating argininosuccinate and adenylosuccinate respectively.

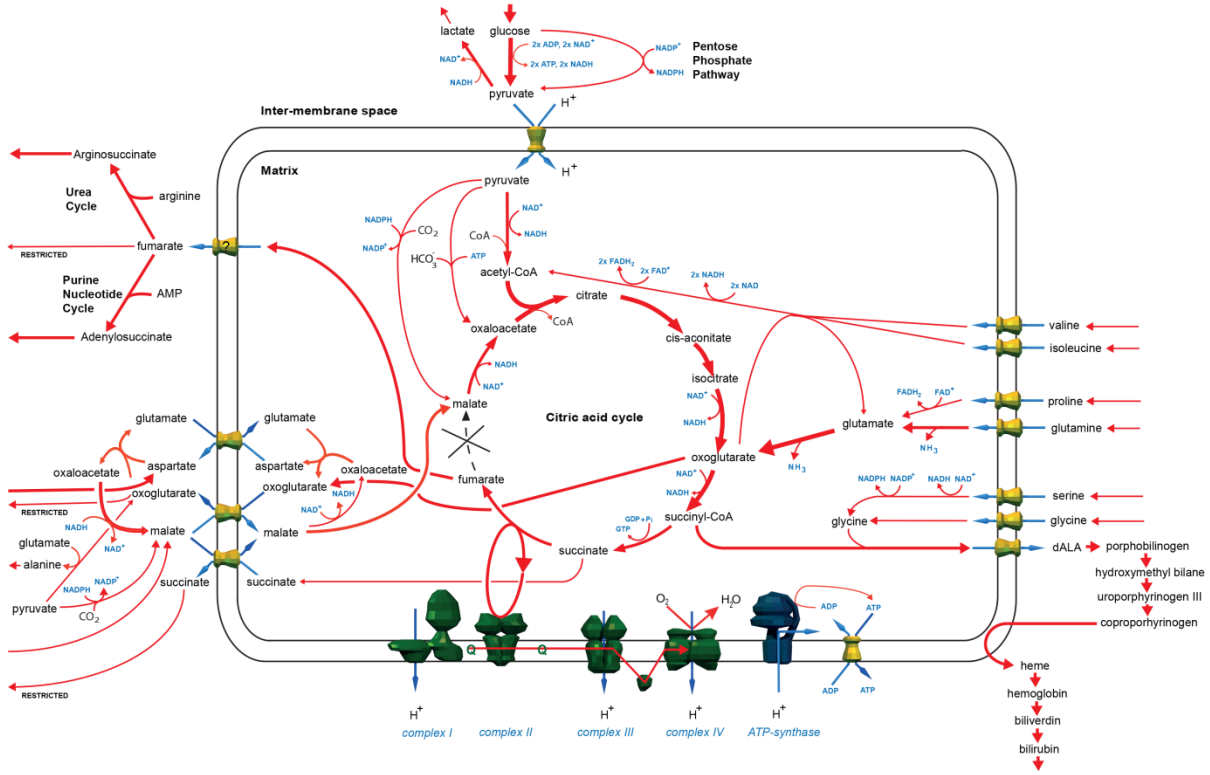

Figure 59 – A flux-balance analysis simulation of myocardial mitochondrial metabolism in the absence of FH
Note in particular the predicted: elevation of glutamine anaplerosis; the conversion of pyruvate to malate.

5.2.2 Metabolomic assessment of metabolites levels in Fh1$^{f/f}$ and Fh1$^{f/f}$ Cre/+ hearts

Fourier transform ion cyclotron resonance (FT-ICR) mass spectrometry and subsequent statistical analysis was performed by Dr Warrick Dunn at the University of Birmingham. This revealed substantial metabolic differences between *Fh1$^{f/f}$* and *Fh1$^{f/f}$ Cre/+* hearts. In accordance, with FBA prediction of inhibition or even reversal of the urea cycle by fumarate accumulation, argininosuccinic acid was more than 3-fold elevated in *Fh1$^{f/f}$ Cre/+* hearts comparative to *Fh1$^{f/f}$*. Likewise, adenylo-succinate and succinyl adenosine were significantly increased, suggestive of inhibition or reversal of the purine nucleotide cycle. The second most highly elevated metabolite was putatively identified as phosphoribosylaminoimidazolesuccinocarboxamide (SAICAR). In addition to its role converting adenylosuccinate to AMP and fumarate in the purine nucleotide cycle, adenylosuccinate lyase cleaves SAICAR to generate fumarate and 5-Aminoimidazole-4-

carboxamide ribonucleotide (AICAR). This reaction may feasibly be inhibited by end-product inhibition by accumulated fumarate.

5.2.3 Malic enzyme expression

There are 3 isoforms of malic enzyme: Me1, which is cytosolic and $NADP^+$-dependent; Me2, which is mitochondrial and NAD^+-dependent; and Me3, which is mitochondrial and $NADP^+$-dependent. As previously described, FBA suggested that a conversion of pyruvate to malate (in the reverse of the traditional reaction utilising NADPH) by malic enzyme was likely to occur in the *Fh1* knockout heart to replenish malate and oxaloacetate levels. The analysis suggested that the NADPH-dependent forms of malic enzyme were most likely to perform this step. In addition, it revealed that it was more favourable for this step to occur in the cytoplasm since import of pyruvate into the mitochondria is proton-coupled, which would therefore otherwise dissipate the proton motive force. Accordingly, based on insights provided by this model, Me1 is likely to be central to replenishment of the second span (after Fh1) of the TCA cycle in the *Fh1* knockout heart.

Elevation of malic enzyme 1 (*Me1*) RNA expression in *Fh1-/-* mouse embryonic fibroblasts (MEFs) relative to wildtype has previously been described [144]. In 5 week old $Fh1^{-/-}$ *Cre/+* hearts, *Me1* transcript was similarly increased (Figure 60A). In contrast, in aged (105 days) $Fh1^{-/-}$ *Cre/+* hearts *Me1* mRNA was actually reduced compared to $Fh1^{f/f}$ controls (Figure 60B).

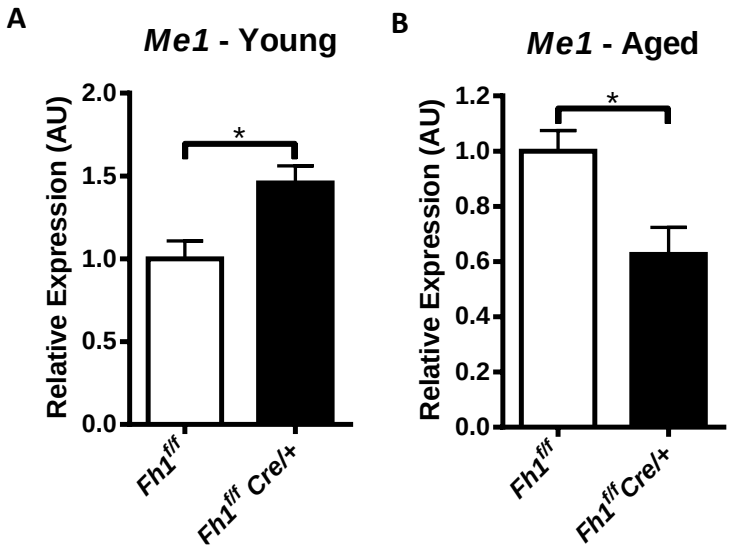

Figure 60 – Me1 transcript expression is elevated in young but decreased in old *Fh1$^{f/f}$ cre/+* hearts
Relative expression in arbitary units of malic enxyme 1 (*Me1*) normalised to Fh1$^{f/f}$. **A.** Young (5 weeks old) hearts. **B.** Aged (105 day old) hearts.

5.2.4 Knockdown and inhibition of Me1 in MEFs

To further investigate the role of Me1 in the context of Fh1 deletion, siRNA was utilised to knockdown expression of *Me1* in *Fh1$^{+/+}$* and *Fh1$^{-/-}$* MEFs. Consistent with published data, qRT-PCR assessment of gene expression revealed *Me1* expression to be 3-fold higher in *Fh1$^{-/-}$* MEFs treated with non-targeting siRNA compared to similarly treated *Fh1$^{+/+}$* MEFs (Figure 61A). Greater than 99 % and 91 % reduction in *Me1* transcript levels were achieved in *Fh1$^{+/+}$* and *Fh1$^{-/-}$* MEFs, respectively. Furthermore, 97.5 % and 92.5 % knockdown of the control gene cyclophilin B (*Ppib*) was also achieved in *Fh1$^{+/+}$* and *Fh1$^{-/-}$* MEFs, respectively (Figure 61B). In order to investigate the effect of Me1 knockdown on proliferation of these *Fh1$^{+/+}$* and *Fh1$^{-/-}$* MEFs, a water-soluble tetrazolium salt (WST-8) based calorimetric cell counting assay was performed 48 hours after siRNA transfection. However, no significant difference in cell numbers was observed between groups (Figure 61C).

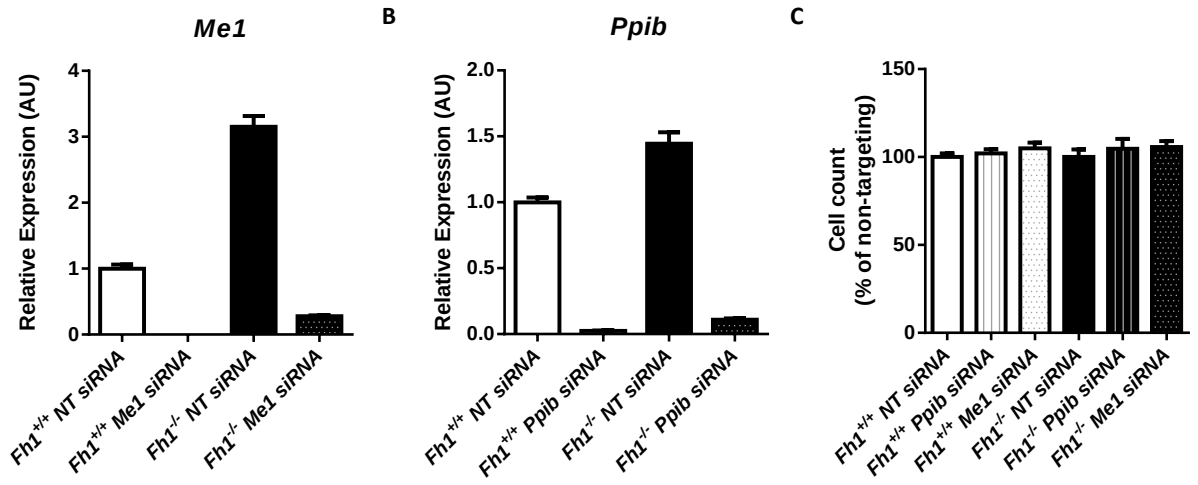

Figure 61 – Knockdown of Me1 and Ppib in *Fh1*$^{+/+}$ and *Fh1*$^{-/-}$ mouse embryonic fibroblasts
Expression of **A.** *Me1* Malic enzyme 1 **B.** *Ppib* depicted in arbitary units assessed by qRT-PCR. **C.** Cell count assessed by water-soluble tetrazolium salt calorimetric assay.

Although 91 % *Me1* transcript knockdown was achieved with siRNA-induced gene silencing in *Fh1*$^{-/-}$ MEFs, the residual transcript expression level was still equivalent to 28 % that of wildtype. Although not formally interrogated, it is likely that the corresponding protein levels are even higher and may be sufficient to catalyse the conversion of pyruvate to malate. Interestingly, fumarate acts as an allosteric activator of malic enzyme[277], hence it is possible that despite the reduction in Me1 levels by siRNA treatment, any Me1 present may be more active due to fumarate accumulation in Fh1 knockout tissue. It is also conceivable that Me3 could catalyse the conversion of pyruvate to malate. Accordingly, a decision was made to utilise pharmacological inhibition of the malic enzymes and malate dehydrogenase with the compound tartronic acid to better delineate the role played by this enzyme in the setting of Fh1 deficiency[274, 277]. When *Fh1*$^{+/+}$ and *Fh1*$^{-/-}$ MEFs were treated with 10 mM tartronic acid for 48 hours, cell counts (assessed by WST8 proliferation assay normalised to untreated cell counts) were significantly lower for *Fh1*$^{-/-}$ MEFs than *Fh1*$^{+/+}$ MEFs. Supporting this finding, trypan blue staining revealed reduced viable cell counts for tartronic acid treated *Fh1*$^{-/-}$ MEFs compared to *Fh1*$^{+/+}$ MEFs.

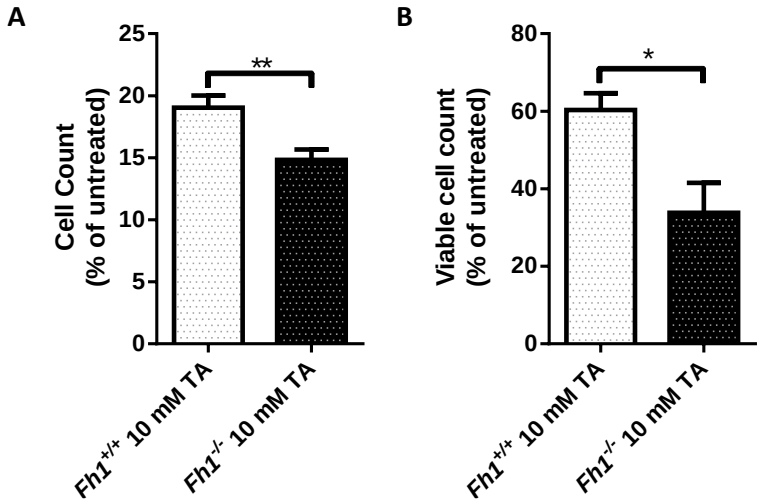

Figure 62 – Tartronic acid is more lethal to *Fh1*$^{-/-}$ MEFs than *Fh1*$^{+/+}$ MEFs
A. Cell count assessed by water-soluble tetrazolium salt calorimetric assay and normalised to untreated. **B.** Viable cell count assessed by trypan blue staining and normalised to untreated.

5.2.5 Tartronic acid treatment of Fh1$^{f/f}$ *and Fh1*$^{f/f}$ *Cre/+* mice

To investigate the role of malic enzyme in cardiac Fh1 deletion *in vivo*, *Fh1*$^{f/f}$ and *Fh1*$^{f/f}$ *Cre/+* mice aged 41-47 were treated with saline or the malic enzyme inhibitor, tartronic acid by intraperitoneal injection for 6 days. Cardiac function was then assessed by invasive haemodynamic pressure recording. The only significant difference in cardiac function was an improvement in the relaxation rate of control *Fh1*$^{f/f}$ mice treated with tartronic acid. Potentially supporting this signal was the trend toward reduced end-diastolic pressure in this group. Even at this younger age there was a trend, sometimes significant, towards increased absolute and normalised heart weight in the *Fh1*$^{f/f}$ *Cre/+* groups compare to *Fh1*$^{f/f}$ controls. However, no differences with tartronic acid treatment were observed between genotypes, including no significant differences in absolute or normalised lung weights to suggest pulmonary congestion.

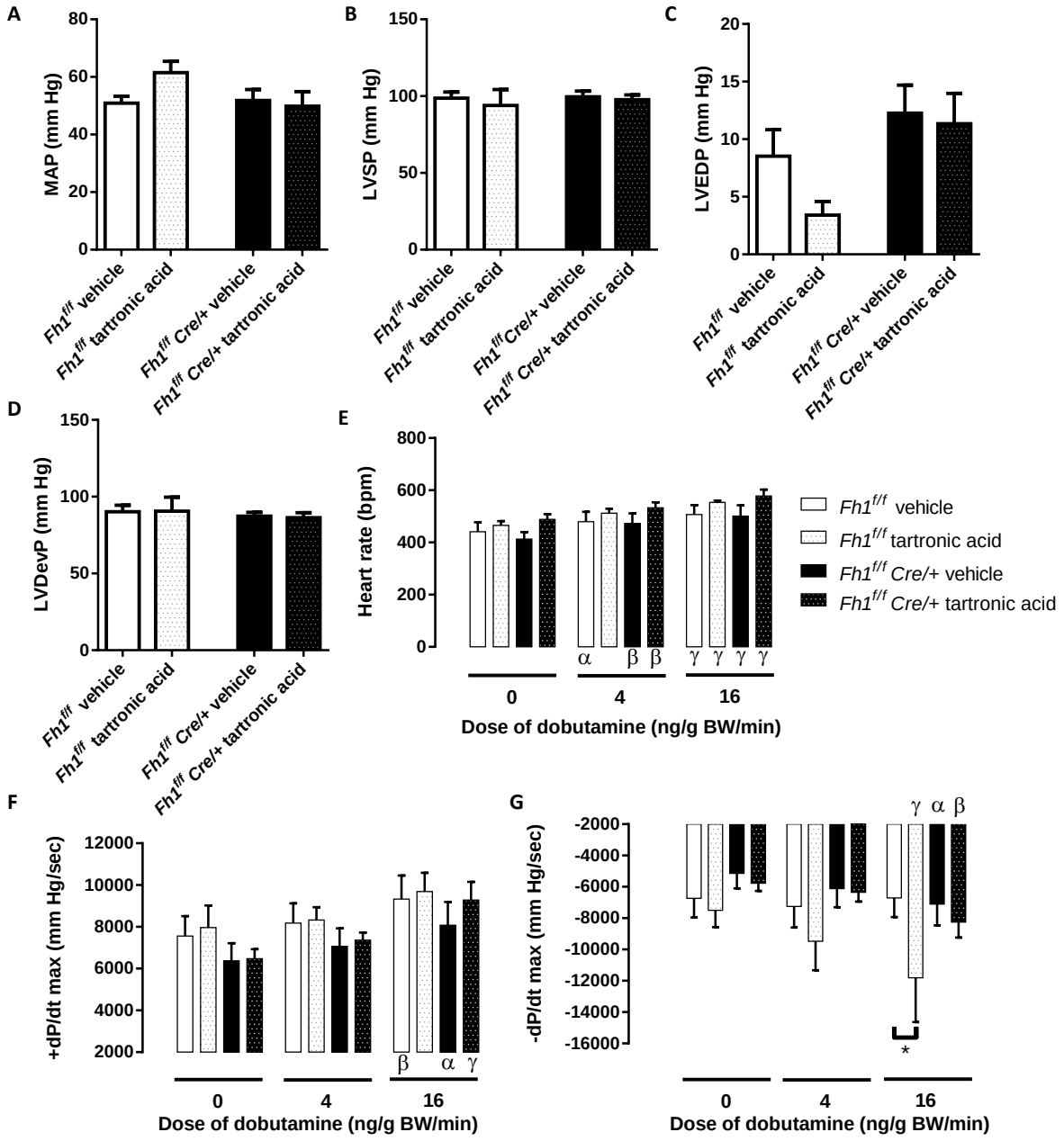

Figure 63 – Invasive haemodynamic assessment of cardiac function of TA treated *Fh1* null mice
A. Mean arterial pressure (MAP) in millimetres of mercury (mm Hg). **B.** Basal left ventricular systolic pressure (LVSP). **C.** Basal left ventricular end-diastolic pressure (LVEDP). **D.** Left ventricular developed pressure (LVDevP). **E.** Heart rate in beats per minute (bpm). Dobutamine dose infused is given in nanograms per gram body weight per min (ng/g BW/min). **F.** The maximal rise in left ventricular pressure with time (+dP/dt) and **G.** the maximal decrease in systolic pressure with time (-dP/dt), both measured in millimetres of mercury per second (mm Hg/sec). * $p<0.05$, α $p<0.05$ compared to no dobutamine, β $p<0.01$ compared to no dobutamine. γ $p<0.001$ compared to no dobutamine.

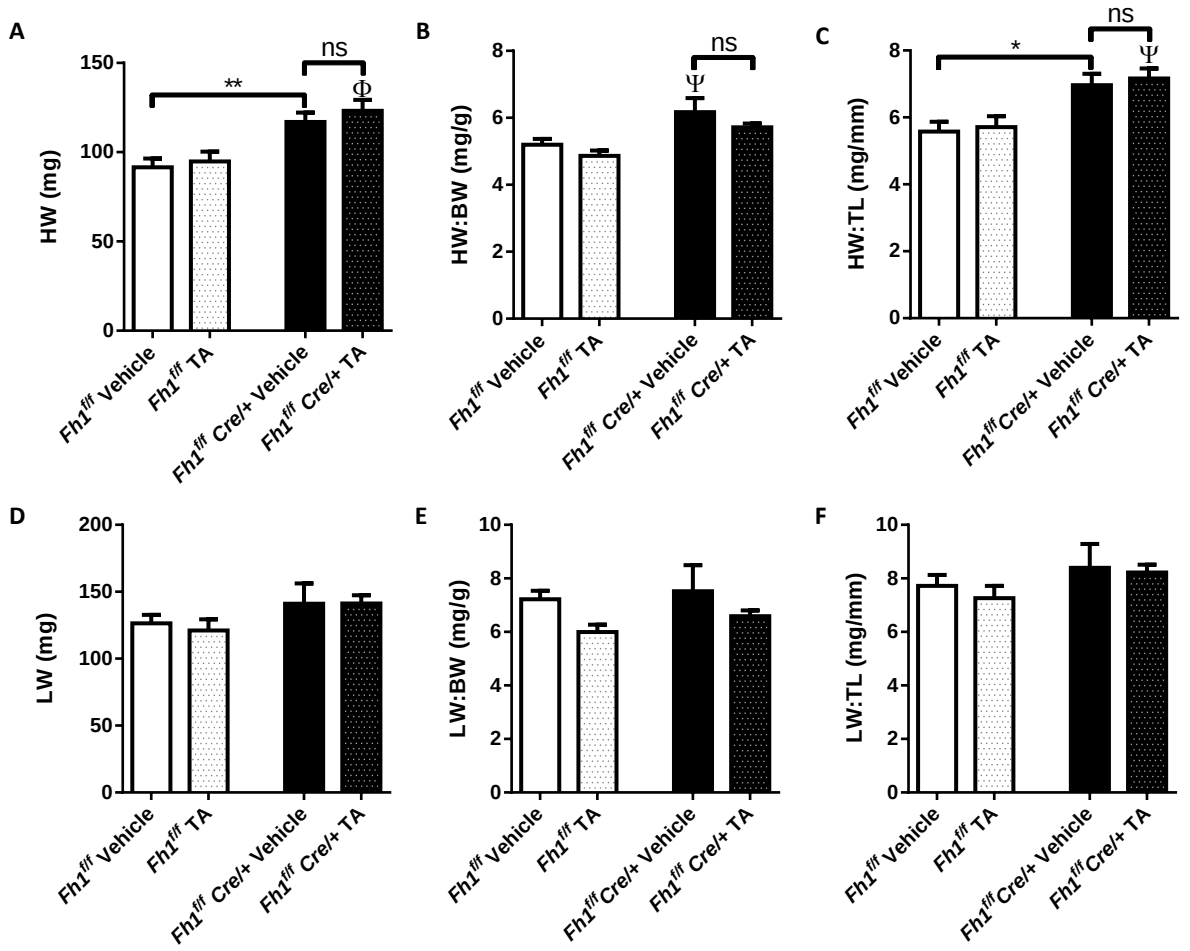

Figure 64 – Absolute and normalised heart and lung weights after tartronic acid treatment
A. Heart weight (HW). **B.** Heart weight to body weight ratio (HW:BW). **C.** Heart weight to tibial length ratio (HW:TL). **D.** Lung weight (LW). **E.** Lung weight to body weight ratio. **F.** Lung weight to tibial length ratio. *p<0.05 between indicated groups. **p<0.01 between indicated groups. ψ p<0.05 compared to all groups except indicated. Φ p<0.01 compared to all groups except indicated.

5.2.6 A reductive environment in Fh1$^{f/f}$ Cre/+ hearts

Published data and findings presented in Chapter 4 indicate activation of Nrf2 signalling in the *Fh1* null heart[166]. Such Nrf2-mediated induction of the antioxidant response is likely to tilt the redox balance of the Fh1 knockout myocardium to create a reductive environment. Specifically, generation of NADPH reducing equivalents by increased flux through the pentose phosphate pathway (PPP) is likely to contribute to this reductive milieu. Indeed, Yang et al utilised radioisotope tracer studies to demonstrate increased flux through the oxidative arm of the PPP in an FH-deficient cancer cell line[278]. In support of increased flux through the PPP in our model, qPCR revealed that transcript levels of glucose-6-phosphate

dehydrogenase (*G6pdx*), encoding the rate-limiting enzyme of the PPP, were significantly elevated in *Fh1*$^{f/f}$ *Cre/+* hearts comparative to *Fh1*$^{f/f}$ controls (Figure 65A). Furthermore, reactive oxygen species (ROS) assessed by lucigenin chemiluminescence were reduced in hearts of *Fh1*$^{f/f}$ *Cre/+* mice to less than half that of *Fh1*$^{f/f}$ control hearts (Figure 65B). Tissue levels of malondialdehyde, a product of lipid peroxidation, are often used as a correlate of oxidative stress[279]. In accordance with a reductive environment, cardiac tissue malondialdehyde was observed to be significantly reduced in *Fh1*$^{f/f}$ *Cre/+* cardiac tissue compared to *Fh1*$^{f/f}$ controls (Figure 65C).

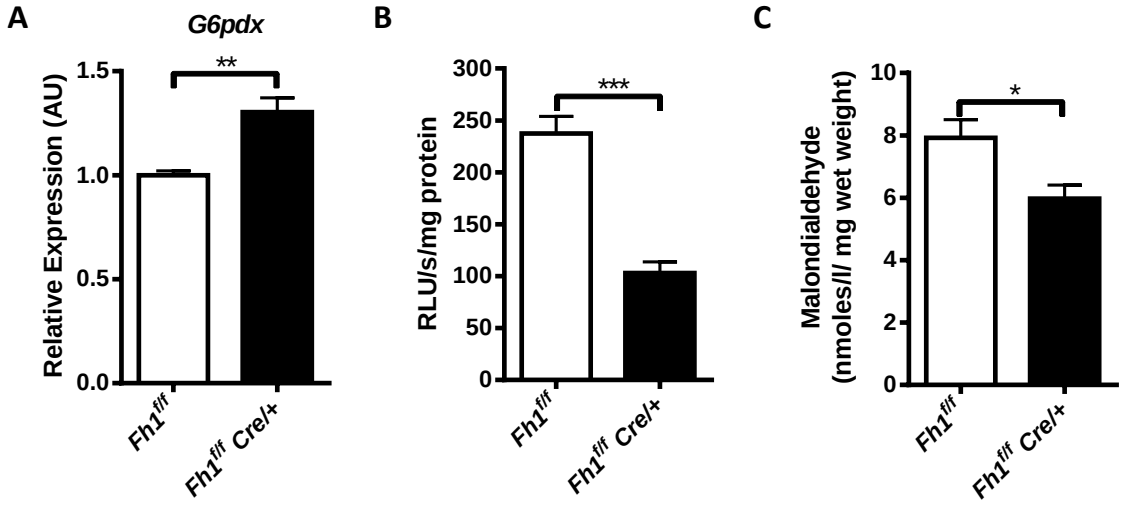

Figure 65 – Evidence of a reductive environment in *Fh1*$^{f/f}$ *Cre/+* hearts
A. Relative expression in arbitrary units of glucose-6-phosphate dehydrogenase (*G6pdx*) assessed by qPCR. **B.** Reactive oxygen species (ROS) in cardiac tissue assessed by lucigenin chemiluminescence and expressed as relative light units per second per mg of protein. **C.** Cardiac tissue malondialdehyde content normalised to tissue wet weight.

5.2.7 Inhibition of the pentose phosphate pathway rescues the Fh1$^{f/f}$ *Cre/+ phenotype*

A causative role for reductive stress has been identified in the development of cardiac dysfunction in a model of protein aggregate cardiomyopathy[245]. Given that flux through the PPP – a major source of reducing equivalents – is predicted to be elevated in *Fh1* null hearts, it was hypothesised that inhibition of this pathway may have a beneficial therapeutic effect upon the cardiomyopathy of *Fh1* knockout mice. To address this, *Fh1*$^{f/f}$ and *Fh1*$^{f/f}$ *Cre/+* mice

were treated with the glucose-6-phosphate dehydrogenase inhibitor, dehydroepiandrosterone (DHEA), from age 40 days until euthanasia aged 102-106 days.

Echocardiographic assessment of cardiac function and dimensions at 100-105 days revealed no significant effect of DHEA compared to vehicle treatment in *Fh1*$^{f/f}$ control mice. However, there was a significant improvement in cardiac function in DHEA treated *Fh1*$^{f/f}$ *Cre/+* mice compared to vehicle treated *Fh1*$^{f/f}$ *Cre/+* mice (Figure 66 A-D). In particular, both LV end-systolic dimension (LVESD) and volume (LVESV) were significantly reduced by DHEA treatment in *Fh1*$^{f/f}$ *Cre/+* mice, although still higher than *Fh1*$^{f/f}$ control mice. Both ejection fraction and radial peak systolic velocity of the LV posterior wall were increased by DHEA treatment of *Fh1*$^{f/f}$ *Cre/+* mice, albeit not to the levels observed in *Fh1*$^{f/f}$ control mice. The marked LV dilatation observed in vehicle-treated *Fh1*$^{f/f}$ *Cre/+* mice was significantly reduced by DHEA treatment, as signified by reduced LV end-diastolic dimension and volume (Figure 66 E and F). In addition, DHEA treatment significantly reduced the cardiac hypertrophy of *Fh1*$^{f/f}$ *Cre/+* mice, as indicated by reduction in calculated left ventricular mass, albeit not to *Fh1*$^{f/f}$ control levels.

Consistent with the findings from echocardiography, invasive haemodynamic assessment also demonstrated significant amelioration of cardiac function in *Fh1*$^{f/f}$ *Cre/+* mice in response to DHEA treatment (Figure 67). Baseline LV systolic and developed pressures were significantly increased in *Fh1*$^{f/f}$ *Cre/+* mice treated with DHEA. The maximal rate of cardiac contraction both at baseline and in response to low or high dose dobutamine were also elevated by DHEA treatment of *Fh1*$^{f/f}$ *Cre/+* mice. Of note, DHEA treatment restored the ability of *Fh1*$^{f/f}$ *Cre/+* mice to increase their maximal rate of cardiac contraction in response to high dose dobutamine and even significantly increased this parameter in *Fh1*$^{f/f}$ controls.

However, DHEA treatment of *Fh1*$^{f/f}$ *Cre/+* mice had no effect upon parameters indicative of diastolic function: LV end-diastolic pressure and the maximal rate of cardiac relaxation (-dP/dt_{max}). A significant increase in LV end-diastolic pressure was observed in *Fh1*$^{f/f}$ controls, suggesting that DHEA could be detrimental to diastolic function.

Concordant with the echocardiographic and invasive haemodynamic data, *ex vivo* morphometric indices demonstrated amelioration of the *Fh1*$^{f/f}$ *Cre/+* cardiac phenotype by DHEA treatment. Consistent with the decrease in LV mass demonstrated by echocardiography, both absolute and normalised *ex vivo* heart weight were significantly reduced by DHEA treatment in *Fh1*$^{f/f}$ *Cre/+* mice. Furthermore, DHEA treatment reduced the absolute and normalised wet lung weights of *Fh1*$^{f/f}$ *Cre/+* mice, suggesting that DHEA treatment reduced pulmonary congestion and heart failure in these mice. Histological assessment of DHEA-treated *Fh1*$^{f/f}$ *Cre/+* hearts revealed a trend towards improvement in levels of interstitial fibrosis compared to *Fh1*$^{f/f}$. Figure 69 shows representive Sirius red stained sections (n=2, 3 images per heart).

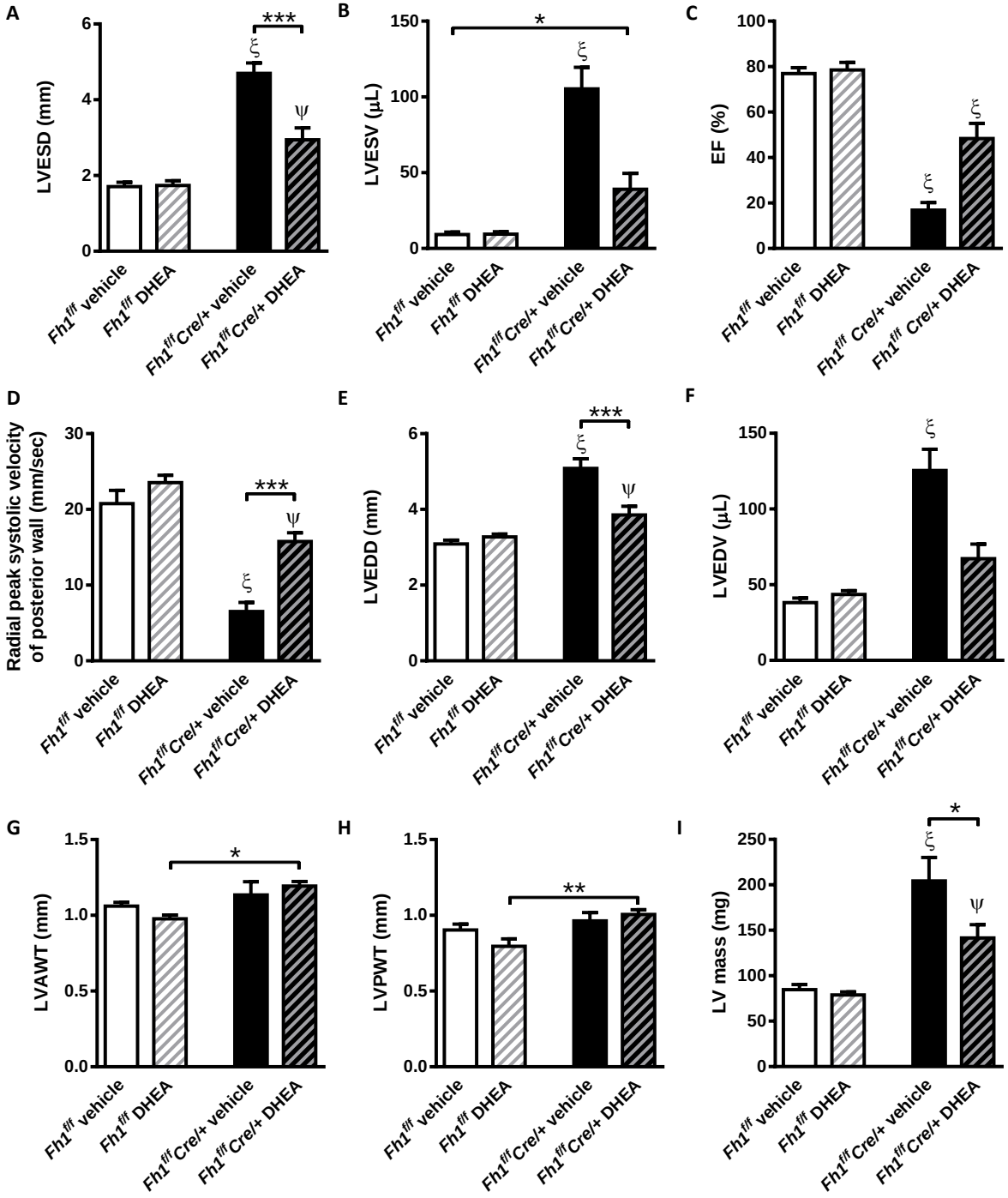

Figure 66 – Echocardiographic assessment of cardiac function reveals amelioration of the *Fh1$^{f/f}$ Cre/+* phenotype by DHEA treatment

A-D. Measures of cardiac systolic function: **A.** Left ventricular end-systolic dimension (LVESD); **B.** Left ventricular end-systolic volume (LVESV); **C.** Ejection fraction (EF); **D.** Radial peak systolic velocity of the LV posterior wall. **E and F.** Measures of cardiac dilatation: **E.** Left ventricular end-diastolic dimension (LVEDD); **F.** Left ventricular end-diastolic volume (LVEDV). **G-I.** Measures of cardiac hypertrophy: **G.** Left ventricular anterior wall thickness (LVWAT); **H.** Left ventricular posterior wall thickness (LVPWT); **I.** Left ventricular mass measured in milligrams (mg). * $p<0.05$ between indicated groups. ** $p<0.01$ between indicated groups. *** $p<0.001$ between indicated groups. Ψ $p<0.05$ compared to all groups except where indicated. ξ $p<0.001$ compared to all groups except where indicated.

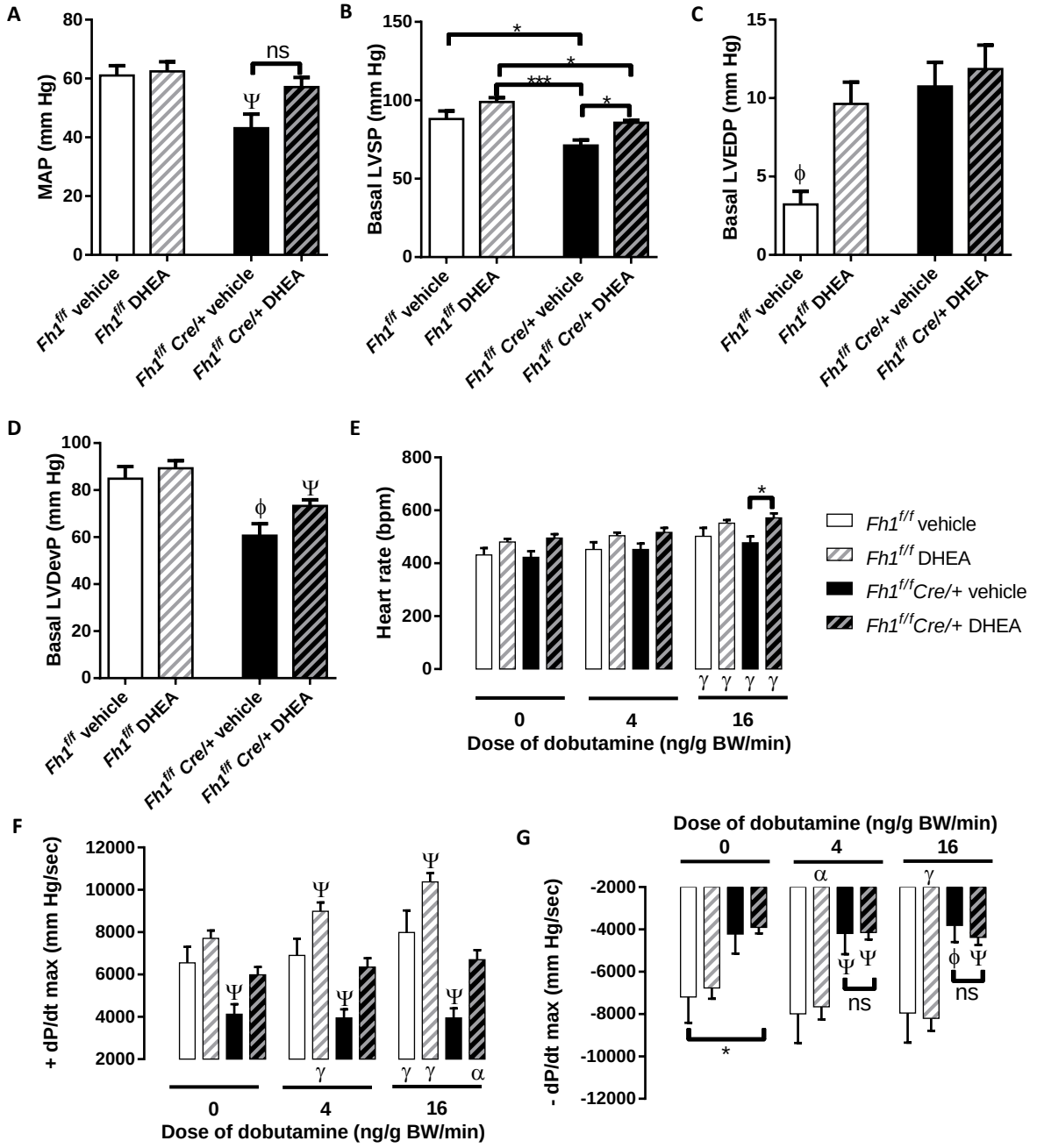

Figure 67 – Invasive cardiac haemodynamic assessment demonstrates improvement of left ventricular systolic function with DHEA treatment in *Fh1$^{f/f}$ Cre/+* mice

A. Basal mean aortic pressure (MAP) in millimetres of mercury (mm Hg). **B.** Basal left ventricular systolic pressure (LVSP). **C.** Basal left ventricular end diastolic pressure (LVEDP). Basal left ventricular developed pressure. (LVDevP). **E.** Heart rate in beats per minute (bpm) in response to dobutamine challenge (dobutamine dose infused is given in nanograms per gram body weight per min). **F.** The maximal rise in left ventricular pressure with time (+dP/dt). **G.** The maximal decrease in systolic pressure with time (–dP/dt)**.** * $p<0.05$ between indicated groups. ** $p<0.01$ between indicated groups. *** $p<0.001$ between indicated groups. ξ $p<0.001$compared to all groups except indicated. Φ $p<0.01$compared to all groups except indicated. Ψ $p<0.05$ compared all groups except indicated. α $p<0.05$ compared to no dobutamine. γ $p<0.001$ compared to no dobutamine.

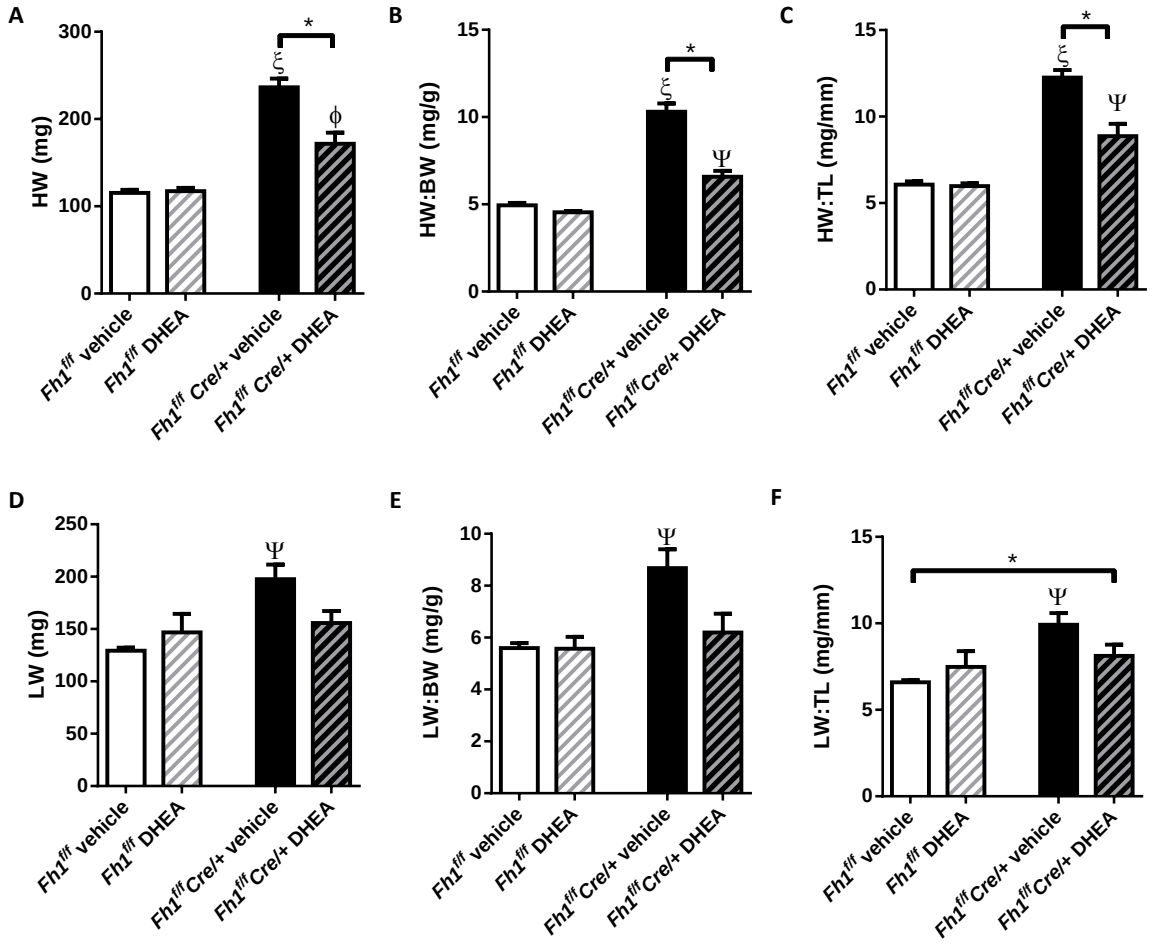

Figure 68 – *Ex vivo* organ weights reveal amelioration of the cardiac hypertrophy and pulmonary congestion of *Fh1$^{f/f}$ Cre/+* by DHEA treatment

A. Heart weight (HW) in milligrams (mg). **B.** Heart weight to body weight ratio (HW:BW) in milligrams/gram (mg/gram). **C.** Heart weight to tibial length ratio (HW:TL) in milligrams/millimetre (mg/mm). **D.** Lung weight. (LW). **E.** Lung weight to body weight ratio (LW:BW). **F.** Lung weight to tibial length ratio (LW:TL). * $p<0.05$ between indicated groups. Ψ $p<0.05$ compared to all groups except indicated. Φ $p<0.01$ compared to all groups except indicated. ξ $p<0.001$ compared to all groups except indicated.

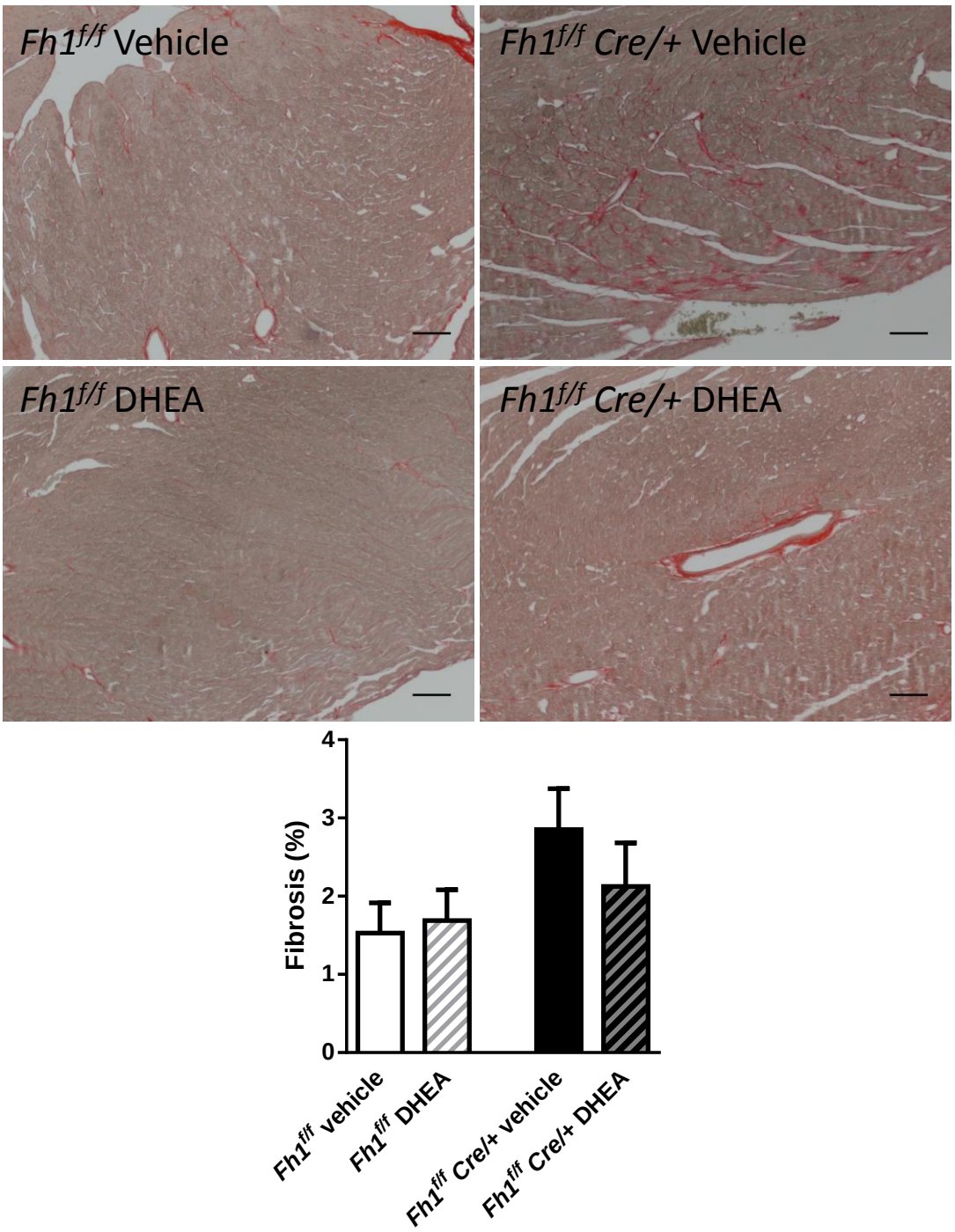

Figure 69 – Sirius red staining demonstrates amelioration of fibrosis in hearts of *Fh1$^{f/f}$ Cre/+* mice treated with DHEA

Representative images from vehicle- and DHEA-treated *Fh1$^{f/f}$* and *Fh1$^{f/f}$ Cre/+* mice. Scale bar = 100 µm. Graph demonstrates fibrosis assessed from Sirius red stained dark field images and expressed as a percentage of the total tissue area from corresponding bright field images.

5.3 Discussion

5.3.1 Summary of chapter findings

Using *Fh1* null MEFs and a cardiac-specific Fh1 knockout mouse line, the work presented in this chapter demonstrates that:

- Replenishment of the TCA cycle by anaplerosis in the *Fh1* knockout heart is predicted by flux balance analysis.
- Removal of excess fumarate through the haem biosynthesis and degradation pathway and incorporation into argininosuccinate and adenylosuccinate is likely.
- Argininosuccinic acid, adenylosuccinate, succinyl-adenosine and SAICAR accumulate in *Fh1* null hearts.
- Malic enzyme 1 (*Me1*) transcript levels are elevated in young but reduced in old *Fh1* null cardiac tissue.
- While treatment of cardiac-specific *Fh1* knockout mice with a malic enzyme inhibitor, tartronic acid (TA), does not affect cardiac function, TA is observed to be more toxic to *Fh1* null MEFs compared to wildtype MEFs.
- There is a reductive environment in $Fh1^{f/f}$ *Cre/+* hearts.
- Targeting of this reductive environment by inhibition of the pentose phosphate pathway using DHEA ameliorates the cardiomyopathy of $Fh1^{f/f}$ *Cre/+* mice.

Aspects of these principal findings, limitations of the present work and direction for future scientific enquiry are discussed in the following sections.

5.3.2 Concordance of flux balance analysis predictions with published data from cancer models

FBA identified a range of metabolic pathways predicted to be altered in the *Fh1* null heart. Altered flux through some of these pathways has previously been highlighted in *Fh1*-deficient cancer models. For example, the importance of increased flux through the haem degradation pathway was predicted and validated in FH deficient cells by Frezza *et al.*[165], whilst Adam *et al.* demonstrated anaplerosis of D5-labelled glutamate into the TCA, accumulation of label in fumarate and incorporation into argininosuccinate in Fh1 null MEFs (with neither fumarate accumulation nor label incorporation into argininosuccinate observed in wildtype MEFs)[180]. This is in accordance with the predicted reversal of the urea and purine nucleotide cycles observed with FBA and the accumulation of argininosuccinic acid, adenylosuccinate and succinyl adenosine observed by metabolomic analysis.

Given the considerable overlap in signalling pathways implicated in the growth and survival of cardiomyocytes and those relevant to cancer[280], applying insights gained from basic cancer studies, or the use of models developed to investigate tumour pathogenesis, is an attractive approach to understand mechanisms in cardiac hypertrophy and failure. Notably, characteristic metabolic features of cancer cells, such as increased aerobic glycolysis (the Warburg effect) and glutaminolysis, also occur in cardiac hypertrophy states[281]. In line with this, experiments using Fh1 deficient cells and tissues have identified a coordinate change in glycolytic and biosynthetic gene expression favouring cellular proliferation and aerobic glycolysis[144].

Germline mutations in the gene encoding fumarate hydratase result in a cancer syndrome (hereditary leiomyomatosis and renal cell carcinoma). Observed in this light, the

identification of changes in both gene expression and metabolomics profile in the existing cardiac Fh1 knockout overlapping those of the reported cancer models is a self-fulfilling prophecy and not unexpected. Specifically with regards to changes in gene expression, a systematic assessment of the cardiac transcriptome, e.g. by microarray or RNASeq, may avoid an over-reliance on target genes and pathways identified in studies of the biology of cancer associated with FH deficiency and allow an unbiased assessment of differential gene expression resulting from cardiac *Fh1* deficiency.

5.3.3 Metabolomics approach

A non-hypothesis driven approach to determine the effect of cardiac Fh1 deficiency on cardiac metabolite profile was undertaken using mass spectrometry. Compared to other systems biology approaches, metabolomics is regarded as being temporally and functionally closer to disease phenotypes and effectively reflect the convergence of multiple gene networks and metabolic pathways into a relatively small number (several thousand) of conserved small-molecule metabolites[282]. While an inherently attractive approach, particularly in a model of TCA cycle disruption which is anticipated to result in profound changes to the cardiac metabolome, metabolomics – particularly with a single chemical analytic approach – has limitations related to the extreme chemical diversity of molecular species present in tissue (molecular weight, charge and polarity) and its bias to identifying metabolites which are highly abundant, more readily processable and/or non-labile[282]. Many metabolites in central metabolic pathways are recognised as being low in abundance and having a high turnover rate, resulting in reduced detection of the metabolite even with rapid metabolic quenching[283]. Tissue samples, in particular, are regarded as amongst the most complex and technically difficult to extract, with muscle tissue notably less easy to disrupt adequately to release intracellular metabolites[284].

In the present study, Fourier transform ion cyclotron resonance (FT-ICR) mass spectrometry was utilised to assess the cardiac metabolome of *Fh1*$^{f/f}$ *Cre/+* mice. Based on the measurement of the frequency of rotation of an ion in a magnetic field (known as the cyclotron frequency) enabling calculation of the ion mass to charge ratio (*m*/*q*), FT-ICR mass spectrometry is regarded as possessing amongst the highest measurement and resolution accuracy for complex mixture chemical analysis without the need for prior chromatographic separation[285, 286]. In the current study, use of an internal standard, e.g. sample spiking with isotopically labelled selected metabolite(s), may have aided internal mass calibration and increased confidence in the detection of TCA cycle intermediates[285].

Although FT-ICR mass spectrometry is highly sensitive, ion-ion interactions can significantly reduce its dynamic range[287]. Standard acquisitions of FT-ICR mass spectrometry are recognised to fail to observe sample constituents at <0.01% abundance[285]. Accordingly, use of a more targeted metabolomics strategy with specific sample extraction, separation/ionisation method and analysis techniques designed to isolate lower abundance classes of metabolites could improve the current experiment's dynamic range and yield highly specific information on a smaller number of metabolites[285] albeit at the expense of breadth of coverage. The use of a 'semi-targeted' approach using multiple reaction monitoring on a triple quadrupole mass spectrometers to detect a more limited number of metabolites from several metabolic pathways/chemical classes has been suggested[284, 288]. Alternative experimental workflows including *O*-benzylhydroxylamine derivatization followed by liquid chromatography-tandem mass spectrometry have been reported to robustly detect and quantify all TCA cycle intermediates from aqueous solution without the need for prior phase transfer (as in the current study), reducing the risk of analyte loss and improving ionisation sensitivity and behaviour[289].

5.3.4 Beyond in silico metabolic network modelling – direct flux measurement

The assessment of metabolite concentrations and, more indirectly, the measurement of transcript levels for key/rate-limiting genes in central metabolic pathways (e.g. the levels of *G6pdx* encoding the rate-limiting enzyme of the PPP) can provide insight into the mechanistic link between the Fh1 null genotype and the resulting cardiac phenotype. Nevertheless, ultimately, both these and other approaches (e.g. proteomics) are static measurements and only indirect markers for metabolic pathway activity which reflects the complex and dynamic interaction between altered gene expression, protein levels, enzymatic activity and metabolite abundance[283]. A more precise depiction of the cell's metabolic state can be obtained by using 'fluxomics', an integrated approach of computational modelling and stable isotope labelling to estimate *in vivo* pathway flux.

Given that several NRF2 targets genes encode for enzymes in the pentose phosphate pathway (PPP), the functional effect of the observed upregulation of NRF2 signalling on central metabolic networks in *Fh1* knockout hearts could be tested directly by studying metabolic flux using stable isotope labelling. By having the same number of protons, stable isotopes share the same physical and chemical properties with their related common elements, but differ in the number of neutrons, They include several isotopes commonly occurring in biomolecules, e.g. ^{2}H, ^{13}C, ^{18}O and ^{15}N [290, 291]. The two most widely used analytic approaches to identify and quantify metabolites are nuclear magnetic resonance (NMR) spectroscopy and mass spectrometry (MS)[292]. While the technique of NMR spectroscopy is non-destructive, it is limited to the detection of isotopes possessing an odd number of nucleons only[290], whereas MS can detect all isotopes and readily distinguish metabolites containing stable isotopes (isotopologs) by virtue of the *m*/*z* ratio[291].

One approach to flux experiments for the current work is to utilise *ex vivo* perfusion in non-recirculating mode of *Fh1*$^{f/f}$ *Cre/+* and WT control hearts with ^{13}C-labelled metabolic substrates, coupled with detection of key downstream labelled and unlabelled metabolites by MS[293]. The natural abundance of the heavy isotope compared to the corresponding element has to be considered when quantifying metabolite isotopologs, which in the case of ^{13}C is 1.11% [291]. A range of choices of tracers can be used for metabolic flux analysis, but usually include common substrates such as ^{13}C-glucose and ^{13}C-glutamine, and rely on pathway-specific carbon skeleton rearrangements of the original substrate[290]. Employing the commonly utilised [1-^{13}C]glucose, metabolism of 3 units of [1-^{13}C]glucose via glycolysis will produce 3 molecules of pyruvate and 3 molecules of [1-^{13}C]pyruvate, while metabolism purely via the PPP will lead to loss of tracer as CO_2 and 5 molecules of unlabelled pyruvate only[290]. Using tumour cell lines, Metallo and colleagues[294] identified [1,2-^{13}C2]glucose as the optimal tracer for glycolysis and the PPP, outperforming the commonly used [1-^{13}C]glucose. Alternatively, [2,3,4,5,6-^{13}C]glucose has been identified as an optimal ^{13}C tracer for assessing PPP flux in mammalian cells[295].

To directly assess the fate of mitochondrial pyruvate in the *Fh1*$^{f/f}$ *Cre/+* heart and directly test the FBA model predictions of augmented pyruvate conversion into oxaloacetate and malate, the tracer [U-^{13}C]pyruvate could be used to enter the TCA cycle via decarboxylation to acetyl-CoA or through anaplerotic carboxylation via pyruvate carboxylase to oxaloacetate and/or conversion to malate. Such an approach has been used in patient fibroblast cell lines to infer the relative partitioning of pyruvate between decarboxylation and anaplerotic reactions from ^{13}C enrichment of the TCA intermediates and related metabolites, e.g. citrate, malate and aspartate[296]. Alternatively, based on ^{13}C metabolic flux analysis in tumour cell lines, ^{13}C glutamine tracers (such as [1,2]Gln, [3,4]Gln or [U]Gln) have been proposed to optimally

characterise net TCA cycle flux, specific intermediate reactions (e.g. conversion of succinate to fumarate or malate to oxaloacetate) and anaplerotic exchange reactions (interconversion of malate and pyruvate). Such tracer studies could be used to evaluate the remodelling of the TCA cycle predicted by FBA[294]. With these approaches, it must be borne in mind that the *ex vivo* approach does not faithfully reflect cardiac substrate availability *in vivo*.

Conventional magnetic resonance spectroscopy has limited sensitivity for the assessment of metabolism, due to inherent low signal levels of biomolecules in a magnetic field[297]. Using MR spectroscopy coupled with dynamic nuclear polarisation (DNP) of ^{13}C-labelled metabolites in solution can temporarily increase the otherwise low signal available for detection by 100,000-fold[297]. This approach could be used for direct real-time assessment of (the first span of) TCA cycle flux in the current model. Thus, hyperpolarised MR spectroscopy has been used to follow the metabolic fate of [2-^{13}C]pyruvate following *ex vivo* cardiac perfusion, followed this into [2-^{13}C]lactate, [1-^{13}C]acetyl carnitine, [1-^{13}C]citrate, [2-^{13}C]alanine and [5-^{13}C]glutamate [298]. Fumarate metabolism has been studied using MR spectroscopy of hyperpolarised [1,4-^{13}C2]fumarate, following its conversion to [1,4-^{13}C2]malate, and shown to reflect tumour cell necrosis[299]. Such an approach could be applied to the *Fh1$^{f/f}$ Cre/+* heart as a marker of loss of fumarase activity.

5.3.5 Inhibition of malic enzyme using tartronic acid has little effect upon cardiac function despite increased cytotoxicity in Fh1$^{-/-}$ MEFs

In young Fh1 null hearts *Me1* transcript expression is increased, whilst by 105 days it is decreased. This may suggest that malic enzyme may play an important role in the *Fh1* knockout heart. In support of this flux balance analysis suggests that conversion of pyruvate to malate by Me1 may occur in the reductive environment of the Fh1 null heart thereby replenishing the second span of the TCA cycle. However, if malic enzyme performs its more

traditional cataplerotic function converting malate to fumarate this could be maladaptive in the *Fh1* null environment. Treatment of *Fh1*$^{-/-}$ MEFs with the malic enzyme inhibitor, TA, resulted in markedly reduced cell counts supporting the concept that malic enzyme plays a key metabolic role in these cells. Use of TA *in vivo* did not have any discernible effects on cardiac function in *Fh1*$^{f/f}$ *Cre/+* mice, however. Given the predicted importance of malic enzyme mediated replenishment of malate and oxaloacetate levels in *Fh1*$^{f/f}$ *Cre/+* mice this was unexpected. However, several possibilities may explain the divergence between *in vitro* and *in vivo* data using TA. Firstly, this work has demonstrated that *Fh1*$^{-/-}$ MEFs do not model all aspects of the *Fh1* null cardiac phenotype; for example, a pseudohypoxic response is observed in *Fh1* null MEFs but not hearts (Chapter 4). Furthermore, given that cardiomyocytes are usually considered a non-proliferative cell type, a cell count based readout of TA effect in a highly-proliferative MEF model may not be a good indicator of the effect on cardiomyocytes. Although the TA dosage used in this investigation was previously published in an obesity study[185] and resulted in weight loss in our mice, it is possible that this dose of TA did not sufficiently inhibit *cardiac* malic enzyme activity. On animal welfare grounds, treating mice with a higher dose was deemed not feasible due to the significant weight loss observed with TA treatment in both *Fh1* null and control mice.

As alluded to above one strategy to explore this area further is to investigate how much (if any) replenishment of the oxaloactate pool by carboxylation of pyruvate to malate or oxalacetate (by malic enzyme or pyruvate carboxylase) occurs in *Fh1*$^{f/f}$ *Cre/+* and control hearts by *ex vivo* cardiac perfusion with isotopes and mass isotopomer analysis to determine the fate of labelled metabolic intermediates, e.g. perfusion of hearts with pyruvate labelled at carbon 1 with monitoring of labelled carbon incorporation into TCA cycle intermediates. The subsequent appearance of C-labelled TCA cycle intermediates would occur only through the

anaplerotic carboxylation of pyruvate, because the C1 carbon of pyruvate is lost in CO_2 when converted to acetyl-coenzyme A by pyruvate dehydrogenase. If carboxylation of pyruvate was identified, then to differentiate between anaplerosis via malic enzyme or pyruvate carboxylase, *Fh1*$^{f/f}$ *Cre/+* and control hearts could be perfused with inhibitors of malic enzyme and/or pyruvate carboxylase prior to assessment of incorporation of labelled carbon into TCA cycle intermediates, coupled with readouts of *ex vivo* cardiac function. Notably, as these experiments would be performed *ex vivo*, TA dose would not need to be limited due to systemic effects of weight loss.

In perfused hearts oxidizing the ketone body – acetoacetate – as a sole substrate, contractile dysfunction and inhibition of the TCA cycle enzyme 2-oxoglutarate dehydrogenase occurs[274]. Akin to the *Fh1*-deficient model, this inhibition of 2-oxoglutarate dehydrogenase effectively forms a gap in the TCA cycle, with the corollary that anapleorsis must regenerate oxaloacetate to condense with acetyl-coenzyme A. Perfusion with pyruvate in addition to acetoacetate improves cardiac function, but cardiac dysfunction persists upon perfusion with a combination of pyruvate, acetoacetate and tartronate (the salt form of TA). Taken together, this data suggests that replenishment of oxaloactetate by the activity of malic enzyme is important in the context of an interrupted TCA cycle.

It may also have been informative to investigate the effect of other malic enzyme inhibitors *in vivo* or utilising the *ex vivo* approach described above. A genetic approach to the inhibition of Me1 in *Fh1*$^{f/f}$ *Cre/+* mice by interbreeding with *Me1* knockout mice may shed further light on the importance of this NADPH-dependent cytosolic malic enzyme isoform in this model, whilst obviating off-target effects frequently observed in inhibitor studies. If pursued, utilisation of a conditional cardiac-specific *Me1* knockout would have the advantage of

permitting investigation of the potential anaplerotic role of Me1 in the *Fh1* knockout heart without the development of any confounding extra-cardiac phenotype.

The findings from FBA suggested that a conversion of pyruvate to malate by malic enzyme (ME) took place in the Fh1 knockout heart. This is the reverse of the traditional role of ME in lipogenic tissues (e.g. adipose and liver) where it normally catalyses the $NADP^+$-dependent oxidative decarboxylation of malate to pyruvate and carbon dioxide to yield NADPH[300]. Given findings supporting a reductive milieu, if the ME-catalysed reaction were to occur in its traditional direction, then this could – via NADPH production – contribute to maintenance of a reductive environment in *Fh1*$^{f/f}$ *Cre/+* cardiomyocytes, compounding the effects of enhanced PPP flux. Notably, the cataplerotic pathway involving decarboxylation of malate to pyruvate, acting as a source of intermediate efflux from the TCA cycle, has not been described experimentally in the heart[293], with the direction of the reaction in the heart shown to be in favour of pyruvate carboxylate to form malate[275].

Notably, increased ME mRNA and protein content and enhanced second span TCA cycle anaplerosis via increased pyruvate carboxylation to malate by cytosolic ME has been identified in another model of cardiac hypertrophy - rat hearts subject to pressure-overload[301, 302]. Although acting to replenish TCA cycle intermediates beyond the fumarase-catalysed reaction, such upregulation can be considered deleterious in shifting pyruvate metabolism away from its normal oxidation by pyruvate dehydrogenase, therefore bypassing NADH-generating reactions in the first span of the TCA cycle.

5.3.6 Inhibition of the pentose phosphate pathway by DHEA partially rescues the cardiomyopathy associated with chronic Fh1 deficiency

Measurement of ROS and malondialdehyde confirmed that *Fh1*$^{f/f}$ *Cre/+* hearts have a more reductive milieu than control hearts. Treatment with DHEA, an inhibitor of G6pdx and therefore flux through the PPP (a major source of reducing equivalents), resulted in striking amelioration of the severe *Fh1*$^{f/f}$ *Cre/+* cardiac phenotype as determined by echocardiography, invasive cardiac haemodynamic assessment and *ex vivo* morphometric indices. Whilst these findings support the concept of reductive stress contributing to the *Fh1* null cardiac phenotype with amelioration via inhibition of the PPP, alternative mechanisms of DHEA action are plausible and discussed below. In future experiments, it would be valuable to clarify whether DHEA treatment of *Fh1*$^{f/f}$ *Cre+* mice alters ROS levels, NADP:NADPH, oxidised:reduced glutathione ratios as a surrogate of redox status and PPP flux.

Ribose-5-phosphate produced by the PPP can either flow back into glycolysis via transaldolase and transketolase activity or continue to into the purine nucleotide synthesis pathway. Inhibition of the PPP is likely to lead to channelling of more glucose into glycolysis, leading to more ATP production from glycolysis and enhanced flux through the first span (up to Fh1) of the TCA cycle, producing NADH for ATP production by the electron transport chain. Accordingly, DHEA treatment has the potential to provide an energetic rescue of the *Fh1*$^{f/f}$ *Cre/+* phenotype independent of effects on myocardial redox state.

Carbon from the PPP may flow into the purine nucleotide synthesis pathway. One step in this pathway involves conversion of phosphoribosylaminoimidazolesuccinocarboxamide (SAICAR) to 5-aminoimidazole-4-carboxamide ribonucleotide (AICAR), by

adenylosuccinate lyase, to produce fumarate. Flux through the PPP and purine nucleotide synthesis pathway may contribute to accumulation of fumarate and SAICAR (due to end-product inhibition) in fumarate hydratase deficient cells. Intriguingly, SAICAR has been identified as an allosteric activator of pyruvate kinase M2 and implicated in the activation of proliferative signalling of cancer cells[303, 304]. Speculatively, this potential SAICAR accumulation may be pertinent to the pathogenesis of *Fh1*-deficient cancers. It is possible that reduced flux through the PPP and subsequently purine nucleotide synthesis pathway resulting from DHEA treatment alleviates fumarate and/or SAICAR accumulation to ameliorate the cardiac phenotype.

5.3.6.1 Pleiotropic effects of DHEA

DHEA is a steroid hormone that can be converted into other hormones, including testosterone and oestrogen, both of which are known to modify cardiovascular risk[305-308] as well as other biologically active steroids, including 5-androstene-3β,17β-diol and 4-androstene-3,17-dione[309], In addition to inhibition of the PPP via G6pdx, DHEA can affect multiple other pathways likely to influence cardiac function. For example DHEA has been shown to reduce atherosclerotic plaque formation, stimulate nitric oxide signalling and attenuate inflammation[306-308]. These are discussed further below. In humans, several epidemiological studies provide evidence that low levels of endogenous DHEA correlate with elevated cardiovascular risk and mortality independently of other risk factors such as age, obesity and hypertension[306-308].

Importantly, DHEA has been shown to exert direct cardioprotective effects in pressure overload models. The administration of oral DHEA to ovariectomised female rats for 2 weeks after aortic banding attenuated cardiac hypertrophy and improved left ventricular contractility

and relaxation as measured by haemodynamics. Coadminstration of a specific sigma-1 (σ1) receptor antagonist, *N*,*N*-Dipropyl-2-[4-methoxy-3-(2-phenylethoxy) phenyl]-ethylamine monohydrochloride (NE-100), inhibited DHEA-induced amelioration of these parameters post-pressure overload[310]. σ1 receptors are ligand-regulated molecular chaperones known to interact with steroids[306]. DHEA is a precursor to oestradiol *in vivo*. While oestrogen administration post-aortic banding conferred similar protective effects against pressure overload–induced cardiac hypertrophy and dysfunction, these were not altered in the presence of co-administration of the σ1 receptor antagonist, suggesting that the cardioprotective effects of DHEA were at least in part distinct to those of oestradiol and mediated via the σ1 receptor[310]. DHEA treatment was found to increase Akt activation and eNOS (endothelial NO synthase) expression and eNOS phosphorylation (Ser1177), which have been found to be reduced post-aortic banding. Of note in this regard, DHEA has also been found to stimulate eNOS production from intact vascular endothelial cells via a steroid-specific, cell surface G-protein coupled mechanism[311].

A σ1 receptor-dependent effect for the observed DHEA partial rescue of the cardiac *Fh1* knockout phenotype could be assessed by concurrent administration of the specific σ1 receptor antagonist NE-100 – preservation of the rescue by DHEA in the presence of NE-100 would suggest DHEA-induced cardioprotective/remodelling mechanism(s) relatively independent of the σ1 receptor.

In addition to the σ1 receptor, DHEA or its metabolites have been reported to bind or indirectly modulate multiple other receptors, including peroxisome proliferator activated receptor α, pregnane X receptor, constitutive androstanol receptor and estrogen receptor β [309]. In addition, largely in studies focused on the pathogenesis and treatment of pulmonary

hypertension, DHEA has been reported to exert effects on multiple other intracellular signalling pathways and moieties, including PI3K/NFAT, Src/STAT3, RhoA/RhoA kinase and soluble guanylate cyclase[306], further complicating the straightforward interpretation of an *in vivo* pharmacological rescue experiment using DHEA.

5.3.6.2 Further readouts of PPP activity and the reductive environment

Given the potential diversity of DHEA's biological effects, it is important for future work to firstly confirm increased PPP flux in vehicle-treated *Fh1*$^{f/f}$ *Cre/+* hearts using ^{13}C-based tracer studies, followed by similar assessment of PPP flux in the context of DHEA treatment to substantiate that the selected dosing regimen significantly inhibited glucose flux through the PPP. Alternatively, different pharmacological inhibitors of G6pdx could be used (e.g. 6-aminonicotinamide).

To more directly test the hypothesis that enhanced PPP flux via G6PD plays a key pathogenic role in the phenotype of *Fh1* null cardiomyopathy, a genetic approach intercrossing *Fh1*$^{f/f}$ *Cre/+* mice with G6PD mutant mice, which display 20% of normal G6PD activity under the control of the native promoter could be used[245], anticipating a reduction in cardiomyopathy severity in the compound transgenic.

Even if this were confirmed, this does not indicate that DHEA's protective effect in the setting of cardiac *Fh1* ablation were mediated by restoring redox balance. Specifically, the effects of DHEA treatment on the redox environment of *Fh1*$^{f/f}$ *Cre/+* hearts versus vehicle treatment could be tested more directly by: measurement of reduced (GSH) versus oxidised (GSSG) glutathione in cardiac tissue homogenates, permitting assessment of the GSH/GSSG ratio; evaluation of myocardial superoxide production by lucigenin-enhanced chemiluminescence; assessment of malondialdehyde levels as a measure of lipid

peroxidation; anti-dinitrophenylhydrazine immunostaining as a marker of protein oxidation; measurement of 2-hydroxyethidium by HPLC as a sensitive readout of total intracellular superoxide or dihydroethidium staining[312].

5.3.7 FBA predicts the alteration of flux through multiple pathways in Fh1 null hearts

FBA predicted changes in flux through multiple metabolic pathways in *Fh1* null hearts this highlights more pathways pertinent to investigate in future experiments. Two mechanisms predicted to be of particular importance were the elimination of accumulated fumarate and replenishment of the second span of the TCA cycle. Metabolomic analysis has identified the accumulation of argininosuccinic acid, adenylosuccinate, succinyl adenosine and SAICAR, this may simply be due to end-product inhibition of argininosuccinate lyase and adenylosuccinate lyase by accumulated fumarate or reversal of the action of these enzymes may occur in Fh1 knockout hearts. Use of radio-labelled tracers in a perfused heart model may permit testing of the hypothesis that argininosuccinate lyase and adenylosuccinate lyase activity is reversed in the presence of excess fumarate found in *Fh1* null heart, resulting in the incorporation of labelled carbon into argininosuccinate, adenylosuccinate and/or SAICAR.

If fumarate accumulation does not lead to end-product inhibition of adenylosuccinate lyase activity, accumulated SAICAR may be converted to AICAR and fumarate. In the cytosol AICAR can be phosphorylated into ZMP (5-aminoimidazole-4-carboxamide ribonucleoside) which can, both directly and via metabolism into AMP via IMP, activate AMPK-activated protein kinase (AMPK) signalling[313]. AMPK is regarded as the cell's energy gauge and is physiologically regulated by adenine nucleotides, with endogenous AMP activating AMPK through direct allosteric enzyme activation and inhibition of dephosphorylation of a key residue (Thr172) on the activation loop of the catalytic α-subunit[314]. AICAR is used

experimentally to activate AMPK and its metabolite, ZMP, acts as an AMP analogue, mimicking the effect of AMP on AMPK and binding to the same regions[314]. Activating mutations in AMPK cause hypertrophic cardiomyopathy in both mouse models[315] and humans[316]. Thus, it is possible that enhanced SAICAR and ultimately ZMP production via AICAR in the Fh1 null heart is associated with cardiomyocyte AMPK activation contributing to hypertrophy. AMPK signalling in Fh1 knockout hearts could be determined by measurement of AMPK α-Thr172 phosphorylation and phosphorylation of recognised downstream target proteins (e.g. acetyl-CoA carboxylase) by immunoblotting or direct measurement of AMPK enzymatic activity by kinase assay using radiolabeled ATP[317].

Given that inhibition of malic enzyme by TA did not alter cardiac function in *Fh1*$^{f/f}$ *Cre/+* mice, further investigation into potential anaplerotic mechanisms which may replenish the second span of the TCA cycle may shed light upon the adaptive metabolic remodelling that facilitates survival of mice lacking a key TCA cycle enzyme. Augmentation of the oxaloacetate pool by transamination of aspartate is one candidate mechanism. In order to investigate the importance of aspartate transamination as a potential adaptive mechanism, future experiments could probe the effect of aspartate supplementation or inhibition of aspartate transaminase (also known as glutamate-oxaloacetate transaminase) which would be predicted to ameliorate or exacerbate the *Fh1*$^{f/f}$ *Cre/+* phenotype, respectively.

6 CHAPTER 6: THE ROLE OF CYTOSOLIC FH

6.1 Aims and hypothesis

It is unclear whether loss of cytosolic fumarate hydratase (Fh1) activity contributes to the pathology of cardiac Fh1-null mice or if mitochondrial Fh1-deficiency and associated disruption of the tricarboxylic acid (TCA) cycle accounts for all the detrimental aspects of the phenotype. The observations that heterozygous deletion of nuclear factor (erythroid-derived 2)-like 2 (NRF2) – a transcription factor activated in Fh1-knockout hearts – significantly extends the life span of *Fh1*$^{f/f}$ *Cre/+* mice and that inhibition of the cytosolic enzyme glucose-6-phosphate dehydrogenase (G6pdx) ameliorates the *Fh1*$^{f/f}$ *Cre/+* phenotype, both suggest that cytosolic fumarate hydratase activity could be important. Indeed, cytosolic fumarate hydratase is likely to play a physiological role to eliminate cytosolic fumarate produced by the purine nucleotide biosynthesis pathway, the purine nucleotide cycle and the urea cycle[135, 136]. A mitochondrial targeting sequence is responsible for directing FH to the mitochondria.

To examine the specific role of cytosolic, as opposed to mitochondrial, FH, three adenoviral constructs were generated with the aim of targeting human FH to: both the mitochondria and cytoplasm; or exclusively to the cytoplasm; or solely to the mitochondria. A fourth control adenovirus expressing only green fluorescent protein was also generated. In addition, two knock-in mouse models encoding FH with or without a mitochondrial targeting sequence were generated and bred with *Fh1*$^{f/f}$ *Cre/+* mice to investigate the potential for genetic rescue of the cardiac Fh1 knockout phenotype by dual-localised or cytosol-specific FH knock-in.

The main hypotheses of this chapter are:

- Deletion of the MTS will lead to localisation of FH to the cytoplasm but not mitochondria.

- As described in yeast, mutation of the second start codon of FH will lead to exclusive mitochondrial targeting of FH.
- Cytosolic (and dual-localised) FH adenoviral constructs will be sufficient to reverse the pseudohypoxic and antioxidant responses of *Fh1*$^{-/-}$ mouse embryonic fibroblasts.
- Knock-in of dual-localised FH will be sufficient to rescue the FH null cardiac phenotype.
- Knock-in of cytoplasmic FH expression will lead to an amelioration of the *Fh1* knockout cardiac phenotype.

Consequently, utilising a combination of cellular and *in vivo* models, the aims of this chapter are:

- To explore the possibility of localising FH protein specifically in the cytoplasm.
- To investigate the potential to target FH exclusively to the mitochondria.
- To determine whether knock-in of human dual-localised and cytosolic-specific FH is sufficient to ameliorate and/or fully rescue the cardiac Fh1 null phenotype.

6.2 Results

6.2.1 Expression and localisation of adenoviral encoded FH

The AdEasy Adenoviral Vector System (Stratagene) was used to generate adenoviruses encoding full length human fumarate hydratase with a MTS (AdFH), without a MTS (AdFHcyt) and with a mutated second start codon (AdFHΔATG), intended to express FH dual-localised to the mitochondria and cytoplasm, in the cytoplasm only or exclusively in mitochondria, respectively. The adenoviruses utilise a cytomegalovirus promoter to express C-terminal FLAG-tagged FH in conjunction with an internal ribosomal entry sequence (IRES) to express green fluorescent protein (GFP). A control virus (AdGFP) solely expressing GFP was also produced. Successful infection of *Fh1*$^{-/-}$ mouse embryonic fibroblasts with these adenoviruses was demonstrated by expression of GFP assessed by fluorescence microscopy at 48 hours post-transfection (Figure 70). Immunoblotting using an anti-fumarate hydratase antibody confirmed expression of FH in whole cell lysates from *Fh1*$^{-/-}$ MEFs treated with AdFH, AdFHcyt and AdFHΔATG (Figure 71). As expected, FH was not expressed in *Fh1*$^{-/-}$ MEFs treated with the control AdGFP adenovirus. Adenoviral expressed FH had a higher molecular weight than endogenous Fh1 expressed in *Fh1*$^{+/+}$ MEFs due to the presence of a FLAG-tag.

Originally, it was planned to determine adenoviral titre by counting GFP positive cells. However, as shown in Figure 70, the intensity of GFP expression varied between cells making it difficult to determine whether faintly fluorescent cells were reliably adenoviral infected. Therefore, a different approach employing anti-hexon immunocytochemical staining was used to stain cells expressing adenoviral capsid protein positive cells, thus allowing adenoviral titres to be more accurately estimated (Figure 25). For all subsequent experiments equal titres – calculated in infection forming units – of each adenovirus were used.

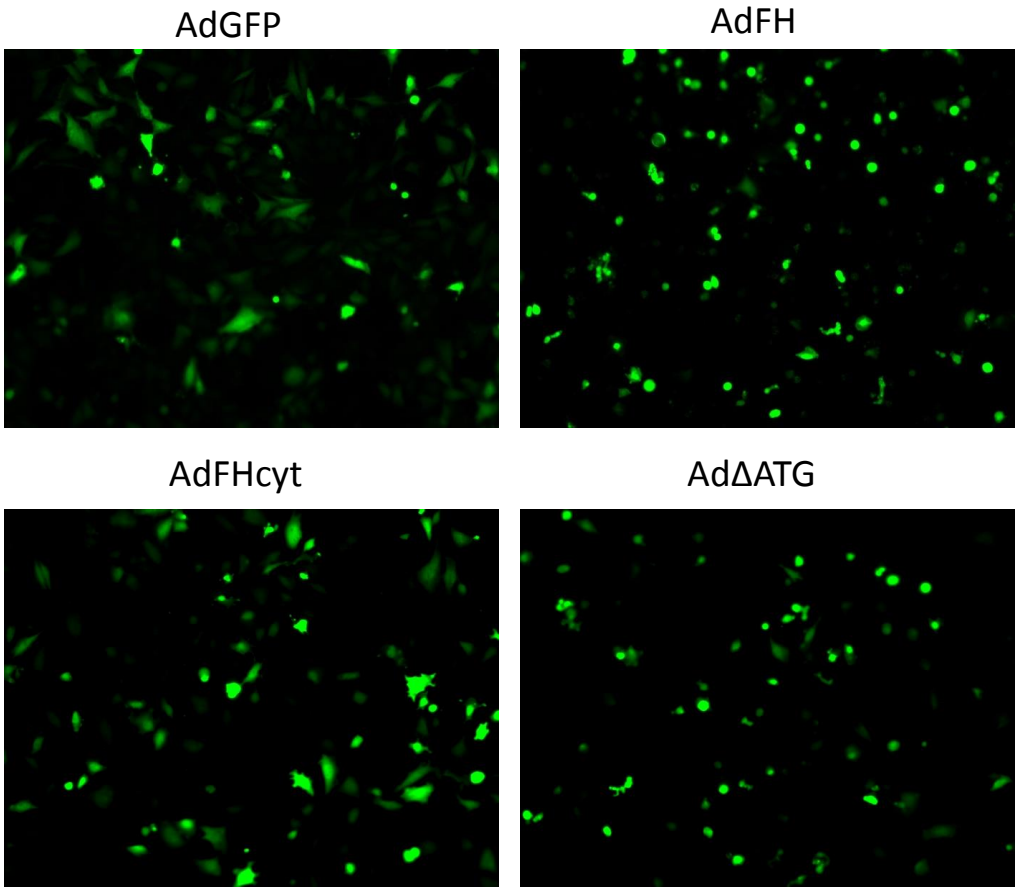

Figure 70- Visualisation of green fluorescent protein expression indicating successful transfection of Fh1-/- mouse embryonic fibroblasts with the indicated adenoviruses

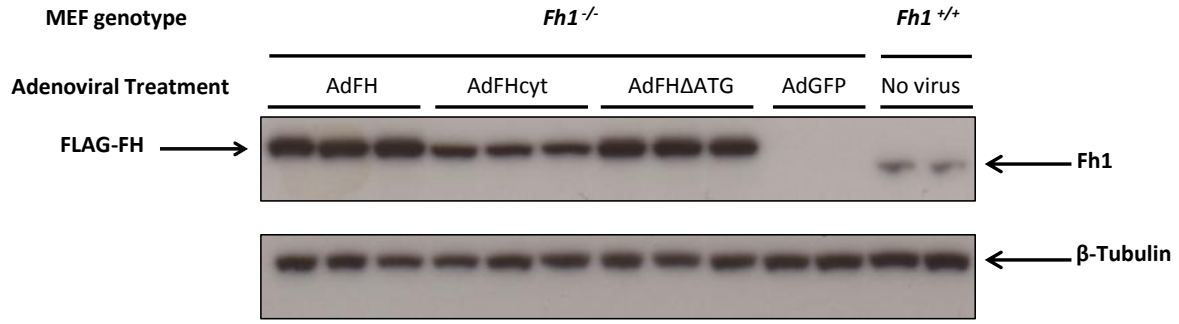

Figure 71 – Expression of FLAG-tagged FH in whole cell lysates *Fh1*$^{-/-}$ mouse embryonic fibroblasts (MEFs) treated with FH encoding adenoviruses
Western blotting using an anti-fumarate hydratase antibody demonstrates expression of FH protein in *Fh1*$^{-/-}$ MEFs treated with AdFH, AdFHcyt and AdFHΔATG but not AdGFP. Endogenous murine Fh1 expression is seen in non-transfected *Fh1*$^{-/-}$ MEFs. Adenoviral encoded human FH is at a slightly higher molecular weight than endogenous Fh1 due to the presence of a FLAG-tag. Expression of the loading control protein, β-Tubulin, is also demonstrated.

Adenoviral transfected *Fh1*$^{-/-}$ MEFs were treated with mitotracker (red) to highlight the mitochondria and immunofluorescent staining with an anti-flag-tag antibody was used to

reveal the localisation of adenoviral-encoded FH (blue) (Figure 72). As expected, despite successful transfection of cells demonstrated by a fluorescent GFP signal, no FH FLAG-tag expression was observed in cells treated with the control AdGFP adenovirus. Clear co-localisation of FLAG-tagged FH with the mitochondria was observed in AdFH and AdΔATG treated MEFs. In contrast, AdFHcyt treatment resulted in diffuse expression of FLAG-tagged FH throughout the cytoplasm with no evidence of mitochondrial co-localisation.

Although immunofluorescence clearly reveals that AdFHcyt encoded FLAG-tagged FH localises to the cytosol, any cytosolic expression by AdFH or AdFHΔATG is likely to be eclipsed by the strong mitochondrial signal. Therefore, to confirm localisation of adenoviral-encoded FH, western blotting was performed upon mitochondrial and cytosolic subcellular fractions obtained from *Fh1*$^{-/-}$ MEFs treated with each adenovirus (Figure 73). The success of subcellular fractionation was validated by the lack of contamination of the cytosolic fraction with a mitochondrial marker (VDAC1) and of the mitochondrial fraction with a cytosolic marker (β-tubulin). FLAG-tagged FH was present in the cytosolic fractions of AdFH, AdFHcyt and AdFHΔATG transfected MEFs. This finding indicates that in mammalian cells, unlike yeast, mutation of the second start codon of FH does not result in exclusively mitochondrial localisation of fumarate hydratase. FLAG-tagged FH expression was observed in the mitochondrial fractions of AdFH and AdFHΔATG, but not AdFHcyt-treated MEFs. Consistent with the immunofluorescent microscopy results presented earlier, this finding demonstrates that deletion of the MTS in the AdFHcyt construct prevents the mitochondrial targeting of FH, resulting in cytosol-specific FH expression.

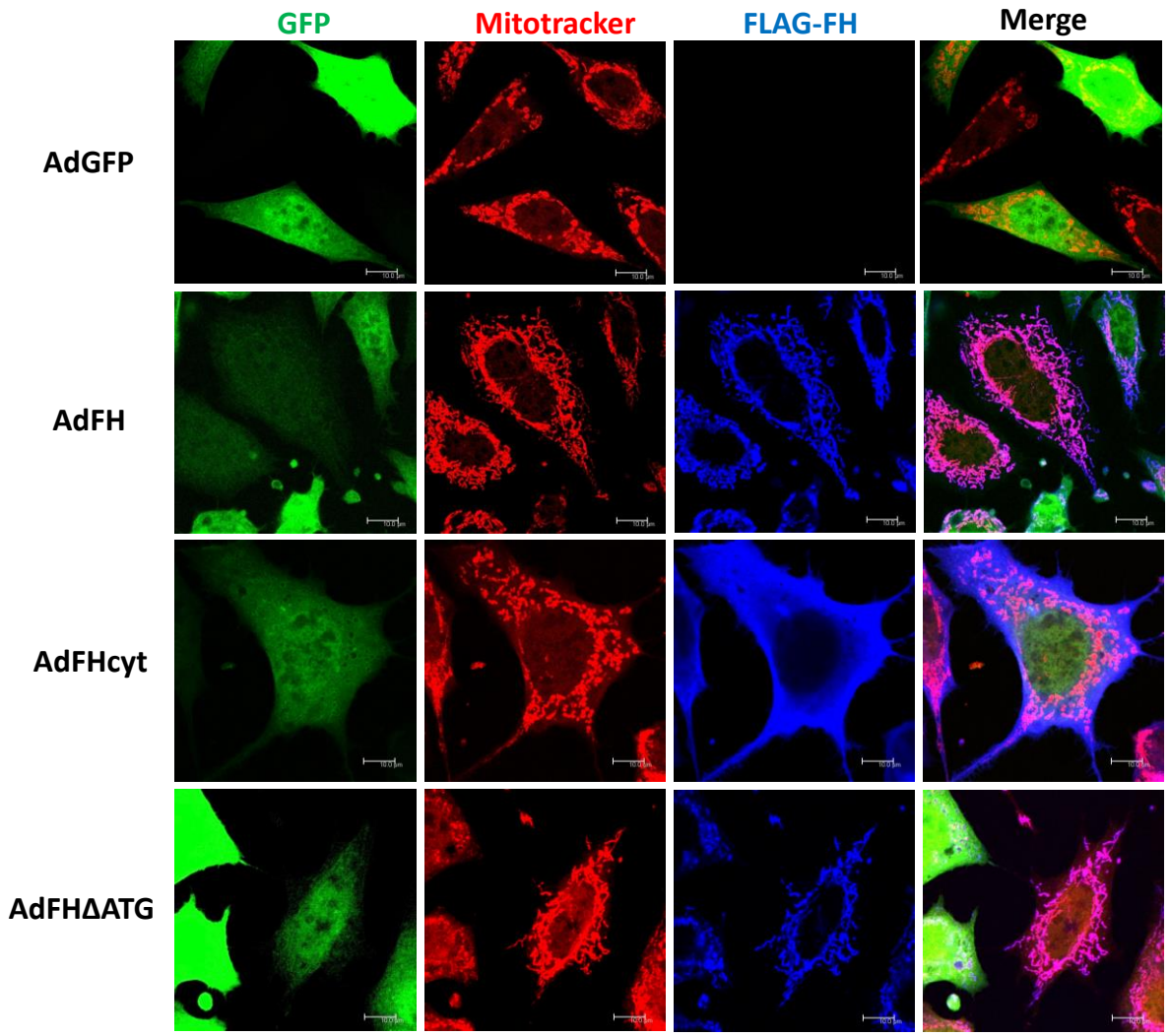

Figure 72 – Assement of localisation of adenoviral transfected FLAG-tagged FH by immunofluorescence
Fh1$^{-/-}$ MEFs transfected with adenoviruses encoding hrGFP with no insert (AdGFP), wildtype FH (AdFH), FH without a mitochondrial targeting sequence (FHcyt) and with a mutated second start codon (FHΔATG), treated with mitotracker and stained for FLAG-tag expression. Green demonstrates hrGFP expression indicating successful transfection of cells. Red is mitotracker which labels the mitochondria. Blue indicates localisation of FLAG-tagged FH. Scale bar = 100 μm.

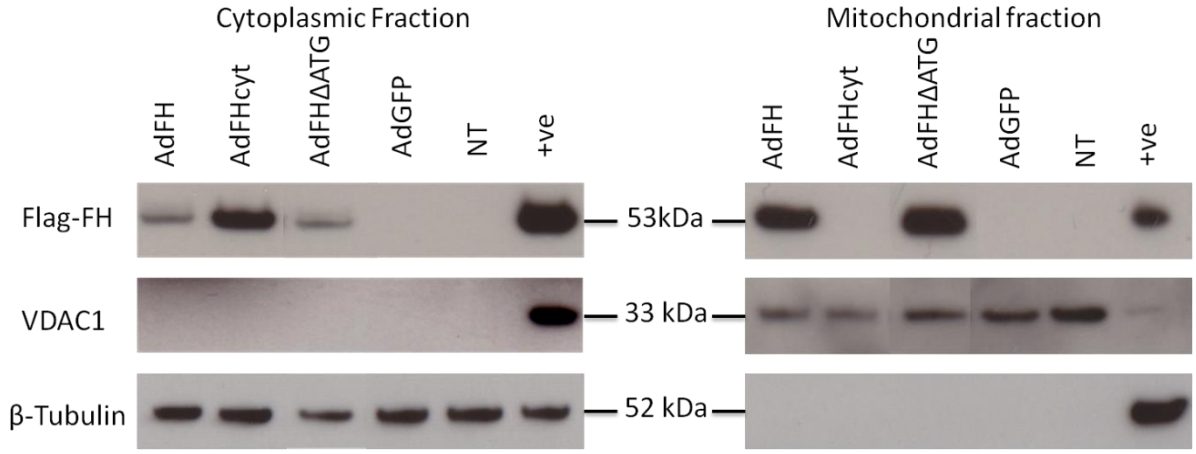

Figure 73 – FLAG-tagged FH expression in cytoplasmic and mitochondrial subcellular fractions from mouse embryonic fibroblasts (MEFs) transfected with adenovirus encoding FH
Representative western blot of mitochondrial and cytoplasmic fractions purified from MEFs transfected with adenoviruses encoding hrGFP with no insert (AdGFP), wildtype FH (AdFH), FH without a mitochondria targeting sequence (AdFHcyt) and with a mutated second start codon (AdFHΔATG). NT represents non-transfected MEFs. Whole cell lysate from AdFH treated MEFs was used as a positive control (+ve). Flag-FH represents the adenoviral encoded FLAG-tagged FH. Voltage dependant anion channel 1 (VDAC1) is a mitochondrial-specific marker. β-tubulin is a cytoplasmic marker.

6.2.2 Fh1$^{-/-}$ MEFs demonstrate pseudohypoxic and antioxidant responses which are reversed by cytosolic FH expression

Published data have revealed normoxic activation of HIF signalling in FH deficient cells and tissues, i.e. a pseudohypoxic response[115, 116, 143, 179]. Consistent with these reports, qPCR revealed highly significant elevation of a panel of traditional hypoxia inducible factor (HIF) target genes in *Fh1*$^{-/-}$ MEFs compared to *Fh1*$^{+/+}$ MEFs (Figure 74A). For example, lactate dehydrogenase A and pyruvate dehydrogenase kinase transcript levels were upregulated six fold in *Fh1*$^{-/-}$ MEFs. Nuclear factor (erythroid-derived 2)-like 2 (Nrf2)-mediated upregulation of its target genes in the antioxidant response pathway has previously been reported in FH null tissues[145, 161]. In agreement with this, qPCR demonstrated significantly increased mRNA expression of several NRF2 target genes (Figure 74B), most strikingly a 15-fold elevation of NAD(P)H dehydrogenase quinone 1 *(Nqo1)* transcript levels. Compared to treatment with the control AdGFP adenovirus, transfection of *Fh1*$^{-/-}$ MEFs with AdFH or AdFHcyt adenovirus resulted in significant reversal of induction of expression of the same panel of HIF target genes (Figure 75A). Similarly, significant reduction in transcript level of two out of the three

NRF2 target genes tested was observed in *Fh1*$^{-/-}$ MEFs treated with AdFH or AdFHcyt compared to AdGFP (Figure 75B). These findings indicate that replenishment of cytosolic FH is sufficient to partly ameliorate the aberrant activation of both HIF and NRF2 observed in *Fh1*$^{-/-}$ MEFs.

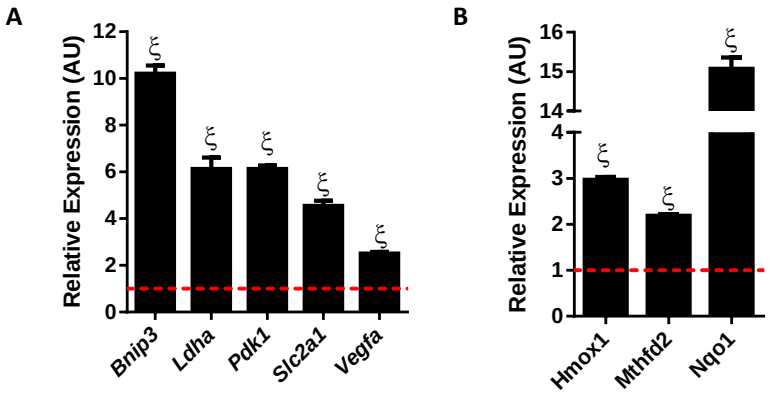

Figure 74 – *Fh1*$^{-/-}$ mouse embryonic fibroblasts (MEFs) display increased expression of HIF and NRF2 target genes relative to *Fh1*$^{+/+}$ MEFs

A. Relative HIF target gene expression in arbitrary units (AU) assessed by qRT-PCR and analysed by the comparative C_T method ($2^{-\Delta\Delta Ct}$) using the internal control, cardiac β-actin (encoded by *Actb*) and normalised to expression in *Fh1*$^{+/+}$ MEFs. *Bnip3*: Bcl2 and nineteen-kilodalton interacting protein 3; *Ldha*: lactate dehydrogenase A; *Pdk1*: pyruvate dehydrogenase kinase 1; *Slc2a1*: solute carrier family 2 (facilitated glucose transporter), member 1 (Glut1); *Vegfa1*: vascular endothelial growth factor A. **B.** Relative NRF2 target gene expression in arbitrary units (AU) assessed by qPCR and normalised to expression in *Fh1*$^{+/+}$ MEFs. *Hmox1*: Haem oxygenase 1; *Mthfd2*: methylenetetrahydrofolate-dehydrogenase 2; *Nqo1*: NAD(P)H dehydrogenase, quinone 1. Red dashed line represents mean expression in *Fh1*$^{+/+}$ MEFs. ξ p<0.001 compared to *Fh1*$^{+/+}$ MEFs.

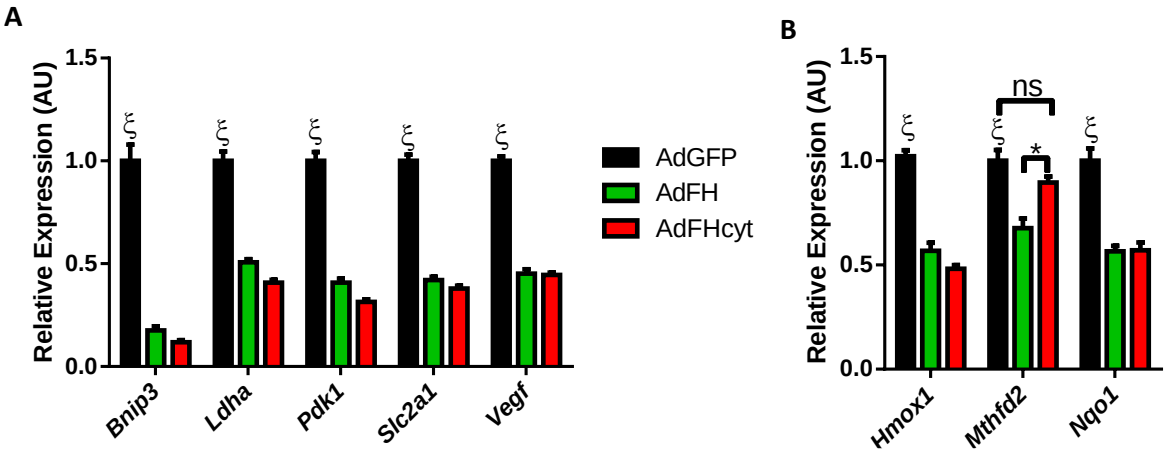

Figure 75 – Treatment with AdFH or AdFHcyt reverses elevation of HIF and NRF2 targets in *Fh1*$^{-/-}$ mouse embryonic fibroblasts

A. Relative expression in arbitrary units of HIF target genes in adenoviral-treated *Fh1*$^{-/-}$ MEFs assessed by qRT-PCR and analysed by the $2^{-\Delta\Delta Ct}$ or comparative C_T method using the internal control in cardiac beta actin (encoded by *Actb*) and normalised to expression levels in *Fh1*$^{-/-}$ MEFs treated with AdGFP. *Bnip3:* Bcl2 and nineteen-kilodalton interacting protein 3; *Ldha:* lactate dehydrogenase A; *Pdk1:* pyruvate dehydrogenase kinase 1; *Slc2a1:* solute carrier family 2 (facilitated glucose transporter), member 1 (Glut1); *Vegfa1:* vascular endothelial growth factor A. **B.** Relative expression in arbitrary units of HIF target genes in adenoviral-treated *Fh1*$^{-/-}$ MEFs assessed by qPCR and normalised to expression levels in *Fh1*$^{-/-}$ MEFs treated with AdGFP. *Hmox1*: Haem oxygenase 1; *Mthfd2*: methylenetetrahydrofolate-dehydrogenase 2; *Nqo1*: NAD(P)H dehydrogenase, quinone 1. ξ p<0.001 compared to all groups except where indicated. * p<0.05 between indicated groups.

6.2.3 KI^{FH} and KI^{FHcyt} mice expressing human FH from the Rosa26 locus

To investigate the role of cytosolic FH in the cardiomyopathy associated with cardiomyocyte Fh1 ablation, mice expressing C-terminal V5-tagged, dual-localised (KI^{FH}) or cytosol-specific FH (KI^{FHcyt}) at the *Rosa26* locus under the control of a CAG (cytomegalovirus early enhancer, chicken β-actin promoter, rabbit β-globin splice acceptor) promoter were interbred with *Fh1$^{f/f}$ Cre/+* mice. The KI^{FH} line were utilised as a control to confirm that introduction of human FH at this genetic locus was sufficient to rescue the mouse Fh1 null phenotype. As previously demonstrated (in Chapter 4), anti-FH immunoblotting of whole heart lysates confirmed a clear reduction in Fh1 protein expression (with some residual expression probably from non-cardiomyocyte cells in whole heart lysates) in *Fh1$^{f/f}$ Cre/+* mice comparative to *Fh1$^{f/f}$* controls. Expression of KI^{FH} and KI^{FHcyt} were confirmed by Western blot for both fumarate hydratase and the V5-tag in *Fh1$^{f/f}$ Cre/+ KI^{FH}* and *Fh1$^{f/f}$ Cre/+ KI^{FHcyt}* hearts (Figure 76). The bands corresponding to KI^{FH} or KI^{FHcyt} are of a higher molecular weight than the endogenous Fh1 due to the C-terminal V5-tag. Hence, two bands are seen for *Fh1$^{f/f}$ Cre/+ KI^{FH}* and *Fh1$^{f/f}$ Cre/+ KI^{FHcyt}* hearts one representing residual Fh1 expression in non-cardiomyocyte cells and a second more dense band corresponding the KI^{FH} or KI^{FHcyt}.

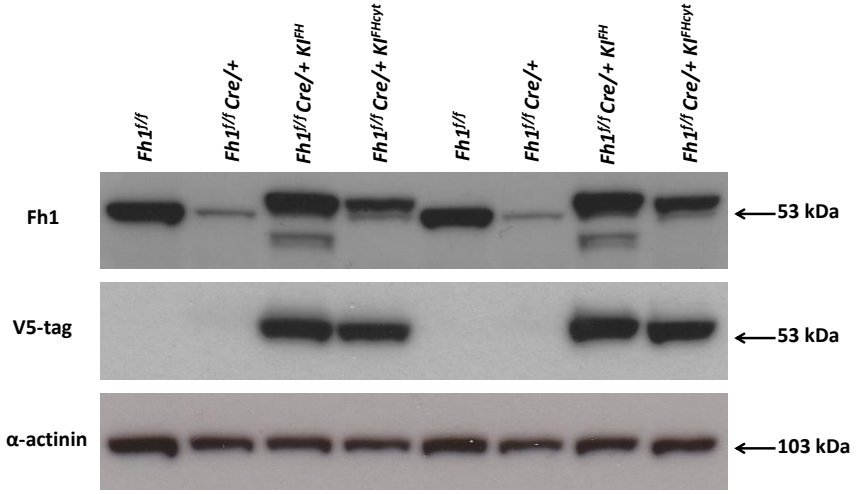

Figure 76 – V5-tagged Fh1 expression in knock-in mice
Western blots from heart lysates demonstrating depletion of Fh1 expression in *Fh1$^{f/f}$ Cre/+* mice and expression of knock-in V5-tagged FH in *Fh1$^{f/f}$ Cre/+ KI^{FH}* and *Fh1$^{f/f}$ Cre/+ KI^{FHcyt}*. α-actinin acts as loading control.

6.2.4 *Knock-in of cytosol-specific FH partially rescues the cardiac Fh1 null phenotype*

6.2.4.1 *Extension of lifespan by cytosolic FH*

Kaplan-Meier survival analysis demonstrated a highly significant extension of life expectancy by *cytosolic* FH augmention, prolonging median lifespan from 106 days in *Fh1*$^{f/f}$ *Cre/+* mice to 176 days for *Fh1*$^{f/f}$ *Cre/+ KI*^{FHcyt} animals (Figure 77). KI^{FH} facilitated a complete rescue to the *Fh1*$^{f/f}$ *Cre/+* lethality phenotype with no deaths observed for the duration of monitoring (220 days), demonstrating that dual-localised human FH expressed at the *Rosa26* locus under the control of the CAG promoter is sufficient to reverse the lethality associated with Fh1 deletion. No deaths were seen in the *Fh1*$^{f/f}$, *Fh1*$^{f/f}$ *KI*^{FH} and *Fh1*$^{f/f}$ *KI*^{FHcyt} control groups monitored for 220 days, demonstrating that expression of human FH in either the dual localised knock-in model to the mitochondria and cytosol, or specifically expressed in the cytosol, is not lethal.

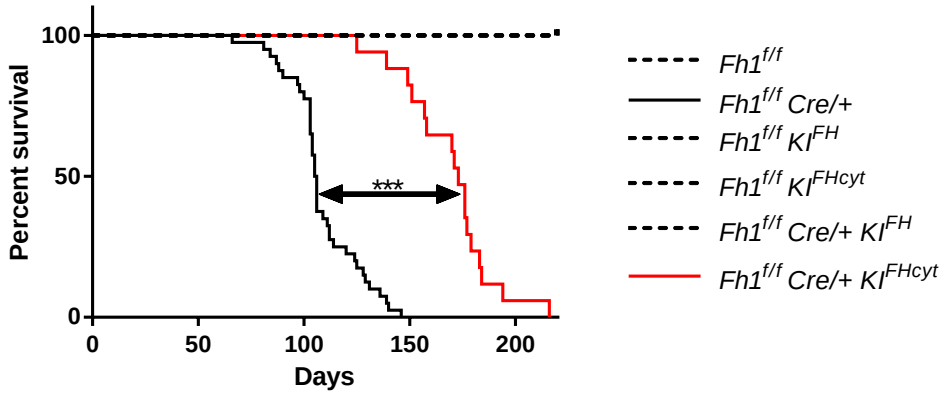

Figure 77 – Kaplan-Meier survival curves demonstrating the complete or partial reversal of the *Fh1*$^{f/f}$ *Cre/+* lethality phenotype by *KI*^{FH} and *KI*^{FHcyt}, respectively
*** p<0.001.

6.2.4.2 *Echocardiographic assessment of cardiac function*

Cardiac function was assessed by echocardiography in a cohort of mice aged 100 days (Figure 78). No differences in heart rate during image acquisition were observed. Furthermore, no significant differences in parameters of cardiac size or function were

observed in *Fh1*$^{f/f}$ *KI*^{FH} or *Fh1*$^{f/f}$ *KI*^{FHcyt} mice compared to *Fh1*$^{f/f}$ control mice, indicating that expression of human FH from the knock-in constructs *per se* was not deleterious to cardiac function. As previously described (in Chapter 4), cardiac function was significantly impaired in *Fh1*$^{f/f}$ *Cre/+* mice. This was observed to be completely restored by introduction of *KI*^{FH}. In contrast, cytosol-specific FH expression was sufficient to partially, but not completely, ameliorate the profound cardiac dysfunction observed in Fh1 null hearts. For example, left ventricular end-systolic dimension (LVESD) and LV end-systolic volume (LVESV), as markers of LV contractile function, were both elevated in *Fh1*$^{f/f}$ *Cre/+* *KI*^{FHcyt} hearts compared to *Fh1*$^{f/f}$ and *Fh1*$^{f/f}$ *Cre/+* *KI*^{FH} controls, but significantly less than that observed in *Fh1*$^{f/f}$ *Cre/+* hearts (Figure 78A and B). Similarly, a derived parameter, LV ejection fraction, was significantly increased from a mean of 34 % in *Fh1*$^{f/f}$ *Cre/+* to 50 % in *Fh1*$^{f/f}$ *Cre/+* *KI*^{FHcyt} mice, albeit not to control levels of 77 % (Figure 78C). LV dilatation, indicated by elevated LV end-diastolic dimension and LV end-diastolic volume in *Fh1*$^{f/f}$ *Cre/+* mice, was significantly reduced by cytosolic FH, albeit not to control levels (Figure 78E and F). In contrast, echocardiography did not reveal amelioration of the cardiac hypertrophy seen in Fh1 null hearts, in fact, one indicator of hypertrophy – LV posterior wall thickness – was significantly elevated, albeit its effect on overall cardiac mass offset by the fact that the overall LV dimension had been reduced (Figure 78G-I).

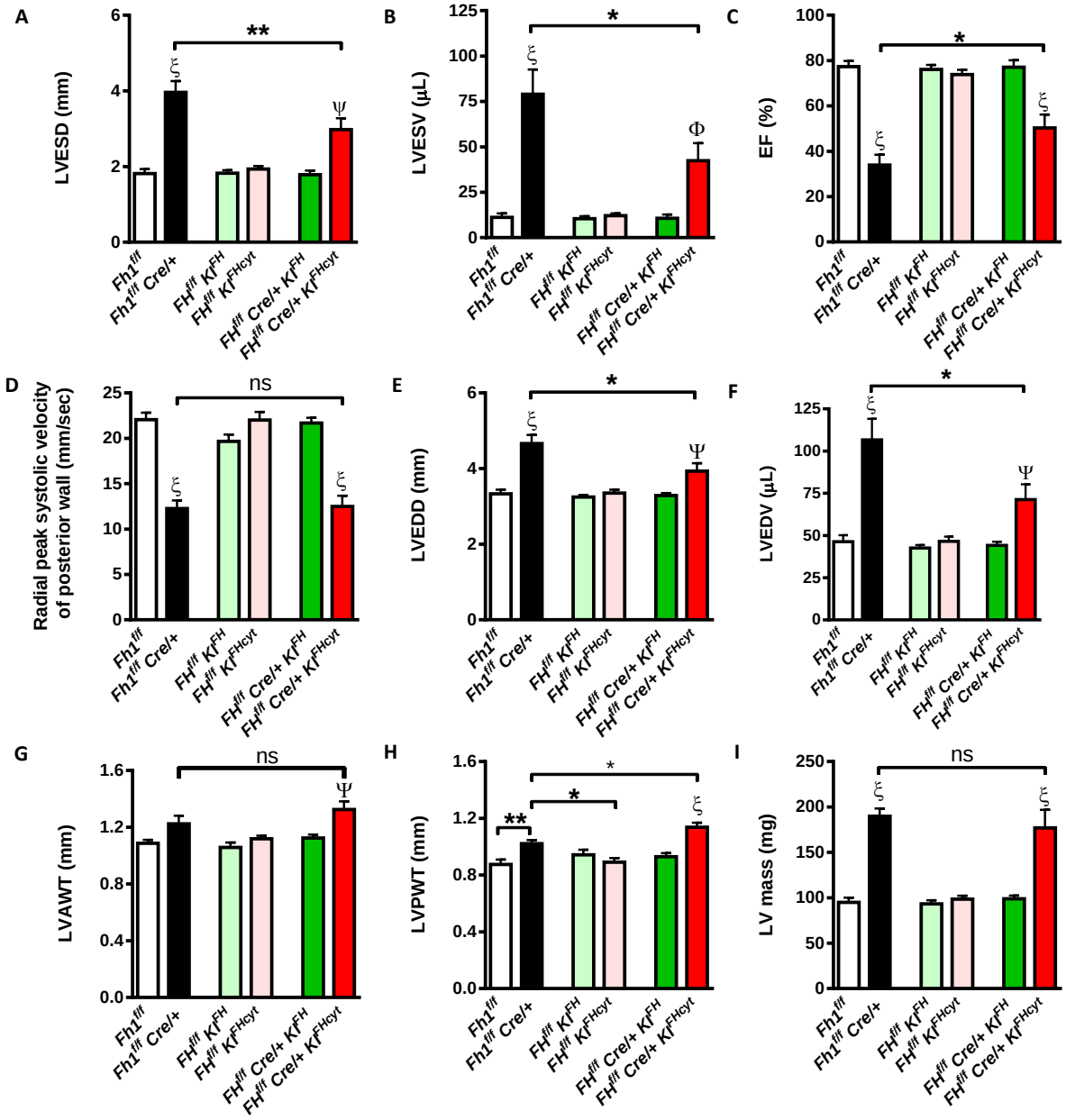

Figure 78 – Echocardiographic assessement of cardiac function and dimensions reveals complete or partial amelioration of the *Fh1$^{f/f}$ Cre/+* phenotype by KI^{FH} and KI^{FHcyt} respectively

A-D. Measures of cardiac function: **A.** Left ventricular end-systolic dimension measured in millimetres (mm) (LVESD); **B.** Left ventricular end-systolic volume (LVESV); **C.** Ejection fraction (EF); **D.** Radial peak systolic velocity of the posterior wall. **E and F.** Measures of cardiac dilatation: **E.** Left ventricular end-diastolic dimension (LVEDD); **F.** Left ventricular end-diastolic volume (LVEDV). **G-I.** Measures of cardiac hypertrophy: **G.** Left ventricular anterior wall thickness (LVAWT); **H.** Left ventricular posterior wall thickness (LVPWT); **I.** Left ventricular mass measured in milligrams (mg). * $p<0.05$ between indicated groups. ** $p<0.01$ between indicated groups. Ψ $p<0.05$ compared to all groups except where indicated otherwise. Φ $p<0.01$ compared to all groups except indicated. ξ $p<0.001$ compared to all groups except indicated. Ns, no significant difference between indicated groups.

6.2.4.3 Invasive haemodynamic assessment of cardiac function

Invasive haemodynamic assessment of cardiac function was performed at 105 days upon the same cohort of mice which underwent echocardiography. Six mice in the *Fh1*$^{f/f}$ *Cre/+* group included in the echocardiography dataset died prior to or during invasive haemodynamics and were therefore not included in the invasive haemodynamic dataset. No significant alteration in invasive haemodynamic parameters were observed in the *Fh1*$^{f/f}$ *KI*^{FH} or *Fh1*$^{f/f}$ *KI*^{FHcyt} groups compared to *Fh1*$^{f/f}$ controls (Appendix Table 21). Cardiac function was significantly impaired in *Fh1*$^{f/f}$ *Cre/+* and *Fh1*$^{f/f}$ *Cre/+ KI*^{FHcyt} mice, exemplified by significant reductions in LV systolic pressure, LV developed pressure and the maximal rates of cardiac contraction and relaxation (Figure 79). Whilst there was a trend towards improved cardiac function in *Fh1*$^{f/f}$ *Cre/+ KI*^{FHcyt} mice compared to *Fh1*$^{f/f}$ *Cre/+* mice, this was not statistically significant. In contrast, all invasive haemodynamic parameters assessed indicated restoration of cardiac function in *Fh1*$^{f/f}$ *Cre/+ KI*^{FH} mice to control levels.

6.2.4.4 Ex vivo organ weights

No difference in *ex vivo* morphometric indices were observed between *Fh1*$^{f/f}$, *Fh1*$^{f/f}$ *KI*^{FH} and *Fh1*$^{f/f}$ *KI*^{FHcyt} mice, suggesting (as with the findings from echocardiography and invasive haemodynamics) that expression of human FH dual localised to the mitochondria and cytoplasm, or to the cytoplasm only was not deleterious. Compared to control groups, *Fh1*$^{f/f}$ *Cre/+ KI*^{FHcyt} mice demonstrated significantly higher absolute and normalised heart weight, however, these values were significantly lower (albeit mildly) than for *Fh1*$^{f/f}$ *Cre/+* mice, consistent with amelioration of the cardiac hypertrophy associated with FH deletion by expression of cytosolic FH. Similarly, both absolute and normalised wet lung weights were slightly, but significantly, elevated in *Fh1*$^{f/f}$ *Cre/+ KI*^{FHcyt} mice compared to *Fh1*$^{f/f}$ controls. However, both these parameters were substantially reduced in *Fh1*$^{f/f}$ *Cre/+ KI*^{FHcyt} mice in

comparison to *Fh1*$^{f/f}$ *Cre/+* mice, suggesting a degree of improvement in the congestive heart failure phenotype by the presence of cytosolic FH.

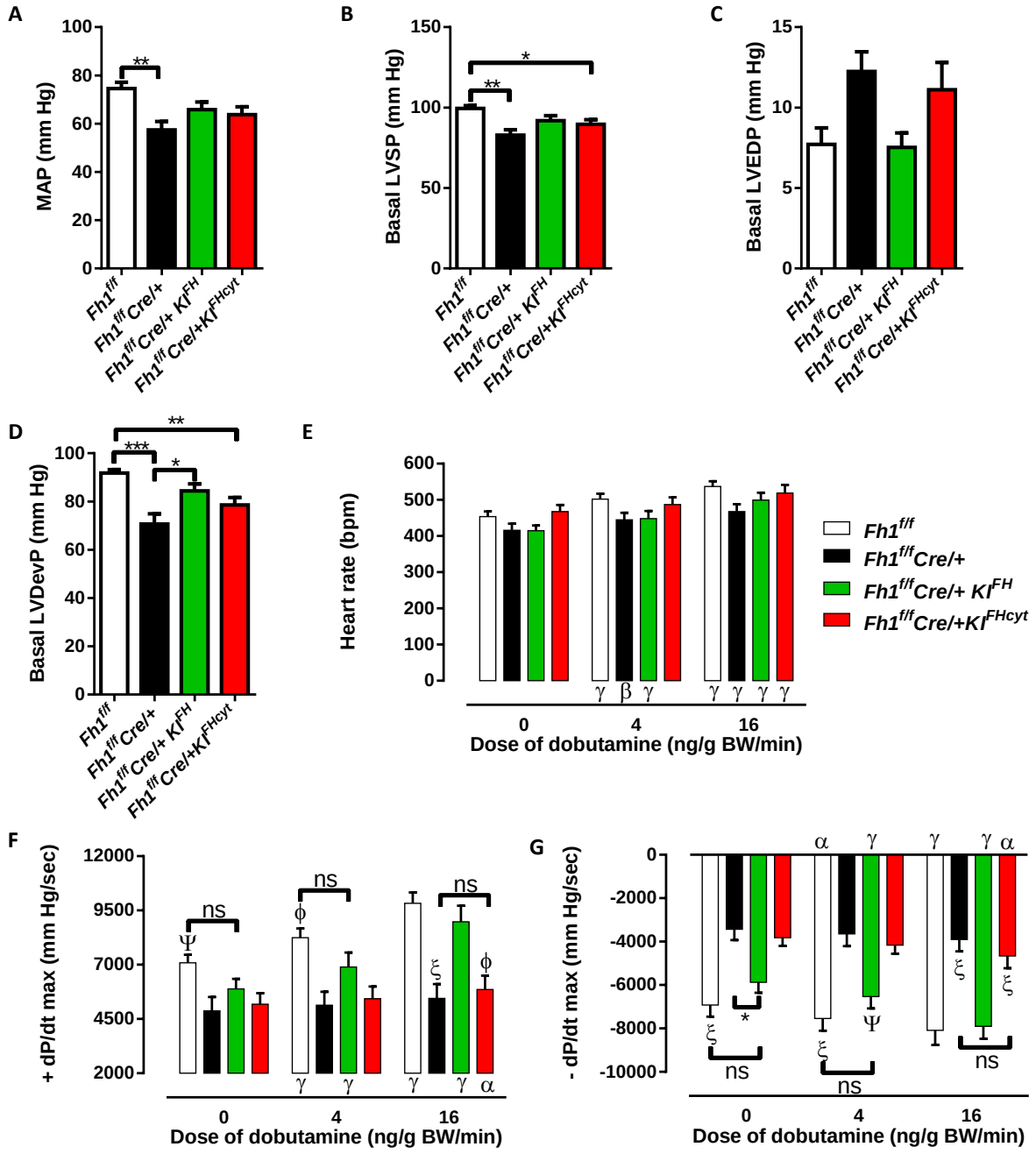

Figure 79 – Invasive haemodynamic assessment of cardiac function demonstrates amelioration of the *Fh1*$^{f/f}$ *Cre/+* phenotype with KI^{FH}

A. Basal mean aortic pressure (MAP) in millimetres of mercury (mm Hg). **B.** Basal left ventricular systolic pressure (LVSP). **C.** Basal left ventricular end diastolic pressure (LVEDP). **D.** Basal left ventricular developed pressure. (LVDevP). **E.** Heart rate in beats per minute (bpm) in response to dobutamine challenge. Dobutamine dose infused is given in nanograms per gram body weight per min. **F.** The maximal rise in left ventricular pressure with time (+dP/dt) **G.** The maximal decrease in systolic pressure with time (–dP/dt)**.** * $p<0.05$ between indicated groups. ** $p<0.01$ between indicated groups. *** $p<0.001$ between indicated groups. ξ $p<0.001$ compared to all groups except indicated. Φ $p<0.01$compared to all groups except indicated. Ψ $p<0.05$ compared to all groups except indicated. α $p<0.05$ compared to no dobutamine. β $p<0.01$ compared to no dobutamine. γ $p<$ compared to no dobutamine. Ns, no significant difference between indicated groups.

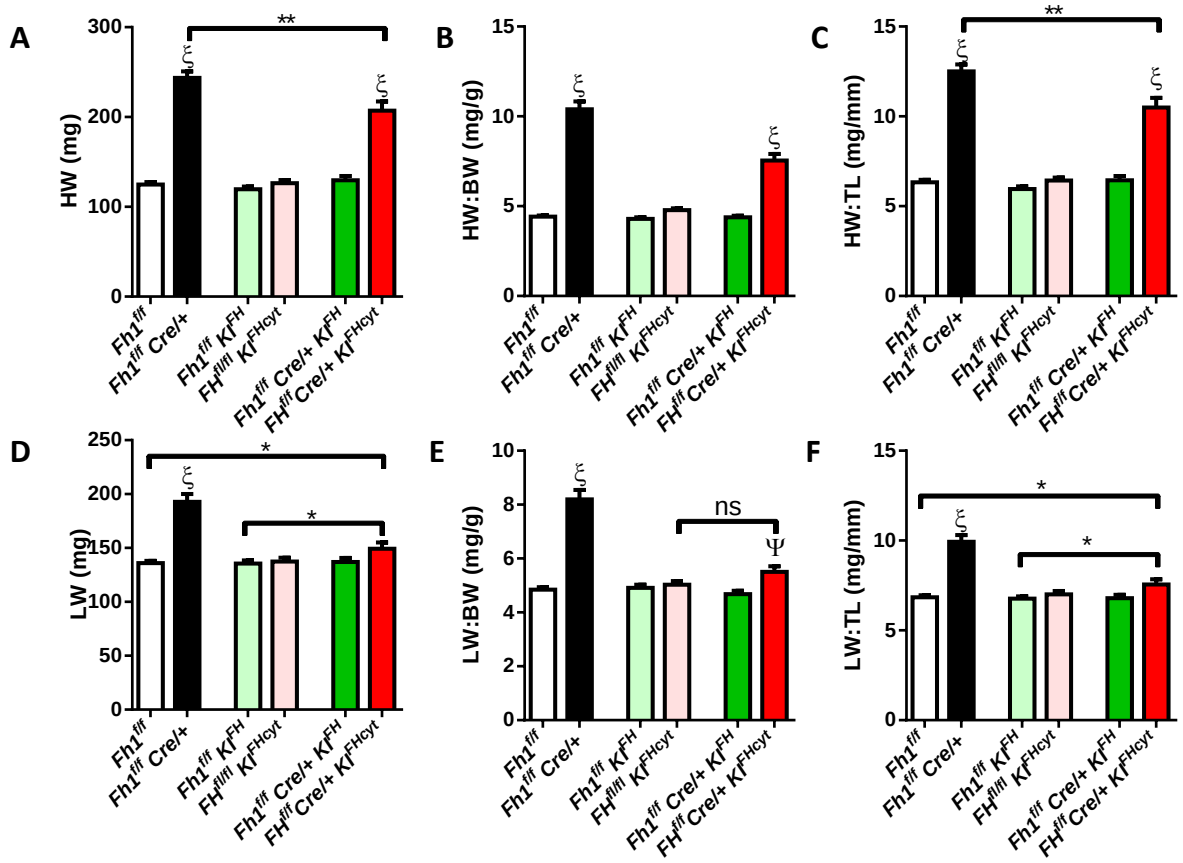

Figure 80 – Complete and partial amelioration of the elevations in heart and lung weight found in *Fh1$^{f/f}$ Cre/+* mice by concomitant expression of full length FH (*Fh1$^{f/f}$ Cre/+ KI^{FH}*) or cytosolic FH (*Fh1$^{f/f}$ Cre/+ KI^{FHcyt}*), respectively

A. Heart weight (HW) in milligrams (mg). **B.** Heart weight to body weight ratio (HW:BW) in milligrams/gram (mg/gram). **C.** Heart weight to tibial length ratio (HW:TL) in milligrams/millimetre (mg/mm). **D.** Lung weight. (LW). **E.** Lung weight to body weight ratio (LW:BW). **F.** Lung weight to tibial length ratio (LW:TL). * $p<0.05$ between indicated groups. Ψ $p<0.05$ compared to all groups except indicated. ξ $p<0.001$ compared to all groups except indicated. Ns, no significant difference between indicated groups.

6.2.4.5 Expression of cardiac stress markers

Heart failure is associated with a reversion from an adult to a foetal pattern of expression of cardiac genes[200, 201]. Concordant with echocardiographic, haemodynamic and morphometric indices indicative of established heart failure, analysis of gene expression from *Fh1$^{f/f}$ Cre/+* hearts by qPCR demonstrated a significant reduction in adult and increase in foetal isoform expression (Figure 81). Moreover, consistent with a partial rescue by cytosolic FH of the *Fh1* null cardiac phenotype, *Fh1$^{f/f}$ Cre/+ KI^{FHcyt}* hearts demonstrated levels of foetal and adult

isoform gene expression that were either intermediate between those of control and *Fh1*$^{f/f}$ *Cre/+* hearts, or equivalent to that of control (Figure 81).

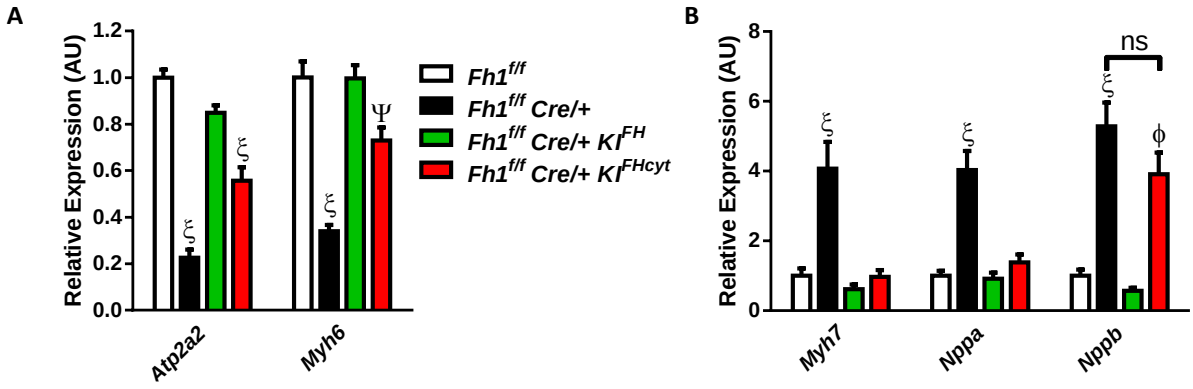

Figure 81 – Reversion from adult to foetal pattern of gene expression in *Fh1*$^{f/f}$ *cre/+* mice is ameliorated by KI^{FH} or KI^{FHcyt}

Relative expression in arbitrary units assessed by qRT-PCR and analysed by the $2^{-\Delta\Delta Ct}$ or comparative C_T method using the internal control in cardiac beta actin (encoded by *Actb*) and normalised to levels in *Fh1*$^{f/f}$ hearts. **A.** Expression of adult genes. *Atp2a2*: Sarcoplasmic-endoplasmic reticulum ATPase 2a; *Myh6:* α-myosin heavy chain. **B.** Expression of foetal genes. *Myh7*: β-myosin heavy chain; *Nppa*: natriuretic peptide A; *Nppb*: natriuretic peptide B. Ψ $p<0.05$ compared to all groups except indicated. Φ $p<0.01$ compared to all groups except indicated. ξ $p<0.001$ compared to all groups except indicated. Ns, no significant difference between indicated groups.

6.2.4.6 Histology demonstrates hypertrophy and fibrosis in Fh1$^{f/f}$ *Cre/+ and Fh1*$^{f/f}$ *Cre/+ KI*^{FHcyt} *hearts*

Figure 82 illustrates sections from hearts of *Fh1*$^{f/f}$, *Fh1*$^{f/f}$ *Cre/+*, *Fh1*$^{f/f}$ *Cre/+KI*^{FH} and *Fh1*$^{f/f}$ *Cre/+ KI*^{FHcyt} hearts stained with haematoxylin and eosin. Clear hypertrophy of *Fh1*$^{f/f}$ *Cre/+* and *Fh1*$^{f/f}$ *Cre/+ KI*^{FHcyt} hearts in comparison to control hearts was evident. Consistent with the findings of gross hypertrophy and elevated cardiac mass of *Fh1*$^{f/f}$ *Cre/+* and *Fh1*$^{f/f}$ *Cre/+ KI*^{FHcyt} hearts, wheat germ agglutinin staining indicated statistically significant hypertrophy of individual cardiomyocytes. This hypertrophy was partially ameliorated in *Fh1*$^{f/f}$ *Cre/+ KI*^{FHcyt} hearts comparative to *Fh1*$^{f/f}$ *Cre/+*. Figure 83 depicts representative wheat germ agglutinin images of hearts of each genotype (2 hearts per genotype, 4 images obtained per slide). Sirius red staining (Figure 84) revealed mild interstitial fibrosis in both *Fh1*$^{f/f}$ *Cre/+* and, but not *Fh1*$^{f/f}$, *Fh1*$^{f/f}$ *Cre/+ KI*^{FH} or *Fh1*$^{f/f}$ *Cre/+ KI*^{FHcyt} hearts (representative images

from Sirius red stained hearts of each genotype illustrated, 2 hearts per genotype, 3 images per heart obtained).

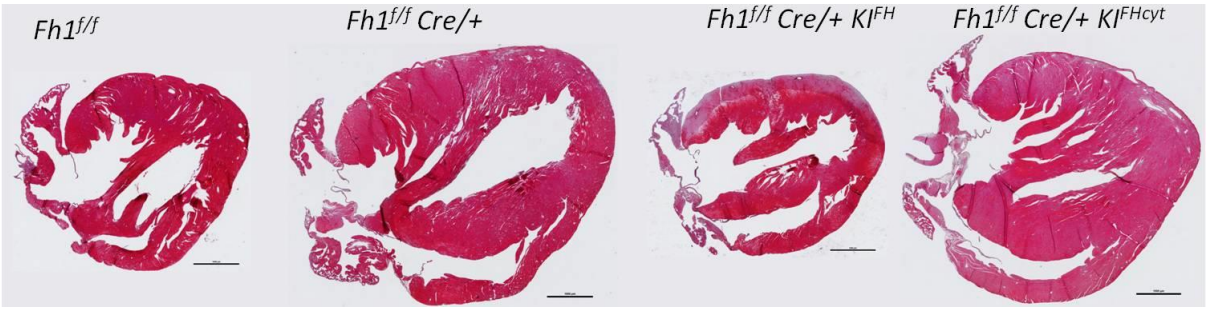

Figure 82 – Haematoxylin and eosin stained sections demonstrating hypertrophy in *Fh1$^{f/f}$ Cre/+* and *Fh1$^{f/f}$ Cre/+ KI^{FHcyt}* hearts
Scale bar = 1 mm.

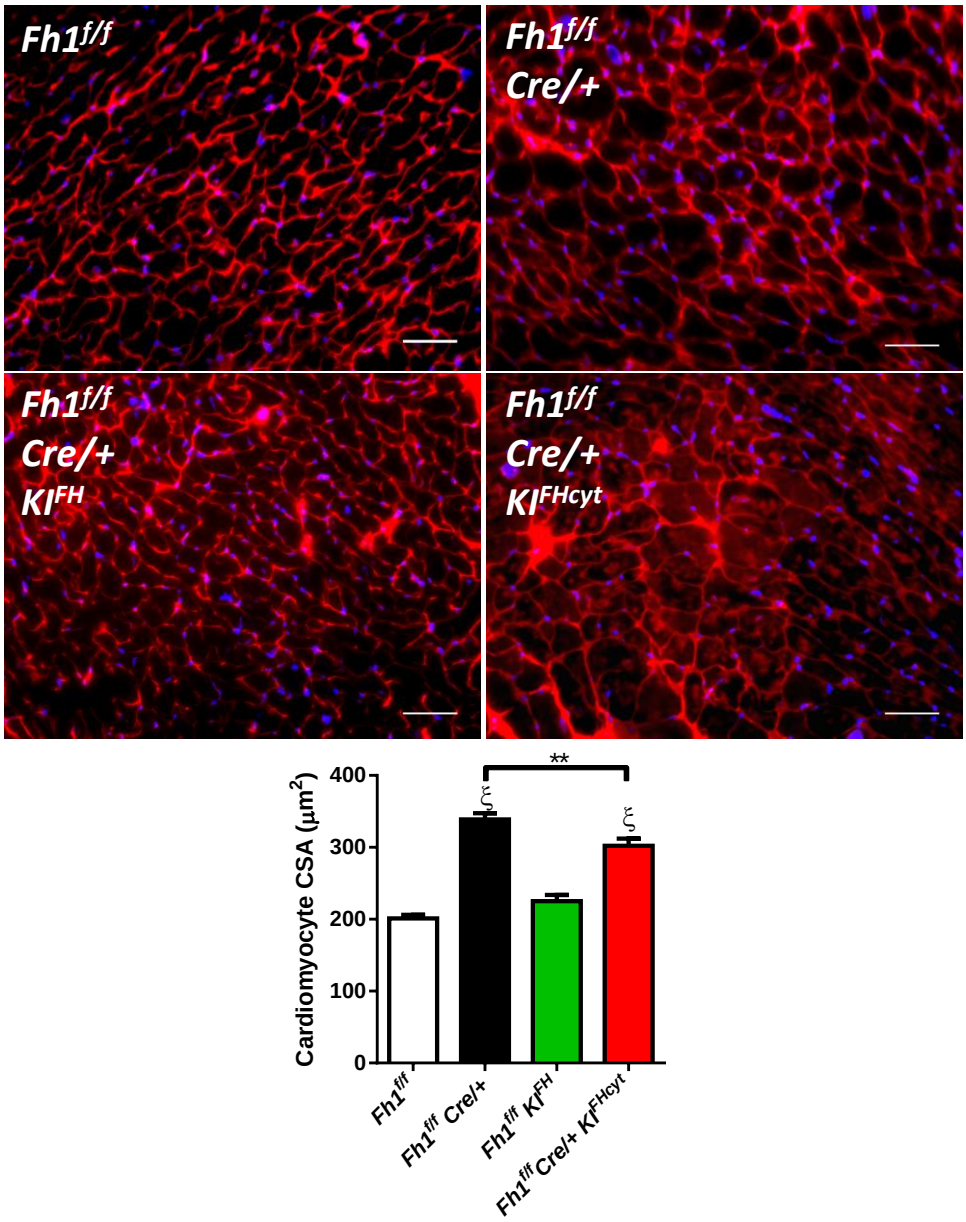

Figure 83 – Wheatgerm agglutinin staining demonstrating increased cardiomyocyte size in *Fh1*$^{f/f}$ *Cre/+* and *Fh1*$^{f/f}$ *Cre/+ KI*^{FHcyt}
Scale bar = 100 µm.

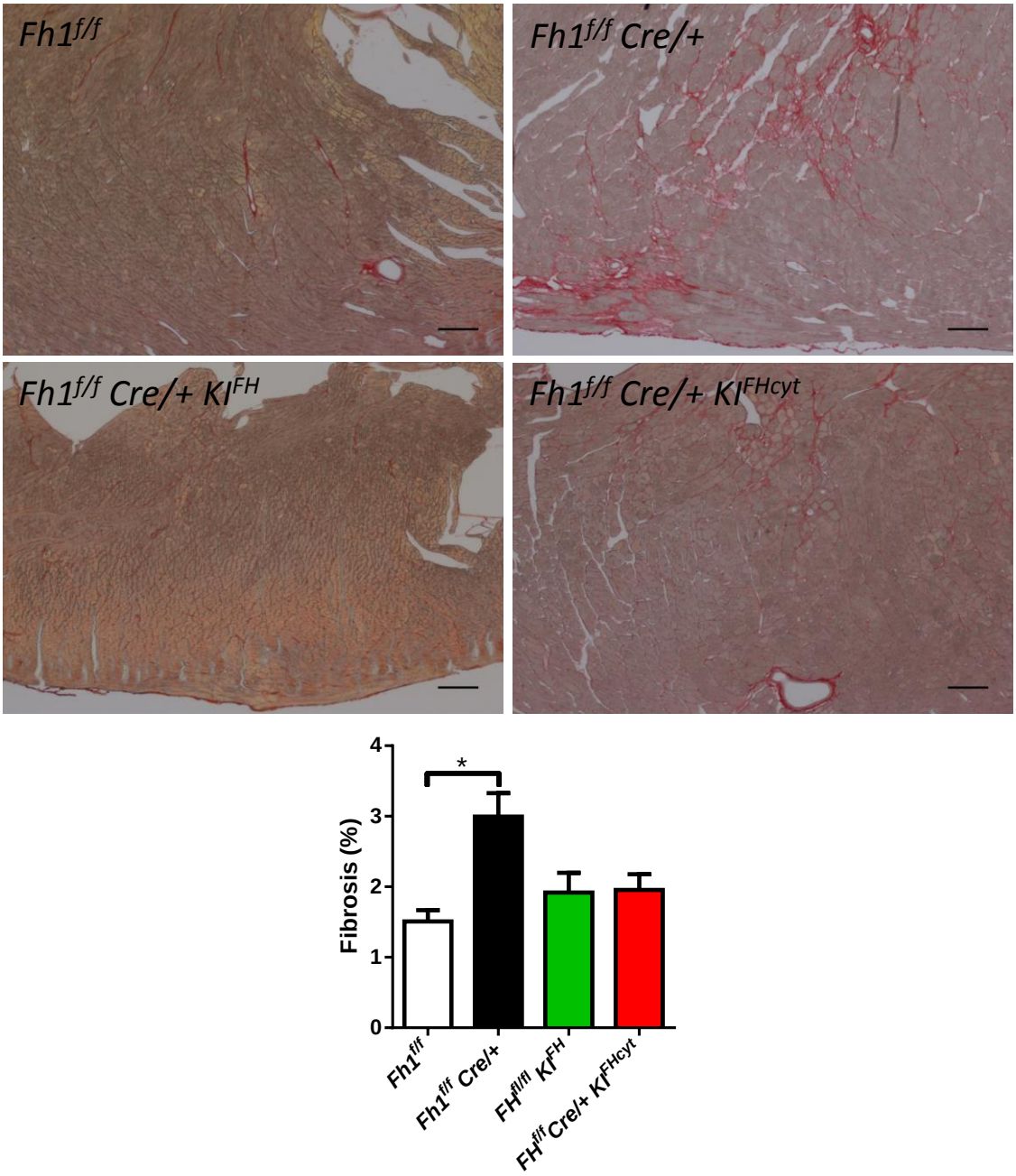

Figure 84 – Sirius red staining demonstrating myocardial fibrosis in *Fh1 Cre/+* and *Fh1 Cre/+ KI^{FHcyt}* mice
Scale bar = 100 µm.
Graph demonstrates fibrosis assessed from Sirius red stained dark field images and expressed as a percentage of the total tissue area from corresponding bright field images.

6.2.5 Reversal of NRF2 target gene activation by dual-localised and cytosolic FH

As described in Chapter 4, NRF2 target gene expression is observed to be significantly increased in *Fh1$^{f/f}$ Cre/+* hearts. Expression of dual localised FH significantly reduced

transcript expression of three out of four NRF2 target genes tested by qPCR, namely: haem oxygenase 1 (*Hmox1*), methylenetetrahydrofolate-dehydrogenase 2 (*Mthfd2*) and NAD(P)H dehydrogenase, quinone 1 (Nqo1). In comparison, cytosolic FH expression reduced expression of only *Hmox1* and *Nqo1*.

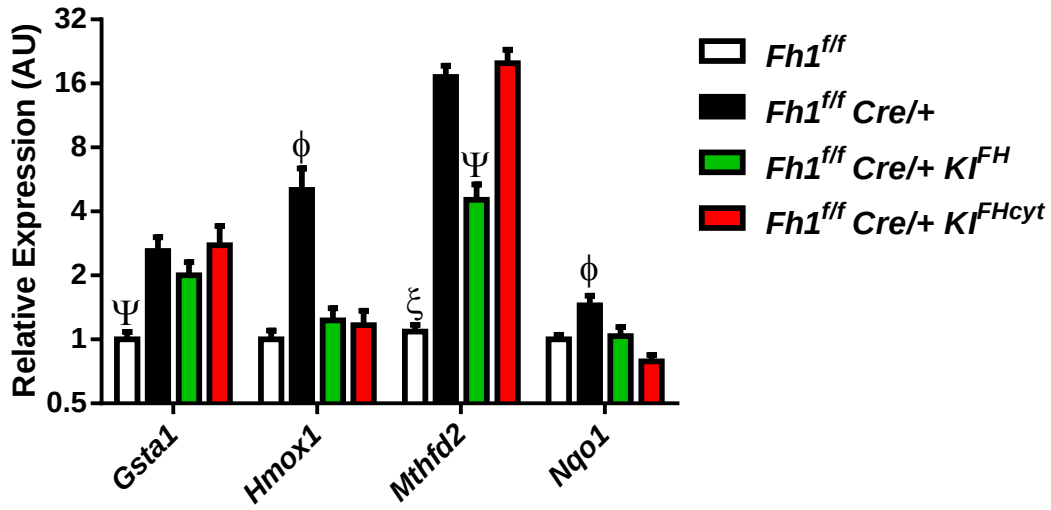

Figure 85 – KI^{FH} and KI^{FHcyt} return the elevated levels of NRF2 target genes found in the FH null heart towards normal
Relative expression in arbitrary units (AU) of NRF2 target genes assessed by qPCR and normalised to levels in *Fh1$^{f/f}$*. *Gsta1*: Glutathione S transferase A1; *Hmox1*: Haem oxygenase 1; *Mthfd2*: methylenetetrahydrofolate-dehydrogenase 2; *Nqo1*: NAD(P)H dehydrogenase, quinone 1. Ψ $p<0.05$ compared to all groups. Φ $p<0.01$ compared to all groups. ξ $p<0.001$ compared to all groups. Note logarithmic scale.

6.2.6 Cardiac total adenine nucleotide and creatine pools

Consistent with the findings presented in Chapter 4, high performance liquid chromatography revealed a reduction in total adenine nucleotide (TAN) and creatine (TCr) pools of *Fh1$^{f/f}$ Cre/+* hearts compared to *Fh1$^{f/f}$* controls. The introduction of dual-localised FH restored TAN and TCr to control levels. Cytosolic-FH expression resulted in partial amelioration of the adverse *Fh1* null cardiac energetic phenotype, with TAN and TCr levels intermediate between those observed in control and *Fh1* knockout hearts (Figure 86).

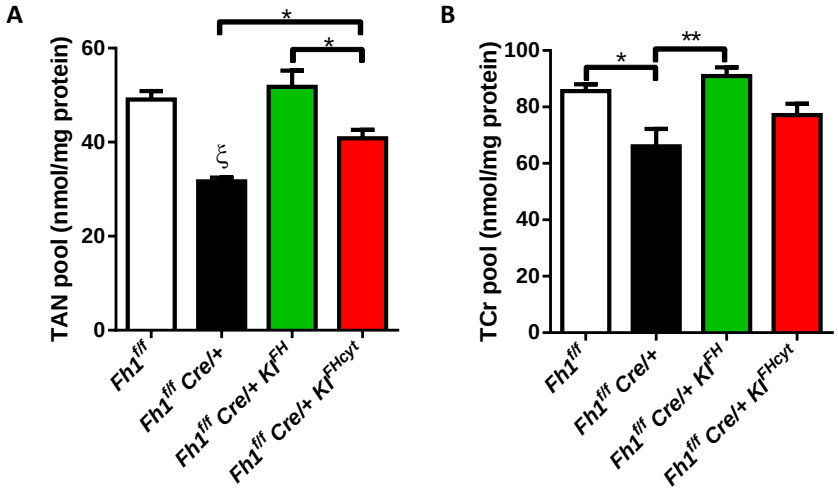

Figure 86 – Depletion of the total adenine nucleotide (TAN) pool in *Fh1$^{f/f}$ Cre/+* hearts is reversed by KI^{FH} and KI^{FHcyt}

A. Total adenine nucleotide (TAN) and **B.** Total creatine (TCr) pools, both measured by high performance liquid chromatography and normalised to total protein content measured by Lowry assay. * $p<0.05$ between indicated groups. ξ $p<0.001$ compared to all groups unless otherwise indicated.

6.3 Discussion

6.3.1 Summary of chapter findings

Using a combination of *in vitro* (adenoviral transfection of *Fh1* null MEFs with FH encoding constructs) and *in vivo* (knock-in of dual-localised or cytosol-specific FH in the context of cardiac Fh1 ablation) approaches, the work presented in this chapter demonstrates that:

- Deletion of the mitochondrial targeting sequence of FH results in its exclusion from the mitochondria, leading to cytosolic FH localisation.
- In mammalian cells, mutation of the second start codon of FH does not result in exclusive mitochondrial targeting.
- Cytosolic FH expression is sufficient to reverse the pseudohypoxic response of *Fh1*$^{-/-}$ MEFs.
- Knock-in of human FH under the control of a global promoter results in complete reversal of the cardiomyopathy arising from cardiac *Fh1* deletion.
- Cytosolic FH mediates a partial reversal of NRF2 antioxidant pathway signalling in *Fh1* null MEFs and hearts and, in addition, is sufficient to partially rescue the severe dilated cardiomyopathic phenotype associated with cardiac Fh1 deletion.

6.3.2 Specific localisation of FH to the cytosol or mitochondria

Like many other mitochondrial proteins, FH is directed to the mitochondria by an amino-terminal mitochondrial targeting sequence (MTS)[171]. Several studies in mammalian and yeast cells have attempted to address the exact mechanism(s) by which fumarate hydratase and its yeast ortholog, fumarase, are dual-localised to the mitochondria and cytosol. While localisation of fumarase in yeast has been extensively investigated, studies in mammalian cells have been more limited and it appears that this mechanism may be subtly different in

yeast and mammalian cells[171]. In yeast, fumarase is expressed as a single translation product with a MTS. This precursor is targeted to the mitochondria. All fumarase molecules begin to be imported into the mitochondria and, during import, mitochondrial processing peptidase (MPP) cleaves the MTS to generate mature fumarase. Some fumarase molecules fully translocate into the mitochondria, whilst others return to the cytoplasm in a process termed reverse translocation. In support of this, when mitochondrial import of fumarase is blocked, all fumarase molecules accumulate in the cytosol as high molecular weight precursors[174]. In both yeast and mammalian cells the FH MTS begins with a start codon and is followed by another in-frame start codon at the beginning of the region encoding the mature FH peptide. In mammalian cells, it is thought that alternative initiation of translation from the pre-MTS or post-MTS start codon results in production of mitochondrial or cytosolic FH, respectively. This is supported by evidence that *in vitro* (cell free) translation results in formation of both high molecular weight FH (with MTS) and lower molecular weight FH (without an MTS)[176, 318].

In accordance with published data, immunofluorescence microscopy and western blotting of subcellular fractions from adenoviral transfected *Fh1*$^{-/-}$ MEFs demonstrated that deletion of the MTS resulted in a cytosol-specific distribution of FH[171, 179, 180]. To fully distinguish between the specific mitochondrial and cytosolic roles of FH, however, a method of targeting FH specifically to the mitochondria but not the cytoplasm would have been desirable.

Using fumarase-deficient yeast, Wu *et al.* demonstrated that introduction of a fumarase construct with a point mutation in the second start condon resulted in fumarase activity in the mitochondrial but not the cytosolic fraction[178]. In mammalian cells RNAse H1 is dual-localised to the mitochondria or nucleus by differential initiation of translation from

alternative start codons preceding or following the MTS[319]. Mutation of the start codon following the MTS results in specifically mitochondrial (and not nuclear localisation) of RNAse H1[319]. Based upon this evidence from both yeast and mammalian models, an adenoviral construct with a mutated second start codon of FH (termed AdFHΔATG) was generated with the specific aim of targeting FH solely to mitochondria. However, anti-FH immunoblotting of the cytosolic fraction from cells expressing the AdFHΔATG construct revealed similar levels of cytosolic FH in AdFHΔATG expressing cells to those expressing a wildtype FH construct. Consistent with this finding, in a yeast model, Stein *et al.* demonstrated that fumarase with the second start codon replaced by a valine codon (i.e. changing all 3 bases) was expressed in both the cytosol and the mitochondria[174]. However, this fumarase also had reduced activity which the authors speculated to be due to failure of MPP to cleave the mitochondrial targeting sequence[174].

It is possible for mammalian cells to initiate translation from a non-canonical (non-AUG) start codon. Supporting this is the observation that seven of the nine possible point mutations of the dihydrofolate reductase start codon retained the ability to initiate translation[320]. Therefore it may be pertinent to use *in vitro* (cell free) translation to investigate whether low molecular weight FH (without an MTS) can be produced from FHΔATG derived mRNA. If a low molecular weight (FH without an MTS) product is formed, it would be informative to generate constructs with different second ATG mutations or complete deletion of the second start codon and explore if any of these constructs produce only high molecular weight FH in a cell-free translation system. Subsequently subcellular fractionation and immunoblotting could be used to investigate whether any of these second start codon mutations reduced FH expression in the cytosolic fraction. Introduction of a Kozak sequence 5’ of the first ATG

may increase translational initiation from this codon and thereby increase the proportion of FH in the mitochondria as opposed to cytoplasm.

If *in vitro* translation revealed that only FH with an MTS (and not low molecular weight without an MTS) was produced by the FHΔATG construct, this would suggest that cytosolic FH was not exclusively produced by differential translation from the second AUG. Indeed, whilst the production of two different sized products by cell-free translation of FH mRNA suggests that differential initiation of translation occurs, it does not entirely preclude a role for reverse translocation in the generation of cytosolic FH in mammalian cells. If this were the case, use of mechanisms shown to increase mitochondrial localisation in yeast may have a similar effect in mammalian cells. For example, Regev-Rudzki *et al.* demonstrated that swapping the MTS of fumarase in yeast for that of aconitase (which has a more mitochondrial distribution than fumarase) increased the proportion of fumarase molecules in the mitochondrial fraction[321], whilst expression of the *E. coli* fumarase ortholog FumC fused to a the "strong" MTS of *Neurospora crassa* mitochondrial ATPase subunit 9 (Su9) in yeast has been shown to result in mitochondrial-specific expression of FumC [322]. In addition, it appears that the MTS of exclusively mitochondrial proteins are more potent than those of dual-localised proteins, containing less hydrophobic and basic residues[323]. Therefore, in principle it may be possible to direct fumarate hydratase exclusively to the mitochondria by replacing the native MTS with a more effective MTS from a protein exhibiting exclusive mitochondrial targeting. To explore this possibility further, one approach would be to replace the FH MTS with the MTS of a panel of different mitochondrial proteins and assess the resulting effect upon the relative distribution of FH between mitochondria and cytoplasm. In yeast, fusion of dual-localised aconitase with a degron (encoding a degradation signal) leads to depletion of cytosolic aconitase by proteasomal degradation, whilst protecting

mitochondrial aconitase[324]. It may be possible to elicit degradation of cytosolic FH in a similar manner, effectively producing a model of mitochondrial-specific FH expression.

6.3.3 Cytosolic FH is sufficient to ameliorate aberrant HIF and NRF2 signalling associated with the FH null state

Concordant with published data, *Fh1* null MEFs exhibit a pseudohypoxic response which is completely reversed by augmentation of dual-localised or cytosol-specific FH[179]. However, in Fh1 null cardiac tissue no basal pseudohypoxic response was observed (Chapter 4).

Fh1 knockout MEFs also exhibit up-regulation of antioxidant signalling characterised by elevated expression of classic NRF2 target genes. This was ameliorated by expression of dual-localised or cytosol-specific FH. However, expression of one NRF2 target, *Mthfd2*, was not significantly reduced by cytosolic FH expression. Akin to MEFs and consistent with published data, upregulation of NRF2 targets was demonstrated in Fh1 null hearts[166]. *Hmox1* and *Nqo1* transcript expression were restored to control levels by knock-in of either dual-localised or cytosolic FH. However, no reversal of the elevation in *Gsta1* transcript and only a partial reduction in *Mthfd2* transcript level was observed following expression of dual-localised FH, with no change upon introduction of cytosolic FH. The failure of KI^{FH} to restore levels of *Gsta1* and *Mthfd2* to normal was particularly surprising as $Fh1^{f/f}$ *Cre/+* KI^{FH} mice were indistinguishable from $Fh1^{f/f}$ controls in every other parameter assessed. It is possible that the catalytic activity of V5-tagged human FH in mouse cardiomyocytes is lower than the endogenous Fh1 activity in $Fh1^{f/f}$ controls with the consequence that some fumarate accumulation occurs sufficient to activate a subset of NRF2 target genes. This phenomenon could occur due to the inhibition of FH catalytic activity by the V5 tag, or interspecies differences in enzyme activity (with human FH potentially less effective in murine cells), or

simply due to lower protein expression in cardiomyocytes. In support of the latter, western blotting demonstrated that whilst V5-tagged FH was expressed in the heart, FH levels were lower in the *Fh1*$^{f/f}$ *Cre/+ KI*^{FHcyt} group compared to *Fh1*$^{f/f}$ controls, with the presence of a lower molecular weight band suggestive of a degree of KI^{FH} degradation.

6.3.4 Cytosol-specific FH expression confers substantial amelioration of the Fh1$^{f/f}$ *Cre/+ cardiac phenotype*

Kaplan-Meier survival analysis, echocardiographic assessment of function, *ex vivo* organ weights and expression of cardiac stress markers all demonstrated significant rescue of the *Fh1*$^{f/f}$ *Cre/+* cardiomyopathy by the expression of cytosolic FH. The presence of residual cardiac dysfunction and left ventricular hypertrophy in *Fh1*$^{f/f}$ *Cre/+ KI*^{FHcyt} hearts at the 105 day time point chosen for assessment indicated that this rescue was only partial however. Cytosolic FH augmentation appeared to delay the transition to overt heart failure already evident in *Fh1*$^{f/f}$ *Cre/+* mice by this age. In contrast to other modalities, invasive haemodynamic assessment did not demonstrate improvement of cardiac dysfunction by cytosolic FH. However, several of the sickest *Fh1*$^{f/f}$ *Cre/+* mice, but no *Fh1*$^{f/f}$ *Cre/+ KI*^{FHcyt} mice, died prior to or during invasive haemodynamic assessment likely skewing the dataset. It is possible that inclusion of these mice (if it had been feasible) would have provided a more faithful readout of the true degree of impairment in invasive haemodynamic indices present in the *Fh1* null population. Accordingly, this would have improved the power of the study to identify a biologically relevant signal for difference between these and *Fh1*$^{f/f}$ *Cre/+ KI*^{FHcyt} mice. In hindsight, one strategy to circumvent these difficulties could have been to formally assess cardiac function at an earlier time point, for example 90 days, before significant loss of *Fh1*$^{f/f}$ *Cre/+* mice.

There are several potential mechanisms by which cytosolic FH augmentation could provide a partial rescue of the *Fh1* null phenotype. As the cardiac total adenine nucleotide (TAN) and total creatine (TCr) levels of *Fh1*$^{f/f}$ *Cre/+ KI*^{FHcyt} mice were intermediate between those of *Fh1*$^{f/f}$ controls and *Fh1*$^{f/f}$ *Cre/+* mice, it is possible that cytosolic FH expression results in an energetic rescue of the FH null phenotype. Flux balance analysis suggests that cytosolic FH would fully rescue the energetic phenotype of Fh1 depletion if flux of excess fumarate from the mitochondria were unlimited; however, as there is no known specific fumarate transporter this appears unlikely. Cytosolic FH activity could plausibly convert any fumarate generated by the TCA cycle and released from the mitochondria, in addition to fumarate from the urea cycle, purine nucleotide cycle and *de novo* purine biosynthesis pathways into malate. This malate may then be transported into the mitochondria by the action of the malate-aspartate shuttle to replenish the second span of the TCA cycle, facilitating ATP generation by oxidative phosphorylation. However, as previously discussed in Chapter 4, it is difficult to determine whether the observed elevations in TAN and TCr are a cause or consequence of improved cardiac function.

A further possible mechanism by which cytosolic FH augmentation may improve cardiac function is by preventing or reducing cytosolic fumarate accumulation. Fumarate accumulation may lead to oxido-reductive stress via activation of Nrf2 signalling which is partially ameliorated by cytosolic FH augmentation. As described in Chapter 4, published studies have identified a role for aberrant Nrf2 signalling and reductive stress in a model of protein aggregation cardiomyopathy[245, 247]. While homozygous knockout of *Nrf2* does not reverse the *Fh1* null phenotype, heterozygous deletion of *Nrf2* significantly lengthened the lifespan of *Fh1*$^{f/f}$ *Cre/+ Nrf2*$^{+/-}$ mice (Chapter 4), suggesting that the role of Nrf2 signalling in the pathogenesis of Fh1 null cardiomyopathy is complex. Nrf2 has multiple target genes and

it is feasible that elevation of some targets is detrimental, whilst others may be beneficial in the context of loss of Fh1. *Fh1*$^{f/f}$ *Cre/+ KI*^{FHcyt} hearts exhibited reduced activation of a subset of Nrf2 targets, which may contribute to alleviation of reductive stress and consequent amelioration of cardiac dysfunction. It is worthwhile noting in this regard that while cytosolic FH would only decrease activation of Nrf2 targets to control levels, homozygous knockout of *Nrf2* would be expected to entirely ablate any contribution of Nrf2 to baseline expression of its target genes. For example, *Nqo1* transcript is significantly reduced in *Fh1*$^{f/f}$ *Cre/+ Nrf2*$^{-/-}$ mice compared to *Fh1*$^{f/f}$ controls (Chapter 4).

An additional mechanism whereby metabolism of fumarate by cytosolic FH may ameliorate the *Fh1*$^{f/f}$ *Cre/+* cardiac phenotype is by elimination of cytosolic fumarate, thereby relieving end-product inhibition of the urea cycle, purine nucleotide cycle and *de novo* purine synthesis. Inhibition of the urea cycle, by fumarate, may lead to accumulation of toxic ammonia and thereby potentially contribute cardiac dysfunction in *Fh1* null mice. Traditionally, ammonia detoxification by the urea cycle is thought to play the most important role in the liver and kidneys, however a functioning partial urea cycle also plays a key role in nitric oxide signalling in cardiomyocytes which can affect cardiac contraction and relaxation rates[325, 326]. This partial urea cycle includes the fumarate-producing enzyme argininosuccinate lyase (ASL) (Figure 87)[327]. Fumarate accumulation and subsequent end-product inhibition of adenylosuccinate lyase is likely to prevent *de novo* purine synthesis and recycling of purine nucleotides by the purine nucleotide cycle, leading to reduced purine nucleotide levels and potentially cardiac dysfunction. In cellular models, accumulation of succinyl-5-aminoimidazole-4-carboxamide-1-ribose-5'-phosphate (SAICAR), a substrate of adenylosuccinate lyase, activates ERK1/2 signalling[303]. The ERK1/2 pathway has been

associated with cardiac hypertrophy and remodelling suggesting a further potential mechanism by which cytosolic FH may alleviate the *Fh1* null phenotype.

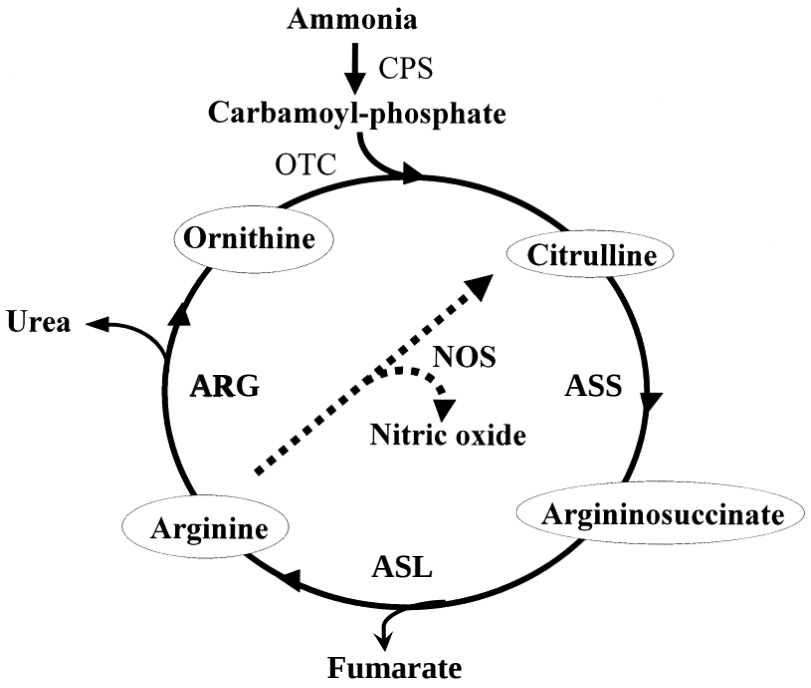

Figure 87 – The urea cycle[14]
Carbamoyl phosphate synthetase (CPS), ornithine transcarbamylase (OTC), argininosuccinate synthetase (ASS), argininosuccinate lyase (ASL), arginase (AR), nitric oxide synthase (NOS).

While the precise mechanism(s) underlying the cardiomyopathy rescue by cytosolic augmentation of Fh1 are unclear, it does highlight the importance of extra-mitochondrial excess fumarate in this model. This may appear surprising given the overall relatively modest levels of fumarate increase identified in the hearts of *Fh1*$^{f/f}$ *Cre/+*mice. However, such measurements of total myocardial fumarate do not provide much insight into baseline wild-type relative compartmental concentrations, or the fold-change of fumarate in response to interventions such as replenishing cytosolic FH. Neither do they provide direct information on the flux of pathways metabolising fumarate. Even small increases in cytosolic fumarate have the potential to cause a multitude of non-linear downstream cellular changes via

[14] Adapted from Nagasaka, H. et al. Nitric oxide synthesis in ornithine transcarbamylase deficiency: Possible involvement of low NO synthesis in clinical manifestations of urea cycle defect. *The Journal of Pediatrics* **145**, 259-262 (2004).

interaction with KEAP1 to promote NRF2 signalling, induction of succination (~2.5-fold pan-succination evaluated using an anti-2SC antibody in the present model)[166] and inhibition or reversal of urea cycle metabolism[180]. The evolutionarily high degrees of conservation of cytosolic FH and the significant relative proportion of cytosolic FH molecules[171] suggest an important physiological role. Accordingly, the restoration of cytosolic fumarate hydratase activity, has the potential to ameliorate *Fh1*$^{f/f}$ *Cre/+*cardiomyopathy probably by relieving the consequences of cytosolic fumarate excess or providing a bypass mechanism for fumarate from cytosolic and potentially mitochondrial sources (if released from the mitochondria) to be converted to malate and transported into the mitochondria to replenish the TCA cycle.

7 CHAPTER 7: DISCUSSION AND CONCLUSIONS

7.1 Summary

This thesis explores the regulation of metabolism in the heart through two broad but interrelated approaches: i) cardiac-specific deletion of the master transcription factor, hypoxia inducible factor-1α (HIF-1α), which (amongst other functions) augments glycolysis and inhibits oxidative phosphorylation; and ii) cardiac ablation of the integral tricarboxylic acid (TCA) cycle enzyme, fumarate hydratase, which has been shown in some experimental settings to stabilise HIF-1α in normoxic conditions via a pseudohypoxic response.

The body of work presented in chapter 3 demonstrates that chronic loss of endogenous *Hif-1α* after coronary artery ligation induced-myocardial infarction does not appear to have an overt effect upon cardiac function in mice. Taking into consideration previous studies which demonstrate that HIF-1α is acutely beneficial in myocardial ischaemia [98, 99, 101, 102, 328], whilst chronic supraphysiological Hif-1α augmention is deleterious in the heart [60, 112], the findings from the present work further underline the complex effects of HIF-1α signalling in ischaemic states and suggests that the effect of HIF-1α in the ischaemic myocardium are both temporally and dosage-dependent.

The survival and viability of mice with cardiac-specific deletion of a key TCA cycle enzyme – fumarate hydratase – explored in subsequent data chapters (4, 5 and 6), demonstrates the metabolic plasticity and adaptability of the heart, an organ with very high energetic demands. Whilst disruption of the mitochondrial TCA cycle is highly likely to directly contribute to the eventual cardiomyopathy observed in cardiac *Fh1* null mice, partial rescue of the phenotype by cytosolic FH augmentation demonstrates that loss of cytosolic FH activity is likely to influence the phenotype. Heterozygous deletion of nuclear factor (erythroid-derived 2)-like 2

(Nrf2) (a key transcription factor involved in the antioxidant response) lengthens the lifespan of cardiac *Fh1* knockout mice significantly, while use of a pharmacologically non-specific inhibitor (DHEA) of the cytosolic enzyme, glucose-6-phosphate dehydrogenase (G6pdx) – the rate limiting enzyme in the pentose phosphate pathway (PPP), a major source of reducing equivalents – ameliorates *Fh1* null cardiac dysfunction. In conjunction with the reductive environment identified in *Fh1* null hearts, these initial findings lend some support to a hypothesis of reductive stress as playing a role in the pathogenesis of Fh1 null cardiomyopathy. If confirmed with future experimental work, the findings from the present work might add to an emerging concept that excessive reducing power may, analogous to oxidative stress in cardiovascular disease, also be deleterious in the heart, emphasising the importance of maintaining redox balance to health.

7.2 Insights into the chronic role of HIF-1α post-myocardial infarction

Whilst multiple studies have established an *acute* cardioprotective effect for endogenous and supraphysiological levels of HIF-1α using both *ex vivo* and *in vivo* models of cardiac ischaemia[98, 99, 101, 102, 328], others have reported deleterious effects of both long-term supraphysiological HIF-1α augmentation in the unstressed heart[60, 112] and for endogenous levels of HIF-1α in the context of pressure overload[61]. However, the chronic role played by endogenous, oxygen-labile HIF-1α in the setting of myocardial infarction has remained obscure. Using a cardiac-specific, temporally-inducible murine model of *Hif-1α* ablation in conjunction with the established coronary artery ligation (CAL) model of myocardial infarction, the data presented in Chapter 3 demonstrates that under the specific experimental conditions used, ablation of *Hif-1α* chronically (commencing two weeks post-ischaemic insult) had no discernible effect on cardiac function. Whilst this finding contrasts with studies of the acute and chronic effects of supraphysiological HIF-1α augmentation[60, 98, 99, 101, 102, 112,

[328], this apparent discrepancy may be attributed to temporal and HIF-1α 'dosage' differences between these models and that of the present work. Notwithstanding this, the findings from chapter 3 provide evidence that (unlike supraphysiological HIF-1α expression[110]) endogenous HIF-1α expression is not likely to be *chronically* deleterious in myocardial infarction, suggesting that therapeutic attempts focused on inhibition of chronic HIF signalling post-myocardial infarction may not necessarily lead to clinical benefit.

No evidence was found of chronic HIF-1α target gene activation by CAL in either control or *Hif-1α* null hearts. This was surprising given that HIF activation has been demonstrated in murine and human failing hearts, whilst in a mouse CAL model HIF-1α elevation persisted 4 weeks post-surgery in the peri-infarct region in control animals[60, 61, 101]. The disparity between this study and that of the current work may simply relate to the use of different time points for investigating HIF-1α signalling, being 12 weeks in the case of the current work. It is also plausible that acute HIF-1α stabilisation may have occurred at an earlier time point in the current work's model and may even have persisted in the peri-infarct region, but the signal obscured by use of whole left ventricular samples for analysis. In explanted human heart failure samples, Zolk *et al* identified upregulation of prolyl hydroxylase domain protein 3 (PHD3), HIF-3α and HIF-1α antisense transcript all of which act as negative regulators of HIF-1α[214] , whilst in cancer studies chronic hypoxia has been observed to induce expression of another negative regulator of HIF-1α – HIF-associated factor (HAF)[216]. Expression of any of these negative regulators may potentially explain why CAL surgery failed to chronically elevate HIF signalling. Importantly, a failure of CAL to chronically up-regulate HIF signalling in control hearts could readily explain why knockout of *Hif-1α* does not affect late-phase cardiac function.

The clear correlation identified between infarct size and cardiac function served to reiterate the therapeutic importance of minimising ultimate infarct size, a key goal in the clinical management of myocardial infarction. There is extensive evidence that acute HIF-1α elevation is cardioprotective and can significantly diminish infarct size post-myocardial ischaemia[98-104, 110]. Multiple HIF-1α target genes have been implicated in this effect, including inducible nitric oxide synthase (iNOS), vascular endothelial growth factor and the adenosine A_{2B} receptor[98, 101]. A recent publication has implicated induction of hexokinase II expression by HIF-1α in the prevention of mitochondrial permeability pore opening, suggesting an additional mechanism whereby HIF-1α may prevent cell death and thereby reduce infarct size[328]. Importantly infarct size is a key determinant of clinical outcomes and strongly related to parameters of cardiac function and remodelling. Seen in this light, the ability of a therapy or intervention targeting one molecular node administered beyond the acute infarct stage may be unlikely to influence infarct size unless it exerted sufficient effects on remodelling and function that outweigh the potent adverse signal caused by the initial infarct.

In summary, the findings from the present work in conjunction with published models, lends support to the concept that harnessing the cardioprotective power of HIF-1α signalling could be therapeutically beneficial in the acute phase of myocardial infarction, but that chronic inhibition of HIF-1α beyond the acute setting may not be so readily beneficial.

7.3 Failure to manipulate HIF signalling

In cancer models of fumarate hydratase (FH) deficiency, fumarate accumulation results in normoxic HIF stabilisation and signalling – i.e. a pseudohypoxic response[115, 116]. As outlined in the preceding section, HIF activation has been established as protective in models of acute

myocardial ischaemia, reducing infarct size and improving cardiac function. Accordingly, a cardiac-specific *Fh1*-null model was developed to investigate the potential for fumarate accumulation to elicit a pseudohypoxic response in the heart. However, despite successful ablation of Fh1 protein, *Fh1*-null hearts did not demonstrate pseudohypoxic HIF target gene activation. For the pseudohypoxic response to occur, accumulated fumarate competes with the prolyl hydroxylase domain protein (PHD) co-substrate 2-oxoglutarate, thereby inhibiting hydroxylation and subsequent degradation of HIFs. Thus the ratio of fumarate to 2-oxoglutarate is key in eliciting a pseudohypoxic response. In cancer models, a striking accumulation of fumarate occurs (30-400 fold); in contrast in the *Fh1* null heart only a modest increase in fumarate (1.63 fold) was observed (assessed at 5 weeks)[115, 144, 160, 166]. It is likely that this level of fumarate accumulation is insufficient to inhibit PHD activity and thereby elicit a pseudohypoxic response.

Pharmacological approaches to stabilising HIF-1α under normoxic conditions are being actively pursued as a strategy to treat a broad range of ischemic and inflammatory disorders. The loss of PHD activity is central to stabilisation of HIF-1α in both hypoxia and pseudohypoxia. In hypoxia this is due to lack of the natural PHD substrate, molecular oxygen, whilst in pseudohypoxia this occurs through competition by metabolic intermediates such as fumarate and succinate, or other small molecules (e.g. dimethyloxalylglycine (DMOG)[329]. Such small molecule inhibitors of PHDs are likely to have a range of off-target effects, in particular the inhibition of other 2-OG dependent dioxygenases. The latter are ubiquitous enzymes that catalyse the introduction of molecular oxygen-derived oxygen atoms into substrates while converting 2-OG to succinate and carbon dioxide as part of a broad range of oxidative reactions[146]. In addition to hypoxia sensing these include physiological processes as diverse as the synthesis of collagen, DNA repair, chromatin modification and

fatty acid oxidation[146]. Accordingly, an excess of intracellular fumarate sufficient to inhibit cytosolic PHD, elicit a pseudohypoxic response and activate HIF mediated signalling is also likely to non-specifically inhibit a host of other 2-OG dependent enzymes with potentially significant consequences. Furthermore in the specific case of fumarate other off-target effects involving non-oxygenase proteins can also occur such as the succination of cysteine residues in KEAP1 resulting in derepression of NRF2 activity and promotion of antioxidant response pathways. Thus, as a therapeutic means of promoting HIF-1α signalling, the relatively non-specific 2-OG dioxygenase inhibition by fumarate appears less attractive. Accordingly, a more optimal means of harnessing HIF-1α activation therapeutically would be the use of more HIF-1α selective stabilisers by ensuring better specificity for the PHD proteins. A further potential limitation is that systemic or tissue wide activation of the pseudohypoxic response by pharmacological administration of 2-OG inhibitors like fumarate is likely to activate HIF-1α irrespective of the particular cell or tissue's requirement for it. This contrasts with the pathophysiological insult of hypoxia that will in general selectively activate the HIF-1α pathway in the specific cells or tissue exposed to the hypoxic stimulus. An additional consideration is the temporal nature of the stimulus to activate HIF-1α. Typically, hypoxia will be experienced as an intermittent stimulus to the cell. Conversely, in the setting of pharmacological or genetic inhibition of PHDs e.g. by exogenous fumarate, this stimulus is chronic. This distinction may be directly relevant in both the present study's models (post-myocardial infarct and Fh1 deletion) where significant upregulation of HIF-1α signalling was expected but not identified. Thus, whilst investigations have clearly documented HIF-1α activation acutely after myocardial infarction, a more chronic state of cardiac ischaemia may do so less effectively; speculatively due to negative feedback loops such as hypoxic induction of PHD3, HIF-3α, anti-sense HIF transcript and/or hypoxia-associated factor signalling [214, 215]. In common with the CAL model, genetic ablation of Fh1 as a means of augmenting

cardiac tissue fumarate appeared insufficient to activate a pseudohypoxic response. In particular the HIF-1α target PHD3 is more highly expressed in the heart than other tissues and negative feedback via PHD3-mediated hydroxylation may explain why a pseudohypoxic response does not occur in the heart as in the kidney. Alternatively, it is possible that the different metabolic milieu of the heart, specifically a lower ratio of inhibitory fumarate to 2-OG, may underlie differential HIF activation response compared to the kidney.

7.4 Cardiac ablation of the TCA cycle enzyme fumarate hydratase is compatible with life but associated with heart failure in adult mice

Despite lack of the anticipated pseudohypoxic response, the cardiac-specific *Fh1* knockout mouse model developed provided a platform to investigate the effect of disrupting the tricarboxylic acid cycle (TCA) in the highly metabolically active heart. Perhaps surprisingly, $Fh1^{f/f}$ *Cre/+* mice were viable, fertile and survived into adulthood, demonstrating the remarkable adaptability of cardiac metabolism despite perturbation of a key metabolic hub. By 3-4 months of age, however, cardiac *Fh1* null mice developed a lethal cardiomyopathy characterised by cardiac hypertrophy and severe contractile dysfunction.

Intuitively, energetic compromise, signified by the reduction in total adenine nucleotide (TAN) and total creatine (TCr) pools of *Fh1* null hearts, seems a likely consequence of ablation of a key TCA cycle enzyme, which may ultimately initiate the progression towards heart failure observed in these mice. However, depletion of the TAN and TCr pools is frequently observed in end-stage heart failure[75, 244], raising the question of whether the observed bioenergetic compromise and decline in these pools is the cause of heart failure or simply an epiphenomenon. Given that no depletion of these pools is seen at 5 weeks of age in *Fh1* null mice (prior to development of heart failure and despite transection of the TCA

cycle), it is plausible that the TAN and TCr pool reduction may be a consequence of heart failure in this model[166].

7.5 Cardiac Fh1 deletion as a model of systemic heart failure

An animal model of human heart failure will ideally mirror the human disease, recapitulate core pathophysiological features of heart failure (e.g. with respect to cardiac haemodynamics and energetic status), have a predictable progression allowing measurements and tissue analysis at defined time point, in addition to modelling extra-cardiac alterations observed in human heart failure, such as neurohormonal activation, renal dysfunction, salt and fluid retention and skeletal muscle wasting [231].

Energetic compromise is a fundamental feature of heart failure[75]. Accordingly, the use of a model disrupting a metabolic hub central to cellular energy production, as with the current Fh1 null model, is attractive. The visible muscle and weight loss of older Fh1 null mice points to the utility of this model as a platform to better understand the systemic consequences of heart failure[231, 232]. These could be specifically evaluated in the current model, e.g. assessment of plasma and/or urinary biochemistry (such as catecholamines or their metabolites, inflammatory markers, creatinine), vascular tone and muscle strength. In contrast to the CAL model involving a sudden, overwhelming insult to the heart to induce heart failure, a more progressive metabolic model of heart failure such as the Fh1 null heart may better model the gradual systemic adaptations and maladaptations that take place in the transition from compensated stable cardiac dysfunction to symptomatic heart failure. However a criticism of the Fh1 knockout model is its lack of a direct human correlate, in marked contrast to the CAL model. While providing the opportunity to make inferences from whole heart tissue assessment (i.e. more homogenous pathological/molecular changes in a

genetic model of heart failure compared to marked regional differences post-CAL), metabolic models of heart failure might not be expected to necessarily model the systemic consequences more faithfully than successful CAL surgery. Given the inherent variability in infarct size post-CAL, however, the use of a genetic metabolic model would minimise variability due to myocardial insult by ensuring more uniform disruption of myocardial homeostasis independent of anatomical variability or operator technique.

An additional consideration is the broad range of existing genetic mouse models of heart failure, including highly cardiac specific models without infarction but which are more clinically relevant because they incorporate the disease alleles identified in human disease, (e.g. transgenic mice bearing the Arg403Gln α-myosin heavy-chain mutation[220] or E99K mutation in α-cardiac actin[330]). Overall, given the complexity of human heart failure and that it does not reflect a single disease, a better understanding of the pathogenesis of both cardiac and systemic consequences is likely to be obtained by integrating insights from a number of models and approaches.

7.6 A role for reductive stress in *Fh1* null cardiomyopathy?

In *Fh1*-deficient cancers, succination of Keap1 by accumulated fumarate prevents it from interacting with and promoting the degradation of Nrf2. Despite a failure to replicate the pseudohypoxic response demonstrated in FH-deficient cancers, activation of NRF2 signalling was evident in *Fh1* null hearts, suggesting that lower levels of fumarate are required for succination of Keap1 than for inhibition of PHD activity. Activation of the NRF2 antioxidant pathway, in combination with the finding of an extension in lifespan of cardiac *Fh1* knockout mice with concurrent heterozygous deletion of *Nrf2* and preliminary data supporting the

presence of a significant reductive milieu in the *Fh1* null heart, raised the possibility that reductive stress could potentially contribute to the development of cardiomyopathy associated with the *Fh1* null state. Rajasekaran *et al* set a precedent for a causative role for reductive stress leading to cardiac dysfunction in their model of protein aggregation cardiomyopathy (PAC)[245]. However, whilst homozygous Nrf2 deficiency reverses the cardiac dysfunction associated with PAC, it failed to ameliorate the cardiac dysfunction in *Fh1* null mice. It is possible that in the context of *Fh1* deletion the expression of some Nrf2 targets is beneficial, whilst others directly contribute to the reductive stress environment and are harmful. In support of this, the Nrf2 target, malic enzyme 1, was predicted by flux balance analysis to facilitate replenishment of the second span of the TCA cycle.

Initial exploration of this hypothesis, with the intention of relief of putative reductive stress without inhibiting the potentially beneficial aspects of Nrf2 signalling, utilised treatment of cardiac *Fh1* null mice with the endogenous steroid dehydroepiandrosterone (DHEA). Amongst DHEA's diverse effects, is the inhibition of glucose-6-phosphate dehydrogenase (G6pdx), the rate limiting enzyme in the pentose phosphate pathway and a major source of reducing equivalents within the cell. DHEA treatment resulted in striking improvement of cardiac systolic function of *Fh1* null mice as reflected by echocardiography and invasive haemodynamic assessment. Future experiments will be required to delineate to what extenet and whether this substantial phenotypic rescue by DHEA is due to PPP inhibition and reduction of cellular reducing equivalents. Of note, whilst oxidative stress has been implicated and well-described in numerous cardiac pathologies[245, 331], the potential causative role of reductive stress in cardiac disease has largely been overlooked. A relatively small number of studies [245, 332] lend support to a concept that excessive reducing power *per se* can

be deleterious to cardiac function, thereby emphasising the critical importance of redox homeostasis in the heart.

7.7 Expression of cytosolic FH partially rescues *Fh1* null cardiomyopathy

Succination of Keap1 (ultimately leading to activation of NRF2 signalling) and inhibition of the urea cycle, purine nucleotide cycle and *de novo* purine synthesis by accumulated fumarate are all likely to be cytosolic phenomena. Cytosol-specific FH augmentation resulted in partial amelioration of the cardiac dysfunction seen in *Fh1* null hearts, providing strong support for the concept that loss of cytosolic *Fh1* activity *per se* directly contributes to the deleterious phenotype. The mechanism of cytosolic FH rescue remains obscure however. Bypass of the mitochondrial TCA cycle by cytosolic conversion of fumarate to malate and subsequent import of malate into the mitochondria is one plausible mechanism. However, other possibilities include: relief of inhibition of any of the urea cycle, the purine nucleotide cycle and/or de novo purine biosynthesis, or prevention of reductive stress through partial reversal of NRF2 signalling. That cytosolic FH only mediated a partial reversal of NRF2 target gene activation likely reflects its failure to sufficiently reduce cytosolic fumarate levels.

7.8 Further study

Flux-balance analysis (FBA) identified a large number of pathways predicted to have altered flux in the *Fh1* null cardiomyocyte. In particular, FBA highlighted the importance of anaplerotic replenishment of the second span of the TCA cycle, potentially by pyruvate conversion to malate through malic enzyme activity, and/or pyruvate conversion to oxaloacetate by pyruvate carboxylase and/or transamination of aspartate. Although an attempt was made to investigate the role of malic enzyme in this model *in vivo*, the dose and duration of inhibitor treatment was limited by non-cardiac side effects and it is possible that

sufficient inhibition of malic enzyme in the heart was not achieved. Therefore it may be pertinent to investigate the role of malic enzyme and/or pyruvate carboxylase in replenishment of the second span of the TCA cycle further using an *ex vivo* model as described in Chapter 5. The importance of asparatate transamination could be investigated by supplementation of asparate or inhibition of aspartate-transminase *in vivo* or using an *ex vivo* perfused heart system. Notably, metabolomics revealed SAICAR accumulation in the *Fh1* null heart. Given that cancer models demonstrate that SAICAR can act as a signalling molecule leading to Erk1/2 activation, it would be of interest to investigate whether the Erk1/2 signalling pathway (thought to exert pro-hypertrophic effects) is activated in *Fh1* null hearts[303, 333].

Given that treatment of *Fh1*$^{f/f}$ *Cre/+* mice with the non-specific G6pdx inhibitor, DHEA, led to a striking amelioration of the *Fh1* null cardiac phenotype, it would be valuable to further investigate the mechanisms underlying this and determine whether PPP flux was indeed affected by the dosing regimen used. As discussed in Chapter 5, DHEA is steroid hormone and may rescue the *Fh1* knockout cardiomyopathy through multiple other mechanisms, include apparent direct cardioprotective effects. Accordingly, further experiments to investigate the redox status of *Fh1* null hearts after DHEA treatment (for example by measuring ROS, NADP:NADPH ratio or reduced:oxidised glutathione ratio) may be revealing in this regard.

Fumarate can inhibit the activity of the ten-eleven translocation (TET) family of DNA hydroxylases which initiate the first step in DNA demethylation, as well as Jumonji domain (JMJD) lysine demethylases (KDMs) which demethylate histones[135]. In future studies, it may be informative to investigate DNA and histone methylation patterns to investigate whether

cardiac *Fh1*-deficiency leads to epigenetic changes in gene expression. However, given that the observed levels of fumarate accumulation in the *Fh1* null heart were insufficient to inhibit PHD activity to stabilise HIF, it is possible that this would be insufficient to inhibit either of these 2-oxoglutarate dependent dioxygenases also.

To shed further light on whether the energetic compromise (signified by reduced TAN and TCr pools) observed in *Fh1* null hearts is a cause or consequence of cardiac dysfunction, serial non-invasive assessment of cardiac function and energetic status could be undertaken by ^{31}P nuclear magnetic resonance spectroscopy. However, this technique is technically challenging when applied to the mouse heart *in vivo* and if energetic compromise and cardiac function emerge near contemporaneously may be unable to further define a potential causal role for energetic dysfunction in the phenotype[241].

Finally, developing a strategy to exclusively target FH to the mitochondria (but not cytosol) may help to distinguish the relative cytosolic and mitochondrial roles of FH activity. If mitochondrial-specific FH augmentation were sufficient to completely reverse the Fh1 null phenotype, this would provide strong support for the hypothesis that TCA cycle dysfunction initiates the development of *Fh1* null cardiomyopathy. However, even in this case it would be difficult to distinguish whether TCA cycle dysfunction contributes to cardiac dysfunction through reduced flux and energetic compromise or detrimental fumarate accumulation, or both. Although there are cytosolic sources of fumarate (including the urea cycle, the purine nucleotide cycle and *de novo* purine biosynthesis), it is probable that overspill of fumarate from the mitochondria contributes to cytosolic fumarate levels and hence to succination of Keap1 and subsequent Nrf2 signalling. Accordingly, augmentation of FH exclusively in the mitochondrial compartment could reveal whether cytosolic sources of fumarate are sufficient

to initiate Nrf2 signalling, generate a reductive environment and ultimately lead to the prominent cardiac dysfunction characteristic of the FH null state.

8 REFERENCES

1. Semenza, G.L. Hypoxia-inducible factors in physiology and medicine. *Cell* **148**, 399-408 (2012).
2. Semenza, G.L. Hydroxylation of HIF-1: oxygen sensing at the molecular level. *Physiology* **19**, 176-182 (2004).
3. Schofield, C.J. & Ratcliffe, P.J. Oxygen sensing by HIF hydroxylases. *Nat Rev Mol Cell Biol* **5**, 343-354 (2004).
4. Semenza, G.L. & Wang, G.L. A nuclear factor induced by hypoxia via de novo protein synthesis binds to the human erythropoietin gene enhancer at a site required for transcriptional activation. *Molecular and Cellular Biology* **12**, 5447-5454 (1992).
5. Semenza, G.L. Hypoxia-inducible factor 1 and cardiovascular disease. *Annu Rev Physiol* **76**, 39-56 (2014).
6. Semenza, G.L. Life with oxygen. *Science* **318**, 62-64 (2007).
7. Kaelin Jr, W.G. & Ratcliffe, P.J. Oxygen sensing by metazoans: The central role of the HIF hydroxylase pathway. *Mol Cell* **30**, 393-402 (2008).
8. Wang, G.L., Jiang, B.-H., Rue, E.A. & Semenza, G.L. Hypoxia-inducible factor 1 is a basic-helix-loop-helix-PAS heterodimer regulated by cellular O2 tension. *Proceedings of the National Academy of Sciences* **92**, 5510-5514 (1995).
9. Iyer, N.V. et al. Cellular and developmental control of O2 homeostasis by hypoxia-inducible factor 1α. *Genes & development* **12**, 149-162 (1998).
10. Tian, H., Hammer, R.E., Matsumoto, A.M., Russell, D.W. & McKnight, S.L. The hypoxia-responsive transcription factor EPAS1 is essential for catecholamine homeostasis and protection against heart failure during embryonic development. *Genes & development* **12**, 3320-3324 (1998).
11. Peng, J., Zhang, L., Drysdale, L. & Fong, G.-H. The transcription factor EPAS-1/hypoxia-inducible factor 2α plays an important role in vascular remodeling. *Proceedings of the National Academy of Sciences* **97**, 8386-8391 (2000).
12. Compernolle, V. et al. Loss of HIF-2α and inhibition of VEGF impair fetal lung maturation, whereas treatment with VEGF prevents fatal respiratory distress in premature mice. *Nature medicine* **8**, 702-710 (2002).
13. Scortegagna, M. et al. Multiple organ pathology, metabolic abnormalities and impaired homeostasis of reactive oxygen species in Epas1−/− mice. *Nature genetics* **35**, 331-340 (2003).
14. Hu, C.-J. et al. Differential regulation of the transcriptional activities of hypoxia-inducible factor 1 alpha (HIF-1α) and HIF-2α in stem cells. *Molecular and cellular biology* **26**, 3514-3526 (2006).
15. Keith, B., Johnson, R.S. & Simon, M.C. HIF1α and HIF2α: sibling rivalry in hypoxic tumour growth and progression. *Nature Reviews Cancer* **12**, 9-22 (2012).
16. Hu, C.-J., Wang, L.-Y., Chodosh, L.A., Keith, B. & Simon, M.C. Differential roles of hypoxia-inducible factor 1α (HIF-1α) and HIF-2α in hypoxic gene regulation. *Molecular and cellular biology* **23**, 9361-9374 (2003).
17. Raval, R.R. et al. Contrasting properties of hypoxia-inducible factor 1 (HIF-1) and HIF-2 in von Hippel-Lindau-associated renal cell carcinoma. *Molecular and Cellular Biology* **25**, 5675-5686 (2005).
18. Lau, K., Tian, Y., Raval, R., Ratcliffe, P. & Pugh, C. Target gene selectivity of hypoxia-inducible factor-α in renal cancer cells is conveyed by post-DNA-binding mechanisms. *British journal of cancer* **96**, 1284-1292 (2007).

19. Mole, D.R. et al. Genome-wide association of hypoxia-inducible factor (HIF)-1alpha and HIF-2alpha DNA binding with expression profiling of hypoxia-inducible transcripts. *Journal of Biological Chemistry* **284**, 16767-75 (2009).
20. Hu, C.-J., Sataur, A., Wang, L., Chen, H. & Simon, M.C. The N-terminal transactivation domain confers target gene specificity of hypoxia-inducible factors HIF-1α and HIF-2α. *Molecular biology of the cell* **18**, 4528-4542 (2007).
21. Tian, H., McKnight, S.L. & Russell, D.W. Endothelial PAS domain protein 1 (EPAS1), a transcription factor selectively expressed in endothelial cells. *Genes & development* **11**, 72-82 (1997).
22. Wiesener, M.S. et al. Widespread hypoxia-inducible expression of HIF-2α in distinct cell populations of different organs. *The FASEB Journal* **17**, 271-273 (2003).
23. Ratcliffe, P.J. HIF-1 and HIF-2: working alone or together in hypoxia? *Journal of Clinical Investigation* **117**, 862-865 (2007).
24. Heikkilä, M., Pasanen, A., Kivirikko, K.I. & Myllyharju, J. Roles of the human hypoxia-inducible factor (HIF)-3α variants in the hypoxia response. *Cellular and molecular life sciences* **68**, 3885-3901 (2011).
25. Makino, Y. et al. Inhibitory PAS domain protein is a negative regulator of hypoxia-inducible gene expression. *Nature* **414**, 550-4 (2001).
26. Makino, Y. et al. Transcriptional Up-regulation of Inhibitory PAS Domain Protein Gene Expression by Hypoxia-inducible Factor 1 (HIF-1) A NEGATIVE FEEDBACK REGULATORY CIRCUIT IN HIF-1-MEDIATED SIGNALING IN HYPOXIC CELLS. *Journal of biological chemistry* **282**, 14073-14082 (2007).
27. Kaelin Jr, W.G. The von Hippel–Lindau tumour suppressor protein: O2 sensing and cancer. *Nature Reviews Cancer* **8**, 865-873 (2008).
28. Huang, Y. et al. Hypoxia inducible factor 3α plays a critical role in alveolarization and distal epithelial cell differentiation during mouse lung development. *PloS one* **8**, e57695 (2013).
29. Yamashita, T. et al. Abnormal heart development and lung remodeling in mice lacking the hypoxia-inducible factor-related basic helix-loop-helix PAS protein NEPAS. *Molecular and cellular biology* **28**, 1285-1297 (2008).
30. Zhang, P. et al. Hypoxia-inducible factor 3 is an oxygen-dependent transcription activator and regulates a distinct transcriptional response to hypoxia. *Cell Reports* **6**, 1110-1121 (2014).
31. Bruick, R.K. & McKnight, S.L. A conserved family of prolyl-4-hydroxylases that modify HIF. *Science* **294**, 1337-1340 (2001).
32. Epstein, A.C. et al. C. elegans EGL-9 and mammalian homologs define a family of dioxygenases that regulate HIF by prolyl hydroxylation. *Cell* **107**, 43-54 (2001).
33. Lando, D. et al. FIH-1 is an asparaginyl hydroxylase enzyme that regulates the transcriptional activity of hypoxia-inducible factor. *Genes & development* **16**, 1466-1471 (2002).
34. Ratcliffe, P.J. Oxygen sensing and hypoxia signalling pathways in animals: the implications of physiology for cancer. *The Journal of physiology* **591**, 2027-2042 (2013).
35. Masson, N., Willam, C., Maxwell, P.H., Pugh, C.W. & Ratcliffe, P.J. Independent function of two destruction domains in hypoxia-inducible factor-α chains activated by prolyl hydroxylation. *The EMBO journal* **20**, 5197-5206 (2001).
36. Ivan, M. et al. HIFα targeted for VHL-mediated destruction by proline hydroxylation: implications for O2 sensing. *Science* **292**, 464-468 (2001).
37. Jaakkola, P. et al. Targeting of HIF-α to the von Hippel-Lindau ubiquitylation complex by O2-regulated prolyl hydroxylation. *Science* **292**, 468-472 (2001).

38. Maxwell, P.H. et al. The tumour suppressor protein VHL targets hypoxia-inducible factors for oxygen-dependent proteolysis. *Nature* **399**, 271-5 (1999).
39. Metzen, E. et al. Intracellular localisation of human HIF-1α hydroxylases: implications for oxygen sensing. *Journal of cell science* **116**, 1319-1326 (2003).
40. Appelhoff, R.J. et al. Differential function of the prolyl hydroxylases PHD1, PHD2, and PHD3 in the regulation of hypoxia-inducible factor. *Journal of Biological Chemistry* **279**, 38458-38465 (2004).
41. Berra, E. et al. HIF prolyl-hydroxylase 2 is the key oxygen sensor setting low steady-state levels of HIF-1α in normoxia. *The EMBO journal* **22**, 4082-4090 (2003).
42. Takeda, K. et al. Placental but not heart defects are associated with elevated hypoxia-inducible factor α levels in mice lacking prolyl hydroxylase domain protein 2. *Molecular and cellular biology* **26**, 8336-8346 (2006).
43. Lando, D., Peet, D.J., Whelan, D.A., Gorman, J.J. & Whitelaw, M.L. Asparagine hydroxylation of the HIF transactivation domain: a hypoxic switch. *Science* **295**, 858-861 (2002).
44. Zhang, N. et al. The asparaginyl hydroxylase factor inhibiting HIF-1α is an essential regulator of metabolism. *Cell Metabolism* **11**, 364-378 (2010).
45. Dayan, F., Roux, D., Brahimi-Horn, M.C., Pouyssegur, J. & Mazure, N.M. The oxygen sensor factor-inhibiting hypoxia-inducible factor-1 controls expression of distinct genes through the bifunctional transcriptional character of hypoxia-inducible factor-1α. *Cancer Research* **66**, 3688-3698 (2006).
46. Brunelle, J.K. et al. Oxygen sensing requires mitochondrial ROS but not oxidative phosphorylation. *Cell metabolism* **1**, 409-414 (2005).
47. Guzy, R.D. et al. Mitochondrial complex III is required for hypoxia-induced ROS production and cellular oxygen sensing. *Cell metabolism* **1**, 401-408 (2005).
48. Mansfield, K.D. et al. Mitochondrial dysfunction resulting from loss of cytochrome c impairs cellular oxygen sensing and hypoxic HIF-α activation. *Cell metabolism* **1**, 393-399 (2005).
49. Masson, N. et al. The FIH hydroxylase is a cellular peroxide sensor that modulates HIF transcriptional activity. *EMBO reports* **13**, 251-257 (2012).
50. Kaelin Jr, W.G. ROS: really involved in oxygen sensing. *Cell Metabolism* **1**, 357-358 (2005).
51. Percy, M.J. et al. A novel erythrocytosis-associated PHD2 mutation suggests the location of a HIF binding groove. *Blood* **110**, 2193-2196 (2007).
52. Percy, M.J. et al. A gain-of-function mutation in the HIF2A gene in familial erythrocytosis. *New England Journal of Medicine* **358**, 162-168 (2008).
53. Smith, T.G., Robbins, P.A. & Ratcliffe, P.J. The human side of hypoxia-inducible factor. *Br J Haematol* **141**, 325-34 (2008).
54. Smith, T.G. et al. Mutation of von Hippel–Lindau tumour suppressor and human cardiopulmonary physiology. *PLoS medicine* **3**, e290 (2006).
55. Aragonés, J., Fraisl, P., Baes, M. & Carmeliet, P. Oxygen sensors at the crossroad of metabolism. *Cell Metabolism* **9**, 11-22 (2009).
56. Semenza, G.L. Defining the role of hypoxia-inducible factor 1 in cancer biology and therapeutics. *Oncogene* **29**, 625-634 (2010).
57. Semenza, G.L. Molecular mechanisms mediating metastasis of hypoxic breast cancer cells. *Trends in molecular medicine* **18**, 534-543 (2012).
58. Townsend, N. et al. Coronary heart disease statistics 2012 edition. *British Heart Foundation: London*, P107 (2012).

59. Shohet, R.V. & Garcia, J.A. Keeping the engine primed: HIF factors as key regulators of cardiac metabolism and angiogenesis during ischemia. *J Mol Med (Berl)* **85**, 1309-15 (2007).
60. Hölscher, M. et al. Unfavourable consequences of chronic cardiac HIF-1α stabilization. *Cardiovascular Research* (2012).
61. Krishnan, J. et al. Activation of a HIF1α-PPARγ axis underlies the integration of glycolytic and lipid anabolic pathways in pathologic cardiac hypertrophy. *Cell Metabolism* **9**, 512-524 (2009).
62. Jürgensen, J.S. et al. Persistent induction of HIF-1α and -2α in cardiomyocytes and stromal cells of ischemic myocardium. *The FASEB Journal* (2004).
63. Duncker, D.J. & Bache, R.J. Regulation of coronary blood flow during exercise. *Physiol Rev* **88**, 1009-86 (2008).
64. van de Hoef, T.P. et al. Coronary pressure-flow relations as basis for the understanding of coronary physiology. *J Mol Cell Cardiol* **52**, 786-93 (2012).
65. Tune, J.D., Gorman, M.W. & Feigl, E.O. Matching coronary blood flow to myocardial oxygen consumption. *J Appl Physiol (1985)* **97**, 404-15 (2004).
66. Westerhof, N., Boer, C., Lamberts, R.R. & Sipkema, P. Cross-talk between cardiac muscle and coronary vasculature. *Physiol Rev* **86**, 1263-308 (2006).
67. Makino, N., Kanaide, H., Yoshimura, R. & Nakamura, M. Myoglobin oxygenation remains constant during the cardiac cycle. *Am J Physiol* **245**, H237-43 (1983).
68. Zweier, J.L., Thompson-Gorman, S. & Kuppusamy, P. Measurement of oxygen concentrations in the intact beating heart using electron paramagnetic resonance spectroscopy: a technique for measuring oxygen concentrations in situ. *J Bioenerg Biomembr* **23**, 855-71 (1991).
69. Hyvärinen, J. et al. Hearts of hypoxia-inducible factor prolyl 4-hydroxylase-2 hypomorphic mice show protection against acute ischemia-reperfusion injury. *Journal of Biological Chemistry* **285**, 13646-13657 (2010).
70. Pugh, C.W. & Ratcliffe, P.J. Regulation of angiogenesis by hypoxia: role of the HIF system. *Nature Medicine* **9**, 677-684 (2003).
71. Bishop, T. & Ratcliffe, P.J. in Translational Vascular Medicine 17-25 (Springer, 2012).
72. Elson, D.A. et al. Induction of hypervascularity without leakage or inflammation in transgenic mice overexpressing hypoxia-inducible factor-1α. *Genes & development* **15**, 2520-2532 (2001).
73. Walton, C.B. et al. Cardiac angiogenesis directed by stable Hypoxia Inducible Factor-1. *Vasc Cell* **5**, 5-15 (2013).
74. Thurston, G. et al. Leakage-resistant blood vessels in mice transgenically overexpressing angiopoietin-1. *Science* **286**, 2511-2514 (1999).
75. Neubauer, S. The failing heart — An engine out of fuel. *New England Journal of Medicine* **356**, 1140-1151 (2007).
76. Semenza, G.L. Regulation of cancer cell metabolism by hypoxia-inducible factor 1. *Seminars in Cancer Biology* **19**, 12-16 (2009).
77. Kim, J.-w., Tchernyshyov, I., Semenza, G.L. & Dang, C.V. HIF-1-mediated expression of pyruvate dehydrogenase kinase: a metabolic switch required for cellular adaptation to hypoxia. *Cell Metabolism* **3**, 177-185 (2006).
78. Papandreou, I., Cairns, R.A., Fontana, L., Lim, A.L. & Denko, N.C. HIF-1 mediates adaptation to hypoxia by actively downregulating mitochondrial oxygen consumption. *Cell Metabolism* **3**, 187-197 (2006).

79. Tello, D. et al. Induction of the mitochondrial NDUFA4L2 protein by HIF-1α decreases oxygen consumption by inhibiting complex I activity. *Cell Metabolism* **14**, 768-779 (2011).
80. Chan, S.Y. et al. MicroRNA-210 controls mitochondrial metabolism during hypoxia by repressing the iron-sulfur cluster assembly proteins ISCU1/2. *Cell metabolism* **10**, 273-284 (2009).
81. Kulshreshtha, R. et al. A microRNA signature of hypoxia. *Molecular and cellular biology* **27**, 1859-1867 (2007).
82. Chen, Z., Li, Y., Zhang, H., Huang, P. & Luthra, R. Hypoxia-regulated microRNA-210 modulates mitochondrial function and decreases ISCU and COX10 expression. *Oncogene* **29**, 4362-4368 (2010).
83. Favaro, E. et al. MicroRNA-210 regulates mitochondrial free radical response to hypoxia and krebs cycle in cancer cells by targeting iron sulfur cluster protein ISCU. *PloS one* **5**, e10345 (2010).
84. Fukuda, R. et al. HIF-1 regulates cytochrome oxidase subunits to optimize efficiency of respiration in hypoxic cells. *Cell* **129**, 111-122 (2007).
85. Bellot, G. et al. Hypoxia-induced autophagy is mediated through hypoxia-inducible factor induction of BNIP3 and BNIP3L via their BH3 domains. *Molecular and Cellular Biology* **29**, 2570-2581 (2009).
86. Hamacher-Brady, A. et al. Response to myocardial ischemia/reperfusion injury involves Bnip3 and autophagy. *Cell Death & Differentiation* **14**, 146-157 (2006).
87. Zhang, H. et al. Mitochondrial autophagy is an HIF-1-dependent adaptive metabolic response to hypoxia. *Journal of Biological Chemistry* **283**, 10892-10903 (2008).
88. Dorn, G., II. Mitochondrial pruning by Nix and Bnip3: An essential function for cardiac-expressed death factors. *Journal of Cardiovascular Translational Research* **3**, 374-383 (2010).
89. Zhang, H. et al. HIF-1 inhibits mitochondrial biogenesis and cellular respiration in VHL-deficient renal cell carcinoma by repression of C-MYC activity. *Cancer Cell* **11**, 407-420 (2007).
90. Dorn, G.W. Apoptotic and non-apoptotic programmed cardiomyocyte death in ventricular remodelling. *Cardiovascular research* **81**, 465-473 (2009).
91. Regula, K.M., Ens, K. & Kirshenbaum, L.A. Inducible expression of BNIP3 provokes mitochondrial defects and hypoxia-mediated cell death of ventricular myocytes. *Circulation Research* **91**, 226-231 (2002).
92. Sowter, H.M., Ratcliffe, P.J., Watson, P., Greenberg, A.H. & Harris, A.L. HIF-1-dependent regulation of hypoxic induction of the cell death factors BNIP3 and NIX in human tumors. *Cancer Research* **61**, 6669-6673 (2001).
93. Zhang, J. & Ney, P.A. Role of BNIP3 and NIX in cell death, autophagy, and mitophagy. *Cell Death & Differentiation* **16**, 939-946 (2009).
94. Diwan, A. et al. Inhibition of ischemic cardiomyocyte apoptosis through targeted ablation of Bnip3 restrains postinfarction remodeling in mice. *Journal of Clinical Investigation* **117**, 2825-2833 (2007).
95. Resar, J.R. et al. Hypoxia-inducible factor 1α polymorphism and coronary collaterals in patients with ischemic heart disease. *CHEST Journal* **128**, 787-791 (2005).
96. Duran, J. et al. The HIF1A C85T single nucleotide polymorphism influences the number of branches of the human coronary tree. *Cardiology* **121**, 156-159 (2012).
97. Hlatky, M.A. et al. Polymorphisms in hypoxia inducible factor 1 and the initial clinical presentation of coronary disease. *American heart journal* **154**, 1035-1042 (2007).

98. Eckle, T., Köhler, D., Lehmann, R., El Kasmi, K.C. & Eltzschig, H.K. Hypoxia-inducible factor-1 Is central to cardioprotection. *Circulation* **118**, 166-175 (2008).
99. Cai, Z. et al. Complete loss of ischaemic preconditioning-induced cardioprotection in mice with partial deficiency of HIF-1α. *Cardiovascular Research* **77**, 463-470 (2008).
100. Zhao, H.-X. et al. Attenuation of myocardial injury by postconditioning: role of hypoxia inducible factor-1α. *Basic research in cardiology* **105**, 109-118 (2010).
101. Kido, M. et al. Hypoxia-inducible factor 1-alpha reduces infarction and attenuates progression of cardiac dysfunction after myocardial infarction in the mouse. *J Am Coll Cardiol* **46**, 2116-2124 (2005).
102. Wu, J. et al. HIF-1alpha in heart: protective mechanisms. *Am J Physiol Heart Circ Physiol* **305**, 19 (2013).
103. Natarajan, R., Salloum, F.N., Fisher, B.J., Kukreja, R.C. & Fowler, A.A., 3rd. Hypoxia inducible factor-1 activation by prolyl 4-hydroxylase-2 gene silencing attenuates myocardial ischemia reperfusion injury. *Circulation Research* **98**, 133-40 (2006).
104. Hölscher, M. et al. Cardiomyocyte-specific prolyl-4-hydroxylase domain 2 knock out protects from acute myocardial ischemic injury. *Journal of Biological Chemistry* **286**, 11185-11194 (2011).
105. Huang, M. et al. Short hairpin RNA interference therapy for ischemic heart disease. *Circulation* **118**, S226-S233 (2008).
106. Jiang, Y. et al. Dietary copper supplementation reverses hypertrophic cardiomyopathy induced by chronic pressure overload in mice. *The Journal of Experimental Medicine* **204**, 657-666 (2007).
107. Sano, M. et al. p53-induced inhibition of Hif-1 causes cardiac dysfunction during pressure overload. *Nature* **446**, 444-448 (2007).
108. Huang, Y. et al. Cardiac myocyte-specific HIF-1α deletion alters vascularization, energy availability, calcium flux, and contractility in the normoxic heart. *The FASEB Journal* **18**, 1138-1140 (2004).
109. Minamishima, Y.A. et al. Somatic inactivation of the PHD2 prolyl hydroxylase causes polycythemia and congestive heart failure. *Blood* **111**, 3236-3244 (2008).
110. Moslehi, J. et al. Loss of hypoxia-inducible factor prolyl hydroxylase activity in cardiomyocytes phenocopies ischemic cardiomyopathy. *Circulation* **122**, 1004-1016 (2010).
111. Lei, L. et al. Hypoxia-inducible factor-dependent degeneration, failure, and malignant transformation of the heart in the absence of the von Hippel-Lindau protein. *Molecular and Cellular Biology* **28**, 3790-3803 (2008).
112. Bekeredjian, R. et al. Conditional HIF-1α expression produces a reversible cardiomyopathy. *Plos One* **5**, e11693 (2010).
113. Eckle, T. et al. Adora2b-elicited Per2 stabilization promotes a HIF-dependent metabolic switch crucial for myocardial adaptation to ischemia. *Nature Medicine* **18**, 774-782 (2012).
114. Silter, M. et al. Impaired Ca2+-handling in HIF-1α+/− mice as a consequence of pressure overload. *Pflügers Archiv-European Journal of Physiology* **459**, 569-577 (2010).
115. Pollard, P.J. et al. Accumulation of Krebs cycle intermediates and over-expression of HIF1α in tumours which result from germline FH and SDH mutations. *Human Molecular Genetics* **14**, 2231-2239 (2005).
116. Isaacs, J.S. et al. HIF overexpression correlates with biallelic loss of fumarate hydratase in renal cancer: Novel role of fumarate in regulation of HIF stability. *Cancer Cell* **8**, 143-153 (2005).

117. Tomlinson, I.P. et al. Germline mutations in FH predispose to dominantly inherited uterine fibroids, skin leiomyomata and papillary renal cell cancer. *Nat Genet* **30**, 406-10 (2002).
118. Toro, J.R. et al. Mutations in the fumarate hydratase gene cause hereditary leiomyomatosis and renal cell cancer in families in North America. *Am J Hum Genet* **73**, 95-106 (2003).
119. Alam, N.A. et al. Missense mutations in fumarate hydratase in multiple cutaneous and uterine leiomyomatosis and renal cell cancer. *The Journal of Molecular Diagnostics* **7**, 437-443 (2005).
120. Gottlieb, E. & Tomlinson, I.P. Mitochondrial tumour suppressors: a genetic and biochemical update. *Nature Reviews Cancer* **5**, 857-866 (2005).
121. Eng, C., Kiuru, M., Fernandez, M.J. & Aaltonen, L.A. A role for mitochondrial enzymes in inherited neoplasia and beyond. *Nature Reviews Cancer* **3**, 193-202 (2003).
122. Bourgeron, T. et al. Mutation of the fumarase gene in two siblings with progressive encephalopathy and fumarase deficiency. *Journal of Clinical Investigation* **93**, 2514 (1994).
123. Gellera, C. et al. Fumarase deficiency is an autosomal recessive encephalopathy affecting both the mitochondrial and the cytosolic enzymes. *Neurology* **40**, 495-495 (1990).
124. Astuti, D. et al. Gene mutations in the succinate dehydrogenase subunit SDHB cause susceptibility to familial pheochromocytoma and to familial paraganglioma. *The American Journal of Human Genetics* **69**, 49-54 (2001).
125. Burnichon, N. et al. SDHA is a tumor suppressor gene causing paraganglioma. *Human Molecular Genetics* **19**, 3011-3020 (2010).
126. Baysal, B.E. et al. Mutations in SDHD, a mitochondrial complex II gene, in hereditary paraganglioma. *Science* **287**, 848-851 (2000).
127. Niemann, S. & Müller, U. Mutations in SDHC cause autosomal dominant paraganglioma, type 3. *Nature genetics* **26** (2000).
128. Selak, M.A. et al. Succinate links TCA cycle dysfunction to oncogenesis by inhibiting HIF-α prolyl hydroxylase. *Cancer Cell* **7**, 77-85 (2005).
129. Bourgeron, T. et al. Mutation of a nuclear succinate dehydrogenase gene results in mitochondrial respiratory chain deficiency. *Nature genetics* **11**, 144-149 (1995).
130. Yan, H. et al. IDH1 and IDH2 mutations in gliomas. *New England Journal of Medicine* **360**, 765-773 (2009).
131. Parsons, D.W. et al. An integrated genomic analysis of human glioblastoma multiforme. *Science* **321**, 1807-1812 (2008).
132. Mardis, E.R. et al. Recurring mutations found by sequencing an acute myeloid leukemia genome. *New England Journal of Medicine* **361**, 1058-1066 (2009).
133. Ward, P.S. et al. The common feature of leukemia-associated IDH1 and IDH2 mutations is a neomorphic enzyme activity converting α-ketoglutarate to 2-hydroxyglutarate. *Cancer Cell* **17**, 225-234 (2010).
134. Frezza, C., Pollard, P.J. & Gottlieb, E. Inborn and acquired metabolic defects in cancer. *J Mol Med* **89**, 213-20 (2011).
135. Adam, J., Yang, M., Soga, T. & Pollard, P.J. Rare insights into cancer biology. *Oncogene* **1**, 222 (2013).
136. Yang, M., Soga, T. & Pollard, P.J. Oncometabolites: linking altered metabolism with cancer. *J Clin Invest* **123**, 3652-8 (2013).
137. Yang, M., Soga, T., Pollard, P.J. & Adam, J. The emerging role of fumarate as an oncometabolite. *Front Oncol* **2**, 00085 (2012).

138. Dang, L. et al. Cancer-associated IDH1 mutations produce 2-hydroxyglutarate. *Nature* **462**, 739-744 (2009).
139. Zhao, S. et al. Glioma-derived mutations in IDH1 dominantly inhibit IDH1 catalytic activity and induce HIF-1α. *Science* **324**, 261-265 (2009).
140. Sasaki, M. et al. D-2-hydroxyglutarate produced by mutant IDH1 perturbs collagen maturation and basement membrane function. *Genes & development* **26**, 2038-2049 (2012).
141. Xu, W. et al. Oncometabolite 2-hydroxyglutarate is a competitive inhibitor of α-ketoglutarate-dependent dioxygenases. *Cancer Cell* **19**, 17-30 (2011).
142. Koivunen, P. et al. Transformation by the (R)-enantiomer of 2-hydroxyglutarate linked to EGLN activation. *Nature* **483**, 484-488 (2012).
143. Pollard, P.J. et al. Targeted inactivation of Fh1 causes proliferative renal cyst development and activation of the hypoxia pathway. *Cancer Cell* **11**, 311-319 (2007).
144. Ashrafian, H. et al. Expression profiling in progressive stages of fumarate-hydratase deficiency: The contribution of metabolic changes to tumorigenesis. *Cancer Research* **70**, 9153-9165 (2010).
145. Adam, J. et al. Renal Cyst Formation in Fh1-Deficient Mice Is Independent of the Hif/Phd Pathway: Roles for Fumarate in KEAP1 Succination and Nrf2 Signaling. *Cancer Cell* **20**, 524-537 (2011).
146. Rose, N.R., McDonough, M.A., King, O.N., Kawamura, A. & Schofield, C.J. Inhibition of 2-oxoglutarate dependent oxygenases. *Chemical Society Reviews* **40**, 4364-4397 (2011).
147. Nwogu, J.I. et al. Inhibition of collagen synthesis with prolyl 4-hydroxylase inhibitor improves left ventricular function and alters the pattern of left ventricular dilatation after myocardial infarction. *Circulation* **104**, 2216-2221 (2001).
148. Philipp, S. et al. Stabilization of hypoxia inducible factor rather than modulation of collagen metabolism improves cardiac function after acute myocardial infarction in rats. *European journal of heart failure* **8**, 347-354 (2006).
149. Koivunen, P. et al. Inhibition of Hypoxia-inducible Factor (HIF) Hydroxylases by Citric Acid Cycle Intermediates POSSIBLE LINKS BETWEEN CELL METABOLISM AND STABILIZATION OF HIF. *Journal of Biological Chemistry* **282**, 4524-4532 (2007).
150. Haas, J. et al. Alterations in cardiac DNA methylation in human dilated cardiomyopathy. *EMBO molecular medicine* **5**, 413-429 (2013).
151. Nührenberg, T., Gilsbach, R., Preissl, S., Schnick, T. & Hein, L. Epigenetics in cardiac development, function, and disease. *Cell and tissue research*, 1-16 (2014).
152. Lorenzen, J.M., Martino, F. & Thum, T. Epigenetic modifications in cardiovascular disease. *Basic research in cardiology* **107**, 1-10 (2012).
153. Zhang, Q.-J. et al. The histone trimethyllysine demethylase JMJD2A promotes cardiac hypertrophy in response to hypertrophic stimuli in mice. *The Journal of clinical investigation* **121**, 2447 (2011).
154. Xiao, M. et al. Inhibition of α-KG-dependent histone and DNA demethylases by fumarate and succinate that are accumulated in mutations of FH and SDH tumor suppressors. *Genes & development* **26**, 1326-1338 (2012).
155. Letouzé, E. et al. SDH mutations establish a hypermethylator phenotype in paraganglioma. *Cancer Cell* **23**, 739-752 (2013).
156. Turcan, S. et al. IDH1 mutation is sufficient to establish the glioma hypermethylator phenotype. *Nature* **483**, 479-483 (2012).

157. Akbay, E.A. et al. D-2-hydroxyglutarate produced by mutant IDH2 causes cardiomyopathy and neurodegeneration in mice. *Genes & development* **28**, 479-490 (2014).
158. Blatnik, M., Thorpe, S.R. & Baynes, J.W. Succination of proteins by fumarate: mechanism of inactivation of glyceraldehyde-3-phosphate dehydrogenase in diabetes. *Ann N Y Acad Sci*, 047 (2008).
159. Bardella, C. et al. Aberrant succination of proteins in fumarate hydratase-deficient mice and HLRCC patients is a robust biomarker of mutation status. *Journal of Pathology* **225**, 4-11 (2011).
160. Ternette, N. et al. Inhibition of mitochondrial aconitase by succination in fumarate hydratase deficiency. *Cell Reports* **3**, 689-700 (2013).
161. Ooi, A. et al. An antioxidant response phenotype shared between hereditary and sporadic type 2 papillary renal cell carcinoma. *Cancer Cell* **20**, 511-523 (2011).
162. Mitsuishi, Y., Motohashi, H. & Yamamoto, M. The Keap1–Nrf2 system in cancers: stress response and anabolic metabolism. *Frontiers in oncology* **2** (2012).
163. Mitsuishi, Y. et al. Nrf2 redirects glucose and glutamine into anabolic pathways in metabolic reprogramming. *Cancer Cell* **22**, 66-79 (2012).
164. Sullivan, L.B. et al. The proto-oncometabolite fumarate binds glutathione to amplify ROS-dependent signaling. *Molecular cell* **51**, 236-248 (2013).
165. Frezza, C. et al. Haem oxygenase is synthetically lethal with the tumour suppressor fumarate hydratase. *Nature* **477**, 225-228 (2011).
166. Ashrafian, H. et al. Fumarate is cardioprotective via activation of the Nrf2 antioxidant pathway. *Cell Metab* **15**, 361-71 (2012).
167. Mullen, A.R. et al. Reductive carboxylation supports growth in tumour cells with defective mitochondria. *Nature* **481**, 385-8 (2012).
168. Laplante, A., Vincent, G., Poirier, M. & Des Rosiers, C. Effects and metabolism of fumarate in the perfused rat heart. A 13C mass isotopomer study. *American Journal of Physiology-Endocrinology And Metabolism* **35**, E74 (1997).
169. Yet, S.-F. et al. Cardiac-specific expression of heme oxygenase-1 protects against ischemia and reperfusion injury in transgenic mice. *Circulation research* **89**, 168-173 (2001).
170. Li, J. et al. Nrf2 protects against maladaptive cardiac responses to hemodynamic stress. *Arteriosclerosis, Thrombosis, and Vascular Biology* **29**, 1843-1850 (2009).
171. Yogev, O., Naamati, A. & Pines, O. Fumarase: a paradigm of dual targeting and dual localized functions. *FEBS Journal* **278**, 4230-4242 (2011).
172. Akiba, T., Hiraga, K. & Tuboi, S. Intracellular distribution of fumarase in various animals. *Journal of biochemistry* **96**, 189-195 (1984).
173. Tolley, E. & Craig, I. Presence of two forms of fumarase (fumarate hydratase E.C. 4.2.1.2) in mammalian cells: Immunological characterization and genetic analysis in somatic cell hybrids. Confirmation of the assignment of a gene necessary for the enzyme expression to human chromosome 1. *Biochemical Genetics* **13**, 867-883 (1975).
174. Stein, I., Peleg, Y., Even-Ram, S. & Pines, O. The single translation product of the FUM1 gene (fumarase) is processed in mitochondria before being distributed between the cytosol and mitochondria in Saccharomyces cerevisiae. *Molecular and Cellular Biology* **14**, 4770-4778 (1994).
175. Sass, E., Karniely, S. & Pines, O. Folding of fumarase during mitochondrial import determines its dual targeting in yeast. *Journal of Biological Chemistry* **278**, 45109-45116 (2003).

176. Suzuki, T., Yoshida, T. & Tuboi, S. Evidence that rat-liver mitochondrial and cytosolic fumarases are synthesized from one species of messenger-RNA by alternative translational initiation at 2 in-phase AUG codons. *European Journal of Biochemistry* **207**, 767-772 (1992).
177. Tuboi, S., Sato, M., Ono, H., Kobayashi, K. & Hiraga, K. Mechanism of synthesis and localization of mitochondrial and cytosolic fumarases in rat liver. *Adv Enzyme Regul* **25**, 461-84 (1986).
178. Wu, M., Wong, S.M., Tan, H.M. & Ting, R. A Single Base-Pair Change (ATG → ATC) Nullifies the Activity of Cytosolic Fumarase in Saccharomyces cerevisiae. *Biochemical and Biophysical Research Communications* **215**, 578-590 (1995).
179. O'Flaherty, L. et al. Dysregulation of hypoxia pathways in fumarate hydratase-deficient cells is independent of defective mitochondrial metabolism. *Human Molecular Genetics* **19**, 3844-3851 (2010).
180. Adam, J. et al. A role for cytosolic fumarate hydratase in urea cycle metabolism and renal neoplasia. *Cell Reports* **3**, 1440-1448 (2013).
181. Ryan, H.E. et al. Hypoxia-inducible factor-1α is a positive factor in solid tumor growth. *Cancer Research* **60**, 4010-4015 (2000).
182. Sohal, D.S. et al. Temporally regulated and tissue-specific gene manipulations in the adult and embryonic heart using a tamoxifen-inducible cre protein. *Circulation Research* **89**, 20-25 (2001).
183. Chen, J. et al. Selective requirement of myosin light chain 2v in embryonic heart function. *Journal of Biological Chemistry* **273**, 1252-1256 (1998).
184. Chen, J., Kubalak, S.W. & Chien, K.R. Ventricular muscle-restricted targeting of the RXRalpha gene reveals a non-cell-autonomous requirement in cardiac chamber morphogenesis. *Development* **125**, 1943-1949 (1998).
185. Iakusheva, T. The effect of sodium tartronate on the body weight and on the fat and glycogen content of mouse and rat livers. *Bulletin of Experimental Biology and Medicine* **45**, 52-53 (1958).
186. Boros, L.G. et al. Oxythiamine and dehydroepiandrosterone inhibit the nonoxidative synthesis of ribose and tumor cell proliferation. *Cancer Research* **57**, 4242-4248 (1997).
187. Itoh, K. et al. An Nrf2/small Maf heterodimer mediates the induction of phase II detoxifying enzyme genes through antioxidant response elements. *Biochemical and Biophysical Research Communications* **236**, 313-322 (1997).
188. Chen, C.-m., Krohn, J., Bhattacharya, S. & Davies, B. A comparison of exogenous promoter activity at the ROSA26 locus using a PhiC31 integrase mediated cassette exchange approach in mouse ES cells. *Plos One* **6**, e23376 (2011).
189. Collins, K.A., Korcarz, C.E. & Lang, R.M. Use of echocardiography for the phenotypic assessment of genetically altered mice. *Physiological genomics* **13**, 227-239 (2003).
190. Lang, R.M. et al. Recommendations for chamber quantification: a report from the American Society of Echocardiography's Guidelines and Standards Committee and the Chamber Quantification Writing Group, developed in conjunction with the European Association of Echocardiography, a branch of the European Society of Cardiology. *J Am Soc Echocardiogr* **18**, 1440-63 (2005).
191. Stypmann, J. et al. Echocardiographic assessment of global left ventricular function in mice. *Lab Anim* **43**, 127-37 (2009).
192. Takagawa, J. et al. Myocardial infarct size measurement in the mouse chronic infarction model: comparison of area-and length-based approaches. *Journal of Applied Physiology* **102**, 2104-2111 (2007).

193. Schneider, J.E. et al. Fast, high-resolution in vivo cine magnetic resonance imaging in normal and failing mouse hearts on a vertical 11.7 T system. *Journal of Magnetic Resonance Imaging* **18**, 691-701 (2003).
194. Luo, J. et al. A protocol for rapid generation of recombinant adenoviruses using the AdEasy system. *Nat. Protocols* **2**, 1236-1247 (2007).
195. Smith, A.C. & Robinson, A.J. A metabolic model of the mitochondrion and its use in modelling diseases of the tricarboxylic acid cycle. *BMC systems biology* **5**, 102 (2011).
196. Koitabashi, N. et al. Avoidance of transient cardiomyopathy in cardiomyocyte-targeted tamoxifen-induced MerCreMer gene deletion models. *Circulation Research* **105**, 12-15 (2009).
197. Lygate, C.A. & Neubauer, S. in A handbook of mouse models of cardiovascular disease (ed. Xu, Q.) 333-348 (John Wiley & Sons, Chichester, England; Hoboken, NJ, 2006).
198. Bayat, H. et al. Progressive heart failure after myocardial infarction in mice. *Basic research in cardiology* **97**, 206-213 (2002).
199. Francis, G.S. & Desai, M.Y. Contractile Reserve: Are We Beginning to Understand It?. *JACC: Cardiovascular Imaging* **1**, 727-728 (2008).
200. Razeghi, P. et al. Metabolic gene expression in fetal and failing human heart. *Circulation* **104**, 2923-2931 (2001).
201. Taegtmeyer, H., Sen, S. & Vela, D. Return to the fetal gene program. *Annals of the New York Academy of Sciences* **1188**, 191-198 (2010).
202. Hall, M.E., Smith, G., Hall, J.E. & Stec, D.E. Systolic dysfunction in cardiac-specific ligand-inducible MerCreMer transgenic mice. *Am J Physiol Heart Circ Physiol* **301**, H253-60 (2011).
203. Bersell, K. et al. Moderate and high amounts of tamoxifen in αMHC-MerCreMer mice induce a DNA damage response, leading to heart failure and death. *Disease models & mechanisms* **6**, 1459-1469 (2013).
204. Schneider, J.E. et al. Cardiac structure and function during ageing in energetically compromised Guanidinoacetate N-methyltransferase (GAMT)-knockout mice - a one year longitudinal MRI study. *J Cardiovasc Magn Reson* **10**, 9 (2008).
205. Gray, G.A. et al. Imaging the healing murine myocardial infarct in vivo: ultrasound, magnetic resonance imaging and fluorescence molecular tomography. *Exp Physiol* **98**, 606-13 (2013).
206. Bohl, S. et al. Advanced methods for quantification of infarct size in mice using three-dimensional high-field late gadolinium enhancement MRI. *Am J Physiol Heart Circ Physiol* **296**, H1200-8 (2009).
207. Lee, S.H. et al. Early expression of angiogenesis factors in acute myocardial ischemia and infarction. *N Engl J Med* **342**, 626-33 (2000).
208. Schmittgen, T.D. & Livak, K.J. Analyzing real-time PCR data by the comparative C(T) method. *Nat Protoc* **3**, 1101-8 (2008).
209. Vesentini, N. et al. Selection of reference genes in different myocardial regions of an in vivo ischemia/reperfusion rat model for normalization of antioxidant gene expression. *BMC Res Notes* **5**, 124 (2012).
210. Vandesompele, J. et al. Accurate normalization of real-time quantitative RT-PCR data by geometric averaging of multiple internal control genes. *Genome Biol* **3**, RESEARCH0034 (2002).
211. Baker, M. Digital PCR hits its stride. *Nat Meth* **9**, 541-544 (2012).
212. Blow, N. PCR's next frontier. *Nat Meth* **4**, 869-875 (2007).

213. Vogelstein, B. & Kinzler, K.W. Digital PCR. *Proceedings of the National Academy of Sciences of the United States of America* **96**, 9236-9241 (1999).
214. Zolk, O., Solbach, T.F., Eschenhagen, T., Weidemann, A. & Fromm, M.F. Activation of negative regulators of the hypoxia-inducible factor (HIF) pathway in human end-stage heart failure. *Biochemical and Biophysical Research Communications* **376**, 315-320 (2008).
215. Koh, M.Y., Darnay, B.G. & Powis, G. Hypoxia-associated factor, a novel E3-ubiquitin ligase, binds and ubiquitinates hypoxia-inducible factor 1α, leading to its oxygen-independent degradation. *Molecular and Cellular Biology* **28**, 7081-7095 (2008).
216. Koh, M.Y. & Powis, G. Passing the baton: the HIF switch. *Trends in biochemical sciences* **37**, 364-372 (2012).
217. Lutgens, E. et al. Chronic myocardial infarction in the mouse: cardiac structural and functional change. *Cardiovascular Research* **41**, 586-593 (1999).
218. Wang, Q.-D., Bohlooly, M. & Sjöquist, P.-O. Murine models for the study of congestive heart failure: implications for understanding molecular mechanisms and for drug discovery. *Journal of pharmacological and toxicological methods* **50**, 163-174 (2004).
219. Lompre, A. et al. Species-and age-dependent changes in the relative amounts of cardiac myosin isoenzymes in mammals. *Developmental biology* **84**, 286-290 (1981).
220. Hasenfuss, G. Animal models of human cardiovascular disease, heart failure and hypertrophy. *Cardiovascular research* **39**, 60-76 (1998).
221. Patten, R.D. et al. Ventricular remodeling in a mouse model of myocardial infarction. *American Journal of Physiology - Heart and Circulatory Physiology* **274**, H1812-H1820 (1998).
222. Ahn, D. et al. Induction of myocardial infarcts of a predictable size and location by branch pattern probability-assisted coronary ligation in C57BL/6 mice. *Am J Physiol Heart Circ Physiol* **286**, H1201-7 (2004).
223. Roell, W. et al. Cellular cardiomyoplasty in a transgenic mouse model. *Transplantation* **73**, 462-5 (2002).
224. Gargiulo, S. et al. PET/CT imaging in mouse models of myocardial ischemia. *J Biomed Biotechnol* **2012**, 541872 (2012).
225. Scherrer-Crosbie, M., Rodrigues, A.C., Hataishi, R. & Picard, M.H. Infarct size assessment in mice. *Echocardiography* **24**, 90-6 (2007).
226. Pitts, K.R. et al. Washout of heme-containing proteins dramatically improves tetrazolium-based infarct staining. *J Pharmacol Toxicol Methods* **55**, 201-8 (2007).
227. Roger, V.L. Epidemiology of heart failure. *Circ Res* **113**, 646-59 (2013).
228. Breckenridge, R. Heart failure and mouse models. *Dis Model Mech* **3**, 138-43 (2010).
229. Mouse Genome Sequencing, C. et al. Initial sequencing and comparative analysis of the mouse genome. *Nature* **420**, 520-62 (2002).
230. Gould, K.E. et al. Heart failure and greater infarct expansion in middle-aged mice: a relevant model for postinfarction failure. *Am J Physiol Heart Circ Physiol* **282**, H615-21 (2002).
231. Mann, D.L. & Bristow, M.R. Mechanisms and models in heart failure: the biomechanical model and beyond. *Circulation* **111**, 2837-49 (2005).
232. Florea, V.G. & Cohn, J.N. The autonomic nervous system and heart failure. *Circ Res* **114**, 1815-26 (2014).
233. Houser, S.R. et al. Animal models of heart failure: a scientific statement from the American Heart Association. *Circ Res* **111**, 131-50 (2012).

234. Bristow, M.R. et al. Decreased catecholamine sensitivity and beta-adrenergic-receptor density in failing human hearts. *N Engl J Med* **307**, 205-11 (1982).
235. Eschenhagen, T. Beta-adrenergic signaling in heart failure-adapt or die. *Nat Med* **14**, 485-7 (2008).
236. Hougen, K. et al. Cre-loxP DNA recombination is possible with only minimal unspecific transcriptional changes and without cardiomyopathy in Tg(alphaMHC-MerCreMer) mice. *Am J Physiol Heart Circ Physiol* **299**, H1671-8 (2010).
237. Ogita, H. et al. Raloxifene prevents cardiac hypertrophy and dysfunction in pressure-overloaded mice. *Hypertension* **43**, 237-42 (2004).
238. Sarkar, K. et al. Hypoxia-inducible factor 1 transcriptional activity in endothelial cells is required for acute phase cardioprotection induced by ischemic preconditioning. *Proceedings of the National Academy of Sciences* **109**, 10504-10509 (2012).
239. Weber, K.T., Brilla, C.G. & Janicki, J.S. Myocardial fibrosis: functional significance and regulatory factors. *Cardiovascular Research* **27**, 341-348 (1993).
240. Frederich, M. & Balschi, J.A. The relationship between AMP-activated protein kinase activity and AMP concentration in the isolated perfused rat heart. *J Biol Chem* **277**, 1928-32 (2002).
241. Ingwall, J.S. & Weiss, R.G. Is the failing heart energy starved? On using chemical energy to support cardiac function. *Circulation Research* **95**, 135-145 (2004).
242. Schild, L., Blair, P.V., Davis, W.I. & Baugh, S. Effect of adenine nucleotide pool size in mitochondria on intramitochondrial ATP levels. *Biochim Biophys Acta* **1413**, 14-20 (1999).
243. Starling, R.C., Hammer, D.F. & Altschuld, R.A. Human myocardial ATP content and in vivo contractile function. *Mol Cell Biochem* **180**, 171-7 (1998).
244. Ingwall, J.S. Energy metabolism in heart failure and remodelling. *Cardiovascular Research* **81**, 412-419 (2009).
245. Rajasekaran, N.S. et al. Human αB-crystallin mutation causes oxido-reductive stress and protein aggregation cardiomyopathy in mice. *Cell* **130**, 427-439 (2007).
246. Rajasekaran, N.S. et al. Sustained activation of nuclear erythroid 2-related factor 2/antioxidant response element signaling promotes reductive stress in the human mutant protein aggregation cardiomyopathy in mice. *Antioxidants & Redox Signaling* **14**, 957-971 (2011).
247. Kannan, S. et al. Nrf2 deficiency prevents reductive stress-induced hypertrophic cardiomyopathy. *Cardiovascular Research*, cvt150 (2013).
248. Doetschman, T. Influence of genetic background on genetically engineered mouse phenotypes. *Methods Mol Biol* **530**, 423-33 (2009).
249. Shah, A.P. et al. Genetic background affects function and intracellular calcium regulation of mouse hearts. *Cardiovasc Res* **87**, 683-93 (2010).
250. Merkley, E.D., Metz, T.O., Smith, R.D., Baynes, J.W. & Frizzell, N. The succinated proteome. *Mass Spectrom Rev* **33**, 98-109 (2014).
251. Frizzell, N., Lima, M. & Baynes, J.W. Succination of proteins in diabetes. *Free Radic Res* **45**, 101-9 (2011).
252. Piroli, G.G. et al. Identification of protein succination as a novel modification of tubulin. *Biochem J* **462**, 231-45 (2014).
253. Zhang, D.D. Mechanistic studies of the Nrf2-Keap1 signaling pathway. *Drug Metab Rev* **38**, 769-89 (2006).
254. Li, F., Xu, W. & Zhao, S. Regulatory roles of metabolites in cell signaling networks. *J Genet Genomics* **40**, 367-74 (2013).
255. Passarella, S., Atlante, A., Valenti, D. & de Bari, L. The role of mitochondrial transport in energy metabolism. *Mitochondrion* **2**, 319-43 (2003).

256. Medeiros, D.M. Assessing mitochondria biogenesis. *Methods* **46**, 288-94 (2008).
257. Andres, A.M., Stotland, A., Queliconi, B.B. & Gottlieb, R.A. A time to reap, a time to sow: Mitophagy and biogenesis in cardiac pathophysiology. *J Mol Cell Cardiol* **78C**, 62-72 (2015).
258. Benard, G. & Rossignol, R. Ultrastructure of the mitochondrion and its bearing on function and bioenergetics. *Antioxid Redox Signal* **10**, 1313-42 (2008).
259. Hoppel, C.L., Tandler, B., Fujioka, H. & Riva, A. Dynamic organization of mitochondria in human heart and in myocardial disease. *Int J Biochem Cell Biol* **41**, 1949-56 (2009).
260. Lanza, I.R. & Nair, K.S. Functional assessment of isolated mitochondria in vitro. *Methods Enzymol* **457**, 349-72 (2009).
261. de Jong, S., van Veen, T.A., de Bakker, J.M. & van Rijen, H.V. Monitoring cardiac fibrosis: a technical challenge. *Neth Heart J* **20**, 44-8 (2012).
262. Danila, D., Johnson, E. & Kee, P. CT imaging of myocardial scars with collagen-targeting gold nanoparticles. *Nanomedicine* **9**, 1067-76 (2013).
263. Stefanon, I. et al. Left and right ventricle late remodeling following myocardial infarction in rats. *PLoS One* **8**, e64986 (2013).
264. Oh, C.J. et al. Dimethylfumarate attenuates renal fibrosis via NF-E2-related factor 2-mediated inhibition of transforming growth factor-beta/Smad signaling. *PLoS One* **7**, e45870 (2012).
265. Schilling, S., Goelz, S., Linker, R., Luehder, F. & Gold, R. Fumaric acid esters are effective in chronic experimental autoimmune encephalomyelitis and suppress macrophage infiltration. *Clin Exp Immunol* **145**, 101-7 (2006).
266. Loewe, R. et al. Dimethylfumarate impairs melanoma growth and metastasis. *Cancer Res* **66**, 11888-96 (2006).
267. Linker, R.A. et al. Fumaric acid esters exert neuroprotective effects in neuroinflammation via activation of the Nrf2 antioxidant pathway. *Brain* **134**, 678-92 (2011).
268. Peng, H. et al. Dimethyl fumarate inhibits dendritic cell maturation via nuclear factor kappaB (NF-kappaB) and extracellular signal-regulated kinase 1 and 2 (ERK1/2) and mitogen stress-activated kinase 1 (MSK1) signaling. *J Biol Chem* **287**, 28017-26 (2012).
269. Garcia-Caballero, M., Mari-Beffa, M., Medina, M.A. & Quesada, A.R. Dimethylfumarate inhibits angiogenesis in vitro and in vivo: a possible role for its antipsoriatic effect? *J Invest Dermatol* **131**, 1347-55 (2011).
270. Chen, H. et al. Hydroxycarboxylic acid receptor 2 mediates dimethyl fumarate's protective effect in EAE. *J Clin Invest* **124**, 2188-92 (2014).
271. Hein, S., Kostin, S., Heling, A., Maeno, Y. & Schaper, J. The role of the cytoskeleton in heart failure. *Cardiovasc Res* **45**, 273-8 (2000).
272. Parameswaran, S., Kumar, S., Verma, R.S. & Sharma, R.K. Cardiomyocyte culture - an update on the in vitro cardiovascular model and future challenges. *Can J Physiol Pharmacol* **91**, 985-98 (2013).
273. Louch, W.E., Sheehan, K.A. & Wolska, B.M. Methods in cardiomyocyte isolation, culture, and gene transfer. *J Mol Cell Cardiol* **51**, 288-98 (2011).
274. Russell, R. & Taegtmeyer, H. Pyruvate carboxylation prevents the decline in contractile function of rat hearts oxidizing acetoacetate. *Am J Physiol* **261**, H1756-H1762 (1991).
275. Sundqvist, K., Heikkila, J., Hassinen, I. & Hiltunen, J. Role of NADP+-linked malic enzymes as regulators of the pool size of tricarboxylic acid-cycle intermediates in the perfused rat heart. *Biochem. J* **243**, 853-857 (1987).

276. Panchal, A.R. et al. Partitioning of pyruvate between oxidation and anaplerosis in swine hearts. *American Journal of Physiology-Heart and Circulatory Physiology* **279**, H2390-H2398 (2000).
277. Yang, Z., Lanks, C.W. & Tong, L. Molecular mechanism for the regulation of human mitochondrial NAD(P)+-dependent malic enzyme by ATP and fumarate. *Structure* **10**, 951-960 (2002).
278. Yang, Y. et al. Metabolic reprogramming for producing energy and reducing power in fumarate hydratase null cells from hereditary leiomyomatosis renal cell carcinoma. *Plos One* **8**, e72179 (2013).
279. Nielsen, F., Mikkelsen, B.B., Nielsen, J.B., Andersen, H.R. & Grandjean, P. Plasma malondialdehyde as biomarker for oxidative stress: reference interval and effects of life-style factors. *Clinical Chemistry* **43**, 1209-1214 (1997).
280. Hoshijima, M. & Chien, K.R. Mixed signals in heart failure: cancer rules. *J Clin Invest* **109**, 849-55 (2002).
281. Piao, L. et al. Cardiac glutaminolysis: a maladaptive cancer metabolism pathway in the right ventricle in pulmonary hypertension. *J Mol Med (Berl)* **91**, 1185-97 (2013).
282. Ashrafian, H. & Neubauer, S. Metabolomic profiling of cardiac substrate utilization fanning the flames of systems biology? *Circulation* **119**, 1700-1702 (2009).
283. Winter, G. & Kromer, J.O. Fluxomics - connecting 'omics analysis and phenotypes. *Environ Microbiol* **15**, 1901-16 (2013).
284. Dunn, W.B., Broadhurst, D.I., Atherton, H.J., Goodacre, R. & Griffin, J.L. Systems level studies of mammalian metabolomes: the roles of mass spectrometry and nuclear magnetic resonance spectroscopy. *Chem Soc Rev* **40**, 387-426 (2011).
285. Brown, S.C., Kruppa, G. & Dasseux, J.L. Metabolomics applications of FT-ICR mass spectrometry. *Mass Spectrom Rev* **24**, 223-31 (2005).
286. Nikolaev, E.N., Kostyukevich, Y.I. & Vladimirov, G.N. Fourier transform ion cyclotron resonance (FT ICR) mass spectrometry: Theory and simulations. *Mass Spectrom Rev* (2014).
287. Kamleh, M.A., Dow, J.A. & Watson, D.G. Applications of mass spectrometry in metabolomic studies of animal model and invertebrate systems. *Brief Funct Genomic Proteomic* **8**, 28-48 (2009).
288. Lu, W., Bennett, B.D. & Rabinowitz, J.D. Analytical strategies for LC-MS-based targeted metabolomics. *J Chromatogr B Analyt Technol Biomed Life Sci* **871**, 236-42 (2008).
289. Tan, B., Lu, Z., Dong, S., Zhao, G. & Kuo, M.S. Derivatization of the tricarboxylic acid intermediates with O-benzylhydroxylamine for liquid chromatography-tandem mass spectrometry detection. *Anal Biochem* **465C**, 134-147 (2014).
290. Klein, S. & Heinzle, E. Isotope labeling experiments in metabolomics and fluxomics. *Wiley Interdiscip Rev Syst Biol Med* **4**, 261-72 (2012).
291. Chokkathukalam, A., Kim, D.H., Barrett, M.P., Breitling, R. & Creek, D.J. Stable isotope-labeling studies in metabolomics: new insights into structure and dynamics of metabolic networks. *Bioanalysis* **6**, 511-24 (2014).
292. Griffin, J.L., Atherton, H., Shockcor, J. & Atzori, L. Metabolomics as a tool for cardiac research. *Nature Reviews Cardiology* **8**, 630-643 (2011).
293. Des Rosiers, C., Labarthe, F., Lloyd, S.G. & Chatham, J.C. Cardiac anaplerosis in health and disease: food for thought. *Cardiovasc Res* **90**, 210-9 (2011).
294. Metallo, C.M., Walther, J.L. & Stephanopoulos, G. Evaluation of 13C isotopic tracers for metabolic flux analysis in mammalian cells. *J Biotechnol* **144**, 167-74 (2009).

295. Crown, S.B., Ahn, W.S. & Antoniewicz, M.R. Rational design of (1)(3)C-labeling experiments for metabolic flux analysis in mammalian cells. *BMC Syst Biol* **6**, 43 (2012).
296. Riazi, R. et al. Probing pyruvate metabolism in normal and mutant fibroblast cell lines using 13C-labeled mass isotopomer analysis and mass spectrometry. *Mol Genet Metab* **98**, 349-55 (2009).
297. Tyler, D.J. Cardiovascular Applications of Hyperpolarized MRI. *Curr Cardiovasc Imaging Rep* **4**, 108-115 (2011).
298. Schroeder, M.A. et al. Real-time assessment of Krebs cycle metabolism using hyperpolarized 13C magnetic resonance spectroscopy. *FASEB J* **23**, 2529-38 (2009).
299. Gallagher, F.A. et al. Production of hyperpolarized [1,4-13C2]malate from [1,4-13C2]fumarate is a marker of cell necrosis and treatment response in tumors. *Proc Natl Acad Sci U S A* **106**, 19801-6 (2009).
300. Ussher, J.R., Jaswal, J.S. & Lopaschuk, G.D. Pyridine nucleotide regulation of cardiac intermediary metabolism. *Circ Res* **111**, 628-41 (2012).
301. Pound, K.M. et al. Substrate-enzyme competition attenuates upregulated anaplerotic flux through malic enzyme in hypertrophied rat heart and restores triacylglyceride content: attenuating upregulated anaplerosis in hypertrophy. *Circ Res* **104**, 805-12 (2009).
302. Sorokina, N. et al. Recruitment of compensatory pathways to sustain oxidative flux with reduced carnitine palmitoyltransferase I activity characterizes inefficiency in energy metabolism in hypertrophied hearts. *Circulation* **115**, 2033-41 (2007).
303. Keller, K.E., Doctor, Z.M., Dwyer, Z.W. & Lee, Y.-S. SAICAR induces protein kinase activity of PKM2 that is necessary for sustained proliferative signaling of cancer cells. *Mol Cell* **53**, 700-709 (2014).
304. Keller, K.E., Tan, I.S. & Lee, Y.-S. SAICAR stimulates pyruvate kinase isoform M2 and promotes cancer cell survival in glucose-limited conditions. *Science* **338**, 1069-1072 (2012).
305. Eberling, P. & Koivisto, V. Physiological importance of dehydroepiandrosterone. *The Lancet* **343**, 1479-1481 (1994).
306. Savineau, J.-P., Marthan, R. & Dumas de la Roque, E. Role of DHEA in cardiovascular diseases. *Biochemical Pharmacology* **85**, 718-726 (2013).
307. Samaras, N., Samaras, D., Frangos, E., Forster, A. & Philippe, J. A review of age-related dehydroepiandrosterone decline and its association with well-known geriatric syndromes: is treatment beneficial? *Rejuvenation Research* **16**, 285-294 (2013).
308. Traish, A.M., Kang, H.P., Saad, F. & Guay, A.T. Dehydroepiandrosterone (DHEA)—A precursor steroid or an active hormone in human physiology (CME). *The journal of sexual medicine* **8**, 2960-2982 (2011).
309. Webb, S.J., Geoghegan, T.E., Prough, R.A. & Michael Miller, K.K. The biological actions of dehydroepiandrosterone involves multiple receptors. *Drug Metab Rev* **38**, 89-116 (2006).
310. Tagashira, H., Bhuiyan, S., Shioda, N. & Fukunaga, K. Distinct cardioprotective effects of 17beta-estradiol and dehydroepiandrosterone on pressure overload-induced hypertrophy in ovariectomized female rats. *Menopause* **18**, 1317-26 (2011).
311. Liu, D. & Dillon, J.S. Dehydroepiandrosterone stimulates nitric oxide release in vascular endothelial cells: evidence for a cell surface receptor. *Steroids* **69**, 279-89 (2004).
312. Lee, R., Margaritis, M., Channon, K.M. & Antoniades, C. Evaluating oxidative stress in human cardiovascular disease: methodological aspects and considerations. *Curr Med Chem* **19**, 2504-20 (2012).

313. Corton, J.M., Gillespie, J.G., Hawley, S.A. & Hardie, D.G. 5-Aminoimidazole-4-Carboxamide Ribonucleoside - a Specific Method for Activating Amp-Activated Protein-Kinase in Intact-Cells. *European Journal of Biochemistry* **229**, 558-565 (1995).
314. Hardie, D.G. AMPK-Sensing Energy while Talking to Other Signaling Pathways. *Cell Metab* **20**, 939-952 (2014).
315. Ahmad, F. et al. Increased alpha2 subunit-associated AMPK activity and PRKAG2 cardiomyopathy. *Circulation* **112**, 3140-8 (2005).
316. Blair, E. et al. Mutations in the gamma(2) subunit of AMP-activated protein kinase cause familial hypertrophic cardiomyopathy: evidence for the central role of energy compromise in disease pathogenesis. *Hum Mol Genet* **10**, 1215-20 (2001).
317. Hastie, C.J., McLauchlan, H.J. & Cohen, P. Assay of protein kinases using radiolabeled ATP: a protocol. *Nat Protoc* **1**, 968-71 (2006).
318. Ono, H., Yoshimura, N., Sato, M. & Tuboi, S. Translocation of proteins into rat liver mitochondria. Existence of two different precursor polypeptides of liver fumarase and import of the precursor into mitochondria. *Journal of Biological Chemistry* **260**, 3402-3407 (1985).
319. Suzuki, Y. et al. An upstream open reading frame and the context of the two AUG codons affect the abundance of mitochondrial and nuclear RNase H1. *Molecular and Cellular Biology* **30**, 5123-5134 (2010).
320. Peabody, D.S. Translation initiation at non-AUG triplets in mammalian cells. *Journal of Biological Chemistry* **264**, 5031-5035 (1989).
321. Regev-Rudzki, N., Yogev, O. & Pines, O. The mitochondrial targeting sequence tilts the balance between mitochondrial and cytosolic dual localization. *Journal of Cell Science* **121**, 2423-2431 (2008).
322. Burak, E., Yogev, O., Sheffer, S., Schueler-Furman, O. & Pines, O. Evolving dual targeting of a prokaryotic protein in yeast. *Molecular biology and evolution* **30**, 1563-1573 (2013).
323. Dinur-Mills, M., Tal, M. & Pines, O. Dual Targeted Mitochondrial Proteins Are Characterized by Lower MTS Parameters and Total Net Charge. *Plos One* **3**, e2161 (2008).
324. Shlevin, L., Regev-Rudzki, N., Karniely, S. & Pines, O. Location-specific depletion of a dual-localized protein. *Traffic* **8**, 169-76 (2007).
325. Seddon, M., Shah, A.M. & Casadei, B. Cardiomyocytes as effectors of nitric oxide signalling. *Cardiovascular Research* **75**, 315-326 (2007).
326. Massion, P., Feron, O., Dessy, C. & Balligand, J.-L. Nitric oxide and cardiac function ten years after, and continuing. *Circulation Research* **93**, 388-398 (2003).
327. Nagasaka, H. et al. Nitric oxide synthesis in ornithine transcarbamylase deficiency: Possible involvement of low no synthesis in clinical manifestations of urea cycle defect. *The Journal of Pediatrics* **145**, 259-262 (2004).
328. Ong, S.-G. et al. HIF-1 reduces ischaemia–reperfusion injury in the heart by targeting the mitochondrial permeability transition pore. *Cardiovascular Research*, cvu172 (2014).
329. Eltzschig, H.K., Bratton, D.L. & Colgan, S.P. Targeting hypoxia signalling for the treatment of ischaemic and inflammatory diseases. *Nat Rev Drug Discov* **13**, 852-69 (2014).
330. Song, W. et al. Molecular mechanism of the E99K mutation in cardiac actin (ACTC Gene) that causes apical hypertrophy in man and mouse. *Journal of Biological Chemistry* **286**, 27582-27593 (2011).

331. Giordano, F.J. Oxygen, oxidative stress, hypoxia, and heart failure. *Journal of Clinical Investigation* **115**, 500-508 (2005).
332. Yu, Q. et al. Elimination of NADPH oxidase activity promotes reductive stress and sensitizes the heart to ischemic injury. *Journal of the American Heart Association* **3**, e000555 (2014).
333. Rose, B.A., Force, T. & Wang, Y. Mitogen-activated protein kinase signaling in the heart: angels versus demons in a heart-breaking tale. *Physiological reviews* **90**, 1507-1546 (2010).

9 APPENDIX

9.1 Metabolomics Results

Table 20 – Shows metabolites identified by Fourier transform ion cyclotron resonance (FT-ICR) mass spectrometry metabolomics to be significantly different in *Fh1*$^{f/f}$ *Cre/+* mice comparative to *Fh1*$^{f/f}$ controls
a. Molecular weight (Mz) ***b.*** Fold change in metabolite(s) in *Fh1*$^{f/f}$ *Cre/+* mice relative to *Fh1*$^{f/f}$ controls. ***c*** **.**False discovery rate (FDR) (p-value adjusted for multiple comparisons**)**

mz[a]	Fold change[b]	FDR[c]	Metabolite(s)	Metabolite Class
268.1525	1.59	0.025	2-Methylbutyroylcarnitine;Isovalerylcarnitine	Acyl carnitine
232.1542	1.72	0.019	Isobutyryl-L-carnitine;Butanoylcarnitine	Acyl carnitine
291.1293	3.13	0.018	Argininosuccinic acid	Amino acid and related metabolites
240.1015	1.33	0.015	Cystathionine	Amino acid and related metabolites
132.1018	1.39	0.018	Isoleucine;Leucine;Norleucine	Amino acid and related metabolites
150.0582	1.35	0.047	Methionine	Amino acid and related metabolites
295.1136	0.60	0.023	N-Glycosyl-L-asparagine	Amino acid and related metabolites
206.1004	1.32	0.043	Tryptophan	Amino acid and related metabolites
215.1398	0.78	0.031	Dethiobiotin	Biotin metabolism
333.2797	0.77	0.047	docosatetraenoic acid	Fatty acids and related metabolites
348.2881	0.68	0.023	Eicosapetaenoic acid ethyl ester;Docosapentaenoic acid	Fatty acids and related metabolites
350.3044	0.79	0.018	Eicosatrienoylethanolamide;docosatetraenoic acid	Fatty acids and related metabolites
263.1679	1.47	0.015	hydroxy-tetradecadienoate	Fatty acids and related metabolites
415.2196	0.75	0.034	PC(48:0)	Glycerophospholipids
488.3128	0.75	0.023	PE(P-18:0/0:0)	Glycerophospholipids
542.3214	1.35	0.035	LysoPC(18:2)	Lysoglycerophospholipid
567.3248	0.81	0.048	LysoPC(20:4);LysoPC(18:1)	Lysoglycerophospholipid

mz[a]	Fold change[b]	FDR[c]	Metabolite(s)	Metabolite Class
594.3504	0.68	0.015	LysoPC(22:4)	Lysoglycerophospholipid
593.3394	0.60	0.026	LysoPC(22:5)	Lysoglycerophospholipid
568.3394	0.66	0.039	LysoPC(22:6)	Lysoglycerophospholipid
474.2594	1.45	0.041	LysoPE (16:1)	Lysoglycerophospholipid
498.2585	1.43	0.028	LysoPE(16:0)	Lysoglycerophospholipid
570.2764	0.73	0.026	LysoPE(18:1)	Lysoglycerophospholipid
478.2926	1.61	0.023	LysoPE(18:2)	Lysoglycerophospholipid
572.2949	0.61	0.030	LysoPE(20:3);LysoPE(18:0)	Lysoglycerophospholipid
301.1244	0.71	0.048	8-Hydroxy-2'-Deoxyguanosine;8-Hydroxy-deoxyguanosine;Guanosine;;	Nucleosides, nucleotides, purines and related metabolites
487.0667	1.35	0.015	adenylo-succinate	Nucleosides, nucleotides, purines and related metabolites
444.0313	1.41	0.027	GDP	Nucleosides, nucleotides, purines and related metabolites
246.08	0.81	0.036	Pseudouridine;Uridine	Nucleosides, nucleotides, purines and related metabolites
384.1149	2.17	0.015	Succinyladenosine	Nucleosides, nucleotides, purines and related metabolites
455.0808	3.03	0.018	(S)-2-[5-Amino-1-(5-phospho-D-ribosyl)imidazole-4-carboxamido]succinate;1-(5'-Phosphoribosyl)-5-amino-4-(N-succinocarboxamide)-imidazole;5'-phosphoribosyl-4-(N-succinocarboxamide)-5-aminoimidazole	Others and mixed classes
118.0861	1.37	0.036	2-Amino-2-methylbutanoate;4-amino-pentanoic acid;4-Methylaminobutyrate;5-Aminopentanoate;Betaine;Norvaline;Valine	Others and mixed classes
650.1128	0.66	0.033	4,5-Dihydro-4-hydroxy-5-S-glutathionyl-benzo[a]pyrene;"7,8-Dihydro-7-hydroxy-8-S-glutathionyl-benzo[a]pyrene";;dTDP-alpha-D-desosamine;dTDP-D-desosamine;dTDP-L-megosamine	Others and mixed classes
483.0551	1.85	0.039	FARNESYL THIOPYROPHOSPHATE;N-Pyridoxyl-2-methyl-L-glutamic acid-5'-monophosphate	Others and mixed classes
145.0494	1.30	0.047	Methylglutaconic acid;Dimethylmaleate;Methyleneglutarate;Methylitaconate	Others and mixed classes
413.0874	1.39	0.017	Nicotine glucuronide	Others and mixed classes
359.1035	0.61	0.047	Pantetheine 4'-phosphate	Panththenate, CoA metabolism and related metabolites

mz[a]	Fold change[b]	FDR[c]	Metabolite(s)	Metabolite Class
230.1579	0.69	0.047	L-isoleucyl-L-proline;L-leucyl-L-proline	Peptides
632.2271	0.79	0.030	QYNAD	Peptides
413.1993	0.74	0.039	17-Hydroxypregnenolone sulfate	Sterols and steroids
562.2447	1.61	0.041	Choloyl-taurine;1alpha,25-dihydroxy-24-oxo-23-azavitamin D2	Sterols and steroids
611.2484	0.79	0.047	dolichyl diphosphate	Sterols and steroids
393.034	1.82	0.023	2-(alpha-D-Galactosyl)-sn-glycerol 3-phosphate;2-(beta-D-Glucosyl)-sn-glycerol 3-phosphate;"alpha-D-Galactosyl-(1,1')-sn-glycerol 3-phosphate";sn-glycero-3-Phospho-1-inositol	Sugars and related metabolites
345.0772	0.63	0.011	2-(beta-D-Glucosyl)-sn-glycerol;3-beta-D-galactosyl-sn-glycerol;3-beta-D-Galactosyl-sn-glycerol;Galactosylglycerol	Sugars and related metabolites
470.0901	0.60	0.005	3-(4-Deoxy-beta-D-gluc-4-enuronosyl)-N-acetyl-D-glucosamine;"4-Deoxy-beta-D-gluc-4-enuronosyl-(1,3)-N-acetyl-D-galactosamine";Chondroitin	Sugars and related metabolites
485.1202	1.25	0.035	Chitobiose	Sugars and related metabolites
275.0069	1.49	0.023	L-Iduronate 2-sulfate;O2-Sulfo-Glucuronic Acid	Sugars and related metabolites

9.2 Invasive haemodynamic assessment of cardiac function

	Fh1$^{f/f}$	*Fh1$^{f/f}$ Cre/+*	*Fh1$^{f/f}$ KI^{FH}*	*Fh1$^{f/f}$ KI^{FHcyt}*	*Fh1$^{f/f}$ Cre/+ KI^{FH}*	*Fh1$^{f/f}$ Cre/+ KI^{FHcyt}*
MAP (mmHg)	74.5±7.7	57.43±12.4	66.6±10.5	71.9±8.1	65.8±11.4	63.7±12.4
LVSP (mmHg)	99.5±7.5	82.9±12.0	96.3±12.3	104.2±11.8	91.9±11.0	89.7±10.4
LVEDP (mmHg)	7.7±4.4	12.2±4.4	7.2±3.2	7.7±3.3	7.5±3.2	11.1±6.4
LVDevP (mmHg)	91.8±6.3	70.7±15.3	89.1±11.7	96.0±14.1	84.4±10.5	78.6±11.5
Heart rate (bpm)	463.9±70.1	415.9±65.9	424.8±64.0	447.6±58.5	414.7±52.9	467.4±70.0
dP/dt_{max} (mmHg/s)	7084±1593	4872±2307	6745±1654	7382±2170	5887±1672	5181±1889
dP/dt_{min} (mmHg/s)	-6920±2301	-3428±1827	-6821±2158	-6490±2946	-5879±1708	-3815±1419

Table 21 – Invasive haemodynamic assessment of cardiac function demonstrates no significant differences in the cardiac function from *Fh1$^{f/f}$* controls with *KI^{FH}* or *KI^{FHcyt}* expression and whilst *KI^{FH}* ameliorates the *Fh1$^{f/f}$ Cre/+* phenotype

Values given as mean ± standard deviation of the mean. Mean arterial pressure (MAP). LVSP (Left ventricular systolic pressure). LVEDP (Left ventricular end-diastolic pressure). LVDevP (Left ventricular developed pressure). $+dP/dt_{max}$ (Maximal rate of pressure increase). $–dP/dt_{max}$ (Maximal rate of pressure decrease).